



<https://theses.gla.ac.uk/>

Theses Digitisation:

<https://www.gla.ac.uk/myglasgow/research/enlighten/theses/digitisation/>

This is a digitised version of the original print thesis.

Copyright and moral rights for this work are retained by the author

A copy can be downloaded for personal non-commercial research or study, without prior permission or charge

This work cannot be reproduced or quoted extensively from without first obtaining permission in writing from the author

The content must not be changed in any way or sold commercially in any format or medium without the formal permission of the author

When referring to this work, full bibliographic details including the author, title, awarding institution and date of the thesis must be given

Enlighten: Theses

<https://theses.gla.ac.uk/>  
[research-enlighten@glasgow.ac.uk](mailto:research-enlighten@glasgow.ac.uk)

# **Molecular architecture of the human pyruvate dehydrogenase complex**



**Michaela Smolle**

**Division of Biochemistry & Molecular Biology, IBL  
University of Glasgow**

**A thesis submitted for the degree of  
*Doctor of Philosophy***

ProQuest Number: 10391433

All rights reserved

INFORMATION TO ALL USERS

The quality of this reproduction is dependent upon the quality of the copy submitted.

In the unlikely event that the author did not send a complete manuscript and there are missing pages, these will be noted. Also, if material had to be removed, a note will indicate the deletion.



ProQuest 10391433

Published by ProQuest LLC (2017). Copyright of the Dissertation is held by the Author.

All rights reserved.

This work is protected against unauthorized copying under Title 17, United States Code  
Microform Edition © ProQuest LLC.

ProQuest LLC.  
789 East Eisenhower Parkway  
P.O. Box 1346  
Ann Arbor, MI 48106 – 1346

GLASGOW  
UNIVERSITY  
LIBRARY:

Für meine Mutter.

“The scientist does not study nature because it is useful; he studies it because he delights in it, and he delights in it because it is beautiful. If nature were not beautiful, it would not be worth knowing, and if nature were not worth knowing, life would not be worth living.”

Jules Henri Poincaré (1854-1912)

# Acknowledgements

A great many thanks to my supervisors, Prof. Gordon Lindsay and Dr. Olwyn Byron for their continuing support, enthusiasm, inspiration and sense of humour shown throughout the course of this project. I have really enjoyed working with you!

Ich möchte mich vor allem bei meiner Mutter und Grossmutter für ihre liebevolle Unterstützung und Geduld bedanken, fürs Verwöhnen wann auch immer ich zuhause war, sowie für die Möglichkeit meinen eigenen Weg einzuschlagen.

I would like to thank Michael for being who he is, loving and understanding. It may only have been a short while, but it made all the difference.

A big thank you to Nat, Meera, Alex, Jenny, Hannah and Maria for all the good times we spent together, all the laughs, visits and gallons of coffee as well as cheering me up during a few bad patches. I would be a lot less sane without you! I would also like to thank my friends Christoph and Ulli back home in Austria who have brightened many a rainy morning with their emails over the last eight years.

I would like to thank everyone in L233, past and present, in particular, Alison, Donna, Heather, Hiba and Zhenbo for putting up with all my questions over the years and the many Friday lunches spent in Ichiban. You made the lab a great place to work in!

## Acknowledgements

Thanks to Marcelo and Alex, who have both patiently explained various bits of computer programs to me over the years, as well as for the nice times and doing those insane all-nighters with noisy movies while collecting data at various synchrotrons round Europe.

I would like to thank Mrs. Margaret Nutley and Prof. Alan Cooper, University of Glasgow for performing all ITC experiments, and Dr. Sharon Kelly, University of Glasgow for carrying out the CD experiments.

Thanks also to Dr. Günter Grossmann at the SRS Daresbury, UK for his invaluable advice and dedication, to Dr. Phil Callow from the Institut Laue-Langevin in Grenoble, France for his help with everything to do with SANS, to Dr. Dimitri Svergun and Dr. Manfred Rössle from the EMBL Outstation at the Deutsches Elektronen Synchrotron in Hamburg, Germany and to Dr. Heinz Amenitsch at ELETTRA in Trieste, Italy.

# Abstract

Mammalian pyruvate dehydrogenase multi-enzyme complex (PDC) is a key metabolic assembly responsible for the maintenance of glucose homeostasis. PDC comprises a central pentagonal dodecahedral core of 60 dihydrolipoamide acetyltransferase (E2) and 12 E3 binding protein (E3BP) molecules. E2 is thought to form the edges of the icosahedral core structure while a single E3BP molecule is thought to occupy each of the 12 pentagonal faces. Both E2 and E3BP have a modular multi-domain organisation and are responsible for the attachment of up to 30 pyruvate decarboxylase (E1) heterotetramers and 6-12 dihydrolipoamide dehydrogenase (E3) homodimers, respectively. The formation of highly specific E2/E1 and E3BP/E3 subcomplexes is characteristic of PDC from eukaryotes and critical for normal complex function.

This thesis describes the large-scale purification of tagged, recombinant human PDC proteins E2, E3 and E3BP as well as several truncated E2 and E3BP constructs. Due to the limited solubility of recombinant human E1, the protein was obtained by purification from native bovine PDC. The ability to purify relatively large amounts of proteins enabled the characterisation of the individual proteins as well as their subcomplexes using a variety of biochemical and biophysical techniques.

Truncated E3BP, full-length E3 and their resultant subcomplex were analysed in solution by analytical ultracentrifugation (AUC). The stoichiometry of interaction was determined to be 2:1 (E3BP:E3) using native polyacrylamide gel

electrophoresis (PAGE), AUC, isothermal titration calorimetry (ITC) and small angle x-ray scattering (SAXS), thus implying the existence of a network of E3 “cross-bridges” linking pairs of E3BP molecules across the surface of the E2 core assembly. A low resolution structure for E3 obtained by SAXS shows significant differences to the crystal structures obtained previously for human and yeast E3s. The low resolution structure determined for the truncated E3BP/E3 subcomplex was surprisingly anisometric, indicating the asymmetric distribution of lipoyl domains within the subcomplex. Rigid-body modelling with homology models of E3 and the individual E3BP domains resulted in a structure in which only one of the E3BP lipoyl domains was docked into the E3 active site. This new level of architectural complexity in mammalian PDC has important implications for the catalytic mechanism, overall complex efficiency and regulation by its intrinsic PDC kinase.

Analogous to the E3BP/E3 subcomplex, initial investigations of the interaction of truncated E2 with E1 using AUC also seem to indicate the formation of 2:1 subcomplexes, cross-linking neighbouring E2 molecules on the PDC core surface. However, the relatively low stability of bovine E1 – as revealed by AUC – has hampered the investigation of E2/E1 subcomplex formation.

Until recently, mammalian PDC core was thought to consist of 60 E2 and 12 E3BP molecules (the “addition” model). The relatively recent publication of an alternative, “substitution” model by Hiromasa and colleagues (2004), where E3BP replaces 12 E2 molecules, resulting in a 48:12 (E2:E3BP) core structure, initiated the search for experimental approaches able to distinguish between the PDC core models. SAXS data, even in conjunction with *ab initio* reconstruction techniques were deemed insufficient for this purpose, while small angle neutron scattering (SANS) in combination with contrast matching of selectively deuterated components gave promising initial results and could be used in future for the resolution of this fundamental problem in PDC subunit organisation.

---

# Contents

<b>Acknowledgements</b>	iii
<b>Abstract</b>	v
<b>Abbreviations</b>	xiv
<b>List of Figures</b>	xvi
<b>1 Introduction to pyruvate dehydrogenase complex structure and function</b>	
1.1 Multi-enzyme complexes	1
1.2 2-oxoacid dehydrogenase complexes	2
1.3 Reaction mechanism of PDC	3
1.4 PDC component structural information	3
1.4.1 Basic core organisation	3
1.4.2 Dihydrolipoylacetyltransferase (E2)	5
1.4.2.1 The lipoyl domain	5
1.4.2.2 The subunit binding domain	7
1.4.2.3 The C-terminal domain	8
1.4.2.4 The linker regions	10
1.4.3 E3 binding protein	10
1.4.4 Pyruvate decarboxylase (E1)	13

1.4.5	Dihydropyridine dehydrogenase (E3)	15
1.5	Association of E1 and E3 with the PDC core	17
1.6	Substrate channelling and active site coupling	19
1.7	Regulation of PDC activity	21
1.8	PDC and disease	24
1.8.1	Genetic disorders	24
1.8.2	Metabolism and Alzheimer's disease	26
1.8.3	Primary biliary cirrhosis	27
1.8.4	PDC and diabetes	27
1.8.5	Chemical modification of PDC	28
1.9	Project aims	29
<b>2</b>	<b>Biophysical techniques</b>	
2.1	Introduction	31
2.2	Analytical ultracentrifugation	31
2.2.1	Sedimentation velocity	32
2.2.1.1	SV data analysis	35
2.2.2	Sedimentation equilibrium	37
2.2.2.1	SE data analysis	38
2.3	Isothermal titration calorimetry	39
2.4	Small angle x-ray scattering	41
2.4.1	Scattering by an ideal monodisperse solution	41
2.4.2	SAXS data treatment	44
2.4.2.1	Data processing	44
2.4.2.2	Direct modelling or the $p(r)$ function	45
2.4.2.3	<i>Ab initio</i> modelling	48
2.4.2.4	Addition of loops and domains	49
2.4.2.5	Rigid-body modelling	50
2.5	Small angle neutron scattering	51
2.5.1	Contrast variation	51

### 3 Materials and methods

3.1	Molecular biology	53
3.1.1	Plasmid preparation	53
3.1.2	Agarose gel electrophoresis	53
3.1.3	DNA extraction from agarose gels	54
3.1.4	Polymerase chain reaction	54
3.1.5	Restriction digests and plasmid ligation	54
3.2	Bacterial strains	55
3.2.1	Competent cells and transformations	55
3.3	Protein methods	55
3.3.1	Protein overexpression and solubility	55
3.3.2	Protein purification	56
3.3.2.1	Cell lysis	56
3.3.2.2	Metal chelate affinity chromatography	56
3.3.2.3	HQ anion exchange chromatography	57
3.3.2.4	S cation exchange chromatography	58
3.3.2.5	GST purification of XLD	59
3.3.2.6	Gel filtration chromatography	59
3.3.2.7	Purification of PDC from bovine heart	59
3.3.2.8	Sucrose gradient centrifugation	60
3.3.3	Removal of His-tags	60
3.3.4	Dialysis	61
3.3.5	Polyacrylamide gel electrophoresis	61
3.3.5.1	SDS polyacrylamide gel electrophoresis	61
3.3.5.2	Native polyacrylamide gel electrophoresis	61
3.3.6	Determination of protein concentration	61
3.3.7	Modification of proteins with mPEG maleimide	62
3.4	Biophysical methods	62
3.4.1	Calculation of buffer densities and viscosities	62
3.4.2	Sedimentation velocity analytical ultracentrifugation	62

---

3.4.3	Sedimentation equilibrium analytical ultracentrifugation	63
3.4.4	Isothermal titration calorimetry	64
3.4.5	Small angle x-ray scattering	64
3.4.6	Small angle neutron scattering	65
3.4.7	Circular dichroism	66
3.5	Computational methods	66
3.5.1	Sequence alignments	66
3.5.2	Homology modelling	67
3.5.3	Hydrodynamic modelling	67
3.5.4	<i>Ab initio</i> modelling from SAXS data	68
3.5.5	Calculation of scattering curves from structural models	68
3.5.6	Rigid body modelling	68
3.5.7	Superimposition of different model structures	69
<b>4</b>	<b>Cloning, protein overexpression and purification</b>	
4.1	Introduction	70
4.2	Materials and methods	72
4.2.1	Subcloning of the subunit binding domain of E3BP (XSBD)	72
4.2.2	Protein overexpression	74
4.2.3	Protein purification	74
4.3	Results and discussion	75
4.3.1	Subcloning of the subunit binding domain of E3BP (XSBD)	75
4.3.2	Protein overexpression of XSBD	78
4.3.3	Protein purification	78
4.3.3.1	Purification of E3	78
4.3.3.2	Purification of XDD	79
4.3.3.3	Purification of XSBD	80
4.3.3.4	Purification of GST-XLD	80
4.3.3.5	Purification of E2DD	83
4.3.3.6	Purification of E1	83

---

4.3.3.7	Purification of bovine E2/E3BP	84
4.3.3.8	Purification of human E2/E3BP	84
4.3.3.9	Yields	88
<b>5</b>	<b>Characterisation of the human E3BP/E3 subcomplex and its constituents</b>	
5.1	Introduction	89
5.2	Materials and methods	91
5.2.1	Sample preparation	91
5.2.2	Gel filtration analysis	92
5.2.3	Native PAGE.	92
5.2.4	Sedimentation velocity analytical ultracentrifugation	92
5.2.5	Sedimentation equilibrium analytical ultracentrifugation	93
5.2.6	Isothermal titration calorimetry	94
5.2.7	Small angle x-ray scattering and <i>ab initio</i> modelling	95
5.2.8	Homology, hydrodynamic and rigid body modelling	96
5.2.9	Determination of the XDD redox state	96
5.3	Results and analysis	97
5.3.1	Characterisation of E3	97
5.3.1.1	Homology modelling	97
5.3.1.2	Analytical ultracentrifugation and hydrodynamic modelling	97
5.3.1.3	Small angle x-ray scattering and <i>ab initio</i> modelling	101
5.3.2	Characterisation of XDD and XSBD	103
5.3.2.1	Homology modelling of XDD and XSBD	103
5.3.2.2	Analytical ultracentrifugation of XDD	103
5.3.2.3	Small angle x-ray scattering of XDD	107
5.3.2.4	Circular dichroism of XSBD	108
5.3.2.5	Analytical ultracentrifugation of XSBD	108
5.3.2.6	SAXS and <i>ab initio</i> modelling of XSBD	110

5.3.3	Cross-bridge formation between E3BP and E3	111
5.3.3.1	Generation of the XDD/E3 complex	111
5.3.3.2	Gel filtration analysis of XDD/E3 and its constituent proteins	113
5.3.3.3	Native PAGE	114
5.3.3.4	Analytical ultracentrifugation of XDD/E3	114
5.3.3.5	Isothermal titration calorimetry	118
5.3.3.6	Homology and hydrodynamic modelling of XDD/E	118
5.3.3.7	SAXS and rigid body modelling	121
5.3.3.8	Redox states of lipoyl domains within the XDD/E3 complex	122
5.3.3.9	Interaction of E3 with the E3BP lipoyl domain	124
5.4	Discussion	125
<b>6 Characterisation of the E2/E1 subcomplex and its constituents</b>		
6.1	Introduction	128
6.2	Materials and methods	130
6.2.1	Sample preparation	130
6.2.2	Gel filtration analysis	130
6.2.3	Sedimentation velocity analytical ultracentrifugation	130
6.2.4	Sedimentation equilibrium analytical ultracentrifugation	131
6.2.5	Isothermal titration calorimetry	132
6.2.6	Small angle x-ray scattering and <i>ab initio</i> modelling	132
6.2.7	Homology and hydrodynamic modelling	133
6.3	Results and analysis	133
6.3.1	Characterisation of E1	133
6.3.1.1	Analytical ultracentrifugation and hydrodynamic modelling of E1	133
6.3.2	Characterisation of E2DD	135
6.3.2.1	Analytical ultracentrifugation of E2DD	135

6.3.2.2	Small angle x-ray scattering of E2DD	136
6.3.3	Cross-bridge formation of E2DD and E1	137
6.3.3.1	Generation of the E2DD/E1 complex	137
6.3.3.2	Gel filtration analysis of E2DD/E1 and its constituents	138
6.3.3.3	Analytical ultracentrifugation of E2DD/E1	139
6.3.3.4	Isothermal titration calorimetry	143
6.3.3.5	Homology modelling of E2DD/E1	144
6.3.3.6	Small angle x-ray scattering of E2DD/E1	146
6.4	Discussion	148
<b>7 PDC core structure</b>		
7.1	Introduction	152
7.2	Materials and methods	153
7.2.1	Sample preparation	153
7.2.2	Sedimentation velocity	154
7.2.3	Small angle scattering	154
7.2.3.1	Small angle x-ray scattering	154
7.2.3.2	Small angle neutron scattering	154
7.3	Results and discussion	155
7.3.1	Sedimentation velocity of recombinant E2/E3BP core	155
7.3.2	Small angle scattering of PDC and PDC core	157
7.3.2.1	Small angle x-ray scattering	157
7.3.2.2	Small angle neutron scattering	161
<b>8</b>	<b>Conclusions</b>	<b>167</b>
	<b>Bibliography</b>	<b>171</b>

# Abbreviations

$A_{260}$	Absorbance at 260 nm
$A_{280}$	Absorbance at 280 nm
aa	Amino acid
Abs	Absorbance
Amp	Ampicillin
AUC	Analytical ultracentrifugation
BCDC	Branched-chain 2-oxoacid dehydrogenase complex
BSA	Bovine serum albumin
Chl	Chloramphenicol
CoA	Coenzyme A
Cryo-EM	Cryo-electron microscopy
CTD	C-terminal domain
CV	Column volume
DTT	Dithiothreitol
Int	Interference
IPTG	Isopropyl- $\beta$ -D-thiogalactose
ITC	Isothermal titration calorimetry
Kan	Kanamycin
$KPO_4$	Potassium phosphate
LB	Luria-Bertani broth (10 g bacto-tryptone, 5 g bacto-yeast extract, 5 g NaCl made up to 1 l with de-ionised water)
LD	Lipoyl domain
MEB	20 mM MOPS, 2 mM EDTA, 0.01% (w/v) sodium azide, pH 7.4

## Abbreviations

---

2-OADC	2-oxoacid dehydrogenase complex
OD	Optical density
OGDC	2-oxoglutarate dehydrogenase complex
PAGE	Polyacrylamide gel electrophoresis
PBS	Phosphate buffered saline (140 mM NaCl, 2.7 mM KCl, 10 mM Na <sub>2</sub> HPO <sub>4</sub> , 1.8 mM KH <sub>2</sub> PO <sub>4</sub> , pH 7.3)
PDC	Pyruvate dehydrogenase complex
PEB	50 mM potassium phosphate, 2 mM EDTA, pH 7.4
rpm	Revolutions per minute
S	Svedberg units (10 <sup>-13</sup> sec)
SANS	Small angle neutron scattering
SAXS	Small angle x-ray scattering
SBD	Subunit binding domain
SDS	Sodium dodecyl sulphate
SE	Sedimentation equilibrium
SPR	Surface plasmon resonance
SV	Sedimentation velocity
TCA	Tricarboxylic acid
ThDP	Thiamine diphosphate
TE	10 mM Tris-HCl, 1 mM EDTA, pH 7.2
TEB	50 mM Tris-HCl, 2 mM EDTA, pH 7.5
TEBS50	50 mM Tris-HCl, 50 mM NaCl, 2 mM EDTA, pH 7.5
TEBS100	50 mM Tris-HCl, 100 mM NaCl, 2 mM EDTA, pH 7.5
UV	Ultraviolet

# List of Figures

1.1	Involvement of 2-oxoacid dehydrogenases in cellular metabolism	2
1.2	PDC reaction scheme	3
1.3	E2 core formation in 2-oxoacid dehydrogenase complexes	4
1.4	Domain structure of E2 and E3BP	5
1.5	Structure of the human inner E2 lipoyl domain	6
1.6	Structure of the E2 subunit binding domain from <i>B. stearothermophilus</i>	8
1.7	Models of PDC core formation	12
1.8	Structure of human pyruvate decarboxylase	14
1.9	Crystal structure of human E3	16
1.10	Schematic representation of protein associations in eukaryotic PDC	18
1.11	Subcomplex formation of E1 and E3 with E2-SBD in <i>B. stearothermophilus</i>	18
1.12	Active site coupling in <i>B. stearothermophilus</i> PDC	20
1.13	Short-term regulation of PDC activity	23
2.1	Analytical ultracentrifugation	33
2.2	Isothermat titration calorimetry	40
2.3	Schematic representation of SAXS	42
2.4	Scattering curves and distance distribution functions of geometrical bodies	46
2.5	Neutron scattering length densities of biological macromolecules in solution	52

---

4.1	Primer sequences for the subcloning of XSBD	72
4.2	Production of pET30-XSBD	77
4.3	SDS PAGE analysis of XSBD overexpression and solubility	78
4.4	Purification of E3	79
4.5	Purification of XDD	81
4.6	Purification of XSBD	82
4.7	Purification of GST-XLD by GST affinity chromatography	83
4.8	Purification of E2DD	85
4.9	Purification of bovine E1	86
4.10	Purification of bovine E2/E3BP core	86
4.11	Purification of human E2/E3BP core	87
5.1	E3BP constructs used in this project	91
5.2	Sequence alignment and homology modelling of human E3	98
5.3	Sedimentation velocity analysis of E3	99
5.4	Sedimentation equilibrium analysis of E3	100
5.5	Small angle x-ray scattering of E3	101
5.6	Superimposition of the homology and <i>ab initio</i> models of E3	102
5.7	Sequence alignment of E2 and E3BP	104
5.8	Sedimentation velocity analysis of XDD	105
5.9	Sedimentation equilibrium analysis of XDD	106
5.10	Small angle x-ray scattering of XDD	108
5.11	Sedimentation velocity analysis of XSBD	109
5.12	Sedimentation equilibrium analysis of XSBD	110
5.13	Small angle x-ray scattering of XSBD	111
5.14	Superimposition of the homology and <i>ab initio</i> models of XSBD	112
5.15	Purification of the XDD/E3 subcomplex	112
5.16	Molecular weight determination using gel filtration chromatography	113
5.17	Native PAGE of different XSBD:E3 and XDD:E3 stoichiometries	114
5.18	Sedimentation velocity analysis of XDD:E3 stoichiometric mixtures and purified XDD/E3 complex	115

---

5.19	Sedimentation equilibrium analysis of XDD:E3 stoichiometries	117
5.20	Isothermal titration calorimetry of XDD and E3	119
5.21	Homology models generated for the XDD/E3 complex	120
5.22	Small angle x-ray scattering of XDD/E3	121
5.23	Superimposition of XDD/E3 models from <i>ab initio</i> and rigid body modelling	123
5.24	SDS PAGE analysis of mPEG maleimide treated XDD	124
6.1	Sedimentation velocity analysis of bovine E1	134
6.2	Sedimentation velocity analysis of E2DD	135
6.3	Sedimentation equilibrium analysis of E2DD	136
6.4	Small angle x-ray scattering curve of E2DD	137
6.5	Generation of the E2DD/E1 complex	138
6.6	Molecular weight determination using gel filtration chromatography	139
6.7	Sedimentation velocity analysis of E2DD:E1 stoichiometries	140
6.8	Sedimentation velocity analysis of purified E2DD/E1 complex	142
6.9	Sedimentation equilibrium analysis of purified E2DD/E1 complex	142
6.10	Isothermal titration calorimetry of E2DD and E1	144
6.11	Models of the human E2DD/E1 complex	145
6.12	Small angle x-ray scattering of E2DD/E1	146
6.13	Superimposition of E2DD/E1 and <i>ab initio</i> models	147
6.14	Cross-bridge formation in human PDC	150
7.1	Sedimentation velocity analysis of human E2/E3BP core	156
7.2	Small angle x-ray scattering from PDC and PDC cores	158
7.3	<i>Ab initio</i> models of PDC and PDC cores	160
7.4	Matchpoint determination for E3 and E2/E3BP core	162
7.5	Small angle neutron scattering of E2/E3BP core and E2/E3BP•E3	163
7.6	Reconstructions of E2/E3BP and matched E2/E3BP•E3 from SANS data	164

# Chapter 1

## Introduction to pyruvate dehydrogenase complex structure and function

### 1.1 Multi-enzyme complexes

Multi-enzyme complexes combine two or more enzymatic activities within a single assembly. Direct consequences of the evolution of these multi-component complexes are the concomitant development of substrate channelling and active site coupling: products from one reaction can be shuttled effectively from one active site to the next, greatly reducing diffusion times and thus increasing enzyme efficiency, as well as protecting (possibly unstable) intermediates from outside influence.

The 2-oxoacid dehydrogenase complexes are a prime example of multi-subunit, high molecular weight assemblies that consist of three different enzymes (E1, E2 and E3). The lipoamide cofactor associated with the central E2 moiety is required to visit the active sites of all three enzymes via its so-called "swinging arm". Therefore, these complexes serve as excellent models for the investigation of protein-protein interactions within multi-enzyme complexes, enzyme cooperativity, active site coupling, and any associated regulatory advantages. This chapter will provide insights into the metabolic role and importance of 2-oxoacid dehydrogenase complexes, as well as their structural organisation, with particular emphasis on the eukaryotic pyruvate dehydrogenase complex.

## 1.2 2-oxoacid dehydrogenase complexes

The family of 2-oxoacid dehydrogenase complexes consists of three different members, all of which play important metabolic roles: pyruvate dehydrogenase complex (PDC) links glycolysis with the tricarboxylic acid (TCA) cycle (Fig. 1.1) by catalysing the decarboxylation of pyruvate and concomitant generation of acetyl-CoA. As no net production of carbohydrates is possible from acetyl-CoA, PDC is the main regulator of glucose homeostasis in mammals (Sugden & Holness, 2003). Analogously, 2-oxoglutarate dehydrogenase (OGDC) decarboxylates its substrate 2-oxoglutarate, an important intermediate of the TCA cycle, and forms succinyl-CoA (Sheu & Blass, 1999). Finally, the branched-chain 2-oxoacid dehydrogenase complex (BCDC) catalyses the irreversible step in the catabolism of branched chain amino acids, such as leucine, isoleucine and valine (Patel & Harris, 1995).

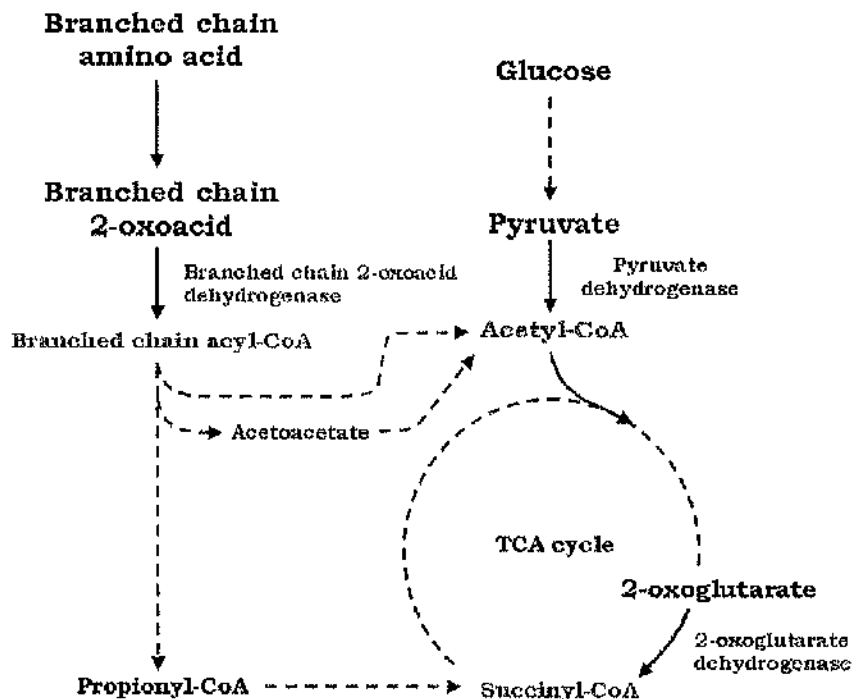


**Figure 1.1** Involvement of 2-oxoacid dehydrogenases in cellular metabolism  
Enzymes are shown in blue and their products in green.

### 1.3 Reaction mechanism of PDC

PDC catalyses the conversion of pyruvate to acetyl-CoA and NADH in three distinct enzymatic steps (Fig. 1.2). Initially, pyruvate is decarboxylated by the thiamine diphosphate (ThDP)-dependent enzyme pyruvate decarboxylase (E1, EC 1.2.4.1) which also catalyses the subsequent transfer of the resulting acetyl group from ThDP onto the lipoamide moiety of dihydrolipoamide acetyltransferase (E2, EC 2.3.1.1) in a reductive acetylation step. This generates a stable transition state where the acetyl group is initially covalently bound to the S<sup>8</sup> position of the lipoamide group (Yang & Frey, 1986). In the presence of CoASH, the latter also interacts with E2 which then catalyses the transacetylation reaction to form acetyl-CoA. Otherwise, the acetyl groups remain bound to the lipoamide cofactor. In the final step the E2 dihydrolipoamide is reoxidised by dihydrolipoamide dehydrogenase (E3, EC 1.8.1.4). E3 transfers electrons via a redox-active pair of cysteines to the isoalloxazine ring of FAD and onto the terminal electron acceptor NAD<sup>+</sup>. The overall reaction can be summarised as

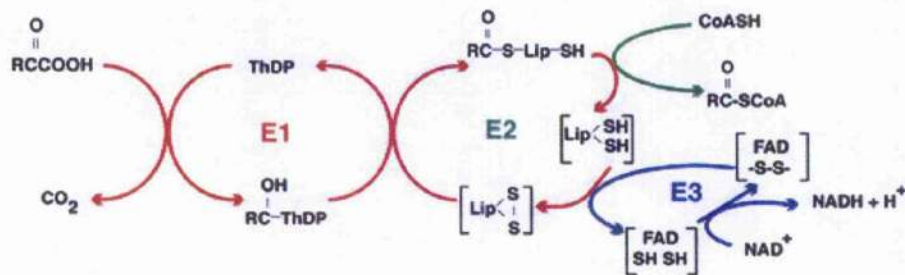


**Figure 1.2** PDC reaction scheme  
Adapted from Milne et al. (2002).

## 1.4 PDC component structural information

### 1.4.1 Basic core organisation

All three 2-oxoacid complexes display a similar mode of quasi-symmetric organisation of their subunits E1, E2 and E3 into high molecular weight assemblies of 4-11 MDa. Apart from playing a role in the catalytic mechanism, E2 also forms a central 24-meric or 60-meric core,

## 1.4 PDC component structural information

consistent with octahedral (432) or icosahedral (532) symmetry, respectively (Fig. 1.3) (Oliver & Reed, 1982; Wagenknecht et al., 1990). For OGDC and BCDC, as well as PDC from Gram-negative bacteria, the E2 core is assembled as an octahedron. Only in Gram-positive bacteria and eukaryotes does the PDC core assume an icosahedral morphology. The E2 core also provides the framework for the interaction with the other two enzymes, E1 and E3 (Patel & Roche, 1990; Perham, 2000). Furthermore, eukaryotic PDC contains an additional protein, E3 binding protein (E3BP, previously designated protein X) which is associated with the E2 core (De Marcucci & Lindsay, 1985; Jilka et al., 1986) and is responsible for binding E3, as suggested by its name.

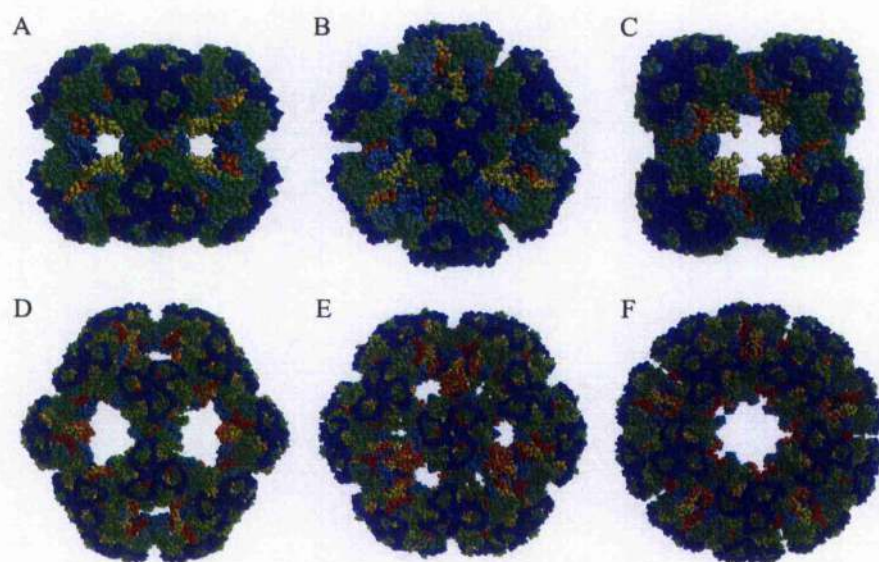


**Figure 1.3 E2 core formation in 2-oxoacid dehydrogenase complexes**

The octahedral core of *Azotobacter vinelandii* PDC (PDB ID 1EAA) is shown with different views along the two- (A), three- (B) and four-fold (C) axes of symmetry. Similarly, the icosahedral core of *Bacillus stearothermophilus* PDC (PDB ID 1B5S) is depicted with representations along the two- (D), three- (E) and five-fold (F) axes of symmetry. All E2 molecules are coloured identically (N-terminus to C-terminus).

### 1.4.2 Dihydrolipoylacetyltransferase (E2)

E2 (and E3BP) exhibit a similar, modular, multi-domain structure (Fig. 1.4) (Borges et al., 1990): the N-terminal arm visits all three active sites in turn and contains one to three lipoyl domains (LD) – the exact number varies from organism to organism (Reed & Hackert, 1990; Perham, 1991) – and is followed by the peripheral subunit binding domain (SBD) necessary for association with E1 and/or E3 (Packman & Perham, 1986; Hipps et al., 1994; Lessard & Perham, 1995; Westphal et al., 1995). A large C-terminal domain (CTD) of approximately 250 residues is responsible for self-association (Reed & Hackert, 1990; Perham, 1991) and also contains the acetyltransferase active site. All domains are interconnected by long, extended linker regions of ca. 30 residues in length, resulting in a flexible, yet extended ensemble that radiates outwards from the core and confers the large conformational flexibility associated with the N-terminal “swinging arm”.

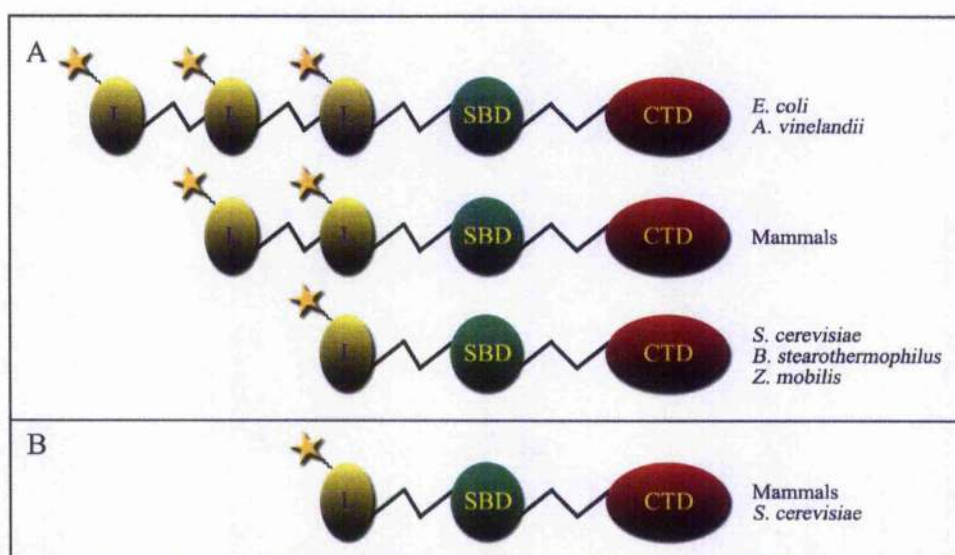


**Figure 1.4 Domain structure of E2 and E3BP**

Schematic representation of the domain structure of E2 (A) and E3BP (B). The number of lipoyl domains (L) varies from one to three for different organisms. Lipoyl groups are indicated by a star. The subunit binding (SBD) and C-terminal domains (CTD) are also shown.

#### 1.4.2.1 The lipoyl domain

Due to its small size (ca. 80 residues) and ability to fold independently the lipoyl domain was amenable to structure determination using NMR spectroscopy. The three-dimensional

## 1.4 PDC component structural information

structures of E2-LD from *B. stearrowthermophilus* PDC (Dardel et al., 1993), *E. coli* PDC and OGDC (Green et al, 1995; Ricaud et al., 1996), *A. vinelandii* PDC and OGDC (Berg et al., 1995; 1996; 1997) as well as human PDC (Howard et al., 1998) have been solved. All solution structures are very similar to each other even when the sequence identity between different lipoyl domains is rather low, e.g. between E2-LD of *A. vinelandii* PDC and OGDC (25%) (Berg et al., 1997). Similarly, no significant differences were recorded in the NMR spectra for lipoylated and non-lipoylated protein (Dardel et al., 1991; Berg et al., 1994).

The LD folds into a flattened  $\beta$ -barrel comprising two four-stranded, antiparallel  $\beta$ -sheets with a two-fold quasi-symmetry axis (Fig.1.5). The lysine residue to be lipoylated is situated within a conserved DKA motif at the tip of a type I  $\beta$ -turn. Lipoylation can only occur if the lysine residue is present at the tip of the turn; movement of the lysine by a single residue towards the N- or C-terminus abolishes lipoylation (Wallis & Perham, 1994). Mutagenesis studies have also established that neither the aspartate nor the alanine within the DKA motif are required for lipoylation. However, both residues are necessary to support reductive acetylation at wild-type levels (Wallis & Perham, 1994; Jones et al., 2000).

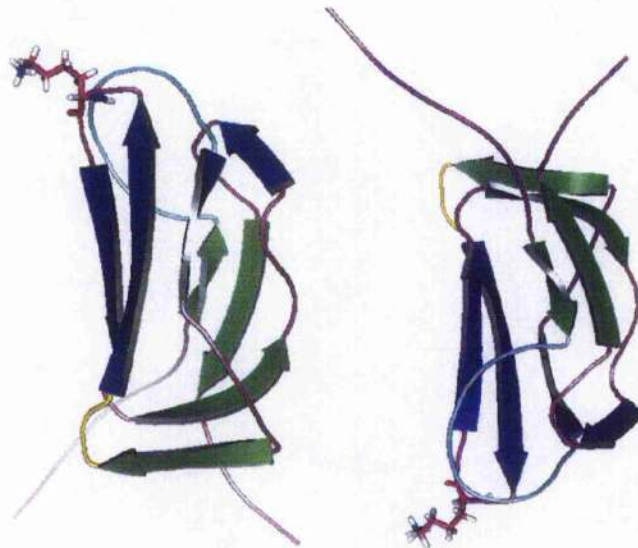


**Figure 1.5 Structure of the human inner E2 lipoyl domain**

Two views of the NMR structure solved for non-lipoylated human E2-LD (PDB ID 1FYC) are shown. The two  $\beta$ -sheets are depicted in green (strands 1, 3, 6, 8) and blue (strands 2, 4, 5, 7). The lysine residue that becomes lipoylated is drawn in stick representation. The surface loop involved in determining E1-specific binding is coloured cyan, while the equivalent loop in the other "half" of the domain is drawn in yellow.

## 1.4 PDC component structural information

---

Despite the large structural similarities between different LDs, they are nevertheless very specific with regard to interactions with their cognate E1 enzymes. Discrimination of different E1 proteins is possible due to a variable surface loop connecting strands 1 and 2. Deletion of this loop in the E2-LD of *B. stearrowthermophilus* PDC results in non-recognition of the LD by E1 and concomitantly abrogates reductive acetylation completely (Wallis et al., 1996).

In *E. coli* covalent modification of the apodomain with exogenous lipoate is catalysed by LplA lipoate protein ligase using a two-step reaction mechanism (Morris et al., 1994). When no free lipoic acid is available from the growth medium, protein lipoylation proceeds via a second, relatively poorly understood pathway using endogenously synthesised lipoate: Lipoyl groups are formed by sulfur insertion into octanoyl entities catalysed by LipA (Miller et al., 2000), while LipB – a lipoyl (octanoyl) transferase – is responsible for attachment of the lipoyl (octanoyl) group to the apoprotein (Morris et al., 1995; Jordan & Cronin, 1997; 2003). In contrast, protein lipoylation in mammals is catalysed by two separate enzymes acting in concert: The ATP-dependent lipoate-activating enzyme promotes formation of lipoyl-AMP, which is subsequently transferred onto the apoprotein by lipoyl-AMP: $N^{\epsilon}$ -lys lipoyltransferase (Fujiwara et al., 1994; 1996).

### 1.4.2.2 The subunit binding domain

With approximately 35-50 amino acids, the subunit binding domain (SBD) is one of the smallest known protein domains capable of independent folding without the stabilising effects of disulphide bridges, ligands or cofactors (Perham, 1991; Spector et al., 1998; 1999a). As its name suggests, the SBD is required for interaction with the E1 and E3 enzymes: in *B. stearrowthermophilus* the E2-SBD is capable of binding both E1 and E3, while in mammalian PDC E2-SBD only mediates interaction with E1 whereas E3 binds to the related E3BP-SBD.

The structure of *B. stearrowthermophilus* SBD has been determined independently in solution (Fig. 1.6) (Kalia et al., 1993) as well as in association with either E1 (Frank et al., 2005) or E3 (Mande et al., 1996). Very recently, the crystal structure of human E3BP-SBD complexed with E3 has also been published (Ciszak et al., 2006). The *B. stearrowthermophilus* and human SBD structures superimpose quite well with a rms deviation of 1-1.4 Å (Ciszak et al., 2006). SBD consists of two short, parallel  $\alpha$ -helices connected to a very short  $3^{10}$ -helix by two loops.

## 1.4 PDC component structural information

When superimposing the *B. stearotherophilus* solution and crystal structures (the human crystal structure was not available in the PDB data bank at the time of writing), differences in structure are mainly observed in loop L2 and may represent conformational changes upon E3 binding or the innate flexibility of the loop itself. The SBD structure is stabilised mainly by hydrophobic interactions between the two parallel helices H1 and H2. A second hydrophobic core is formed by loops L1 and L2, although a network of hydrogen bonds around a highly conserved aspartate at position 34 also contributes to domain stability (Kalia et al., 1993; Mande et al., 1996). Indeed, if Asp34 is replaced by asparagine the domain is still able to fold, but is much less stable (Spector et al. 1998), while replacement by a hydrophobic residue such as valine prevents protein folding entirely (Spector et al. 1999b).

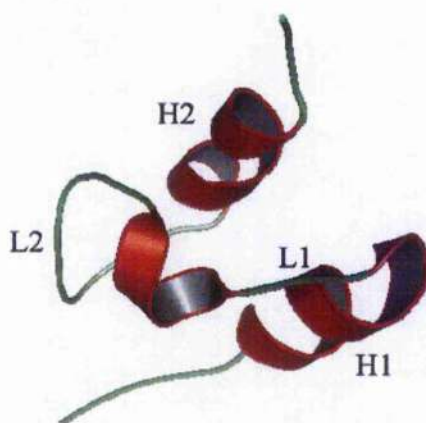


**Figure 1.6** Structure of the E2 subunit binding domain from *B. stearotherophilus*  
The solution structure of E2-SBD from *B. stearotherophilus* was solved by NMR (PDB ID 2PDD) (Kalia et al., 1993). The two  $\alpha$ -helices (H1 & 2) are joined to a short  $3^{10}$ -helix by two loops (L1 & 2).

### 1.4.2.3 The C-terminal domain

The C-terminal domain (CTD) of E2 is capable of self-aggregation and forms the central PDC core by association into trimers which are located at each vertex. Eight trimers are necessary for octahedral core formation in *A. vinelandii* (Mattevi et al., 1992a; 1993b), while 20 trimers associate into the icosahedral cores of *B. stearotherophilus* (Izard et al., 1999; Milne et al., 2002), yeast (Stoops et al., 1992; 1997) and bovine PDC (Behal et al., 1994; Zhou et al., 2001b). The trimers are fairly loosely associated via bridges, 20 Å in length, along the two-fold axes, creating highly dynamic structures. Cryo-electron microscopy (cryo-EM) studies have shown that size variabilities of up to 20% exist between individual molecules which

## 1.4 PDC component structural information

---

equates to a difference in diameter of up to 40 Å and first introduced the concept of PDC core “breathing” (Zhou et al., 2001a; Kong et al., 2003). These inherent, concerted movements are thought to be important for complex function.

Structures obtained for core particles from protein crystallography and cryo-EM represent the PDC core as a hollow and highly solvated particle (Fig. 1.3). The crystal structure solved for the octahedral core of *A. vinelandii* shows that the cube has an outer diameter of ca. 125 Å, while the inner diameter is approximately 46 Å and the “window” on each of the six faces measures 30 Å (Mattevi et al., 1992a). For the crystal structure of the icosahedral core of *B. stearothermophilus* these measurements increase to 237 Å and 118 Å for the outer and inner diameters, respectively, while each of the 12 windows is 52 Å across (Izard et al., 1999). These dimensions agree roughly with those determined for bovine (Zhou et al., 2001b) and *Saccharomyces cerevisiae* E2 cores (Stoops et al., 1992) using cryo-EM although both particles seem to be somewhat larger than suggested from the *B. stearothermophilus* atomic structure, representing the natural size variability of PDC core and/or crystal packing forces.

Interestingly, E2 amino acid sequences from organisms that form either octahedral or icosahedral cores align reasonably well. Even though the final particle shape is very different, only small changes in the subunit interfaces are thought to be sufficient for a change in symmetry. Izard and co-workers (1999) found that the formation of octahedral and icosahedral cores is the result of only a few differences in the mode of E2 interaction: two truly equivalent and several quasi-equivalent contacts were ascertained from a comparison of *A. vinelandii* and *B. stearothermophilus* cores. Differences in the E2 primary sequence could not be used to predict symmetry. These observations are further underlined by the fact that even though E2 core symmetry is roughly divided between Gram-negative bacteria, and Gram-positive bacteria and eukaryotes, respectively, exceptions do exist: for example, PDC from *Zymomonas mobilis*, a Gram-negative bacterium, is organised around an icosahedral core, as is that of another Gram-negative bacterium, *Thiobacillus ferrooxidans* (Neveling et al., 1998a; 1998b).

The acetyltransferase active site is located in a 30 Å long channel at the E2-CTD subunit interface and runs across the trimer. A conserved sequence motif, DHRXXDG, is thought to accommodate the histidine and aspartate necessary for catalysis (Radford et al., 1987).

## 1.4 PDC component structural information

---

Interestingly, it is evident from the crystal structure that the two substrates for transacetylation, CoASH and the acetylated LD have to approach the E2 active site from opposite directions (Izard et al., 1999): CoASH binds to the inside of the E2 core, while acetyl-LD interacts with the outside (Mattevi et al., 1992a; 1993b; 1993c).

### 1.4.2.4 The linker regions

The lipoyl and subunit binding domains of E2 (and E3BP) are separated from the core and each other by a set of linker regions of 30-50 amino acids in length. The linkers are rich in alanine, proline and charged amino acid residues. Analogous domains often adopt an  $\alpha$ -helical secondary structure, but NMR spectra confirmed that the linkers are solvent-exposed and disordered although they do not form random coils (Radford et al., 1989a): in particular, almost all Ala-Pro peptide bonds (> 95%) adopted the *trans* configuration as opposed to a value of ca. 80% expected for random coils. This feature results in a more rigid and extended structure (Texter et al., 1988; Radford et al., 1989a; Green et al., 1992).

The linker regions are essential for PDC function as it is due to their inherent flexibility that the LD can visit the three different active sites within the PDC complex (Perham et al., 1981; Green et al., 1992). Indeed, binding of specific antibody fragments to the linker regions in *E. coli* E2 abolished active site-coupling and critically diminished overall PDC activity while individual enzyme activities were unaffected (Radford et al., 1989b). Analysis of deletion mutants has furthermore shown that the number of residues present in the outer linker can be halved before PDC activity is severely compromised (Miles et al., 1988), indicating that overall linker length can be accommodated to some degree.

### 1.4.3 E3 binding protein

E3BP is an integral component of the PDC core in eukaryotes. However, its position within the core with respect to E2 has not been completely resolved. E3BP (protein X) was initially identified as a contaminant of bovine PDC preparations and thought to be an E2 proteolytic product. Its separate role was only established when western blotting with anti-sera raised against individual components of the PDC failed to elicit a reaction (De Marcucci & Lindsay,

## 1.4 PDC component structural information

---

1985; Jilka et al., 1986) and peptide-mapping and radiolabelling confirmed E3BP as a fourth PDC component (De Marcucci et al., 1986; Hodgson et al., 1986; Jilka et al., 1986; Neagle et al., 1989). Homology between E3BP and E2 was finally established when the *Pdx1* gene encoding *S. cerevisiae* E3BP was cloned and analysed (Behal et al., 1989). The human gene was cloned subsequently (Harris et al., 1997) and confirmed the high similarity between the two proteins: interestingly, the N-terminus encoding the lipoyl and subunit binding domains displays relatively high sequence identity with the equivalent E2 domains (46% and 38%) in both human and yeast PDC. Similarly, the human E3BP C-terminal domain is highly homologous when compared to E2 (50%), while the E3BP-CTD from yeast is quite different (Harris et al., 1997). The histidine within the E2 active site motif DHRXXDD associated with acetyltransferase activity is replaced by serine in human E3BP, while it is completely absent in the yeast protein (Harris et al., 1997) and E3BP is therefore unable to sustain enzyme activity.

To ascertain E3BP function was more difficult, in part because the protein is tightly associated with E2 and could not be separated unless very harsh, denaturing conditions were used. Protection of E3BP from proteolysis in the presence of E3 first suggested its involvement in binding (Rahmatullah et al., 1989a). Subsequently, selective proteolysis of E3BP within the bovine PDC using ArgC (Neagle & Lindsay, 1991) as well as disruption of the yeast *Pdx1* gene (Lawson et al., 1991a) demonstrated the important role of E3BP in mediating high-affinity binding of E3. These observations were later confirmed by *in vitro* binding studies (McCartney et al., 1997). Whether E3BP performs other tasks during the PDC catalytic cycle is still unclear: the E3BP-LD can be reductively acetylated by E1 (De Marcucci et al., 1986; Jilka et al., 1986; Rahmatullah & Roche, 1987). Also, deletion or selective removal of E2-LD in yeast and bovine PDC resulted in a reduction of PDC activity to 10-15% of that of the wild-type complex (Rahmatullah et al., 1990; Lawson et al., 1991b), indicating that E3BP is able to interact with all PDC active sites. In a reverse experiment selective removal of E3BP-LD also caused a loss of PDC activity (Gopalakrishnan et al., 1989; Powers-Greenwood et al., 1989), but this was later shown to be primarily due to reduced E3 binding (Sanderson et al., 1996a). More recent cell culture experiments did not reveal any change in complex activity using an E3BP mutant that cannot be lipoylated and is therefore unable to accept acetyl-groups from E1 (Seyda & Robinson, 2000). Given the central metabolic role of PDC, it is reasonable to hypothesise that E2 and E3BP lipoyl

## 1.4 PDC component structural information

domains may serve a somewhat redundant function, representing a fail-safe mechanism. Whether preferred routes of interaction exist in the native complex between the LD of E3BP and E3, and E2-LD and E1, respectively, may therefore be difficult to answer in the future.

The number of E3BP molecules present per core was established as 12 for bovine (Sanderson et al., 1996b) and yeast PDC (Maeng et al., 1994) and are thought to be associated with each of the icosahedral faces (Fig. 1.7A). Stoops and co-workers (1997) obtained cryo-EM reconstructions of the *S. cerevisiae* E2 C-terminal domain, as well as complexes formed between E2-CTD and E3BP-CTD, E2-CTD and E3BP, and E2-CTD and E3BP/E3, respectively. They located E3BP on the inside of the E2 core, apparently associated with the tips of E2 trimers, while E3 was also anchored on the inside of the core. However, the organisation of yeast and mammalian cores cannot be compared directly, as it has been shown previously that E3BP can be integrated into established yeast E2 cores (Maeng et al., 1994) while co-expression of the mammalian proteins is critical for correct E2/E3BP core formation (Li et al., 1992; Behal et al., 1994; McCartney et al., 1997). Also, the CTD from yeast E3BP is considerably smaller (28 kDa) than its mammalian counterpart (35 kDa) and displays less sequence similarity to its cognate E2 than the human protein, which may account for differences in behaviour.

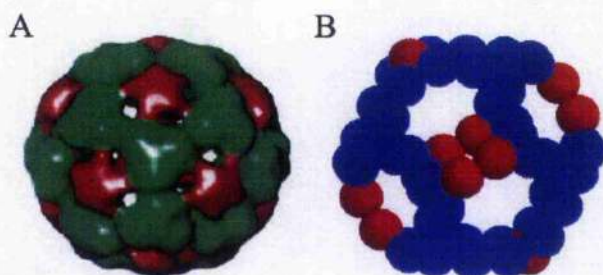


**Figure 1.7 Models of PDC core formation**

The addition (A) and substitution (B) models for E3BP core integration. In the addition model 12 E3BP molecules are thought to bind to the 12 faces of the 60-meric E2 core, while they are envisaged to replace 12 E2 molecules in the substitution model, the core being formed from 48 E2 and 12 E3BP molecules.

Diagrams were adapted from Reed (2001) and Hiromasa et al. (2004).

More recently, Hiromasa and colleagues (2004) proposed an alternative model for human PDC core organisation based on analytical ultracentrifugation (AUC) and small angle x-ray scattering (SAXS). They proposed that 12 E3BP molecules replace an equivalent number of

E2 molecules (Fig. 1.7B), rather than add to the 60-meric E2 core. More experiments are required to firmly establish which, if either, model is correct.

### 1.4.4 Pyruvate decarboxylase (E1)

E1 is a substrate-specific and ThDP-dependent decarboxylase that catalyses the first rate-limiting and irreversible step in the PDC catalytic cycle (Danson et al., 1978; Cate et al., 1980; Berg et al., 1998). The reaction proceeds via a two-step mechanism of initial pyruvate decarboxylation and subsequent transfer of the ThDP-bound acetyl group (2- $\alpha$ -hydroxyethylidene-ThDP) onto E2-lipoamide in a reductive acetylation step (Kern et al., 1997; Pan & Jordan, 1968). E1 occurs as an  $\alpha_2$  homodimer in all 2-oxoacid complexes with octahedral cores or as an  $\alpha_2\beta_2$  heterotetramer in organisms with icosahedral core symmetry – mammalian BCDC E1 is an exception as it is also present as a heterotetramer. However, in both cases E1 has two chemically equivalent active sites, each of which is associated with a ThDP cofactor and  $Mg^{2+}$  ion necessary for catalysis.

A number of crystal structures have been published over the last few years including PDC E1 from *E. coli* (Arjunan et al., 2002) and humans (Ciszak et al., 2001; 2003), as well as 2-oxoisovalerate dehydrogenase from *Pseudomonas putida* (Ævarsson et al., 1999) and human BCDC E1 (Ævarsson et al., 2000). Comparison of these and structures available for other ThDP-dependent enzymes such as transketolase (Fiedler et al., 2002) and benzylformate decarboxylase (Hasson et al., 1998) emphasise their similarities with respect to structure and function (Hawkins et al., 1989; Muller et al., 1993; Schellenberger, 1998).

E1  $\alpha$  and  $\beta$  subunits are arranged tetrahedrally and related by a non-crystallographic two-fold symmetry axis (Fig. 1.8). The active sites, each of which is associated with one ThDP molecule, are located at the interface of the  $\alpha$ - and  $\beta$ -subunits at the bottom of a 20 Å funnel-shaped tunnel and accessible to the E2 lipoyl-lysine moiety which must be fully extended (Ævarsson et al., 1999). This structural feature also explains why free lipoamide is not a good substrate for E1 (Liu et al., 2001) and why mutation of the amino acids surrounding the

lipoyl-lysine cause a drop in the acetylation rate as these residues must be in transient contact with E1 (Wallis & Perham, 1994).

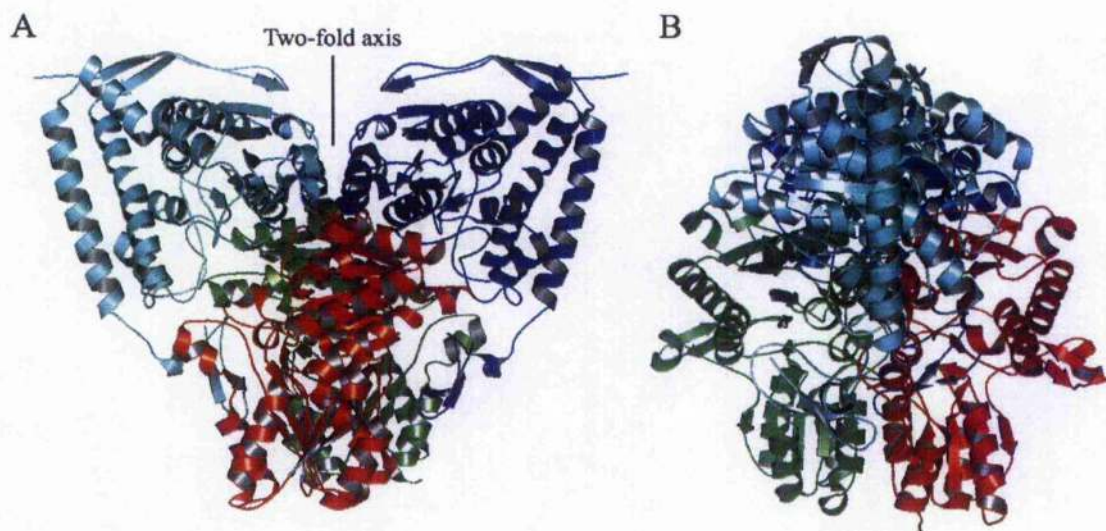


**Figure 1.8** Structure of human pyruvate decarboxylase

Front (A) and side (B) views of the crystal structure solved for the human E1 heterotetramer (PDB ID 1NI4). The two  $\alpha$  subunits are shown in light and dark blue, the  $\beta$  subunits are coloured red and green. The two-fold axis is indicated.

The formation of E1 tetramers proceeds via association of two  $\alpha\beta$  heterodimers. Interaction of the  $\alpha$  and  $\beta$  subunits is promoted mainly by hydrophobic contacts. In particular, both the  $\alpha$  and  $\beta$  subunit each contain a helix with a  $G\Phi XXG$  motif (where  $\Phi$  is usually a  $\beta$ -branched chain amino acid). These helices are thought to tightly pack against each other in order to form a fairly rigid dimer interface, implicated in the concerted movement of each  $\alpha\beta$  heterodimer with respect to the other within the E1 heterotetramer (Kleiger et al., 2001; Ciszak et al., 2003). However, it has also been speculated that three E1 residues (Glu59, Gly136, Val138) are able to detect the catalytic state of the cofactors and to coordinate E1 catalytic action via movement of the pair of helices interconnected by the  $G\Phi XXG$  motif (Ciszak et al., 2003). Although both active sites are chemically equivalent, their dynamic non-equivalence has been established in a series of kinetic, spectral and biochemical experiments on pigeon E1 and other ThDP-dependent enzymes (Khailova & Korochkina, 1985; 1990; Yi et al., 1996; Kovina & Kochetov, 1998; Sergienko et al., 2000; 2002). Thus, one active site

## 1.4 PDC component structural information

---

catalyses the decarboxylation step while the other one concurrently reductively acetylates E2-lipoamide. Similarly, access to ThDP is granted to either pyruvate or the lipoyl-lysine moiety at any given moment, resulting in a flip-flop enzymatic mechanism. It was proposed that the two  $\alpha\beta$  heterodimers undergo a concerted shuttle-like motion causing a “push-and-pull” conformational change in both active sites (Ciszak et al., 2003). More recently however, Frank and colleagues (2004) highlighted the presence of a 20 Å tunnel lined with acidic residues connecting the two active sites. Binding of ThDP to apo-E1 is thought to abstract a single proton which subsequently serves as a means of communication between the two active sites by repeated shuttling through the tunnel, whereby the formation of activated ThDP provides the “molecular switch”. Convincing evidence for this type of active site communication is provided by mutants that had two tunnel residues far from the active site, Asp180 and Glu183 replaced with alanines or asparagine and glutamine, respectively. The rate of E1 decarboxylation was greatly reduced in both mutants (to 31% and 7%). Similarly, PDC function was severely affected when either mutant was used for the reconstitution of PDC from individual components. Overall activities were reduced to 12% and 3% for the D180R and E183Q E1 mutants, respectively, indicating that reductive acetylation of E2 was seriously impaired (Frank et al., 2004).

### 1.4.5 Dihydrolipoamide dehydrogenase (E3)

E3 is a flavoprotein and part of the family of pyridine nucleotide-disulphide oxidoreductases which catalyse electron transfer between pyridine nucleotides and disulphides. The E3 component is identical in all 2-oxoacid dehydrogenase complexes with the exception of *Pseudomonas putida* where multiple genes encode three separate enzymes (Reed, 1974; Carothers et al., 1989; Burns et al., 1989). In PDC it catalyses the reoxidation of the E2 dihydrolipoamide using a two step mechanism: first, two electrons are transferred from the reduced lipoamide group via a redox-active disulphide bridge onto FAD, forming a stable  $\text{EH}_2$  intermediate. The electrons are shared between the FAD and the reactive disulphide, resulting in a charge transfer complex formed between the thiolate anion and FAD cofactor which subsequently donates its electrons to  $\text{NAD}^+$  during the second step (Williams, 1965; 1992; Wilkinson & Williams, 1981).

## 1.4 PDC component structural information

The three-dimensional structures of E3 from several different sources have been solved by x-ray crystallography (Fig.1.9), including E3 from *A. vinelandii* (Schierbeek et al., 1989; Mattevi et al., 1991), *Pseudomonas putida* (Mattevi et al., 1992b), *P. fluorescens* (Mattevi et al., 1993a), *B. stearothermophilus* (Mande et al., 1996), *S. cerevisiae* (Toyoda et al., 1998b) and most recently from humans (Brautigam et al., 2005). E3 tertiary structure is preserved in eukaryotic and prokaryotic E3 enzymes which align well despite a rather low overall amino acid sequence identity of approximately 40%. Major discrepancies are apparent mainly in the loop regions. Similar to other members of the same family, such as glutathione reductase (Schulz et al., 1978; Thieme et al., 1981; Karplus & Schulz, 1987), thioredoxin reductase (Kuriyan, 1991) or trypanothione reductase (Kuriyan et al., 1991), E3 consists of four different domains: the FAD domain (aa 1-150), the NAD domain (aa 151-208), the central domain (aa 281-350) and the interface domain (aa 351-474). E3 is an obligate homodimer that requires the presence of one non-covalently bound FAD per monomer for correct folding and dimerisation (Lindsay et al., 2000). Dimerisation occurs largely via contacts between the interface domains. The two monomers are related by a non-crystallographic two-fold axis. The FAD and NAD domains both display the characteristic  $\beta\alpha\beta$  Rossmann fold associated with proteins involved in nucleotide binding, while the central domain is responsible for binding to E2 or E3BP.

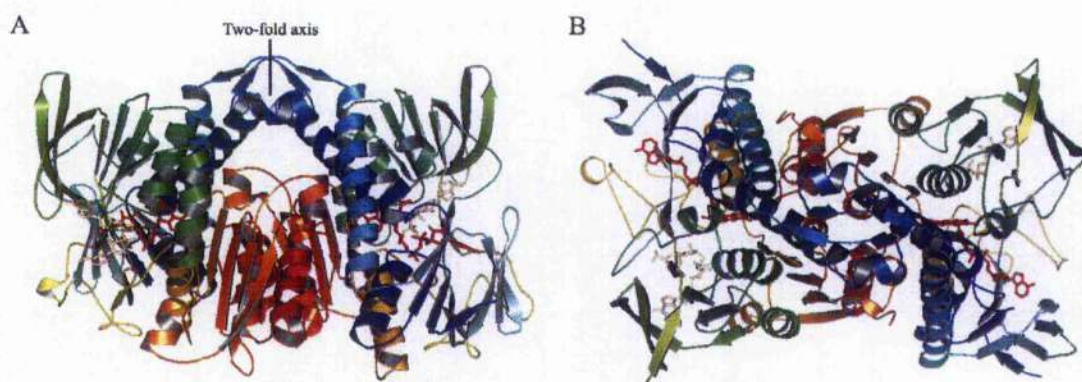


**Figure 1.9** Crystal structure of human E3

Front (A) and top (B) views of human E3 crystallised in the presence of NAD<sup>+</sup> (white) (PDB ID 1ZMC). Both monomers are coloured identically (N-terminus to C-terminus) and the quasi-symmetric two-fold axis is indicated. FAD is shown in red.

The two active sites are located separately at the subunit interface near the FAD cofactors. A redox-active pair of cysteines, Cys45 and Cys50 (residue numbering refers to the human

## 1.5 Association of E1 and E3 with the PDC core

---

protein) that forms the catalytically vital disulphide bridge, as well as the amino acid sequences requisite for FAD and NAD<sup>+</sup> binding are contributed from one subunit, while His452' and Glu457' are part of the other monomer. His452' is thought to act as a proton acceptor/donor during catalysis. Indeed, when the histidine is mutated to glutamine, E3 activity is almost completely abolished to levels of 0.2% of the wild-type enzyme. Similarly, replacement of Glu457 which forms a strong hydrogen bond with His452, by glutamine causes a reduction in activity of 72% (Kim & Patel, 1992; Liu et al., 1995b). Mutation of these two residues in E3 from other organisms and even in glutathione reductase have the same effect and explain their high degree of conservation (Deonarain et al., 1989; Berry et al., 1989; Williams et al., 1989).

During catalysis the lipoamide group has to enter either active site from a pocket on the Cys side of the flavin plane, approximately 15 Å from the E3 surface and therefore deep enough to accommodate the lipoyl-lysine swinging arm. The nicotinamide moiety of NAD<sup>+</sup> associates with a pocket on the other, *re* side of FAD (Mattevi et al., 1991; 1992b; 1993a; Toyoda et al., 1998b).

## 1.5 Association of E1 and E3 with the PDC core

In eukaryotes the E2/E3BP core of PDC provides the structural and mechanistic framework for the tight but non-covalent association of E1 and E3. The stability and overall subunit organisation of the complex is governed by specific and tight protein-protein interactions between E2-SBD and E1, and E3BP-SBD and E3, respectively (Fig. 1.10). However, in Gram-positive bacteria such as *B. stearothermophilus* E1 and E3 both associate with E2 (Fig. 1.11), as E3BP is a purely eukaryotic feature. Consequently, E1 and E3 have to compete for overlapping binding sites on E2; interaction of E2 with either E1 or E3 prevents complex formation with the other. Interestingly, PDC-deficient patients who totally lack the E3BP subunit possess partial complex activity (10-20% of controls) (Ling et al., 1998), apparently because the SBD of E2 has retained a limited ability to mediate low affinity E3 binding, in accordance with binding data obtained for human recombinant proteins *in vitro* using surface plasmon resonance (SPR) (Richards, 1999).

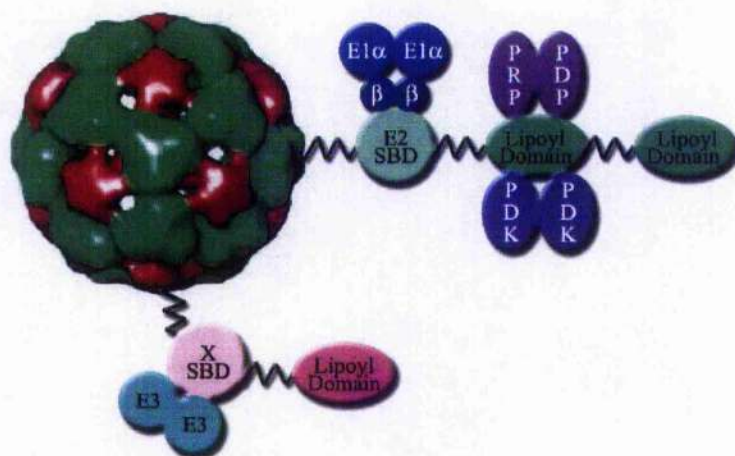


**Figure 1.10 Schematic representation of protein associations in eukaryotic PDC**  
 E1 (blue) binds to E2 (green), while E3BP (X; magenta) associates with E3 (cyan). PDC kinase (PDK) and phosphatase (PRP/PDP) interact with the inner E2-LD. The core is based on a cryo-EM reconstruction (Reed, 2001).

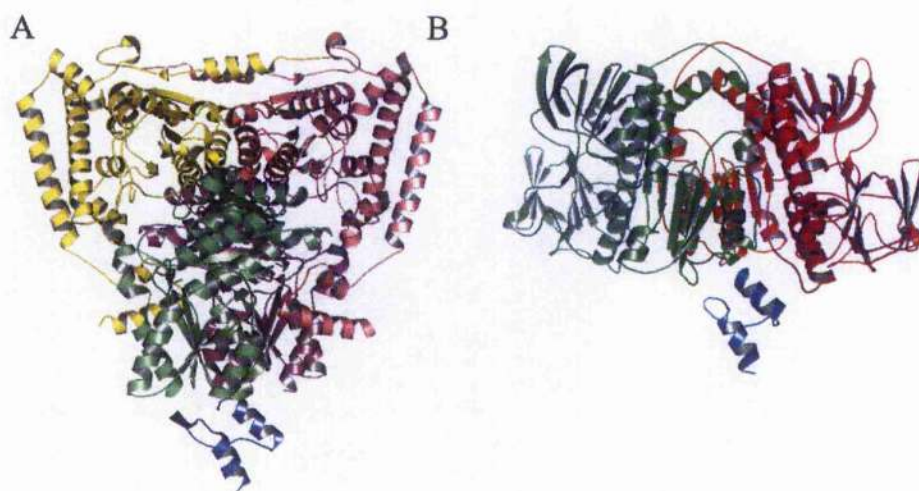


**Figure 1.11 Subcomplex formation of E1 and E3 with E2-SBD in *B. stearrowthermophilus***  
 (A) Complex of *B. stearrowthermophilus* E1 ( $\alpha$ , yellow/pink;  $\beta$ , green/purple) with E2-SBD (blue) (PDB ID 1W85). (B) Complex of *B. stearrowthermophilus* E3 (green/red) with E2-SBD (blue) (PDB ID 1EBD).

## 1.6 Substrate channelling & active site coupling

---

In *B. stearothermophilus* PDC, E1 and E3 both bind to the SBD of E2 with 1:1 stoichiometries (Hipps et al., 1994; Lessard et al., 1998, Jung et al., 2002a; 2002b). The crystal structures determined for the E3/E2-SBD as well as the E1/E2-SBD subcomplexes from *B. stearothermophilus* (Fig. 1.11) show unequivocally that association of a second molecule of E2-SBD to either E1 or E3 is not possible. In the case of E1 the binding site for E2-SBD is located across the two-fold axis (Frank et al., 2005) whereas the binding site on E3 is close to the two-fold axis of symmetry (Mande et al., 1996). Occupation of both binding sites on E3 would result in steric clashes in one of the loop regions. A schematic representation of E1 and E3 binding to the icosahedral core is shown in Fig. 1.10.

### 1.6 Substrate channelling and active site coupling

The ability of PDC to sustain substrate channelling and active site coupling is the basis for its efficient and tightly controlled function. Central to PDC substrate channelling is the presence of the lipoyl swinging arm within the E2 and E3BP lipoyl domains. Lipoamide incorporated into a LD is required for efficient intermediate transfer in PDC. Free lipoate can sustain E2 and E3 activity, but neither lipoate on its own nor lipoylated oligopeptides are reductively acetylated by E1 in an efficient manner (Graham et al., 1989; Berg et al., 1998; Liu et al., 2001). Free LDs can support the reaction, albeit at a much reduced rate (ca. 60-fold) when compared to the tethered domain (Berg et al., 1998), indicating the strategic importance of limiting LD diffusion for substrate channelling.

The swinging arm originally referred to the lipoamide alone. Its conformational freedom has been established by spin-labelling studies (Ambrose & Perham, 1976; Grande et al., 1976) and was also observed by NMR (Roberts et al., 1983; Dardel et al., 1991; Berg et al., 1994). However, it is the presence of the swinging arm incorporated into a “swinging lipoyl domain” that is required for substrate channelling since the lipoyl-lysine could only reach sites up to 28 Å apart (Angelides & Hammes, 1979; De Kok et al., 1998). Fluorescence energy transfer studies revealed that the three different active sites have to be at least 40 Å apart since no energy transfer could be detected for *A. vinelandii* PDC (Shepherd & Hammes, 1977; Scouten

## 1.6 Substrate channelling & active site coupling

et al., 1980). Cryo-EM reconstructions of *B. stearothermophilus* and bovine PDC indicate even larger distances. Milne et al. (2002; 2005) have shown the existence of an annular gap of ca. 90 Å between the E2 core and deposited E1, while that distance is somewhat smaller ( $\approx 75$  Å) between E2 and E3 (Fig. 1.12). The distances reported for bovine PDC are shorter with a space approximately 50 Å in length between the core and both E1 and E3, respectively (Zhou et al., 2001b). The difference in spacing observed in *Bacillus* and bovine PDC remains unexplained: PDC organisation could be different in both organisms, but the different distribution of E1 and E3 within the outer shell may represent artefacts resulting from sample treatment. However, in both cases the distances between the active sites are too large to be accessible if only the lipoyl-lysine group experienced flexibility (Zhou et al., 2001b). Taking the lipoyl domain and its linker into account, bridging the distances between active sites becomes straightforward, as gaps as large as 200 Å or more could be traversed (Perham et al., 1981; 2000).

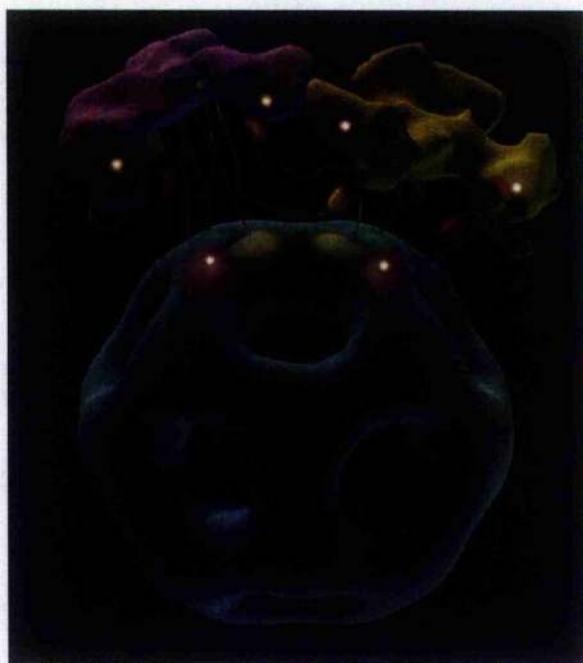


**Figure 1.12 Active site coupling in *B. stearothermophilus* PDC**

Three E1 (purple) and E3 (yellow) molecules of the outer shell are shown above the E2 core (grey). Individual E2 molecules are coloured red, green and yellow. Their SBDs are bound to E1 and E3 – the trimeric distribution of E1 and E3 molecules is for simplified observation only and both enzymes are expected to be distributed randomly in native PDC. Possible conformations for the LD are depicted as they are expected to shuttle between the different active sites (white) and are long enough to interact with more than one trimer of the outer shell.

Adapted from Milne et al. (2005).

A side effect of this arrangement is that a single lipoyl domain can service more than just one E1 and/or E3 enzyme. Simultaneously, the formation of a network of interacting LDs on the complex surface also becomes possible (Grande et al., 1976; Berman et al., 1981; Hackert et.

al., 1983; Sanderson et al., 1996b). Migration of acetyl groups between the S<sup>6</sup> and S<sup>8</sup> atoms of lipoamide has been documented (Frey et al., 1989) and experiments using labelled pyruvate have confirmed that acetyl groups and reducing equivalents can be shuttled between different LDs (Bates et al., 1977; Collins & Reed, 1977; Danson et al., 1978; Cate et al., 1980). The amount of lipoyl domain present per complex can be reduced by up to 50% using trypsin without significant adverse effects on PDC activity (Stepp et al., 1981). Mutagenesis of selected LDs in *E. coli* E2 in order to render them unlipoylatable similarly does not affect catalysis significantly (Allen et al., 1989), showing that different lipoyl domains can function independently of each other.

## 1.7 Regulation of PDC activity

Given its central metabolic role, PDC regulation is of critical importance in balancing metabolism towards glucose or fatty acids and ketone bodies (Randle, 1986). Flux through PDC is dramatically reduced during starvation or diabetes in order to preserve carbohydrate reserves, while it is up-regulated after meals to fuel energy production and fatty acid biosynthesis. PDC regulation is achieved by intrinsic (e.g. metabolites) and extrinsic factors such as nutritional state and hormones.

The main short-term control mechanism of PDC activity is through de-/phosphorylation by a complex specific PDC phosphatase (PDP, EC 3.1.3.43) and kinase (PDK; EC 2.7.1.99). Both enzymes act on the rate-limiting E1 component of PDC (Harris et al., 2002) by catalysing the ATP-dependent phosphorylation of E1 $\alpha$  at any one of three different serine residues (Ser264, Ser271, Ser203 for human PDK), thus causing inactivation of the enzyme (Kolobova et al., 2001; Bao et al., 2004a). Dephosphorylation by PDP results in PDC reactivation (Linn et al., 1969; Wieland, 1983).

Interestingly, PDK is not significantly homologous to other eukaryotic serine protein kinases, but instead is similar to prokaryotic histidine protein kinases even though their catalytic mechanisms are different (Steussy et al., 2001; Harris et al., 2002). In mammals four isozymes of PDK (1-4) have been identified which can form both homo- and heterodimers

## 1.7 Regulation of PDC activity

---

(Boulatnikov & Popov, 2003). They are expressed in a tissue-specific manner and have different specific activities (Popov et al., 1994; Gudi et al., 1995; Rowles et al., 1996; Bowker-Kinley et al., 1998): PDK1 and 4 are mainly expressed in the liver and muscle tissues, while PDK3 is prevalent in the kidney, brain and testes and PDK2 is present in most tissues (Gudi et al., 1995; Bowker-Kinley et al., 1998). PDK1 can phosphorylate all three Ser residues, while the other three isoforms can only act on sites 1 and 2 and do so with different affinities. Phosphorylation at a single site is sufficient for complete inactivation and is independent of the status of the two remaining sites (Yeaman et al., 1978; Korotchkina & Patel, 1995; 2001; Patel & Korotchkina, 2001; Kolobova, 2001).

PDK is tightly bound to the PDC: PDK1-3 associate with the E2 inner lipoyl domain (ILD) while PDK4 preferentially interacts with the E3BP-LD (Roche et al., 2003). The interaction with the LD causes a conformational change in PDK and causes an increase in its activity; in the case of PDK3, the conformation of the ATP lid is affected, thus decreasing its affinity for ADP and stimulating kinase activity (Roche et al., 2003; Bao et al., 2004b; Kato et al., 2005). Furthermore, reduced/acetylated LDs as well as NADH are thought to stimulate kinase activity (Fig. 1.13) (Patel & Korotchkina, 2001; Roche et al., 2003; Bao et al., 2004b). Only a few molecules of kinase are known to be present per core (Yeaman, 1989) and they have been shown capable of quickly inactivating multiple E1 enzymes present on the core surface (Yang et al., 1998). Experiments using E2-LD fused to glutathione *S*-transferase (GST) have shown high-affinity binding of PDK to the dimeric constructs, suggesting the formation of transient cross-links between adjacent pairs of E2 and resulting in a “hand-over-hand” mechanism of migration on the PDC surface (Liu et al., 1995a).

Dephosphorylation and restoration of PDC activity is regulated by two PDP heterodimeric isozymes (1 & 2), consisting of a catalytic and regulatory subunit. Analogously to PDK, isozyme expression is tissue-specific: PDP1 is associated with muscle tissue while PDP2 is predominantly associated with the liver and adipose tissue (Huang et al., 1998). Dephosphorylation of E1 by PDP is dependent on  $Mg^{2+}$  and further stimulated by  $Ca^{2+}$  (Linn et al., 1969; Denton et al., 1972; Damuni & Reed, 1987; Reed et al., 1996). In contrast to PDK, PDP is only loosely associated with PDC, although its catalytic efficiency is increased 7–16-fold by interaction with E2-LD. E2 binding is  $Ca^{2+}$  dependent and the presence of

lipoamide has been shown to enhance enzyme activity (Pettit et al., 1972; Chen et al., 1996). PDP activity is also stimulated by spermine and other polyamines, probably by reversing the effects of its regulatory subunit (Damuni et al., 1984).

Feedback inhibition is also used for short-term regulation of PDC activity: E1 uses pyruvate as a positive and acetyl-CoA as a negative effector. Simultaneously, acetyl-CoA also inhibits E2 activity, while high NADH levels reduce E3 activity (Wieland, 1983). A diagram summarising short-term regulation of PDC is shown in Fig. 1.13.

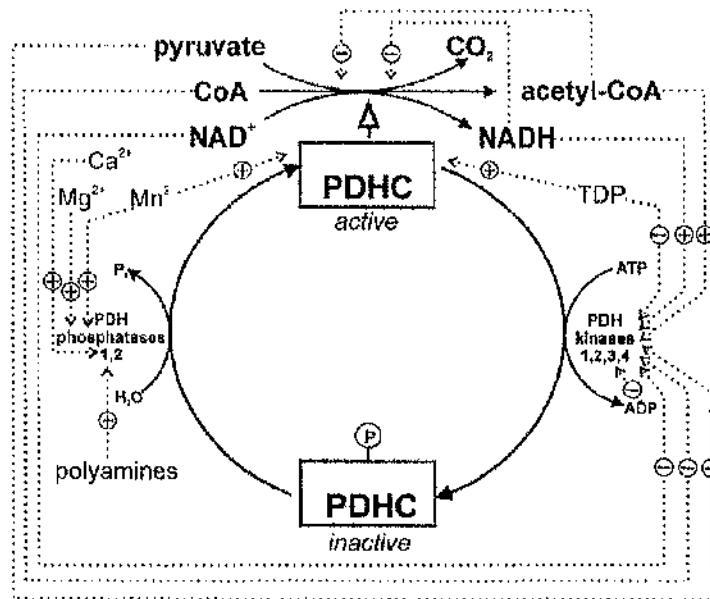


**Figure 1.13 Short-term regulation of PDC activity**

Activators and inhibitors of pyruvate dehydrogenase complex (PDHC) and its regulatory enzymes are shown.

Adapted from Strumilo (2005).

Long-term regulation of PDC in response to hormonal or dietary changes is accomplished at transcriptional level by controlling gene expression of PDC constituent and regulatory enzymes (Patel et al., 1995; 2003). PDC activity in rats that were fed a high-sucrose diet, for instance, increased up to 4-fold with concomitant changes in the amount of PDC present. Similarly, hypoactive thyroid glands in rats resulted in the loss of ca. 30% of total PDC

activity and a similar reduction of E1 protein present (other PDC proteins were not quantified) (Da Silva et al., 1993; Patel et al., 1996). However, a major determinant for PDC activity under different physiological conditions is the amount of PDK. In response to starvation, for example, expression of PDK2 and PDK4 is up-regulated in many tissues. Diabetes also increases PDK4 expression in rats, but the effect can be reversed by treatment with insulin (Harris et al., 2001).

## **1.8 PDC and disease**

### **1.8.1 Genetic disorders**

Aerobic glucose oxidation is of critical importance in nervous tissues like the brain, which are dependent on this pathway for energy generation. Hence, defects in PDC cause developmental problems and/or degenerative changes that are associated with a wide variety of abnormalities, ranging from mild ataxia, lethargy and feeding difficulties to developmental delay, blindness, severe neurological disorders and even death (Robinson et al., 1987; Brown et al., 1989a; Di Mauro & De Vivo, 1996; De Vivo, 1998). Besides reduced energy generation due to a decrease in the production of acetyl-CoA, the accumulation of lactate as a result of anaerobic glucose oxidation causes lactic acidosis. Most patients display either severe and often fatal lactic acidosis or chronic neurodegenerative disease with extensive neuropathology (Brown et al., 1994; Robinson, 1995). However, cases with PDC deficiency who present only mild symptoms and therefore survive into child- and adulthood keep being identified, thus continuously expanding the spectrum of clinical disease associated with PDC deficiency (Seyda et al., 2000; Brown et al., 2002; Head et al., 2005). Current treatment strategies usually include the activation of residual PDC activity by dichloroacetate, an inhibitor of PDK (Morten et al., 1999), the administration of cofactors like lipoic acid or ThDP (Byrd et al., 1989; Naito et al., 2002), and the prescription of a ketogenic diet (Wijburg et al., 1992; Wexler et al., 1997). However, all of the above treatments are applied with varying success.

Over 90% of cases of PDC deficiency are caused by mutations in the *PDHA1* gene encoding the E1 $\alpha$  subunit of PDC: more than 75 different mutations have been identified so far, roughly equally divided between missense/nonsense and insertion/deletion mutations (Fouque et al., 1998; Lissens et al., 2000). The severity of clinical abnormalities due to E1 $\alpha$  mutations varies and depends on the precise nature of the mutation itself. *PDHA1* is located on the short arm of the X chromosome (Brown et al., 1989b; Szabo et al., 1990; Dahl et al., 1992). Therefore, in women expression of E1 $\alpha$  is mosaic, dictated by the pattern of X chromosome inactivation which causes differences in the clinical symptoms observed. Men are usually more severely affected as only one X chromosome is present per cell. Therefore, all E1 $\alpha$  will be mutated and residual PDC activity depends on the severity of gene defect (Lissens et al., 2000). A second gene coding for E1 $\alpha$ , *PDHA2* has been identified, but is expressed exclusively in the testes (Dahl et al., 1990). No mutation in *PDHA2* has been observed as yet (Dahl, 1995).

Missense mutations affecting the *PDHB* gene encoding E1 $\beta$  have been identified in two patients only so far. In both cases a single amino acid substitution is thought to destabilise the E1 heterotetramer and thus results in rapid protein turnover (Brown et al., 2004). Similarly, mutations in E2 are extremely rare and have also been reported only twice: a deletion within the E2 encoding *DLAT* gene removes a glutamic acid residue from the outer LD, while a missense mutation results in the replacement of a highly conserved phenylalanine by leucine in the E2 active site (Head et al., 2005). While the outer LD was shown to be dispensable for *E. coli* PDC activity *in vitro* (Guest et al., 1985) this may not be representative of the situation in human PDC and/or *in vivo* as isogenic *E. coli* strains with three lipoyl domains were able to outgrow those with just one (Guest et al., 1997).

Nonsense mutations that result in premature termination of translation and deletions in the *PDX1* gene encoding E3BP have been identified in 12 patients (Marsac et al., 1993; Geoffrey et al., 1996; Aral et al., 1997; DeMeirleir et al., 1998; Ling et al., 1998; Brown et al., 2002; Dey et al., 2002; 2003; Ramadan et al., 2004). Patients therefore completely lack functional E3BP, but still display 10-20% of normal PDC activity, thus indicating that E2 retains a residual capacity to bind E3 (Marsac et al., 1993). These findings have also been confirmed *in vitro* where a 100-fold excess of E3 was able to restore PDC activity to ca. 25% of wild-type levels (McCartney et al., 1997). The symptoms presented by patients with mutations in genes

encoding different PDC components cannot necessarily be distinguished readily. However, at least some cases of E3BP deficiency are associated with a milder form of the disease (Head et al., 2005).

More than 20 cases of E3 deficiency have been identified, with a disproportionate number affecting Ashkenazi Jews who are all affected by a single substitution of Gly194 by cysteine in the NAD domain (Hong et al., 2003). Another 11 different mutations, most of them resulting in amino acid substitutions in the FAD, central and interface domains have been found, presumably affecting FAD binding, catalysis, core association and E3 dimerisation (Odievre et al., 2005). However, not only does E3 deficiency affect PDC activity, but OGDC and BCDC function is also impaired, resulting in elevated substrate levels in plasma and urine (Hong et al., 1997; Shany et al., 1999).

### **1.8.2 Metabolism and Alzheimer's disease**

Reduced activity of PDC and other metabolic enzymes such as OGDC and isocitrate dehydrogenase have been associated with the development and progression of Alzheimer's disease (AD) (Sheu et al., 1994; Hoyce, 2004; Bubber et al., 2005). Reduction in brain metabolism always seems to accompany clinical AD, although it can precede overt clinical symptoms by years (Small et al., 1995; Reiman et al., 1996). Severe, prolonged impairment of brain glucose oxidation can cause substantial brain damage, including permanent dementia (Plum & Posner, 1980). In particular, decreases in OGDC activity seem to be highly correlated to the clinical dementia rating (Gibson et al., 2000), while treatment with glucose and insulin improves the memory function of AD patients at least temporarily (Craft et al., 2000). However, the molecular mechanisms that link metabolic enzymes such as PDC and OGDC to AD are not clear. Possibilities include inactivation by oxidative stress (Blass & Gibson, 1999; Sims et al., 2000), which in turn increases the generation of reactive oxygen species and reduces the brain's ability to cope with added oxidants (Shi et al., 2005). Defects in PDC may also impair the production of acetylcholine due to a shortage in acetyl-CoA, while lower OGDC activity can promote the accumulation of glutamate, which acts as a neurotoxin at elevated levels (Blass & Gibson, 1991; Shoffner, 1997; Klivenyi et al., 2004).

### 1.8.3 Primary biliary cirrhosis

Primary biliary cirrhosis (PBC) is a chronic autoimmune liver disease resulting in the inflammatory destruction of the biliary epithelial cells lining the intrahepatic bile ducts and leads to cirrhosis and liver failure. It is also the most prevalent autoimmune disease occurring in middle-aged women (Iwayama et al., 1992; Mackay et al., 2000). PBC is characterised by a high titre of anti-mitochondrial autoantibodies in affected individuals. They are primarily directed against the E2 component of PDC (> 95%) and can inhibit enzyme function (Yeaman et al., 1988; Van de Water et al., 1988a). Immunogenicity is mainly caused by the inner E2-LD (Van de Water et al., 1989b; Surh et al., 1990; Fussey et al., 1990), including the lipoate binding site. The presence of covalently bound lipoate also seems to be important for antibody recognition. However, cross-reactivities of sera from PBC patients have been detected for E2 from OGDC and BCDC (Fussey et al., 1988; Fussey et al., 1991), as well as PDC E3BP (Yeaman et al., 1988; Surh et al., 1989) and both PDC E1 subunits (Fussey et al., 1989). E2 and E3BP antigens were subsequently found to be aberrantly expressed at the plasma membrane of biliary epithelial cells from PBC patients (Joplin et al., 1997; Joplin & Gershwin, 1997). The mechanism for this molecular process is unclear. However, as for most autoimmune diseases the exact aetiology of PBC and break-down of tolerance is unclear.

### 1.8.4 PDC and diabetes

Type II diabetes is associated with problems in the balance between glucose and lipid metabolism. High fasting blood glucose levels, in excess of 10 mM, mainly result from excessive glucose production in the liver via gluconeogenesis (Randle et al., 1994; Boden et al., 2001). Increasing the rate of pyruvate oxidation in the peripheral tissues provides an attractive mechanism in order to remove the surplus of gluconeogenic substrates. Treatment of type II diabetics with dichloroacetate (DCA), an inhibitor of PDK, results in a fall of glucose concentrations (Stacpoole et al., 1978), but is unsuitable as a therapeutic agent due to its low potency, metabolism and toxicity (Stacpoole et al., 1998). However, it highlights PDK as an attractive drug target. Both PDK2 and PDK4 are suitable targets: PDK2 is expressed in all tissues and would be able to increase glucose uptake and decrease gluconeogenesis in both liver and peripheral tissues. PDK4 would provide the same service, but in the peripheral

tissues only, although it would also prevent liponeogenesis in the liver as a result of increased acetyl-CoA production which could prove detrimental (Mayers et al., 2005). A series of inhibitors is currently being developed against PDK2 that seem to exhibit reasonable specificity, although PDK1 is also inhibited, albeit at a much lower level, while PDK4 activity is increased (Mayers et al., 2005). Furthermore, PDC activity was increased and glucose levels lowered in obese Zucker rats which are often used as a model system for type II diabetes (Morrell et al., 2003; Mayers et al., 2003), thus improving the prospects for a possible therapy for type II diabetes.

### 1.8.5 Chemical modification of PDC

Some research has also focused on the modification of 2-oxoacid dehydrogenase complexes by toxins and chemical additives found in food. 2-octynoic acid is one example of a widespread additive commonly found in perfumes, lipstick and food flavourings. Lipoylated E2-derived peptides that were treated with 2-octynoic acid cross-reacted with sera obtained from PBC patients (Amano et al., 2005; Long et al., 2005). Experiments on guinea pigs suggest that lipoyl-E2 – once it is xenobiotically modified – can elicit an even stronger autoimmune response than the native protein and which is able to recognise both the modified and native forms of lipoyl-E2 (Amano et al., 2005).

Another interesting example of chemical modification are arsenical compounds: they irreversibly modify the lipoate cofactor present in the E2 components of 2-oxoacid dehydrogenase complexes as well as transketolase, although susceptibility varies from organism to organism (Voet & Voet, 1995). For this reason and in the absence of better alternatives, arsenical compounds are still widely used for the treatment of trypanosomiasis and leishmaniasis: both diseases are caused by parasites who are slightly more sensitive to arsenical compounds than humans. Nevertheless, 50% of patients die because of treatment rather than the disease itself (Rosen, 1995; Dumas, 2000).

## 1.9 Project aims

A lot of research has focused on the elucidation of individual enzyme structures and their modes of interaction in prokaryotic PDCs, in particular PDC from *B. stearothermophilus* and *A. vinelandii*. Structural information on enzymes from eukaryotic PDC has also been more forthcoming since the start of this project, as evidenced by the publication of atomic structures obtained for human E1 (Ciszak et al., 2001; 2003), E3 (Brautigam et al., 2005) and inner E2-LD (Howard et al., 1998), as well as yeast E3 (Toyoda et al., 1998b). Very recently, the crystal structure of human E3 complexed with the E3BP subunit binding domain (Ciszak et al., 2006) has been solved. However, information about interactions of human E1 and E3 with their respective SBDs in solution has not been available until now. Preliminary microcalorimetry experiments in the laboratory of Prof. G. Lindsay, University of Glasgow indicated the formation of unexpected 2:1 stoichiometric complexes – so-called “cross-bridges” – formed between a didomain construct of E3BP (XDD) and E3 (Brown, 2002), implying the existence of a new level of ultrastructure in human PDC that could revise our current understanding of eukaryotic PDC organisation and function.

The aim of this project was to investigate the formation of E3BP/E3 cross-bridges *in vitro* (Chapter 5) by a number of different biochemical and biophysical techniques, including native polyacrylamide gel electrophoresis (PAGE), analytical ultracentrifugation (AUC) and isothermal titration calorimetry (ITC). Low-resolution structures of the complex formed between XDD and E3 as well as free E3 were also obtained using small angle x-ray scattering (SAXS) in combination with molecular modelling approaches. Similarly, the possibility of similar cross-bridges formation between E2 and E1 was also investigated (Chapter 6), although problems with protein stability and monodispersity meant that these data are, to some extent, preliminary.

Another ongoing question in the PDC field is the location of E3BP within the eukaryotic, icosahedral core. Two main models have been published: a 60:12 (E2:E3BP) addition model based on cryo-EM and a 48:12 (E2:E3BP) substitution model proposed from results obtained from AUC and SAXS. Chapter 7 describes initial SAXS and small angle neutron scattering (SANS) experiments in an attempt to develop an experimental strategy able to differentiate between these models.

Most biophysical studies (Chapter 2) require rather large amounts of pure, monodisperse protein. Large-scale protein purification is described in Chapter 4.

# **Chapter 2**

## **Biophysical techniques**

### **2.1 Introduction**

This chapter summarises the biophysical techniques used to analyse PDC and its constituent proteins throughout this project: analytical ultracentrifugation (AUC), isothermal titration calorimetry (ITC) and small angle x-ray and neutron scattering (SAXS/SANS).

### **2.2 Analytical ultracentrifugation**

During ultracentrifugation, solutes – in this case proteins – are spun at high speeds (typically 3000-60000 rpm) resulting in movement of the particles through the solvent in the direction of the centrifugal force and sedimenting as a function of time. The sedimentation process is dependent on mass, shape and charge of a particle and causes depletion of the solute from the meniscus and the formation of distinct solute/solvent boundaries. In analytical ultracentrifugation (AUC) the movement of the boundaries can be observed by monitoring the solute concentration using absorbance (Schachman et al., 1962; Hanlon et al., 1962; Giebeler, 1992), interference (Schachman, 1959; Yphantis et al., 1994; Laue, 1994), schlieren

(Svedberg & Pedersen, 1940) or fluorescence (Schmidt & Riesner, 1992; Laue et al., 1997) optics (Fig. 2.1). Only absorbance and interference optics were used for work described in this thesis.

The fact that experiments are conducted in solution without the need for labelling or chemical modification, or interaction with a surface or supporting matrix represents a major advantage of the technique. In addition, the different optical systems used for data acquisition as well as different sample cell path lengths allow for experiments covering a large range of sample concentrations. Furthermore, by adjusting the rotor speed, AUC can be used to analyse macromolecules over a very large molecular weight range (Lebowitz et al., 2002).

AUC was used to determine the homogeneity, apparent molecular weight and stoichiometry of PDC and its constituent proteins. Apart from the stoichiometries of interactions, the thermodynamic binding constant(s) can be determined as well, provided that association reactions can be observed on the time-scale of the experiment. In addition, recent advances in the analysis of AUC data enable refined characterisation of heterogeneous systems.

### 2.2.1 Sedimentation velocity

In sedimentation velocity (SV) experiments the solute and solvent are placed in the separate channels of a two-channel centrepiece and subjected to centrifugation at high rotor speeds (40-60 krpm) where the exact rotor speed is dependent on the size of the macromolecule. During the experiment, proteins are separated as a result of their different rates of migration through the centrifugal field. The sedimentation process is monitored over time by a set of absorbance/interference profiles (Fig. 2.1). At the start of the experiment the solute is distributed homogeneously throughout the radial range recorded. At later times sedimentation profiles show movement of the solute boundary towards the bottom of the cell. The sedimentation coefficient of a macromolecule is obtained from its sedimentation profile and defined by the Svedberg equation (Svedberg & Pedersen, 1940; Lebowitz et al., 2002)

$$s = \frac{u}{\omega^2 r} = \frac{M(1 - \bar{v}\rho)}{N_A f} = \frac{MD(1 - \bar{v}\rho)}{RT}, \quad (2.1)$$

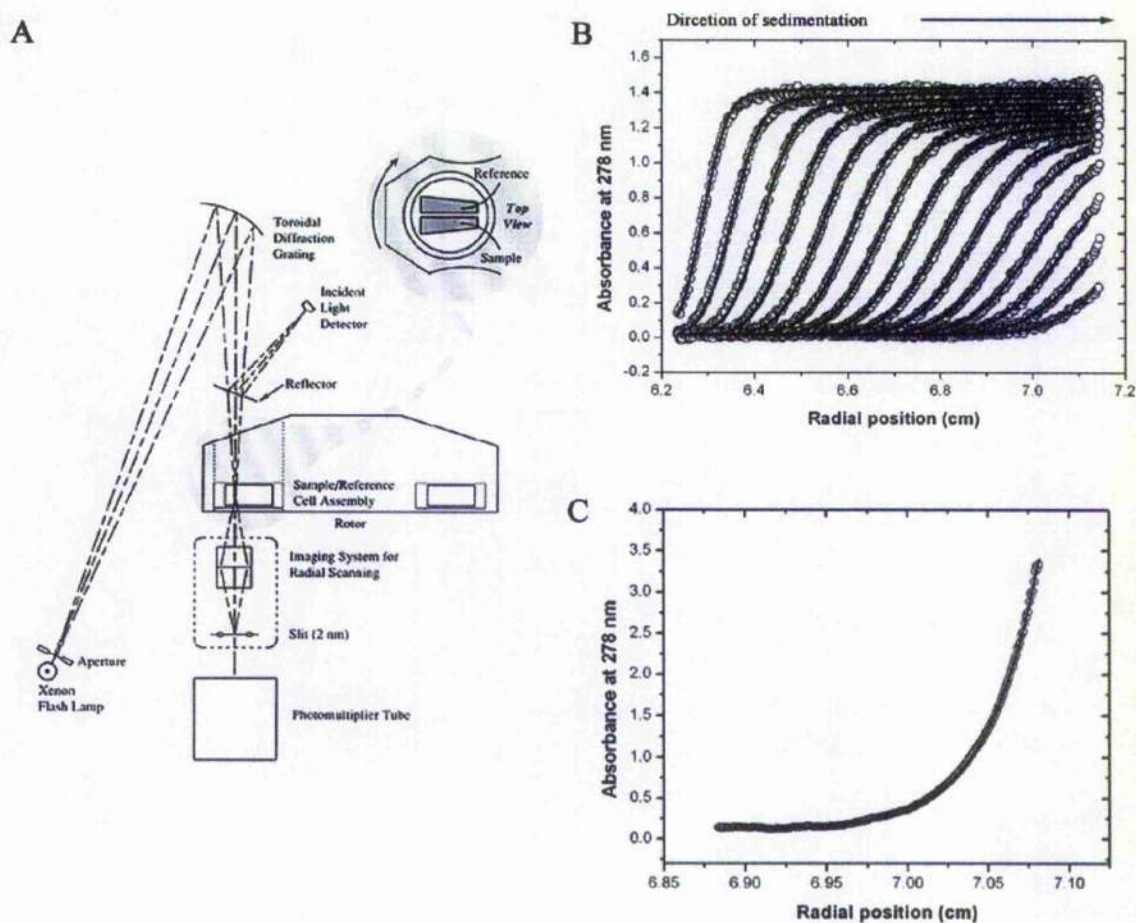


**Figure 2.1 Analytical ultracentrifugation**

(A) Schematic diagram of the absorbance optical system in an XL-A analytical ultracentrifuge. (B) Typical sedimentation velocity profiles  $a(r,t)$  as a function of radial position  $r$  at different times,  $t$ . (C) Characteristic sedimentation equilibrium profile  $a(r)$  as a function of radial position  $r$ . (A) was adapted from (Ralston, 1993).

## 2.2 Analytical ultracentrifugation

where  $u$  is the observed radial velocity of the boundary midpoint,  $\omega$  is the angular velocity,  $r$  is the radial position,  $M$  is the molar mass,  $\bar{v}$  is the partial specific volume,  $\rho$  is the buffer density,  $N_A$  is Avogadro's number,  $f$  is the frictional coefficient,  $R$  is the gas constant and  $T$  is the temperature. The right-hand side of eq. 2.1 was derived from the relationship of the diffusion and frictional coefficients  $D = RT/N_A f$ . Sedimentation coefficients are reported in Svedberg units (S), equivalent to  $10^{-13}$  s.

Assuming spherical symmetry the Stokes equation can be used to calculate the anhydrous frictional coefficient  $f_0$ ,

$$f_0 = 6\pi\eta R_0, \quad (2.2)$$

where  $\eta$  is the viscosity of the solvent and  $R_0$  is the radius of the sphere. By combining the Svedberg and Stokes equations and substituting all constants with the values for water at 20°C, it is possible to define the sedimentation coefficient,  $s$  of an anhydrous spherical particle in terms only of  $M$  (g/mol),  $\bar{v}$  (ml/g) and  $\rho$  (g/ml).

$$s_{\text{sphere}} = 0.012 \frac{M^{2/3} (1 - \bar{v}\rho)}{\bar{v}^{1/3}}. \quad (2.3)$$

Using eq. 2.3 the maximum sedimentation coefficients of spherical proteins in water at 20°C can be calculated since spherical particles have minimal surface area exposed for solvent interaction (hydration shell) and consequently have the lowest frictional coefficients,  $f_0$ . Any asymmetry in particle shape increases interactions of protein surface residues with the solvent and causes the value of  $s$  to decrease as a consequence.

In order to be able to compare sedimentation coefficients obtained under different experimental conditions,  $s$  is corrected to standard conditions (in water at 20°C) using

$$s_{20,w} = s_{T,B} \left( \frac{\eta_{T,B}}{\eta_{20,w}} \right) \left( \frac{(1 - \bar{v}\rho)_{20,w}}{(1 - \bar{v}\rho)_{T,B}} \right), \quad (2.4)$$

where the subscripts  $T$  and  $B$  refer to the temperature and buffer conditions used throughout the experiment, and  $20,w$  indicates standard conditions.

### 2.2.1.1 SV data analysis

Numerous approaches have been developed for the analysis of SV data. Only the methods used throughout this thesis will be described, in particular the sedimentation coefficient distribution and finite element analyses as implemented in the program SEDFIT (Schuck, 2000; Schuck et al., 2002).

The generation of a macromolecular concentration distribution  $\chi$  as a function of time  $t$  and radial position  $r$  under the influence of sedimentation and diffusion processes in a sector-shaped sample cell is described by the Lamm equation (Lamm, 1929):

$$\frac{\partial \chi(r,t)}{\partial t} = \frac{1}{r} \frac{\partial}{\partial r} \left[ rD \frac{\partial \chi(r,t)}{\partial r} - s\omega^2 r^2 \chi(r,t) \right]. \quad (2.5)$$

In the computer program SEDFIT sedimentation profiles are fitted with numerical finite element solutions of the Lamm equation. This process takes into account the entire sedimentation process and has the added advantages of being able to achieve a higher resolution than other methods as well as to model the sedimentation profiles of species for whom no separate boundary is visible in the actual data due to the effects of diffusion (Schuck, 2000; Lebowitz et al., 2002). Furthermore, this type of analysis is capable of handling very small species, e.g. salts as well as very large particles such as viral capsids. If more than one species is present in a sample, the user needs to specify a particular model for fitting the data, including, for example, 'non-interacting' (for  $n$  non-interacting species) and 'interacting' (e.g. monomer-dimer association, etc.).

A method that requires no prior knowledge of the number of species present in a sample or their interaction(s) is sedimentation coefficient distribution,  $c(s)$  developed by Schuck (2000). SV profiles are modelled with distributions of Lamm equation solutions

$$a(r,t) = \int c(s)\chi(s,D,r,t)ds + \varepsilon, \quad (2.6)$$

where  $a(r,t)$  represents the recorded sedimentation data,  $c(s)$  is the concentration of species with sedimentation coefficients between  $s$  and  $s + ds$ ,  $\chi(s,D,r,t)$  denotes the solution of the Lamm equation for a single species and  $\varepsilon$  is a noise component. Simply put, sedimentation data are composed of several different populations, each of which has a different sedimentation,  $s$  and diffusion coefficient,  $D$  and therefore contributes to the radial- and time-dependent absorbance/interference signal  $a(r,t)$  in a manner proportional to the Lamm equation solution  $\chi(s,D,r,t)$  and its loading concentration. However, this approach does assume that none of the species interacts with another on the time-scale of the experiment. It can still be used to analyse mixtures of interacting proteins, but may lead to the observation of peaks in the  $c(s)$  profile generated that do not correspond to any sedimenting macromolecule but instead represent the chemical interconversion of species (Gilbert & Jenkins, 1956; Dam et al., 2005). This case is best diagnosed by analysing different concentrations of the same protein mixture. Sedimentation coefficient distributions can be integrated to yield weight-average sedimentation coefficients.

$c(s)$  analysis was always used as a first step in the analysis of SV data throughout this project in order to determine the number of species present in the experimental system and to provide initial estimates of their sedimentation coefficients and loading concentrations. In experiments with less than or equal to four different species the data were modelled subsequently using finite element analysis, employing either a non-interacting or appropriate association model to determine the true sedimentation coefficient for each species. SEDFIT does not have the capacity to model more than four separate species. In more extreme cases the program SEDPHAT (Schuck, 2003; Vistica et al., 2004) could be used to fit up to ten different species. To correct for the effects of concentration, sedimentation coefficients were extrapolated to infinite dilution to yield the value of  $s$  independent of concentration,  $s_{20,w}^0$ .

### 2.2.2 Sedimentation equilibrium

In sedimentation equilibrium (SE) analytical ultracentrifugation macromolecules are subjected to a lower centrifugal field, i.e. experiments are run at lower rotor speeds. The opposing forces of sedimentation and diffusion on macromolecules lead to the establishment of a thermodynamic equilibrium with no net movement of molecules within the concentration gradient. Within this gradient the distribution of each species is described by an exponential. For a single, thermodynamically ideal macromolecule the sedimentation process can be described by a combination of the Lamm and Svedberg equations:

$$\frac{\partial \ln(c)}{\partial r^2} = \frac{M(1-\bar{v}\rho)\omega^2}{2RT} \quad (2.7)$$

where  $c$  is the macromolecular concentration. For a single ideal species plotting  $\ln(c)$  versus  $r^2$  results in a straight line with a slope of  $\frac{M(1-\bar{v}\rho)\omega^2}{2RT}$ . The molecular mass can be obtained from the slope, provided the partial specific volume  $\bar{v}$  is known. *Ideality* in thermodynamic terms refers to particles in solution that do not interact with each other.

When more than one species is present in the experimental system, the sedimentation profile as a function of its radial position,  $a(r)$ , is the sum of the exponentials recorded for each species

$$a(r) = \sum_{i=1}^n c_{i,0} \varepsilon_i d \exp \left[ \frac{M_i(1-\bar{v}_i\rho)\omega^2}{2RT} (r^2 - r_0^2) \right] + \delta \quad (2.8)$$

where  $n$  represents the number of species,  $c_{i,0}$  denotes the molar concentration of species  $i$  at a reference position  $r_0$ ;  $\varepsilon_i$  is its molar extinction coefficient,  $d$  is the optical path length (12 mm or 3 mm) and  $\delta$  represents the baseline offset which accounts for all non-sedimenting material as well as small imperfections in the cell assembly and data acquisition. When using interference optics the extinction coefficient in eq. 2.7 is replaced by a specific signal increment (2.75 fringes per mg/ml).

The steepness of the concentration gradient is dependent on the square of the rotor speed and the buoyant molar mass  $M_b = M(1 - \bar{v}\rho)$  which corresponds to the mass of a macromolecule corrected by a buoyancy factor due to the amount of displaced solvent. In order to obtain optimum results from SE experiments, usually 2-3 different rotor speeds and 7-9 sample concentrations are used, resulting in the acquisition of 14-27 independent equilibrium profiles.

### 2.2.2.1 SE data analysis

Analysis of SE data includes model-independent and model-dependent approaches: model-independent methods are very useful for the initial characterisation of samples as well as samples that prove too complex to be fitted using model-dependent approaches. By solving eq. 2.7 the weight-average molecular mass,  $M_w$ , is determined. This type of analysis was done using the Beckman XL-A/XL-I software implemented in MicroCal ORIGIN or using SEDPHAT (Schuck, 2003; Vistica et al., 2004). The Beckman XL-A/XL-I software was also used for the determination of the second virial coefficient,  $B$ , when analysing nonideal systems.

All other analyses were performed in SEDPHAT which enables the use of more complex fitting routines. SE data were generally analysed using SEDPHAT's multispeed function which allows simultaneous fitting of data sets obtained from the same cell at different speeds and thereby improves consistency by fitting them with the same baseline. Cells were analysed individually to enable graphical determination of the concentration-independent molecular weight,  $M_w^0$ , by plotting of the apparent molecular weight,  $M_{w,app}$ , versus protein concentration,  $c$ . Finally, data sets were also fitted globally to ensure reliability of the results obtained. Fitting routines available in SEDPHAT include a non-interacting discrete species model (up to four different macromolecules), a monomer  $\rightarrow n$ -mer self-association model and  $A + B \rightarrow C$  hetero-association model.

## 2.3 Isothermal titration calorimetry

Isothermal titration calorimetry (ITC) is one of the most quantitative methods for analysing molecular interactions. Concentrated ligand is combined with the macromolecule under study in a series of discrete injections. ITC directly measures the amount of heat taken up or released upon complex formation and allows direct determination of the binding constant,  $K_a$ , the stoichiometry of the interaction,  $n$  and the enthalpy of binding,  $\Delta H^\circ$ . The free energy of a reaction,  $\Delta G^\circ$  is calculated from  $\Delta G^\circ = -RT \ln K_a$  while the entropy,  $\Delta S^\circ$  is derived from the standard thermodynamic expression  $\Delta G^\circ = \Delta H^\circ - T\Delta S^\circ$ . A typical experimental set-up is shown in Fig. 2.2. The heat of each injection is obtained from calculating the area under each peak. As the amount of uncomplexed protein in the reaction cell progressively decreases with each injection, the peaks become smaller accordingly until complete saturation is achieved. Any further injections simply resemble peaks caused by dilution of the macromolecular solution and need to be subtracted prior to data analysis. For a macromolecule with  $i$  non-interacting binding sites the amount of heat,  $Q$ , generated or absorbed upon ligand binding is described by

$$Q = \frac{V_0 [M]_t \sum_{i=1}^n (n_i \Delta H_i K_{a_i} [L])}{1 + K_{a_i} [L]} \quad (2.9)$$

where  $V_0$  is the volume of the ITC cell,  $[M]_t$  is the total concentration of macromolecules (including bound and free fractions),  $n$  is the stoichiometry of interaction,  $\Delta H$  is the enthalpy of binding per mole of ligand and  $[L]$  is the free ligand concentration.

The most significant limitation of ITC is its inability to characterise well very fast binding events, i.e. very high affinity interactions. When binding constants exceed a value of  $10^8$ - $10^9$   $M^{-1}$  saturation is achieved in only 1-2 injections, titrations lose their characteristic sigmoidal shape and therefore lack the information content necessary to determine the binding constant accurately.

Surface plasmon resonance (SPR) is also often used to determine the strength of molecular associations, but requires attachment of one interaction partner to a matrix which can be problematic.

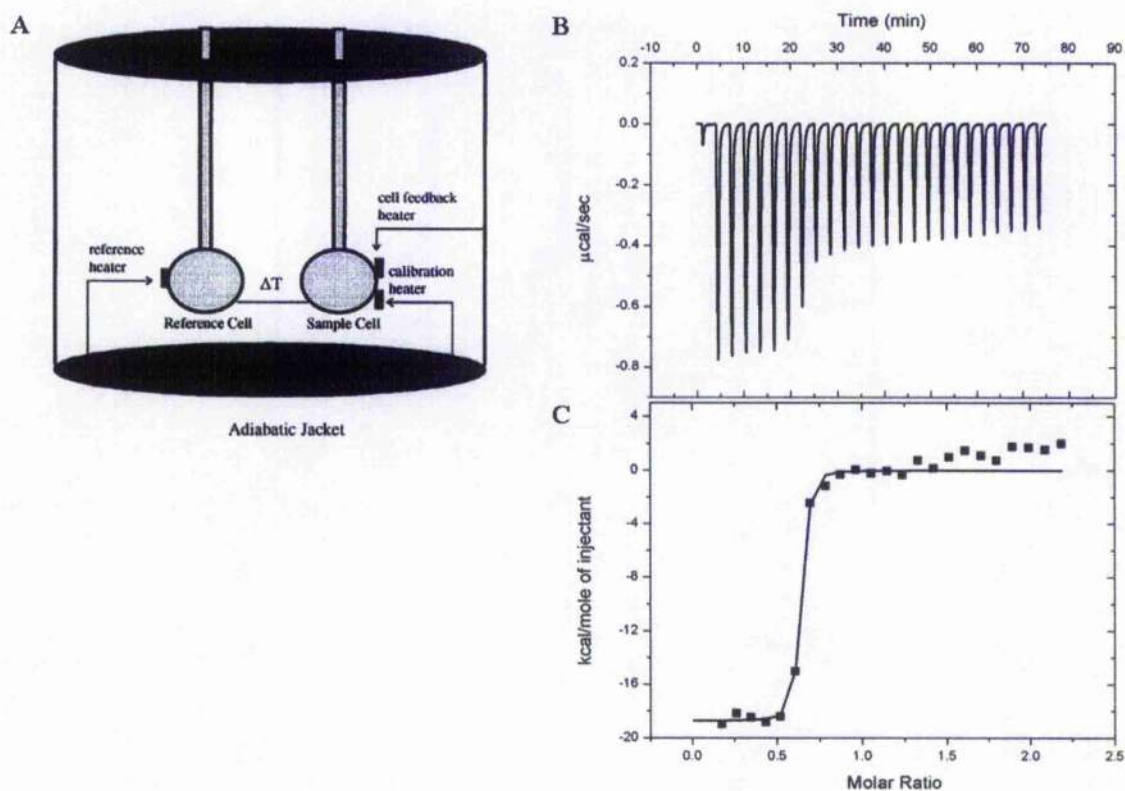


**Figure 2.2** Isothermal titration calorimetry

(A) Schematic representation of an ITC instrument. Two cells are contained within an adiabatic jacket. A small continuous power is applied to the reference cell in the form of a heater and thermocouple detectors sense temperature differences between the reference and sample cells. Upon ligand binding heat is either generated or absorbed. In order to maintain equal temperature within the reference cell changes in the power supply occur via the feedback system. The heat supplied to the sample cell per unit time is measured by the instrument and results in the appearance of the characteristic peak pattern. (B+C) Sample ITC data. The raw data are shown in (B), while the integrated data and fit to the data are shown in (C).

(A) was adapted from Pierce et al. (1999).

## 2.4 Small angle x-ray scattering

Small angle x-ray scattering (SAXS) is a technique used to obtain low resolution structural information, e.g. particle size and shape, for materials that can vary in size from ten to several thousand Angstroms such as proteins and viral capsids (Heller et al., 2004; Lee et al., 2004). The technique is not limited to biological macromolecules and is used widely to characterise synthetic polymers, nanoparticles, porous materials, etc.. However, the following sections will focus on the aspects relevant to the work described in this thesis, i.e. the solution scattering of monodisperse systems of identical, non-interacting particles.

### 2.4.1 Scattering by an ideal monodisperse solution

X-rays interact with the electrons of a sample. In *ideal* solutions particles do not interact with each other. In a *monodisperse* system all particles have the same chemical composition (chemical monodispersity) and shape (shape monodispersity). In an ideal, monodisperse system all particles have the same scattering amplitude which is non-directional (*isotropic*). Furthermore, the recorded scattering intensity is the sum of the intensities of all individual particles and no interference is observed. It is the uniform particle distribution in solution and isotropic scattering in the absence of a crystal lattice that leads to spherical averaging of the single particle scattering, a one-dimensional scattering curve and low resolution compared to x-ray crystallography. Typically, SAXS experiments achieve a resolution of 10-20 Å, although it can be as high as 5 Å in exceptional circumstances (Petoukhov & Svergun, 2003).

Assuming a sample with an electron density  $\rho(\mathbf{r})$  at a point  $\mathbf{r}$  scatters x-rays with an incident wave vector,  $\vec{s}_0$  ( $|\vec{s}_0| = 2\pi/\lambda$ , where  $\lambda$  is the wavelength of the x-rays), then at distances much larger than the size of the particle the amplitude of the scattered radiation is defined by

$$F(\vec{s}) = \int_{V_s} \rho(\mathbf{r}) e^{-2i\pi\vec{s}\cdot\mathbf{r}} dV_s, \quad (2.10)$$

where  $F(\vec{s})$  is the Fourier transform of the electron density distribution,  $\vec{s}$  is the scattering vector and  $V_s$  is the volume of the sample. The scattering vector  $\vec{s}$  resulting from the

scattering of the incident beam by the sample can be calculated by  $\bar{s} = \bar{s}_1 - \bar{s}_0$ , where  $\bar{s}_1$  is the wave vector of the scattered x-rays (Fig. 2.3).

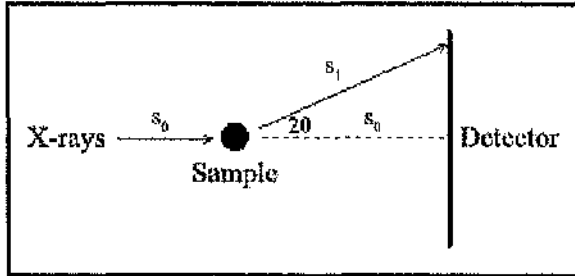


Figure 2.3 Schematic representation of SAXS

For a given scattering angle of  $2\theta$  and x-ray wavelength,  $\lambda$  then

$$s = |\bar{s}| = \frac{4\pi \sin \theta}{\lambda}, \quad (2.11)$$

which is the modulus of the scattering vector.

The scattered intensity  $I(\bar{s})$  is defined as follows:

$$I(\bar{s}) = \iint \Delta\rho(\vec{r}_1) \Delta\rho(\vec{r}_2) e^{i\bar{s}(\vec{r}_1 - \vec{r}_2)} dV_1 dV_2, \quad (2.13)$$

where the integral runs over the particle volume  $V$ ,  $\vec{r}_1$  and  $\vec{r}_2$  are vectors inside the particle and  $\Delta\rho$  represents fluctuations in the electron density of the particle with respect to the solution.

The isotropic scattering intensity  $I(s)$  is often expressed in terms of the distance distribution function  $p(r)$  as follows:

$$I(s) = 4\pi \int p(r) \frac{\sin 2\pi r s}{2\pi r s} dr \quad (2.14)$$

For a monodisperse, ideal solution the  $p(r)$  function can be written as

$$p(r) = \frac{1}{\pi} \int r s I(s) \sin 2\pi r s ds. \quad (2.15)$$

The scattering intensity at zero angle  $I(0)$  can be derived from eq. 2.10 as

$$I(0) = \iint \Delta\rho(r_1) \Delta\rho(r_2) dV_1 dV_2 = \Delta m^2 = m^2 - m_0^2, \quad (2.16)$$

where  $m$  is the total number of electrons in the particle and  $m_0$  is the number of solvent electrons displaced by the particle.

The scattered intensity can be expanded in powers of  $s^2$  to give

$$I(s) = I(0) \left[ 1 - \frac{4\pi}{3} R_g^2 s^2 + k s^4 + \dots \right], \quad (2.17)$$

but close to the origin, i.e. at low angles, the expansion can be restricted to the first order term

$$I(s) \cong I(0) \exp\left(\frac{4\pi^2}{3} R_g^2 s^2\right), \quad (2.18)$$

where  $R_g$  is the particle radius of gyration which is defined by the following relationship (Guinier & Fournet, 1955):

$$R_g^2 = \frac{\int \Delta\rho(\vec{r}) r^2 dV}{\int \Delta\rho(\vec{r}) dV}. \quad (2.19)$$

Eq. 2.16 is also known as the Guinier approximation which states that at very low scattering angles the scattering intensity can be modelled by a Gaussian distribution, the width of which

is inversely proportional to the radius of gyration. The radius of gyration,  $R_g$  is a measure of particle (non)sphericity and can be determined experimentally by plotting  $\ln I(s)$  versus  $s^2$  (Guinier plot). Using linear regression  $R_g$  can be determined from the slope, while the intensity at zero angle,  $I(0)$  is obtained by extrapolation to zero scattering angle. The Guinier region, i.e. the range of scattering angles,  $s$  over which the Guinier approximation is valid is usually defined as  $0.2 < sR_g < 1.3$  although the exact values differ for asymmetric particles (Perkins, 1988). The Guinier approximation relies on the assumption of an ideal, monodisperse solution. Therefore, in the case of a polydisperse solution, e.g. due to aggregate formation, determination of the  $R_g$  becomes ambiguous and unreliable. In order to circumvent this problem the scattering from several sample concentrations is usually recorded.

## 2.4.2 SAXS data treatment

### 2.4.2.1 Data processing

Ideal single particle scattering intensities  $I(s)$  cannot be measured directly; instead, a discrete set of intensities  $I_{\text{exp}}(s_i)$  at  $i$  angles within the angular range  $s_{\text{min}} < s < s_{\text{max}}$  is recorded, further compounded by the presence of statistical error and possible smearing effects from beam divergence, polychromaticity or detector resolution (Feigin & Svergun, 1987). It is vital, therefore, to restore the ideal scattering intensities  $I(s)$  from the experimental set  $I_{\text{exp}}(s_i)$  during data processing. For monodisperse solutions  $I(s)$  is related to the particle distance distribution function  $p(r)$  by the Fourier transform

$$I(s) = 4\pi \int_0^{D_{\text{max}}} p(r) \frac{\sin 2\pi sr}{2\pi sr} dr, \quad (2.20)$$

where  $D_{\text{max}}$  is the maximum particle dimension. Eq. 2.17 is identical to eq. 2.11 except that the integral is now delimited by  $D_{\text{max}}$ . The  $p(r)$  function has the same information content as  $I(s)$  and data processing can be done 'indirectly' by restoring the  $p(r)$ . It also introduces an important constraint due to the 'boundedness' of the function provided by  $D_{\text{max}}$ . This indirect transform approach was used first by Glatter (1977) and also forms the basis of the computer

program GNOM (Semenyuk & Svergun, 1991; Svergun, 1992) that was used for the processing of SAXS data throughout this project. Another important aspect of GNOM is the use of a regularisation parameter,  $\alpha$  which enables the user to compensate for the quality of the data fit and the smoothness of the resulting  $p(r)$  function (Svergun, 1992). The choice of  $\alpha$  is critical for the stability and validity of the solution: too small a value leads to unstable solutions, while too large a value results in systematic deviations from the experimental data. GNOM automatically performs a search for  $\alpha$ , relying on a number of perceptual criteria like discrepancy, systematic deviations, smoothness, positivity of the  $p(r)$  and stability of the solution to small changes in  $\alpha$  to determine the outcome. Failure to find a good solution usually indicates that wrong assumptions were made about the experimental system, such as an incorrect value of  $D_{max}$ . Generally,  $D_{max}$  is not known very accurately and several trial-and-error calculations have to be done for different values of  $D_{max}$ .

Using eq. 2.17 GNOM also automatically back-extrapolates  $I(s)$  beyond the measured  $s$ -range to zero angle and thus provides an estimate of  $I(0)$ . It uses the  $p(r)$  function to determine the radius of gyration,  $R_g$  which proves to be less sensitive to residual interparticle interactions and even to small amounts of aggregate, as it uses the entire scattering curve for its calculation, rather than just the Guinier region.

As mentioned above, scattering curves and their corresponding  $p(r)$  functions share the same information content. Inspection of both also allows rudimentary estimation of particle shapes: as shown in Fig. 2.4 the scattering curves of a sphere and a rod, for example, are profoundly different as anisometric particles yield fairly featureless scattering profiles that decay much more slowly than those of globular particles.

### 2.4.2.2 Direct modelling of the $p(r)$ function

Historically, three-dimensional information from SAXS data was obtained by building relatively simple low resolution models on a trial-and-error basis. Models were made up from geometrical shapes such as spheres, cylinders or ellipsoids and their scattering curves and  $p(r)$

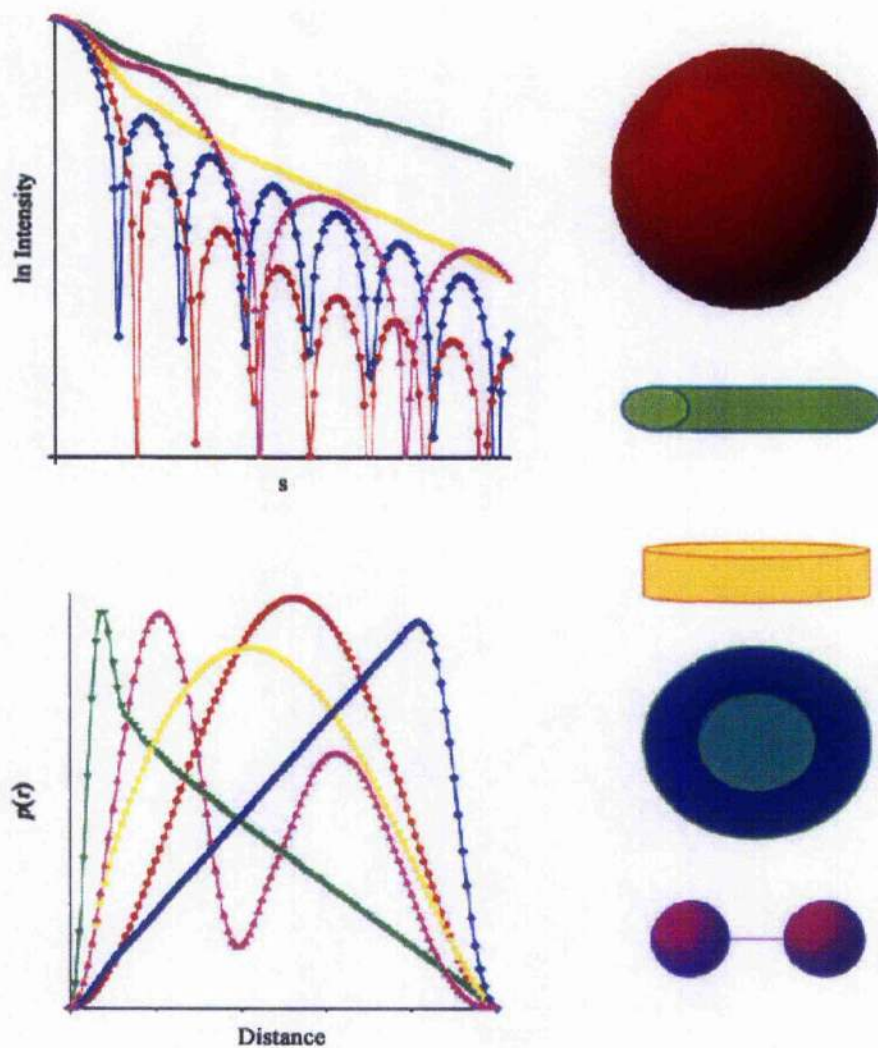


**Figure 2.4** Scattering curves and distance distribution functions of geometrical bodies. Scattering curves and their corresponding  $p(r)$  functions were calculated for a sphere (●), rod (▼), disc (●), hollow sphere (◆) and dumbbell (▲). All particles have the same  $D_{max}$ . This figure was adapted from Svergun and Koch (2003).

functions were calculated subsequently and compared to the experimental data (Kratky & Pils, 1972; Glatter, 1980; Glatter & Kratky, 1982).

A different approach to the evaluation of SAXS data focused on the calculation of theoretical scattering curves from high resolution structures obtained from x-ray crystallography or NMR. In order to be able to simulate scattering curves it is important not only to include the scattering atoms within the particle, but also to account for the effects of the particle excluded volume:

$$I(s) = \left\langle \left| F_{particle}(\vec{s}) - \rho_0 F_{buffer}(\vec{s}) \right|^2 \right\rangle_{\Omega}, \quad (2.21)$$

where  $\rho_0$  is the average electron density of the buffer, and  $\langle \rangle_{\Omega}$  represents the spherical average. The main problem in the calculation of scattering curves is the estimation of the excluded volume contribution (i.e. term 2 in eq. 2.18). Several methods have been developed to deal with this problem. Most recently, Lattman (1989) used spherical harmonics to calculate scattering intensities, an approach that was further improved by Svergun and co-workers (1995) by inclusion of the hydration shell with a different electron density ( $\rho_{hs}$ ) to both that of the particle and the buffer ( $\rho_0$ ):

$$I(s) = \left\langle \left| F_{particle}(\vec{s}) - \rho_0 F_{buffer}(\vec{s}) + \delta\rho_0 F_{hydshell}(\vec{s}) \right|^2 \right\rangle_{\Omega}. \quad (2.22)$$

$F_{hydshell}(\vec{s})$  is the scattering amplitude of the water layer bound to the particle, and  $\delta\rho_0 = \rho_{hs} - \rho_0$ . This method has been implemented in the computer program CRY SOL (Svergun et al., 1995) which computes the scattering profile of any high or low resolution structure and is able to fit it to experimentally determined data sets. In order to improve these fits the electron density of the hydration shell and the average excluded solvent volume per atomic group are allowed to vary.

### 2.4.2.3 *Ab initio* modelling

The extraction of three-dimensional data from a one-dimensional scattering curve is a non-trivial undertaking. In the past, shape information from SAXS data was obtained by building low resolution models on a trial-and-error basis, sometimes including information procured from other methods such as electron microscopy.

Over the last 35 years, however, several other methods have been developed that allow for more detailed three-dimensional information to be obtained from the analysis of SAXS data. The first *ab initio* approach, i.e. the shape restoration of a particle without the need of any prior knowledge about the system, was developed by Stuhrmann (1970) and relied on an angular envelope function described by a series of spherical harmonics to approximate particle shape. Svergun et al. have developed and implemented this approach in their computer program SASHA (Svergun & Stuhrmann, 1991; Svergun et al., 1997b). The low resolution shape is defined by a few parameters that fit the scattering data. For error-free, theoretical data SASIA is able to generate unique solutions (Svergun et al., 1996), indicating that reconstructions for experimental data sets (including errors) are stable and independent of the starting approximation. The stability and/or resolution can be further improved if information on particle symmetry is available (Vachette & Svergun, 2000).

The use of envelopes for shape restoration is limited to relatively globular particles with fairly simple shapes and no internal cavities. More detailed *ab initio* models can be obtained from Monte Carlo searches. Svergun et al. have implemented this approach in their computer program DAMMIN (Svergun, 1999): a sphere of diameter  $D_{max}$  is filled with closely packed dummy atoms on a hexagonal lattice. Each dummy atom is either part of the particle ('1') or the solvent ('0'), thus generating a long binary string. Simulated annealing is used to determine the lowest energy configuration within the search space. The computer program CRY SOL (see above) is employed to determine the scattering of each configuration. Further constraints for DAMMIN reconstructions include compactness and connectivity. As with SASHA the user can specify particle symmetry if known. DAMMIN has been evaluated with several test cases (Svergun, 1999; Volkov & Svergun, 2003) and more than 100 papers featuring DAMMIN reconstructions have been published during the last few years (e.g.

Sokolova et al., 2001; Ackerman et al., 2003; Petoukhov et al., 2003; Marquez et al., 2003; Nöllmann et al., 2004; Arita et al., 2004; Hough et al., 2004).

A similar approach was also used for the computer program DALAIGA (Chacón et al., 1998; Chacón et al., 2000). Again, a sphere of diameter  $D_{max}$  is filled with a large number of closely packed dummy atoms which are either part of the particle or the solvent. However, starting from a random configuration a genetic algorithm is used instead to search for a configuration that adequately describes the data.

The most recent *ab initio* method developed by the Svergun group for the analysis of SAXS data is implemented in the program GASBOR (Svergun et al., 2001; Petoukhov & Svergun, 2003). Apart from particle and solvent beads it introduces a third kind corresponding to the particle hydration shell, although the water molecules bound form part of the primary hydration layer and SAXS is unable to account for a full hydration shell in a hydrodynamic sense. The macromolecule is not represented by hexagonally closely packed beads; instead, one dummy residue is placed per amino acid. GASBOR has encoded within it connectivity constraints that result in models in which the dummy residues form a protein-like fold. As with DAMMIN, simulated annealing is used for an exhaustive search of the configurational search space (a sphere with diameter  $D_{max}$ ). GASBOR uses data at higher scattering angles than DAMMIN ( $s \leq 0.5 \text{ \AA}^{-1}$ ) and thus produces more detailed, i.e. higher resolution models. In some rare cases a resolution as high as 5 Å has been achieved using GASBOR (Svergun et al., 2001), but more typically the resolution of resultant models lies between 10-15 Å. A similar *ab initio* algorithm has been developed more recently by Heller et al. (2002; 2003).

### 2.4.2.4 Addition of loops and domains

Currently, it is not possible to incorporate data obtained with complementary methods in the *ab initio* modelling process. This limits the usefulness of the resultant models although a higher signal-to-noise ratio and/or an extended angular range maximise the likelihood of the restored structure representing the actual solution conformation. Some shapes, in particular very anisometric particles or those containing voids, can be difficult to reconstruct properly (Volkov & Svergun, 2003). In order to address this problem, several programs have been

developed recently that allow inclusion of high resolution structures and/or homology models in the modelling process. For example, the programs CREDO and CHADD (Petoukhov et al., 2002) have been employed to add missing loops and domains to atomic structures, using a GASBOR-like approach to determine the position of the unknown amino acid residues. Neither algorithm, however, can take into account possible conformational changes, e.g. resulting from the comparison of a protein in solution with its crystal structure.

### 2.4.2.5 Rigid-body modelling

When dealing with multisubunit proteins or macromolecular complexes where high resolution structures or models are available, the use of rigid-body modelling in combination with *ab initio* analysis can be very effective. The first computer program available for rigid body modelling with SAXS (MASSHA; Konarev et al., 2001) operates mainly on an interactive basis and its automated fitting function accesses only a limited volume of search space.

More recently, Nöllmann et al. (2005) developed an algorithm implemented in the computer program Rayuela based on Monte Carlo simulated annealing for the rigid-body modelling of multisubunit proteins/complexes with reference to SAXS data. In addition, hydrodynamic parameters obtained from AUC and distances determined using fluorescence resonance energy transfer (FRET) can also be included in order to further increase the stringency of the analysis.

For modelling with Rayuela, a protein or complex is divided into a user-specified number of structural 'domains'. Each domain can be moved by translations and rotations of its centre of mass, generating a large number of possible configurations. For each possible solution the scattering curve, sedimentation coefficient and FRET distances are calculated *in silico* and compared to the experimental data. A scoring function measures the discrepancy between the simulated and experimental data, and determines the lowest energy configuration. A similar approach for rigid-body modelling with SAXS data has also been developed by the Svergun group (Petoukhov et al., 2002; Petoukhov & Svergun, 2005).

### 2.5 Small angle neutron scattering

The underlying principles of the technique as well as the methods described in Section 2.4 also apply for the treatment and analysis of small angle neutron scattering (SANS) data. However, additional information on macromolecular complex formation can be obtained from SANS experiments when compared to SAXS.

While x-rays interact with the particle electron cloud, neutrons are scattered by the nucleus. The efficiency of scattering by different isotopes of the same element, e.g. hydrogen and deuterium varies, resulting in pronounced differences in the scattering length. Molecules of identical chemical composition have the same physical and chemical properties, but differ in their interactions with neutrons. With scattering lengths of  $-0.374 \times 10^{-12}$  cm and  $0.667 \times 10^{-12}$  cm for hydrogen and deuterium, respectively, scattered intensities vary considerably depending on isotope incorporation into macromolecules.

#### 2.5.1 Contrast variation

The difference in scattering lengths between hydrogen and deuterium is exploited in contrast match experiments. When investigating molecular interactions it is possible to render one (or more) complex components virtually "invisible". This can be achieved either by solvent exchange ( $\text{H}_2\text{O}/\text{D}_2\text{O}$ ) (Ibel & Stuhrmann, 1975) or by selective deuteration (Engelman & Moore, 1972) methods. In both instances the scattering density of one complex component is exactly matched with that of the solvent by varying the buffer  $\text{D}_2\text{O}$  content. Solvent exchange can only be used for analysing interactions between two different types of biological macromolecule, e.g. a protein-DNA complex, due to the different match points of protein (ca. 40%) and DNA (ca. 60%) (Fig. 2.4). Using selective deuteration it is also possible to investigate protein-protein interactions as one complex component is overexpressed in deuterated media before being reconstituted with the remaining protonated constituent(s). The exact  $\text{D}_2\text{O}/\text{H}_2\text{O}$  ratio can vary considerably for deuterated proteins and depends on labelling efficiency.

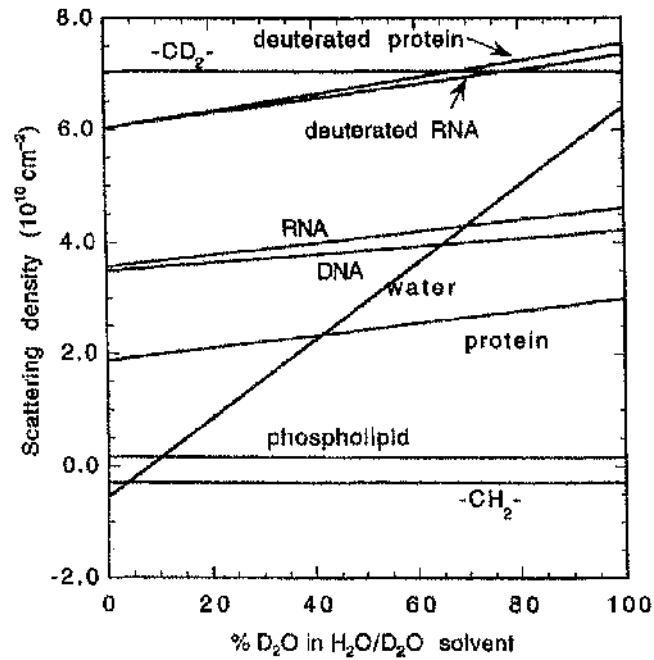


**Figure 2.4** Neutron scattering length densities of biological macromolecules in solution

The scattering length density for H<sub>2</sub>O is close to  $-5 \times 10^9 \text{cm}^{-2}$ , while that for D<sub>2</sub>O is  $64 \times 10^9 \text{cm}^{-2}$ . Scattering length densities vary in a linear fashion and no scattering can be observed at approximately 8% D<sub>2</sub>O.

Adapted from Zaccai (2000).

# **Chapter 3**

## **Materials & methods**

### **3.1 Molecular biology**

#### **3.1.1 Plasmid preparation**

Plasmid DNA was extracted and purified from 5 ml overnight cultures using the Promega (USA) Wizard SV Miniprep DNA Purification System according to manufacturer's instructions. DNA was eluted from spin columns in 100  $\mu$ l TE buffer (10 mM Tris-HCl, 1 mM EDTA, pH 7.5) unless stated otherwise and stored at -20°C. Plasmids used in this project are listed in Table 3.1.

#### **3.1.2 Agarose gel electrophoresis**

Agarose gel electrophoresis, as described by Maniatis et al. (1987a) was used to assess the efficiency and purity of plasmid preparations.

### 3.1.3 DNA extraction from agarose gels

DNA bands visualised with ethidium bromide were excised and the DNA extracted using the QIAquick gel extraction kit (Qiagen, UK) according to manufacturer's instructions. DNA was eluted in 30 µl TE and its quantity and quality assessed by agarose gel electrophoresis.

Plasmid name	Vector	Insert	Source
pET14-E3	pET14b	Human E3 aa 36-509	A. Brown (2002)
pET11-E2	pET11b	Human E2 aa 53-613	A. Brown (2002)
pET14-E2DD	pET14b	Human E2 aa 54-613	A. Brown (2002)
pET14-X	pET14b	Human E3BP aa 54-501	A. Brown (2002)
pET28-X	pET28b	Human E3BP aa 54-501	A. Brown (2002)
pET14-XDD	pET14b	Human E3BP aa 54-216	A. Brown (2002)
pGEX2-XLD	pGEX2T	Human E3BP aa 54-177	A. Brown (2002)
pET30-XSBD	pET30a	Human E3BP aa 166-230	M. Smolle

Table 3.1 Plasmids used throughout this project.

### 3.1.4 Polymerase chain reaction

Oligonucleotides were synthesised by MWG (Germany). Reactions were set up using the Expand High Fidelity PCR System (Roche, USA) according to manufacturer's instructions.

### 3.1.5 Restriction digests and plasmid ligation

Restriction digests of PCR products and plasmids were performed using restriction enzymes obtained from Promega (USA) and NEB (USA) according to manufacturer's instructions. Ligation reactions were set up using the Rapid Ligation Kit from Promega (USA) according to manufacturer's instructions.

## 3.2 Bacterial strains

*Escherichia coli* strain DH5 $\alpha$  (Stratagene, USA) was used for plasmid propagation. *E. coli* BL21 DE3, *E. coli* BL21 DE3 pLysS and *E. coli* BL21 DE3 Star (all Invitrogen, UK) strains were used for recombinant protein overexpression (Table 3.2).

<i>E. coli</i> strain	Genotype
DH5 $\alpha$	F <sup>-</sup> $\Phi$ 80 <i>lacZ</i> $\Delta$ M15 $\Delta$ ( <i>lacZYA-argF</i> )U169 <i>recA1 endA1 hsdR17</i> (r <sub>k</sub> <sup>-</sup> m <sub>k</sub> <sup>+</sup> ) <i>phoA supE44 thi-1 gyrA96 relA1 tonA</i>
BL21 (DE3)	F <sup>-</sup> <i>ompT hsdS<sub>B</sub></i> (r <sub>B</sub> <sup>-</sup> m <sub>B</sub> <sup>-</sup> ) <i>gal dcm</i> (DE3)
BL21 (DE3) pLysS	F <sup>-</sup> <i>ompT hsdS<sub>B</sub></i> (r <sub>B</sub> <sup>-</sup> m <sub>B</sub> <sup>-</sup> ) <i>gal dcm</i> (DE3) pLysS (Chl <sup>R</sup> )
BL21 (DE3) Star	F <sup>-</sup> <i>ompT hsdS<sub>B</sub></i> (r <sub>B</sub> <sup>-</sup> m <sub>B</sub> <sup>-</sup> ) <i>gal dcm rne131</i> (DE3)

**Table 3.2 Bacterial strains used**

DE3 signifies that all BL21 strains contain the  $\lambda$ DE3 lysogen that carries the gene for T7 RNA polymerase. All BL21 strains are deficient in *lon* protease and the outer membrane protein OmpT. The pLysS strain contains the pLysS plasmid which encodes T7 lysozyme and confers chloramphenicol (Chl<sup>R</sup>) resistance.

### 3.2.1 Competent cells and transformations

Cells were made chemically competent using the calcium chloride protocol and transformed as described by Maniatis et al. (1987b).

## 3.3 Protein methods

### 3.3.1 Protein overexpression and solubility

Overnight cultures were set up by inoculating Luria-Bertani broth (LB; 10 g bacto-tryptone, 5 g bacto-yeast extract, 5 g NaCl made up to 1 l with de-ionised water) supplemented with the appropriate antibiotic(s) (Table 3.3) with a single bacterial colony obtained from transformation. For protein overexpression LB including antibiotics was inoculated at a ratio of 1:50 with overnight culture. Bacteria were grown at 37°C to an OD<sub>600</sub> of 0.6-0.8 and induced with 1 mM IPTG for 3-5 hours at 30°C. At induction, XDD, XLD (see Chapter 5), E2DD (see Chapter 6) and E2/E3BP (see Chapter 7) cultures were supplemented with lipoid

acid to a final concentration of 50 µg/ml in order to maximize lipoylation. Cells were harvested by centrifugation at 15300 g for 10 minutes and the cell pellets stored at -20°C.

Antibiotic	Stock solution	Selective conditions	Plasmid
Ampicillin (Amp)	100 mg/ml in dH <sub>2</sub> O	100 µg/ml	pET11, pET14, pGEX2
Kanamycin (Kan)	25 mg/ml in dH <sub>2</sub> O	25 µg/ml	pET28, pET30
Chloramphenicol (Chl)	32.5 mg/ml in ethanol	32.5 µg/ml	pLys5

**Table 3.3 Antibiotics and selective conditions used**

Protein solubility was tested by lysing cells from a 50 ml culture in a final volume of 3 ml using a French press (750 psi) or chemical lysis (see below). Cell debris was removed from the soluble fraction by centrifugation at 15300 g for 20 minutes. The insoluble fraction was solubilised in SDS loading buffer and protein solubility assessed by SDS PAGE (see 3.3.5.1).

### 3.3.2 Protein purification

Details of all buffers used during protein purifications described here can be found in Section 4.2.3.

#### 3.3.2.1 Cell lysis

Frozen cells were resuspended in metal chelate binding buffer (10 ml/250 ml of bacterial culture) supplemented with 1x Bugbuster reagent (Novagen, UK) for chemical lysis. Cells were lysed in the presence of Complete<sup>®</sup> EDTA-free protease inhibitors (Roche, USA), benzonase (25 U/ml) and T7 lysozyme (4.5 U/ml) (both Novagen, UK) by rotation at room temperature for 30-90 minutes. Insoluble cell debris was removed by centrifugation at 15300 g for 20 minutes and the lysate filtered prior to chromatography.

#### 3.3.2.2 Metal chelate affinity chromatography

His-tagged proteins were first purified using metal chelate affinity chromatography on a BioCAD 700E workstation (Applied Biosystems, USA). A 20MC column (Applied

Biosystems, USA) was prepared at a flow rate of 10 ml/min unless mentioned otherwise as follows:

- The column was initially washed with 5 column volumes (CV) of strip solution (50 mM EDTA, 1M NaCl) to remove any remaining metal ions from a previous purification, followed by 5 CV of de-ionised water (dH<sub>2</sub>O).
- Metal ions were loaded onto the column over 30 CV using 100 mM ZnCl<sub>2</sub> or 100 mM NiCl<sub>2</sub> at 5 ml/min followed by another wash step with 5 CV of dH<sub>2</sub>O at 10 ml/min.
- Unbound ions were removed with a wash step of 5 CV of 500 mM NaCl and the column equilibrated with 5 CV of elution buffer followed by 10 CV of binding buffer.
- Sample was injected in 5 ml aliquots and each injection was followed by a wash step of binding buffer for 3 CV.
- After the final injection the column was washed with 9 CVs of binding buffer.
- Bound protein was eluted from the column in a 0-100% gradient of elution buffer and the eluate collected in 2 ml fractions.

Peak fractions were analysed by SDS PAGE and pure fractions were pooled and either subjected to further purification steps or dialysed and stored at 4°C.

#### **3.3.2.3 HQ anion exchange chromatography**

Peak fractions from metal chelate chromatography were pooled and buffer exchanged into binding buffer. A 20HQ column (Applied Biosystems, USA) was prepared as follows:

- The column was washed with 5 CV of dH<sub>2</sub>O and 5 CV of elution buffer at 5 ml/min.

- Equilibration of the column was achieved using 10 CV of binding buffer at 10 ml/min.
- Following sample injection the column was washed with a further 10 CV of binding buffer in order for the absorbance at 280 nm ( $A_{280}$ ) to return to the baseline.
- Protein was eluted from the column using a 0-50% or 0-100% gradient of elution buffer over 30-100 CV, collecting 2 ml fractions. Details vary for different proteins.

Peak fractions were again analysed by SDS PAGE and pure fractions were pooled and concentrated for gel filtration.

#### **3.3.2.4 S cation exchange chromatography**

Peak fractions from anion exchange chromatography were pooled and buffer exchanged into binding buffer. A 20S column (Applied Biosystems, USA) was prepared as follows:

- The column was washed with 5 CV of dH<sub>2</sub>O and 5 CV of elution buffer at 5 ml/min.
- Equilibration of the column was achieved using 10 CV of binding buffer at 10 ml/min.
- Following sample injection the column was washed with a further 10 CV of binding buffer in order for the  $A_{280}$  to return to the baseline.
- Protein was eluted from the column using a 0-100% gradient of elution buffer over 15 CV, collecting 2 ml fractions.

Peak fractions were again analysed by SDS PAGE and pure fractions were pooled and concentrated for gel filtration.

### 3.3.2.5 GST purification of XLD

A 5 ml GST Trap FF column (Amersham, USA) was equilibrated with PBS (140 mM NaCl, 2.7 mM KCl, 10 mM Na<sub>2</sub>HPO<sub>4</sub>, 1.8 mM KH<sub>2</sub>PO<sub>4</sub>, pH 7.3) at 2 ml/min. Sample was loaded at a rate of 0.5 ml/min. The column was then washed with more PBS until the baseline returned to zero. Bound protein was eluted in a single step with 50 mM Tris-HCl, 20 mM glutathione, pH 8.0 and collected in 1 ml fractions. Peak fractions were analysed by SDS PAGE and dialysed for further experiments.

### 3.3.2.6 Gel filtration chromatography

A Sephacryl S-300 or S-100 column (Amersham, USA) was equilibrated with 2 CV of buffer at 1 ml/min. Fractions from previous purifications were pooled and concentrated to less than 1 ml and injected onto the column. Protein was eluted over 1.2 CV of buffer run at 1 ml/min while collecting 2 ml fractions.

### 3.3.2.7 Purification of PDC from bovine heart

PDC from bovine heart was isolated as described by Stanley and Perham (1980), but with the following modifications: 600 g of bovine heart muscle were homogenised for 5 minutes in 500 ml of extraction buffer (50 mM MOPS, pH 7.0, 2.7 mM EDTA, 3% (v/v) Triton X-100, 100 µM DTT, 1 mM PMSF, 1 mM benzamidine, 0.2% (v/v) anti-foam A) and the final volume adjusted to 2 litres. Unbroken cells and cell nuclei were pelleted by centrifugation at 10000 *g* for 20 minutes. The supernatant was pooled, its pH lowered to pH 6.45 with 10% (v/v) acetic acid and subjected to a first round of PEG precipitation by the addition of 0.12 volumes of 35% (w/v) PEG 6000 and left stirring on ice for 30 minutes before centrifugation at 18000 *g* for 15 minutes. The pellets were resuspended in 200 ml homogenisation buffer (50 mM MOPS, pH 7.0, 2.7 mM EDTA, 1% (v/v) Triton X-100, 1.5 µM leupeptin, 1 mM PMSF, 1mM benzamidine) and clarified by centrifugation at 25000 *g* for 40 minutes. The supernatant was collected and filtered through 8 layers of muslin before the dropwise addition of 0.013 volumes of 1 M MgCl<sub>2</sub> and 0.05 volumes of 1 M sodium phosphate, pH 6.3. The pH was not allowed to fall below pH 6.8 by adjustment with 0.5 M NaOH. The pH of the supernatant was then lowered to pH 6.45 with 10% (v/v) acetic acid before a second PEG

precipitation with 0.12 volumes of 35% (w/v) PEG 6000 and was again left to stir for 30 minutes on ice. The precipitate was collected by centrifugation at 25000 g for 10 minutes and the pellets resuspended in 160 ml of homogenisation buffer. The suspension was stored overnight at 4°C with added protease inhibitors (1 mM PMSF, 1 mM benzamidine, 1 µM leupeptin, 100 µM DTT). The next day the suspension was rehomogenised before clarification at 25000 g for 60 minutes. The third and final PEG precipitation was carried out as above by lowering the pH of the supernatant to pH 6.45 and the addition of 0.06 volumes of 35% (w/v) PEG 6000 which was left stirring on ice for 30 minutes. OGDC was pelleted by centrifugation at 25000 g for 10 minutes. The remaining supernatant contained PDC and was spun at 10000 g for 15 minutes to remove remaining OGDC contamination. PDC was pelleted by ultracentrifugation at 120000 g for 120 minutes. Storage buffer (50 mM potassium phosphate, pH 7.4, 2 mM EDTA, 0.02% (w/v) sodium azide, 1 mM benzamidine, 1 mM PMSF) was added to both OGDC and PDC pellets and stored at 4°C for 15-20 hours before homogenisation. The protein concentrations of OGDC and PDC were determined using BioRad assays (see 3.3.6) and preparations stored at a maximum concentration of 10 mg/ml in 50% (v/v) glycerol at -20°C.

#### **3.3.2.8 Sucrose gradient centrifugation**

Discontinuous sucrose gradients were set up as described by Rahmatullah et al. (1989b), but with the following modifications: 4 ml of 20% (w/v) sucrose, 2 ml of 10% (w/v) sucrose and 2 ml of 5% (w/v) sucrose in 50 mM potassium phosphate, 2 M NaCl, 2 mM EDTA, 0.02% (w/v) sodium azide, pH 7.4 were layered on top of each other. The gradient was overlaid with 5-8 ml of sample and spun at 50000 rpm at 4°C for two hours. 1 ml fractions were collected following removal from the top using a peristaltic pump.

#### **3.3.3 Removal of His-tags**

His-tags were removed from E3 by thrombin cleavage. Purified E3 was buffer exchanged into PBS buffer by concentration. Approximately 10 U of thrombin (Amersham, USA) were added per mg of protein and incubated at room temperature overnight. Thrombin and the cleaved tags were removed from E3 preparations by a subsequent gel filtration step.

### **3.3.4 Dialysis**

In order to match buffers for biophysical experiments, proteins were dialysed against 5 l of buffer overnight at 4°C. For salt removal between different chromatography steps, brief dialysis steps for 2-3 hours at room temperature were used. Dialysis membrane was obtained from Visking (UK) and prepared as described by Bollag et al. (1996a). Alternatively, SnakeSkin dialysis tubing and dialysis cassettes from Pierce (USA) were used according to manufacturers' instructions.

### **3.3.5 Polyacrylamide gel electrophoresis**

#### **3.3.5.1 SDS polyacrylamide gel electrophoresis (SDS PAGE)**

SDS PAGE was used to assay the purity and concentration of proteins and was performed as previously described by Laemmli (1970) using 4% stacking and 10-15% resolving gels. Alternatively, 4-12% bis-tris NuPAGE gels (Invitrogen, UK) were used according manufacturer's instructions. Gels were stained with 0.1% (w/v) Coomassie Brilliant Blue, 10% (v/v) acetic acid, 50% (v/v) methanol for at least 30 minutes before being destained with 10% (v/v) acetic acid, 10% (v/v) methanol overnight.

#### **3.3.5.2 Non-denaturing PAGE**

Non-denaturing PAGE as described by Bollag et al. (1996b) was employed to determine protein complex formation and to check for the presence of aggregate species. A 5% stacking and 8% resolving gel were used and gels were run at 10 mA at room temperature for 3-6 hours. Gels were stained with Coomassie Brilliant Blue as described above.

### **3.3.6 Determination of protein concentration**

The protein concentrations of XSBD and XDD were determined using their calculated extinction coefficients at 280 nm of 9800 M<sup>-1</sup> and 11380 M<sup>-1</sup>, respectively. Similarly, E2DD preparations were quantitated using a calculated extinction coefficient at 278 nm of 9800 M<sup>-1</sup>. E3 was quantitated using an experimentally determined extinction coefficient of 22600 M<sup>-1</sup>

for the E3 dimer, exploiting FAD absorbance at 450 nm. Since the amino acid sequence of bovine E1 is not known, the sequence of human E1 was used to calculate an extinction coefficient of  $140000 \text{ M}^{-1}$  at 278 nm. Alternatively, BioRad assays (Bio-Rad, Germany) were performed to determine protein concentrations by producing a standard curve for BSA and/or IgG according to manufacturer's instructions.

### **3.3.7 Modification of proteins with mPEG maleimide**

Monomethoxypolyethylene glycol (mPEG) 5000 maleimide is a thiol reagent that interacts covalently with the reduced forms of cysteine and lipoic acid. Proteins (20-30  $\mu\text{g}$ ) were pre-incubated under reducing or oxidising conditions for 30 minutes at room temperature, followed by the addition of 1 mM mPEG 5000 maleimide and further incubation at 25°C for 30 minutes. Reactions were stopped by the addition of excess DTT (final concentration 35 mM) and proteins (ca. 13  $\mu\text{g}$ ) resolved by SDS PAGE on 12% (v/v) gels.

## **3.4 Biophysical methods**

### **3.4.1 Calculation of buffer densities and viscosities**

Buffer densities and viscosities were calculated from buffer compositions, using the computer program SEDNTERP (Laue et al., 1992) (see Table 3.4).

### **3.4.2 Sedimentation velocity analytical ultracentrifugation**

Sedimentation velocity (SV) experiments were conducted at 4°C in a Beckman Coulter Optima XL-I analytical ultracentrifuge (Palo Alto, USA) using an An-60 Ti rotor and rotor speeds of 45000-49000 rpm. Sample concentrations depended on the specific experiment. Samples (380  $\mu\text{l}$  or 90  $\mu\text{l}$ ) were loaded into 12 mm or 3 mm path length charcoal-filled epon double sector centrepieces, respectively. A series of scans was collected using interference optics or a combination of interference and absorbance optics. The data were analysed using

the computer program SEDFIT (Schuck, 2000; Schuck et al., 2002) which allows the user to subtract radial and time-independent noise, and to directly model the sedimentation boundary as a continuous distribution of discrete, non-interacting species (*c(s)* analysis). Sedimentation coefficients of clearly defined systems were further evaluated using finite element analysis in SEDFIT which finds the sedimentation coefficients that best fit the Lamm equation. More details can be found in Section 2.2.1.1.

Buffer	Buffer composition	Temperature (°C)	Density (g/ml)	Viscosity (Poise)
TEB	2 mM EDTA, 50 mM Tris-HCl, pH 7.5	4	1.002	0.0159
		20	1.000	0.0102
TEBS50	2 mM EDTA, 50 mM NaCl, 50 mM Tris-HCl, pH 7.5	4	1.004	0.0160
		20	1.002	0.0102
TEBS100	2 mM EDTA, 100 mM NaCl, 50 mM Tris-HCl, pH 7.5	4	1.006	0.0161
		20	1.004	0.0103
PEB	2 mM EDTA, 50 mM KPO <sub>4</sub> , pH 7.4	4	1.005	0.0159
		20	1.003	0.0101

**Table 3.4** Density and viscosity of buffers used throughout this project

### 3.4.3 Sedimentation equilibrium analytical ultracentrifugation

Sedimentation equilibrium (SE) experiments were conducted at 4°C in a Beckman Coulter Optima XL-I analytical ultracentrifuge (Palo Alto, USA) using an An-60 Ti rotor and rotor speeds of 8500-32000 rpm. Sample concentrations depended on the specific experiment. The samples (120 µl or 30 µl) were loaded into 12 mm or 3 mm double sector charcoal-filled epon centrepieces, respectively. A series of scans was obtained using interference and/or absorbance optics. For absorbance optics 20 replicate data sets were recorded in step mode using a step size of 0.001 cm over a radial range of 5.7-7.2 cm. Attainment of equilibrium was ascertained with WinMATCH ([www.biotech.uconn.edu/auf/](http://www.biotech.uconn.edu/auf/)) until no net movement of protein was observed in scans recorded three hours apart. The optical baseline was determined by overspeeding at 49000 rpm. SE data were analysed using global analysis in the Beckman XL-A/XL-I software implemented in MicroCal ORIGIN in order to obtain

estimates of the whole cell weight-average protein molar mass. Furthermore, the computer program SEDPHAT (Schuck, 2003; Vistica et al., 2004) which allows global fitting of more than one species was used for the analysis of more complex systems. Analysis of some data sets required the inclusion of non-ideality. The data were analysed in ORIGIN, but fitting included the second virial coefficient,  $B$ . A starting estimate for  $B$  was calculated using the program COVOL (Harding et al., 1999) based on molecule dimensions and charge. The values of the weight-average molecular weight,  $M_w$ , and  $B$  at infinite dilution  $B^0$  were determined by plotting  $1/M_{w,app}$  against concentration (in g/ml), where  $M_w^0$  is the inverse of the y intercept and  $B^0$  can be calculated from the slope.

### 3.4.4 Isothermal titration calorimetry

Isothermal titration calorimetry (ITC) measurements were carried out in a VP-ITC microcalorimeter (MicroCal Inc., USA) at 25°C as described by Jung et al. (2002). Briefly, all proteins were dialysed overnight against 2 mM EDTA, 0.01% (w/v) sodium azide, 20 mM MOPS, pH 7.4. Syringe contents were injected in 10  $\mu$ l steps into the reaction cell. Data were analysed using non-linear regression in the MicroCal ORIGIN software package, assuming a simple binding model. ITC experiments and analyses were done by Mrs. Margaret Nutley in the laboratory of Prof. Alan Cooper, University of Glasgow.

### 3.4.5 Small angle x-ray scattering

Experiments at beamline X33 of the EMBL Hamburg outstation at the storage ring DORIS III of the Deutsches Elektronen Synchrotron (DESY) used beam currents of 80-240 mA, an electron energy of 2 GeV and a wavelength of 1.54 Å. Data for several different sample concentrations were recorded at 10°C using a detector-to-sample distance of 2.6 m, covering a range of momentum transfer of  $0.01 < s < 0.42 \text{ \AA}^{-1}$  ( $s = 4\pi \sin \theta / \lambda$ ), where  $2\theta$  is the scattering angle and  $\lambda$  the wavelength of the x-rays. The 2D MAR detector was calibrated using wet rat tail collagen. Data were collected in 5 x 60 s frames, integrated, normalised to the incident beam and corrected for the detector response using the program PRIMUS

(Konarev et al., 2003). Signs of radiation induced aggregation were checked for by dividing the first frame by the last. Frames unaffected by aggregation were averaged, the scattering of the buffer was subtracted and the difference curves scaled for concentration (in PRIMUS). The final scattering curve was obtained by merging the low angle region of the low concentration curve with the high angle region of the high concentration curve in order to eliminate the effects of interparticle interference. The maximum dimension,  $D_{\max}$  and particle distance distribution function  $p(r)$  were obtained by indirect Fourier transformation using the program GNOM (Semenyuk & Svergun, 1991; Svergun, 1992). The radius of gyration  $R_g$  was obtained by employing both the Guinier approximation and GNOM.

Experiments at beamline 2.1 at the SRS Daresbury, UK were performed using procedures similar to those described above. Due to the smaller detector size two different camera lengths were used, namely 4.25 m and 1.0 m covering a range of momentum transfer of  $0.01 < s < 0.74 \text{ \AA}^{-1}$ . The data were collected in 30 x 60 s frames and were then integrated, normalised to the incident beam, checked for aggregation, averaged and corrected for the detector response using the computer programs BSL and XOTOKO (Boulin et al., 1988). The scattering of the buffer was subtracted and the difference curves scaled for concentration in PRIMUS (Konarev et al., 2003). As before, the low angle region of the low concentration curve was merged with the high angle region of the high concentration curve in order to eliminate the effects of interparticle interference. Furthermore, the low angle region of the long camera length data was merged with the high angle region of the short camera length data in order to produce the final scattering curve. Further data analysis proceeded as described above.

#### 3.4.6 Small angle neutron scattering

Small angle neutron scattering data (SANS) data were obtained on beamline D11 at the Institut Laue-Langevin (ILL, Grenoble, France) using a neutron wavelength,  $\lambda$  of 6 Å. Experiments were performed in 1 mm optical path length quartz cuvettes. Samples were first prepared in normal buffer and subsequently dialysed extensively against D<sub>2</sub>O-based buffer. Low angle scattering data ( $s = 4\pi \sin \theta / \lambda$ ), where  $2\theta$  is the scattering angle were obtained using a detector distance of 10 m, while high angle data were recorded at a detector distance

of 3.3 m. An overall  $s$ -range of  $0.0064 < s < 0.203 \text{ \AA}^{-1}$  was covered. Data collection times of 3 hours were used per sample and scattering was recorded on a two-dimensional gas detector. The computer program *widet* was used to determine the position of the beam centre on a transmission file. A mask file of the beam was subsequently produced using the program *rmask*. Data integration was performed with *rnls*, while *xpolly* was used to generate a detector response file from a vanadium sample transmission, as well as background and H<sub>2</sub>O scattering data. Buffer and sample data were corrected for the detector response and then the buffer subtracted from the sample scattering in *xpolly*. Further details on data treatment can be found in Ghosh et al. (1989). The maximum dimension,  $D_{\text{max}}$  and particle distance distribution function  $p(r)$  were obtained by indirect Fourier transformation using the program GNOM (Semenyuk & Svergun, 1991; Svergun, 1992). The radius of gyration  $R_g$  was obtained by employing both the Guinier approximation and GNOM. SANS experiments were done by Dr. Phil Callow, Institut Laue-Langevin, Grenoble, France.

### 3.4.7 Circular dichroism

XSBD was dialysed against 50 mM sodium phosphate, pH 7.4. Circular dichroism (CD) experiments of 0.5 mg/ml XSBD were performed at room temperature on a JASCO J-810 spectropolarimeter covering a range of 260-180 nm at a scan speed of 50 nm/min and a bandwidth of 1 nm. Results were analysed with the CONTIN program package (Provencher & Glockner, 1981; Sreerama & Woody, 2000) in order to obtain numerical estimates of protein secondary structure content. All CD measurements and analyses were performed by Dr. Sharon Kelly, University of Glasgow.

## 3.5 Computational methods

### 3.5.1 Sequence alignments

Pairwise sequence alignments were performed using EMBOSS-Align ([www.ebi.ac.uk/emboss/align/](http://www.ebi.ac.uk/emboss/align/)), while alignment of multiple nucleotide or protein sequences was done with MULTALIN (Corpet, 1988) ([prodes.toulouse.inra.fr/multalin/multalin.html](http://prodes.toulouse.inra.fr/multalin/multalin.html)).

### 3.5.2 Homology modelling

Homology models of human E3, the LD and SBD of human E3BP as well as the SBD of human E2 were obtained from SWISS-MODEL (Guex & Peitsch, 1997; Peitsch et al., 2000; Schwede et al., 2003). The crystal structure solved for *S. cerevisiae* E3 (Toyoda et al., 1998b) (PDB ID 1JEH) was used as a template for human E3. The E3BP-LD and SBDs of E2 and E3BP were based on the NMR structures determined for the human E2-LD (Howard et al., 1998) (PDB ID 1FYC) and *B. stearrowthermophilus* E2-SBD (Kalia et al., 1993; Mande et al., 1996) (PDB ID 2PDD, 1EBD), respectively. The lack of structural information for the E3 His-tag (aa 1-27) meant that an approach using secondary and tertiary structure prediction was used to obtain a model structure. JPRED (Cuff et al., 1998) was employed to assign secondary structure to each individual residue. Twenty runs with the tertiary structure prediction package DRAGON (Aszódi & Taylor, 1996) were used to obtain a final model of the His-tag which was attached to the N-terminus of the E3 homology model in INSIGHT II (Accelrys, USA). Energy minimisation of all homology models was performed with the computer program QUANTA (Accelrys, USA). All structures were visualised using VMD (Humphrey et al., 1996) or Pymol (DeLano Scientific, USA).

### 3.5.3 Hydrodynamic modelling

The program HYDROPRO (García de la Torre et al., 2000; García de la Torre, 2001) was used to calculate the hydrodynamic parameters of high resolution structures. HYDROPRO first produces a bead model representing the high resolution structure, which is then converted into a shell model where the surface of the molecule is represented by a collection of equally sized minibeads. The hydrodynamic properties, including sedimentation coefficient and translational diffusion coefficient, are calculated for shell models with different minibead sizes. The apparent hydrodynamic parameters are estimated by extrapolation to a minibead radius of zero. The van der Waals radii of the initial bead model range between 1.5-2.0 Å, but represent the molecule *in vacuo* and therefore do not take hydration into account. The atomic element radius (AER) is used to adjust the bead radius of the initial bead model in order to account for hydration. For proteins an AER of approximately 3.3 Å is usually appropriate, although variations do occur (García de la Torre et al., 2000). For all calculations in this project the AER was set to 3.0-3.3 Å. All runs were

performed using at least five minibead radii resulting in shell models with 300-2000 minibeads. In order to ensure the accuracy of the models and their calculated hydrodynamic parameters, the amount of hydration for each model was checked to be within acceptable limits for proteins (0.3-0.4 g water/g protein) (García de la Torre, 2001).

### 3.5.4 *Ab initio* modelling from SAXS data

*Ab initio* shape reconstruction was done using the computer programs DAMMIN (Svergun, 1999) and GASBOR (Svergun et al., 2001; Petoukhov & Svergun, 2003). DAMMIN restores the structure as a collection of densely packed beads in a dummy atom model (DAM) inside a search volume (a sphere with a diameter corresponding to the maximum particle dimension,  $D_{\max}$ ). The program starts from a random configuration and uses a simulated annealing algorithm to explore the landscape of acceptable low resolution structures. GASBOR represents particles as collections of dummy residues (DR) using one DR per amino acid residue. The DRs are randomly distributed within the search volume and simulated annealing is used to obtain a chain-compatible spatial distribution. Ten GASBOR models were superimposed, averaged and the resulting pdb file used as the initial search space for a final DAMMIN reconstruction (see Section 2.4.2.3).

### 3.5.5 Calculation of scattering curves from structural models

Scattering curves for high resolution structures or models and their fits to experimental scattering curves were calculated using the program CRY SOL (Svergun et al., 1995) using default parameters.

### 3.5.6 Rigid body modelling

For the purpose of rigid body modelling with the computer program Rayuela (Nöllmann et al., 2005) the complex structure was defined by several "domains". Rayuela allows translation and rotation of each individual domain, calculates a SAXS curve as well as

sedimentation coefficient for each composite structure, compares it to the corresponding experimental data and determines the lowest energy conformation. Initially, only a single domain was allowed to sample different configurations with respect to the remaining molecule. Separate runs were performed for each domain. During final runs, fine-tuning of all domain positions was achieved by independent movement of all domains.

### 3.5.7 Superimposition of different model structures

Superimposition of different *ab initio* models was done using the computer program SUPCOMB (Kozin & Svergun, 2001). SUPCOMB was developed to superimpose low resolution structures with each other as well as with high resolution structures. It maximises the volume of the two search models in order to optimise superimposition. This approach works very well for the superimposition of several low resolution structures of very similar shape. However, for the superimposition of the final *ab initio* model with a high resolution structure the computer program SITUS (Wriggers & Birmanms, 2001; Wriggers & Chacón, 2001) was used instead. SITUS was initially developed for combining multi-resolution data from a variety of sources, including cryo electron microscopy (EM), electron tomography, SAXS, protein crystallography and NMR. It uses a vector quantisation method where 3-9 vectors are assigned to both the low and the high resolution structures. The program then attempts to optimise the superimposition of both sets of vectors. Results were visualised using the program VMD (Humphrey et al., 1996).

# Chapter 4

## Cloning, protein overexpression and purification

### 4.1 Introduction

Until the advent of recombinant DNA technology, purification of proteins from their original source was a laborious and time-consuming step that all too often yielded only very small amounts of protein. The expression of somatostatin (Itakura et al., 1977), human growth hormone (Goeddel et al., 1979a) and insulin (Goeddel et al., 1979b) in bacterial cell cultures in the late 1970s heralded a new era for biochemical studies: today many different bacterial expression systems are available commercially and are used in most biochemistry laboratories to allow large-scale overexpression of recombinant proteins at very low cost.

Another advantage of recombinant DNA technology is the absolute control over the coding sequence given to the researcher. Only this development has made protein engineering a reality. Furthermore, it allows all types of gene manipulation, including mutagenesis as well as the opportunity to study individual domains of multi-domain proteins in isolation. A large number of tags added onto the N- or C-terminus of recombinant proteins have been developed

that aid protein purification and detection: commonly used tags and fusion proteins include, for example, His-tags, glutathione *S*-transferase (GST)- and maltose binding protein (MBP)-fusions. His-tags usually consist of 6-10 histidine residues joined onto a protein's N- or C-terminus via a short linker region. Histidine residues display an affinity for metal ions which is exploited for protein purification in metal chelate chromatography where imidoacetate groups linked to the resin are loaded with metal ions such as Ni<sup>2+</sup>, Zn<sup>2+</sup> or Co<sup>2+</sup> which in turn interact with the His-tag (Lindner et al., 1992). Protein is eluted using imidazole which competes with the protein for the metal ions. Glutathione affinity purification is based on a similar principle: glutathione *S*-transferase (GST) – a 26 kDa polypeptide – is fused to the protein of interest. During the purification GST interacts with the glutathione in the resin and the protein is eluted with a high concentration of glutathione. GST fusion proteins are often used for the overexpression of small or insoluble proteins. Thus, the application of protein tags can shorten protein purification protocols significantly, often requiring only one or two purification steps.

Overexpression of constituent enzymes of PDC is straightforward and routine as evidenced by the large number of research papers published that employ recombinant PDC proteins from various organisms, including human (Leung et al., 1990; 1996; Quinn et al., 1993; Ciszak et al., 2001; 2003), porcine (Toyoda et al., 1998a), *S. cerevisiae* (Stoops et al., 1992; 1997; Toyoda et al., 1998b), *B. stearrowthermophilus* (Kalia et al., 1993; Lessard et al., 1998; Domingo et al., 1999; Allen et al., 2005), *E. coli* (Allen et al., 1989; Green et al., 1995, Arjunan et al., 2002), *Streptococcus faecalis* (Allen & Perham, 1991), *A. vinelandii* (Schulze et al., 1993; Hengeveld et al., 1999) and nematodes (Klingbeil et al., 1996; Harmych et al., 2002). All proteins are non-glycosylated and therefore do not require the eukaryotic post-translational modification machinery. The recombinant proteins used throughout this project were expressed with an N- or C-terminal His-tag, except for the E3BP lipoyl domain (XLD) which contains an N-terminal GST-tag. Overexpression of all proteins works very well (Brown, 2002) and, with the exception of E1, they are readily soluble. Therefore, the only proteins purified from an original source throughout this project were E1 and E2/E3BP core which were obtained in large amounts from PDC purified from bovine heart muscle.

## 4.2 Materials & methods

### 4.2.1 Subcloning of the E3BP subunit binding domain (XSBD)

The cDNA for E3BP is freely available in the public domain (Harris et al., 1997). Primers were designed for the amplification of residues 166-230 of the mature protein encompassing the subunit binding domain of E3BP as well as approximately 15 amino acid residues on either side of the domain that form part of the linker regions. The SBD of E3BP does not contain any aromatic amino acids which complicates quantification of the purified protein. Protein absorbance between 190-230 nm corresponding to the absorbance of the peptide bond can be used for concentration determination, but is less accurate than using the absorbance at 280 nm. Therefore, a tryptophan residue was added onto the C-terminal end of the sequence by incorporation of the corresponding codon into the reverse primer. As the last few amino acids of this construct form part of the linker region, the presence of a tryptophan residue was not thought to have any detrimental effects on protein structure or its interaction with E3. The forward and reverse primers include *NdeI* and *XhoI* restriction sites for site-directed cloning into pET30a (Fig. 4.1).

**Forward primer XSBDhis166-230f**  
 5' CGGC **CATATG** CAGATTTCCATCCCCTGTCAAG 3'

**Reverse primer XSBDhis166-230r**  
 5' GCCG **TTGACA** CCACTCGGTAATCTTGCCCGTTTG 3'

#### Figure 4.1 Primer sequences for the subcloning of XSBD

The *NdeI* and *XhoI* restriction sites are shown in yellow and green boxes, respectively. Nucleotide sequences corresponding to the methionine start codon (ATG) and C-terminal tryptophan (CCA) are shown in bold.

PCR reactions were set up using the Expand High Fidelity PCR System (Roche, USA). A typical 50 µl reaction included 1.5 mM MgCl<sub>2</sub>, 200 µM of each dNTP, 300 nM of each primer, approximately 100 ng of DNA template (pET14-X), 100 µg/ml BSA and 2.6 U of Expand polymerase in 1x Expand reaction buffer. Negative control reactions without DNA template were also set up. PCR cycles are shown in Table 4.1.

Following PCR, samples were subjected to agarose gel electrophoresis on a 2% (w/v) gel and the DNA extracted from the gel. The PCR product and recipient plasmid pET30a were digested with restriction enzymes *NdeI* and *XhoI* for directional insertion into the vector. *NdeI/XhoI* double digests were set up in a total volume of 40  $\mu$ l containing 25  $\mu$ l DNA, 5 U *NdeI* and 5 U *XhoI* in 1x Promega buffer D. Reactions were incubated at 37°C for 4 hours. The digested DNA was again gel purified and then ligated. For ligation reactions the amount of insert:vector DNA was varied, ranging from a three- to ten-fold excess of insert DNA. Negative controls contained vector DNA only. Ligations were incubated in 1x Rapid Ligation buffer (Promega, USA) with 3 U of T4 ligase at room temperature for 3 hours and then immediately transformed.

Step	Temperature (°C)	Time
1 Denaturation	94	2 min
2 Denaturation	94	15 s
3 Annealing	52	30 s
4 Extension	72	45 s
Repeat steps 2-4 for 9 cycles		
5 Denaturation	94	15 s
6 Annealing	52	30 s
7 Extension	72	50 s + 5s/cycle
Repeat steps 5-7 for 17 cycles		
8 Extension	72	7 min

**Table 4.1** PCR cycling reactions

Diagnostic restriction digests of pET30a and pET30-XSBD were performed with *PvuI* or double restriction with *PvuI* and *NheI* (both NEB, USA). Reactions were set up containing ca. 1  $\mu$ g DNA, 100  $\mu$ g/ml BSA and 5 U of enzyme(s) in 1x NEB buffer 3 (*PvuI* single digest) or 1x NEB buffer 2 (*PvuI/NheI* double digest). All digests were incubated at 37°C for 4 hours and subsequently analysed by agarose gel electrophoresis on a 0.8% (w/v) agarose gel. Both strands of three pET30-XSBD plasmids were sequenced on both strands (MWG, Germany) in order to verify the entire coding sequence.

### 4.2.2 Protein overexpression

Overexpression plasmids were transformed into different bacterial strains as outlined in Table 4.2. Protein overexpression of His-tagged E3, E3BP didomain (XDD), E2 didomain (E2DD), GST-tagged E3BP lipoyl domain (GST-XLD) and coexpression of E2 and E3BP was performed using a standard protocol as outlined in Section 3.3.1. XSBD overexpression was attempted at 30°C and 15°C for 4 hours and overnight, respectively, following induction with 1 mM IPTG and its solubility tested as described in Section 3.3.1.

Plasmid	<i>E. coli</i> strain	Antibiotic <sup>R</sup>
pET14-E3	BL21 DE3 pLysS	Amp, Chl
pET14-XDD	BL21 DE3 pLysS	Amp, Chl
pGEX2-XLD	BL21 DE3 Star	Amp
pET30-XSBD	BL21 DE3 pLysS BL21 DE3 Star	Kan, Chl Kan
pET14-E2DD	BL21 DE3 pLysS	Amp, Chl
pET11-E2 pET28-X	BL21 DE3 pLysS	Amp, Kan, Chl

**Table 4.2** *E. coli* strains and selection conditions used for protein overexpression

### 4.2.3 Protein purification

E3 was purified by a combination of metal chelate and size exclusion chromatography. Its His-tags were removed by thrombin cleavage prior to gel filtration. XDD, E2DD and E2/E3BP purifications included metal chelate, anion exchange and gel filtration chromatography steps. XSBD purification required a sequence of metal chelate, anion exchange, cation exchange and size exclusion chromatography steps. Metal chelate chromatography of all proteins was performed using 100 mM ZnCl<sub>2</sub> to load the column with metal ions, except for the purification of XSBD when 100 mM NiCl<sub>2</sub> was used instead. XLD was purified by glutathione affinity chromatography. E1 was obtained by a combination of sucrose gradient centrifugation of bovine PDC, followed by anion exchange based on a method developed by McCartney (1998) (for modifications see Table 4.3) and gel filtration chromatography. A Sephacryl S-300 column was used for size exclusion chromatography of

all polypeptides except for XSBD which required use of a Sephacryl S-100 column (Amersham, USA) due to its low molecular weight.

Bovine E2/E3BP core was a by-product of E1 purification by sucrose density centrifugation. Pellets containing PDC core were homogenised in 50 mM potassium phosphate, 2 M NaCl, 2 mM EDTA, 0.01% sodium azide, pH 7.4 (see Section 3.3.2.7) and subjected to a second round of sucrose density centrifugation in order to remove any remaining molecules of E1 and E3. E2/E3BP core pellets were again homogenised and extensively dialysed against 50 mM potassium phosphate, 2 mM EDTA, 0.01% sodium azide, pH 7.4.

Technical details of protein purification are given in Section 3.3.2. Details of the buffers used for all chromatography steps are listed in Table 4.3. Protein quantity and quality were assessed by SDS PAGE.

## 4.3 Results and discussion

### 4.3.1 Subcloning of the subunit binding domain of E3BP (XSBD)

XSBD had been previously cloned into the pGEX2T vector (Brown, 2002). However, protein yields were fairly low because the thrombin cleavage required to remove the GST tag also digested XSBD non-specifically, especially when the purification was scaled up. Therefore, XSBD was subcloned into pET30a resulting in a C-terminally His-tagged protein. Residues 166-230 of full-length human E3BP were subcloned, resulting in a smaller construct due to a reduction in the length of linker sequence included. Amplification of the DNA sequence corresponding to amino acid residues 166-230 was successful and yielded the expected 230 bp product (Fig. 4.2A). Using a directional cloning strategy with restriction enzymes *NdeI* and *XhoI*, the PCR product was ligated into pET30a resulting in the creation of plasmid pET30-XSBD (Fig. 4.2B). The presence of the XSBD coding sequence was confirmed using diagnostic restriction digests (Fig. 4.2C) with *PvuI* and *NheI*. The vector pET30a contains only a single *PvuI* site, the *NheI* restriction site is present only within the insert. Therefore, digestion of pET30a yields only a single linearised fragment of 5422 bp. Similarly, digestion

### 4.3 Results & discussion

Protein	Purification	Binding buffer	Elution buffer	Elution gradient
<b>E3</b>	Metal chelate	20 mM Hepes, 100 mM NaCl, 5 mM Imidazole, pH 8.0	20 mM Hepes, 100 mM NaCl, 500 mM Imidazole, pH 7.0	0-100% 8 CV
	Gel filtration	50 mM Tris-HCl, 2 mM EDTA, pH 7.5 (TEB)		
<b>XDD</b>	Metal chelate	20 mM Hepes, 100 mM NaCl, 5 mM Imidazole, pH 8.0	20 mM Hepes, 100 mM NaCl, 500 mM Imidazole, pH 7.0	0-100% 8 CV
	Anion exchange	25 mM Tris-HCl, pH 7.5	25 mM Tris-HCl, 1 M NaCl, pH 7.5	0-100% 100 CV
	Gel filtration	50 mM Tris-HCl, 100 mM NaCl, 2 mM EDTA, pH 7.5 (TEBS100)		
<b>XLD</b>	GST affinity	PBS (140 mM NaCl, 2.7 mM KCl, 10 mM Na <sub>2</sub> HPO <sub>4</sub> , 1.8 mM KH <sub>2</sub> PO <sub>4</sub> , pH 7.3)	50 mM Tris-HCl, 20 mM glutathione, pH 8.0	N/A
<b>XSBD</b>	Metal chelate	20 mM Hepes, 100 mM NaCl, 5 mM Imidazole, pH 8.0	20 mM Hepes, 100 mM NaCl, 500 mM Imidazole, pH 7.0	0-100% 8 CV
	Anion exchange	25 mM Tris-HCl, pH 7.5	25 mM Tris-HCl, 2 M NaCl, pH 7.5	0-100% 30 CV
	Cation exchange	25 mM Tricine, pH 8.5	25 mM Tricine, 1.2 M NaCl, pH 8.5	0-100% 15 CV
	Gel filtration	50 mM Tris-HCl, 2 mM EDTA, pH 7.5 (TEB)		
<b>E2DD</b>	Metal chelate	20 mM Hepes, 100 mM NaCl, 5 mM Imidazole, pH 8.0	20 mM Hepes, 100 mM NaCl, 500 mM Imidazole, pH 7.0	0-100% 8 CV
	Anion exchange	25 mM Tris-HCl, pH 7.5	25 mM Tris-HCl, 2 M NaCl, pH 7.5	0-50% 80 CV
	Gel filtration	50 mM Tris-HCl, 2 mM EDTA, pH 7.5 (TEB)		
<b>E1</b>	Anion exchange	20 mM MOPS, 10 mM NaCl, 2 mM EDTA, 1 mM CHAPS, pH 7.4	20 mM MOPS, 1 M NaCl, 2 mM EDTA, pH 7.4	0-75% 100 CV
	Gel filtration	50 mM KPO <sub>4</sub> , 2 mM EDTA, 0.01% sodium azide, pH 7.4 (PEB)		
<b>E2/ E3BP</b>	Metal chelate	20 mM Hepes, 100 mM NaCl, 5 mM Imidazole, pH 8.0	20 mM Hepes, 100 mM NaCl, 500 mM Imidazole, pH 7.0	0-100% 8 CV
	Anion exchange	20 mM MOPS, 2 mM EDTA, 0.01% sodium azide, pH 7.4 (MEB)	20 mM MOPS, 1 M NaCl, 2 mM EDTA, 0.01% sodium azide, pH 7.4	0-100% 100 CV
	Gel filtration	50 mM KPO <sub>4</sub> , 2 mM EDTA, 0.01% sodium azide, pH 7.4 (PEB)		

**Table 4.3 Chromatography buffers used during this project**

of pET30-XSBD with *PvuI* alone results in the formation of a single fragment of 5439 bp. However, double restriction with *PvuI* and *NheI* generates two fragments of 4233 bp and 1206 bp (Fig. 4.2C). Several bands are visible for the single digests of pET30a and pET30-XSBD. This is a result of incomplete restriction of the plasmid DNA and the two additional bands correspond to relaxed and supercoiled DNA which exhibit different mobilities with respect to linear DNA. DNA sequencing confirmed that no mutations had been introduced by PCR.

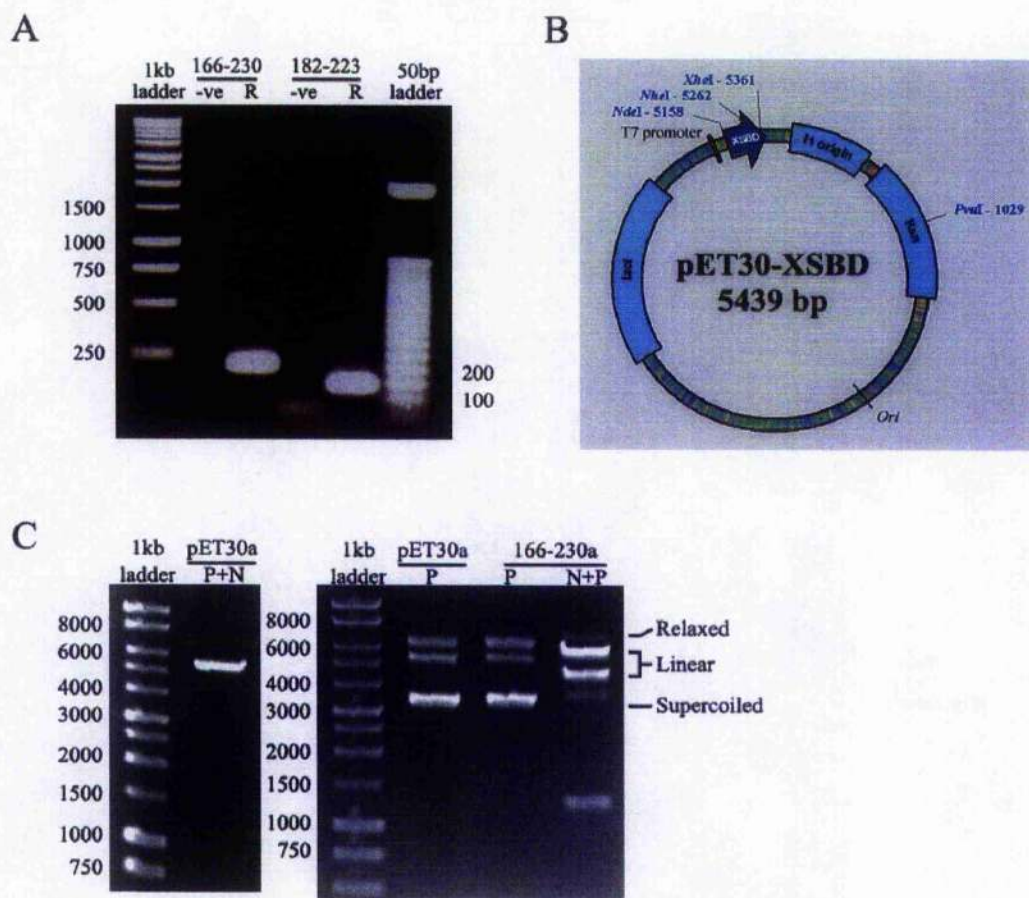


**Figure 4.2 Production of pET30-XSBD**

(A) PCR products obtained for the amplification of E3BP residues 166-230. A second, even shorter construct (aa 182-223) was also designed, but was not used in subsequent experiments. The negative controls (-ve) and PCR reactions (R) are shown. (B) A map of plasmid pET30-XSBD containing E3BP residues 166-230 is shown, including all restriction sites used. (C) Diagnostic restriction digests of pET30a and pET30-XSBD (166-230a) were performed with *PvuI* (P) or *PvuI* and *NheI* (N+P). Band sizes are indicated in bp.

### 4.3.2 Protein overexpression of XSBD

Overexpression of XSBD at 15°C failed to produce any protein at all (results not shown). However, induction at 30°C resulted in good yields (Fig. 4.3A) although the protein seems to migrate faster than expected for an 8.5 kDa protein. This may be attributed to the presence of several proline and glycine residues at the N- and C-termini of the protein that are part of the linker regions on either side of XSBD and could cause abnormal migration. All of the overexpressed protein was found in the soluble fraction (Fig. 4.3B).

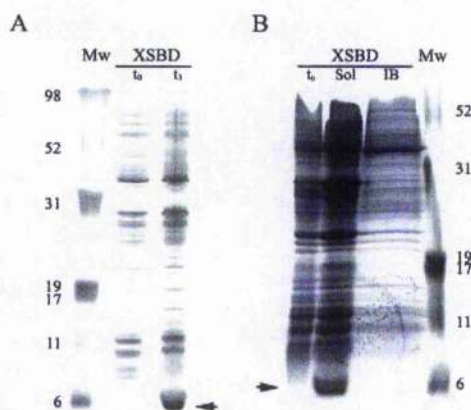


**Figure 4.3 SDS PAGE analysis of XSBD overexpression and solubility**

(A) XSBD was overexpressed at 30°C and samples were taken at the time of induction ( $t_0$ ) and after three hours ( $t_3$ ). (B) In order to determine protein solubility the cells were lysed and the soluble fraction (Sol) and inclusion bodies (IB) resolved by SDS PAGE. Bands corresponding to XSBD are indicated by arrows. Molecular weights of marker proteins (Mw) are shown in kDa.

### 4.3.3 Protein purification

#### 4.3.3.1 Purification of E3

Previous purification protocols included an initial heat step, exploiting E3's stability at 65°C. However, yields were significantly improved when the heating step was omitted. Sometimes small impurities were still visible on SDS PAGE gels following metal chelate chromatography, but these were easily removed using gel filtration (Fig. 4.4).

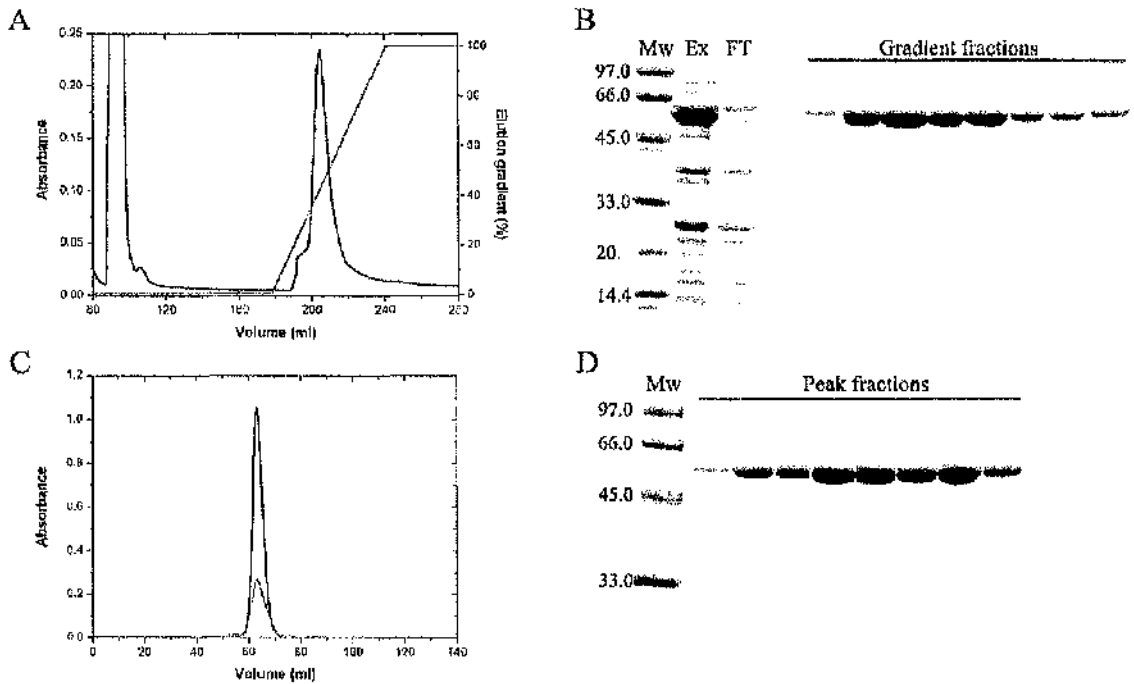


**Figure 4.4 Purification of E3**

(A+B) Metal chelate chromatography of E3. Only the last sample injection is shown in the chromatogram. The imidazole gradient used for elution is shown in cyan. Cell extract (Ex), the flow-through (FT) and fractions collected during the elution gradient were run on SDS PAGE. (C+D) Size exclusion chromatography of E3. Protein absorbance was measured at 280 nm (—) and flavin absorbance at 450 nm (---). Peak fractions were checked for protein purity by SDS PAGE. Molecular weights of marker proteins (Mw) are shown in kDa.

#### 4.3.3.2 Purification of XDD

After the initial metal chelate step XDD preparations still contained a number of contaminating proteins and a substantial amount of DNA (Fig. 4.5A,B). XDD has a low calculated isoelectric point (pI 5.7). Therefore, at the pH used during metal chelate purification (pH 7.0-8.0) the molecules were negatively charged and should not interact with DNA. However, the protein consists of the lipoyl domain – which has a very low pI (5.0) – and the subunit binding domain with a high pI of 9.7. Therefore, at pH 7-8 the SBD is still positively charged overall and can interact non-specifically with the negatively charged phosphate groups in DNA. Anion exchange chromatography was used to remove all DNA and protein contaminants. It also resolves the lipoylated and non-lipoylated forms of the

protein (Fig. 4.5C) whereby the lipoylated protein is eluted from the column first. The different lipoylation states of XDD can be visualised by SDS PAGE: the presence of the lipoic acid co-factor covalently linked to Lys97 retards the protein in the gel and results in the formation of a double band (Fig. 4.5D). Gel filtration was used as a final purification step in order to remove aggregates and minor contaminating species (Fig. 4.5E,F). Only lipoylated fractions from anion exchange were used for gel filtration and experimental purposes, although a very small amount of non-lipoylated protein sometimes remained following size exclusion chromatography.

### 4.3.3.3 Purification of XSBD

XSBD required an extensive purification protocol. Due to its high isoelectric point (pI 9.9), XSBD carries an overall positive charge in buffers used during metal chelate chromatography and significant DNA contamination was found in protein preparations (Fig. 4.6A,B). Anion exchange chromatography was used to remove the DNA. Some XSBD also bound weakly to the anion exchange column, although a significant proportion of the protein was found in the flow-through as expected (Fig. 4.6C,D). Since some contaminating proteins were still present following anion exchange, a further cation exchange step was necessary. Cation exchange chromatography removed most remaining contaminants: some proteolytic products of XSBD were found in the flow-through and contaminants were present in the first peak fraction which contained only little XSBD (Fig. 4.6D,E). Pure peak fractions were pooled and either used directly in experiments or subjected to an additional size exclusion step (Fig. 4.6F,G) in order to remove potential aggregate as well as to provide a means of buffer exchange.

### 4.3.3.4 Purification of GST-XLD

The purification of GST-tagged XLD was straightforward and required only a single affinity purification step using glutathione affinity chromatography (Fig. 4.7A). When peak fractions were run on SDS PAGE no contaminants could be seen using Coomassie blue staining (Fig. 4.7B). Purified protein was dialysed and used for subsequent experiments.

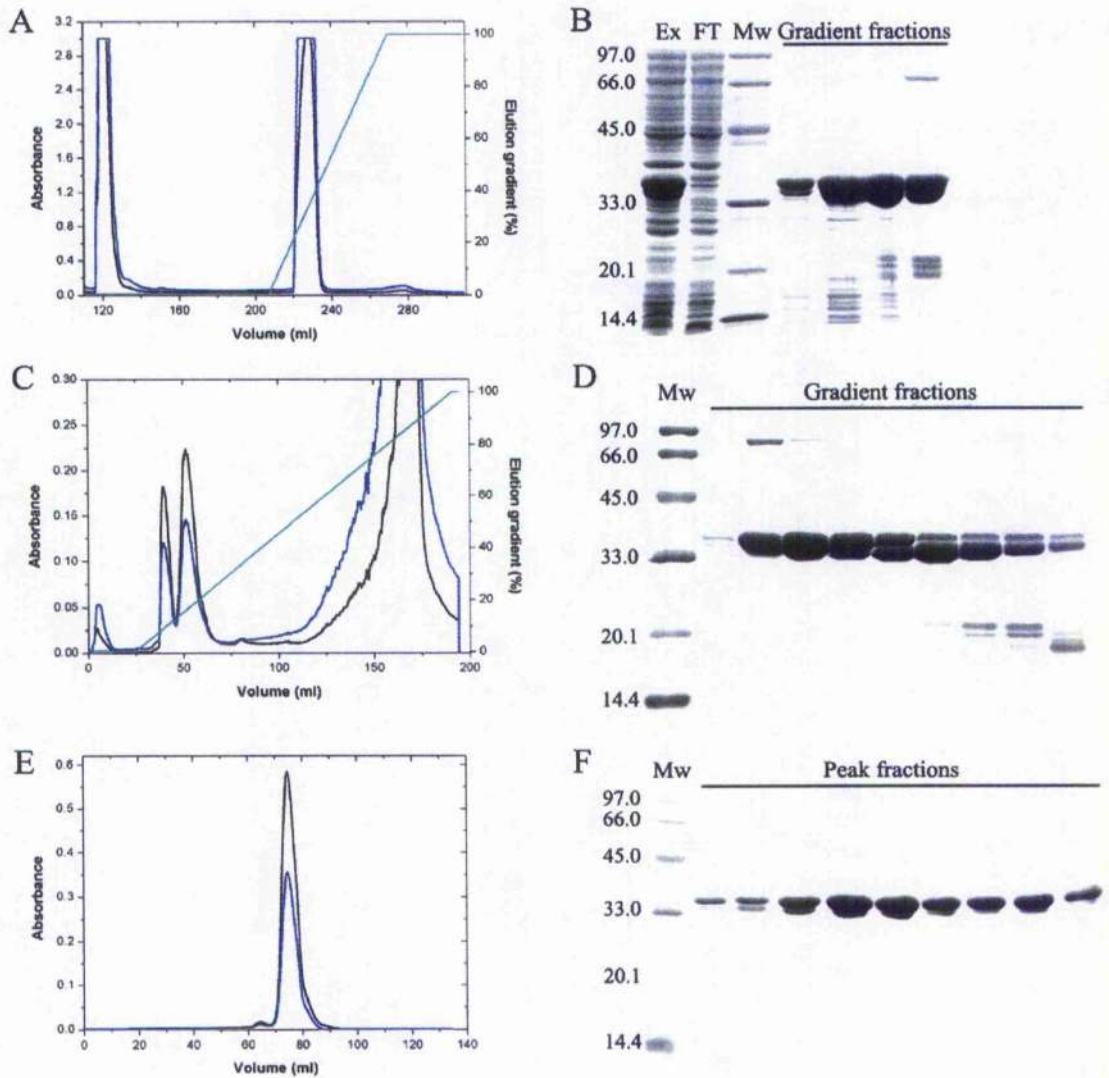


**Figure 4.5 Purification of XDD**

(A+B) Metal chelate chromatography of XDD. Only the last sample injection is shown in the chromatogram. All elution gradients are shown in cyan. Protein absorbance was measured at 280 nm (—) and 260 nm (---). Cell extract (Ex), the flow-through (FT) and fractions collected during elution were run on SDS PAGE. (C+D) HQ anion exchange chromatography of XDD. Only protein fractions ( $A_{280} > A_{260}$ ) collected during elution were run on SDS PAGE. (E+F) Gel filtration chromatography of XDD. Peak fractions were checked for protein purity and lipoylation. Molecular weights of marker proteins (Mw) are shown in kDa.

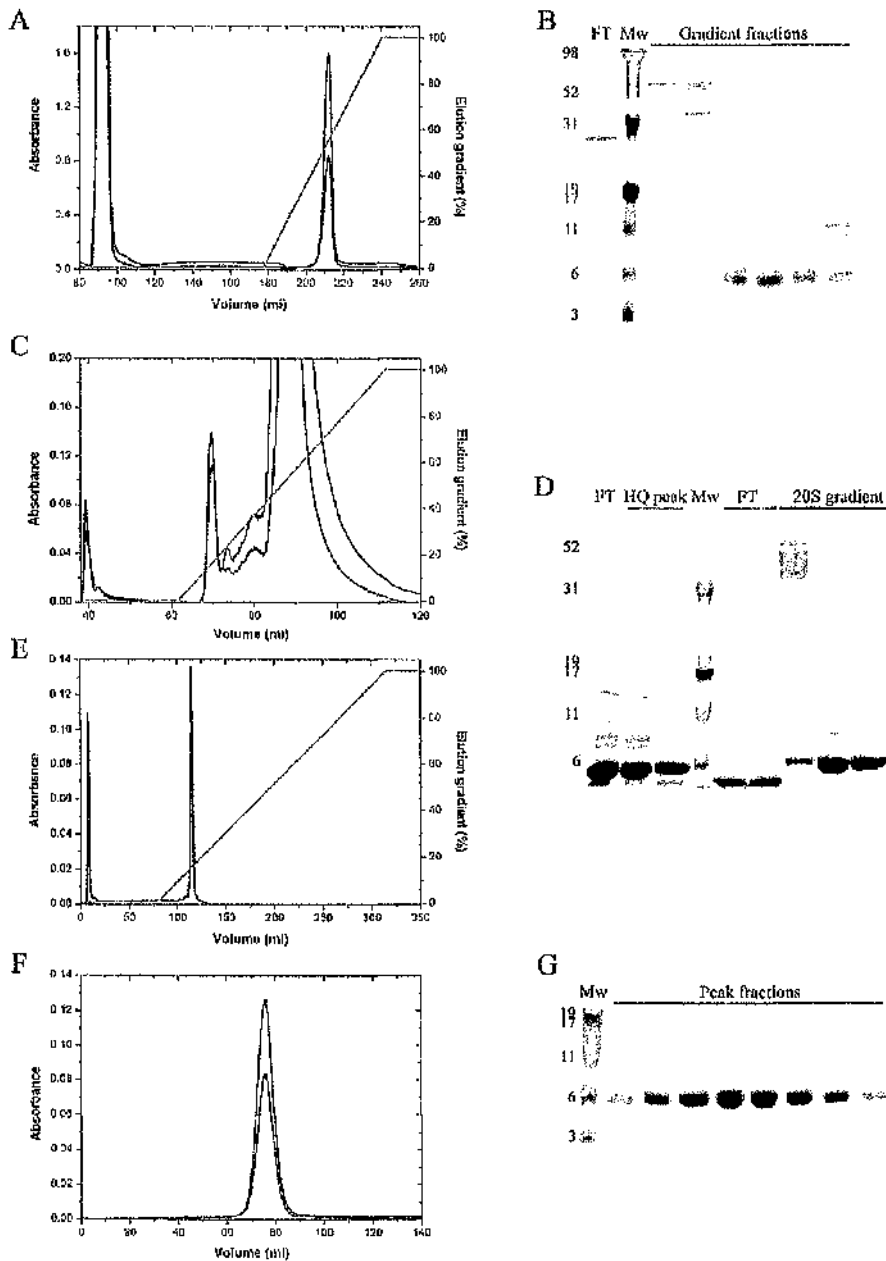


**Figure 4.6 Purification of XSBD**

(A+B) Metal chelate chromatography of XSBD. Only the last sample injection is shown in the chromatogram. All elution gradients are shown in cyan. Absorbance was measured at 280 nm (—) and 260 nm (---). The flow-through (FT) and gradient fractions were loaded on SDS PAGE. (C+D) HQ anion exchange chromatography of XSBD. The flow-through (FT) and protein peak were loaded on SDS PAGE. (D+E) S cation exchange chromatography of XSBD. FT and peak fractions were analysed by SDS PAGE. (F+G) Gel filtration of XSBD. The purity of the final XSBD preparation was assessed by SDS PAGE. Molecular weights of marker proteins (Mw) are shown in kDa.

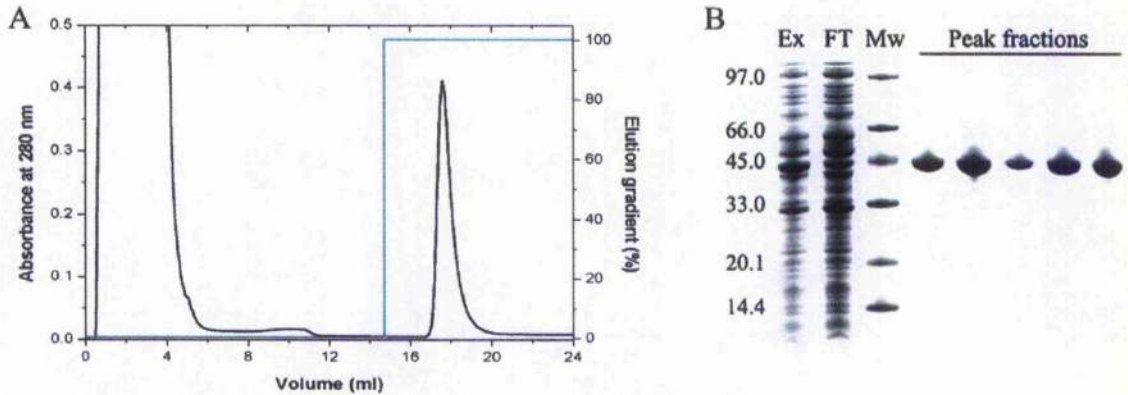


**Figure 4.7 Purification of GST-XLD by GST affinity chromatography**

(A) GST-tagged XLD was purified using glutathione affinity chromatography with a single elution step (—). (B) The cell extract (Ex), flow-through (FT) and peak fractions were analysed by SDS PAGE. Molecular weights of marker proteins (Mw) are shown in kDa.

#### 4.3.3.5 Purification of E2DD

Purification of E2DD was very similar to XDD purification. E2DD also has a rather low calculated isoelectric point (pI 6.1), and similarly consists of a negatively charged LD (pI 4.5) and a positively charged SBD (pI 9.6) at pH 7.0-8.0. Therefore, following initial metal chelate affinity purification (Fig. 4.8A) an anion exchange chromatography step (Fig. 4.8B) was required to remove non-specifically bound DNA. Furthermore, E2DD also runs on SDS PAGE as a double band due to the presence/absence of liponic acid (Fig. 4.8C). As before, only fractions containing lipoylated protein were further purified by gel filtration (Fig. 4.8D,E) in order to remove aggregated protein. In addition, proteolysis did pose some problems despite the presence of protease inhibitors throughout the entire purification. However, the amount of proteolytic products did not exceed 5-10% of the total protein purified, as judged by SDS PAGE (Fig. 4.8E).

#### 4.3.3.6 Purification of E1

E1 was obtained from previously purified bovine PDC (see Section 3.3.2.7) by sucrose gradient centrifugation. The E2 core pelleted at the bottom of the ultracentrifugation tube and retained a significant amount of peripherally bound E1 and E3 (Fig. 4.9A). However, the majority of E1 and E3 was found unassociated in the gradient fractions. All fractions lacking

E2 core were pooled and used for HQ anion exchange chromatography in order to separate E1 from E3. E3 was only slightly retarded on the anion exchange column at pH 7.4 (Fig. 4.9B), presumably due to the proximity of its isoelectric point of 6.5, assuming that bovine and human E3 have similar pIs. The amino acid sequence of bovine E3 (and E1) is not available, but the proteins are thought to be very closely related to the human enzymes. Some unassociated E1 $\alpha$  subunits also eluted in the flow-through. E1 eluted in the first third of the salt gradient as a double peak, and SDS PAGE confirmed the high purity of the E1 preparation (Fig. 4.9C). No difference between E1 from either peak was visible on the SDS PAGE gel, but may represent non-phosphorylated and phosphorylated protein, respectively. E1 containing fractions were pooled and used for gel filtration chromatography in order to remove small amounts of aggregate (Fig. 4.9D,E).

### **4.3.3.7 Purification of bovine E2/E3BP**

Pure bovine E2/E3BP core was obtained by homogenisation of PDC core pellets obtained from sucrose density gradient ultracentrifugation (see Section 3.3.2.8), followed by a second round of ultracentrifugation. The resultant E2/E3BP pellets were homogenised again and run on SDS PAGE to assess the purity of the PDC preparation (Fig. 4.10).

### **4.3.3.8 Purification of human E2/E3BP**

Purification of E2/E3BP was very similar to XDD and E2DD purifications, as protein purified by metal chelate chromatography (Fig. 4.11A,B) still contained significant amounts of contaminating protein and DNA. Peak fractions were pooled and subjected to anion exchange chromatography in order to remove all contaminants (Fig. 4.11C,D). Gel filtration chromatography was used as a final purification step in order to separate excess E3BP not associated with core particles (Fig. 4.11E,F). SDS PAGE shows that despite supplementation of *E. coli* cultures with lipoic acid, both lipoylated and non-lipoylated protein is present in the final preparation.

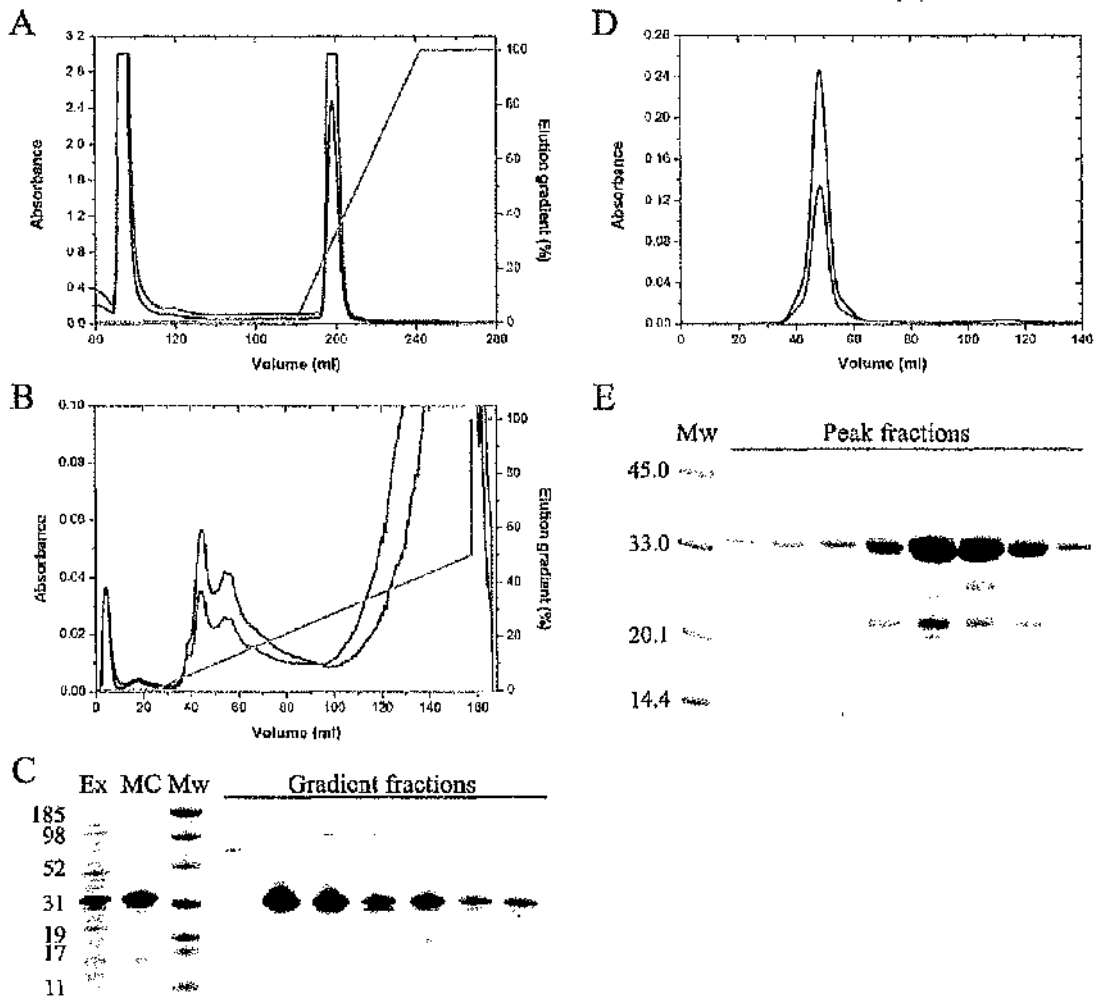


**Figure 4.8 Purification of E2DD**

(A) Metal chelate chromatography of E2DD. Absorbance readings were recorded at 280 nm (—) and 260 nm (---). All elution gradients are shown in cyan. (B) Anion exchange chromatography of E2DD. (C) SDS PAGE analysis of metal chelate and anion exchange chromatography. Cell extract (Ex), pooled metal chelate fractions (MC) and fractions collected during elution from the anion exchange column are shown. (D+E) Size exclusion chromatography of E2DD. Molecular weights of marker proteins (Mw) are shown in kDa.

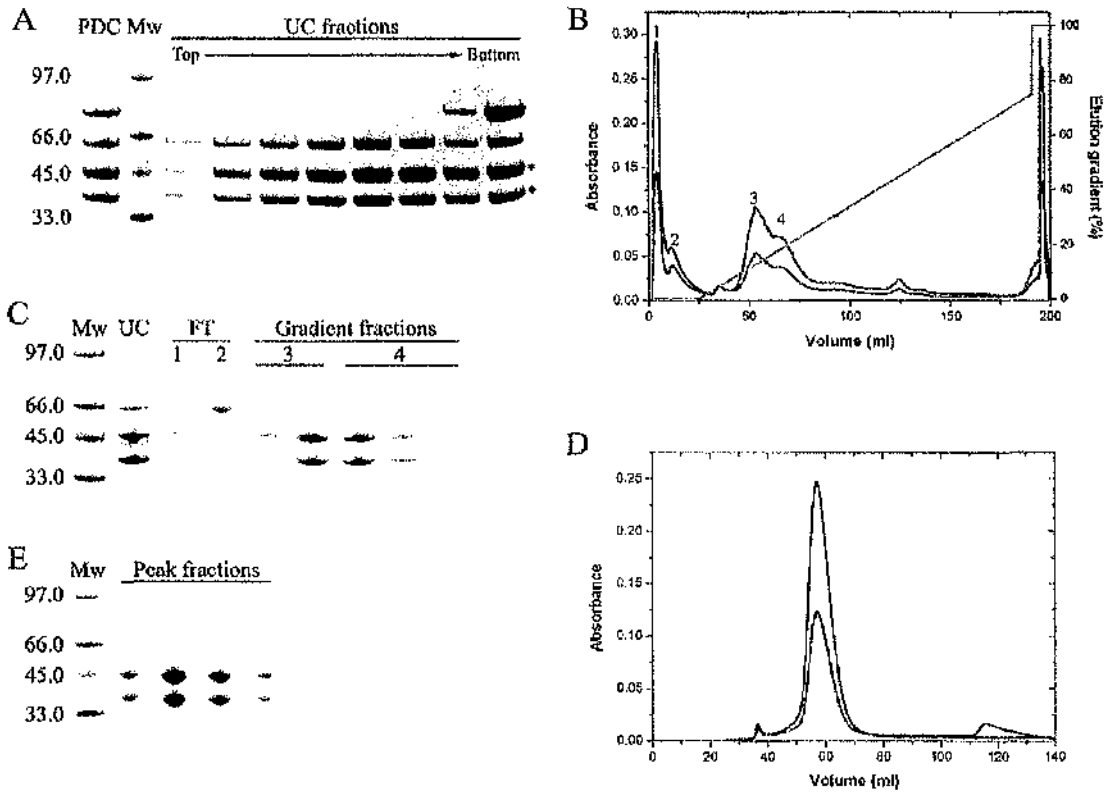


**Figure 4.9 Purification of bovine E1**

(A) SDS PAGE of PDC sucrose gradient ultracentrifugation (UC). E1 $\alpha$  (\*) and E1 $\beta$  (†) subunits are indicated. (B+C) UC fractions containing bovine E1 and E3 only were used for HQ anion exchange chromatography. Absorbance readings were recorded at 280 nm (—) and 260 nm (---). The elution gradient is shown in cyan. Separate peaks in the flow-through (FT) and during elution are indicated and correspond to fractions loaded onto SDS PAGE. (D+E) Fractions from anion exchange peaks 3 and 4 were used for gel filtration chromatography of E1. Only fractions corresponding to the main GFC peak were analysed by SDS PAGE in (E). Molecular weights of marker proteins (Mw) are shown in kDa.

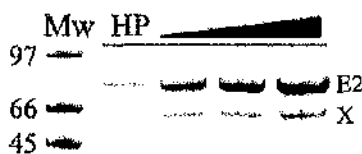


**Figure 4.10 Purification of bovine E2/E3BP core**  
 SDS PAGE of homogenised bovine E2/E3BP pellets (HP) obtained from two rounds of sucrose gradient ultracentrifugation (UC). The positions of E2 and E3BP (X) are indicated. Molecular weights of marker proteins (Mw) are shown in kDa.

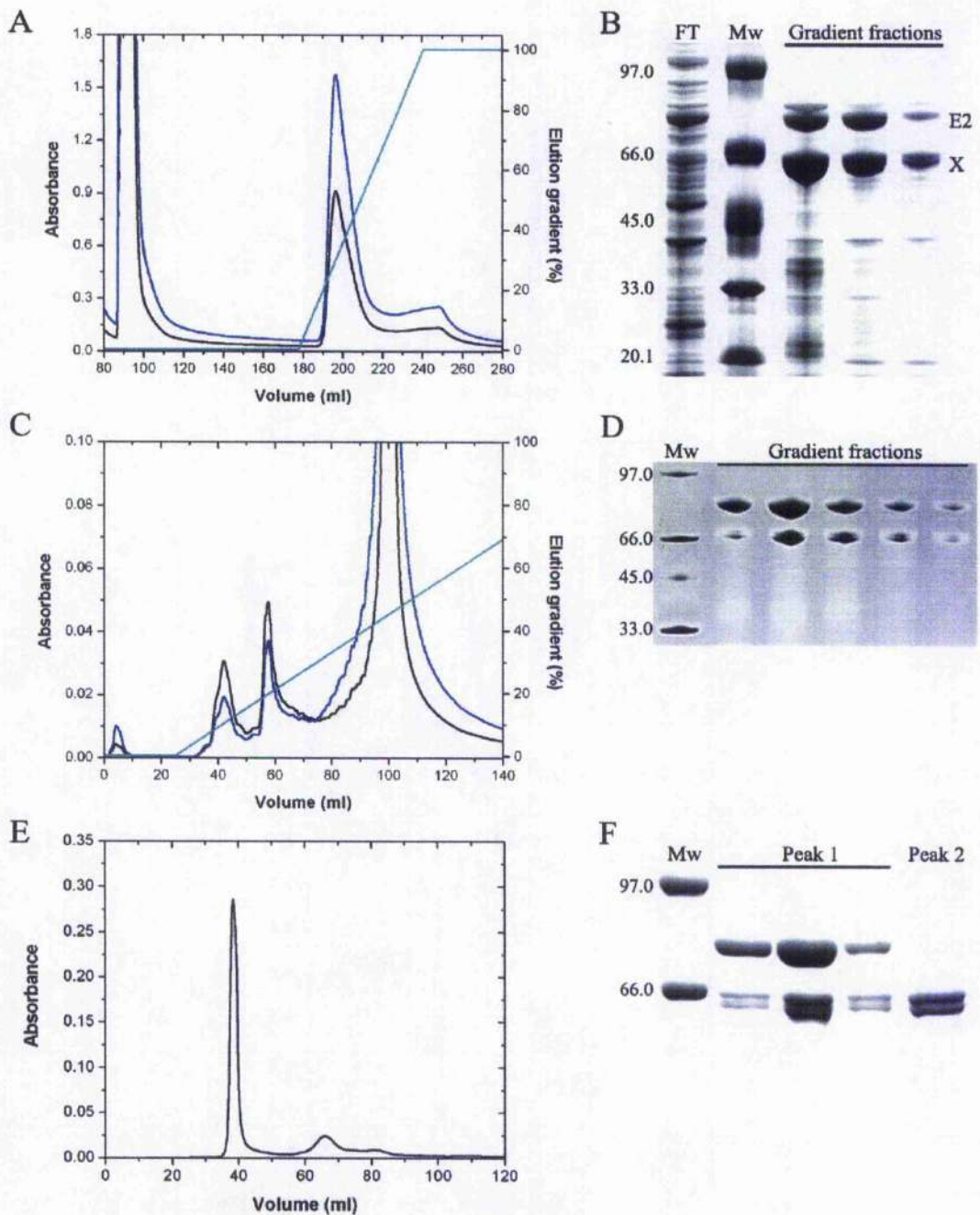


**Figure 4.11 Purification of human E2/E3BP core**

(A+B) Metal chelate chromatography of E2/E3BP. Only the last sample injection is shown in the chromatogram. All elution gradients are shown in cyan. Absorbance was measured at 280 nm (—) and 260 nm (---). The flow-through (FT) and gradient fractions were loaded on SDS PAGE. The positions of E2 and E3BP (X) are indicated. (C+D) Anion exchange chromatography of E2/E3BP. Gradient fractions were analysed by SDS PAGE. (E+F) Gel filtration of E2/E3BP. The purity of the final E2/E3BP preparation was assessed by SDS PAGE. Molecular weights of marker proteins (Mw) are shown in kDa.

#### 4.3.3.9 Yields

Typical yields obtained for all purified proteins used in this project are summarised in Table 4.4.

Protein	Plasmid	Yield
E3	pET14-E3	30-40 mg/l
XDD	pET14-XDD	20-25 mg/l
GST-XLD	pGEX2-XLD	15-20 mg/l
XSBD	pET30-XSBD	5-8 mg/l
E2DD	pET14-E2DD	15-20 mg/l
E1	N/A	25-35 mg/kg bovine heart
Human E2/E3BP	pET11-E2 pET28-X	3-5 mg/l
Bovine E2/E3BP	N/A	100-150 mg/kg bovine heart

**Table 4.4** Summary of protein purification yields

# Chapter 5

## Characterisation of the human E3BP/E3 subcomplex and its constituents

### 5.1 Introduction

In mammals PDC consists of a central icosahedral core assembly comprising 60 E2 polypeptides and 12 copies of the E2-related polypeptide termed E3 binding protein (E3BP) (Sanderson et al., 1996b). Basic trimeric units of E2 form the 20 vertices of the icosahedron with E3BP thought to be bound in each of the 12 faces (Stoops et al., 1997; Zhou et al., 2001b). Both E2 and E3BP have a similar, modular domain structure: human E2 and E3BP contain two (E2) or one (E3BP) N-terminal lipoyl domain(s) of approximately 80 amino acids. Each LD carries a lipoic acid moiety covalently linked to a lysine residue located within a conserved DKA motif situated at the tip of a type I  $\beta$ -turn (Howard et al., 1998). The LD is followed by a subunit binding domain of about 35 residues and a C-terminal domain (CTD) of about 250 residues that is essential for core formation (Izard et al., 1999). In E2 the CTD is also the catalytic domain, while the active site motif is not present in E3BP, thus rendering it incapable of catalysing the acetyltransferase reaction (Behal et al., 1989; Harris et al., 1997). All domains are interconnected by long linker regions rich in alanine, proline and charged amino acids of approximately 30 residues (Borges et al., 1990; Perham, 2000), that

impart the necessary flexibility to the LDs to visit all three active sites during catalysis (Green et al., 1992). In eukaryotes the E2/E3BP core of PDC provides the structural and mechanistic framework for the tight but non-covalent association of the heterotetrameric E1 and homodimeric E3 enzymes. The stability and overall subunit organisation of the complex are governed by specific and tight protein-protein interactions between E2-SBD and E1, and E3BP-SBD and E3, respectively. However, other organisms with icosahedral cores such as the Gram positive bacterium *B. stearothermophilus* do not have the gene for E3BP. Consequently, E1 and E3 have to compete for overlapping binding sites on E2; interaction of E2 with either E1 or E3 prevents complex formation with the other. Interestingly, PDC-deficient patients who totally lack the E3BP subunit possess partial complex activity (10-20% of controls) (Ling et al., 1998), apparently because the SBD of E2 has retained a limited ability to mediate low affinity E3 binding.

In *B. stearothermophilus* PDC, E1 and E3 both bind to the SBD of E2 with 1:1 stoichiometries (Hippis et al., 1994; Lessard et al., 1998; Jung et al., 2002a; 2003). The crystal structures determined for the E3/E2-SBD as well as the E1/E2-SBD subcomplexes from *B. stearothermophilus* show unequivocally that association of a second molecule of E2-SBD to either E1 or E3 is not possible. In the case of E1 the binding site for E2-SBD is located across the two-fold axis (Frank et al., 2005) whereas the binding site on E3 is close to the two-fold axis of symmetry (Mande et al., 1996). Occupation of both binding sites on E3 would result in steric clashes in one of the loop regions. A similar arrangement in the crystal structure of human E3 bound to E3BP-SBD has been reported very recently (Ciszak et al., 2006). While the 1:1 stoichiometry of bacterial PDC E2-SBD/E1 and E2-SBD/E3 has been confirmed in solution, similar studies on eukaryotic PDC have not been conducted until now. Intriguingly, the reported stoichiometries for each of the constituent enzymes of mammalian PDC suggest the possibility of formation of 2:1 stoichiometric subcomplexes in this case. Thus, at maximal occupancy, 30 E1 enzymes can associate with the 60-meric E2 core while 12 E3BP molecules associate with 6 E3 dimers (Sanderson et al., 1996b).

This chapter describes the characterisation of the individual proteins and protein constructs involved in the interaction of E3BP with E3 as well as the complex itself. Full-length E3 as well as two protein constructs of E3BP (Fig. 5.1) consisting of the lipoyl and/or subunit

binding domains, termed XDD and XSBD, respectively, were characterised individually *in vitro*. In addition, the stoichiometry and affinity of the interaction of E3 with XDD and XSBD were investigated using a range of biochemical and biophysical approaches including native polyacrylamide gel electrophoresis (PAGE), analytical ultracentrifugation (AUC) and isothermal titration calorimetry (ITC). Low resolution structures of E3, XSBD as well as of the complex formed between XDD and E3 were obtained by small angle x-ray scattering (SAXS).

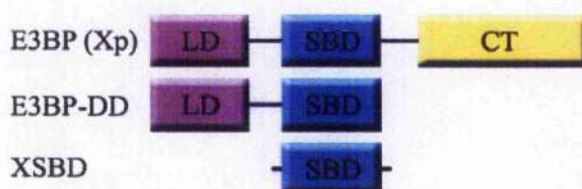


**Figure 5.1 E3BP constructs used in this project**

Full-length E3BP – also termed protein X – consists of three domains: an N-terminal lipoyl domain (LD), a subunit binding domain (SBD) responsible for interaction with E3 and a C-terminal domain (CT) that associates with E2 to form the icosahedral core of PDC. Two constructs were derived from E3BP: a di-domain construct (XDD) consisting of the LD and SBD, as well as XSBD formed solely by the subunit binding domain.

## 5.2 Materials and methods

### 5.2.1 Sample preparation

Individual proteins were purified as outlined in Section 4.2.3. XDD/E3 complex was reconstituted from the purified proteins at a stoichiometric ratio of 3:1 (XDD:E3) using a final size exclusion step on a Sephacryl S-300 column (Amersham, USA) in TEB buffer (see 4.2.3) to remove unbound XDD.

### 5.2.2 Gel filtration analysis

Gel filtration chromatography (GFC) was employed to obtain estimates of the relative molecular weights of E3, XDD and purified XDD/E3 complex. A Sephacryl S-300 column

(Amersham, USA) was standardised with a range of GFC protein markers (Sigma, USA). Blue dextran was used to determine the column's void volume,  $V_0$ . The logarithms of protein molecular weights were plotted versus the ratio of elution volume to void volume ( $V_e/V_0$ ) to produce a standard curve.

### 5.2.3 Non-denaturing PAGE

Stoichiometric mixtures of XSBD:E3 from 4:1 to 1:3, as well as XDD:E3 from 10:1 to 1:3 were prepared, keeping the amount of E3 used constant at 500 pmol. The samples were incubated at 25°C for 15 minutes in 25 mM Tris-HCl, pH 7.0. Protein samples (5-15  $\mu$ g) were loaded onto Tris-glycine gels (5% stacking, 8% resolving gel) and subjected to non-denaturing PAGE. More details can be found in Section 3.3.5.2. Non-denaturing PAGE analysis of the XDD:E3 mixtures was performed by Dr. Alison Prior, University of Glasgow.

### 5.2.4 Sedimentation velocity analytical ultracentrifugation

Sedimentation velocity (SV) experiments were performed as described in Section 3.4.2. Purified E3 was dialysed against TEBS100 and sedimentation data recorded at 4°C at a rotor speed of 45000 rpm, using both interference and absorbance optics in separate experiments. A series of 30 scans, 10 minutes apart with a step size of 0.002 cm in continuous mode and three averages was recorded for each sample using absorbance optics. A total of 300 scans, 2 minutes apart, was recorded using interference optics. Sample concentrations ranged from 1.7  $\mu$ M to 17  $\mu$ M. The samples (380  $\mu$ l) were loaded into 12 mm double sector centrepieces.

Purified XDD was dialysed against 50 mM Tris-HCl, 2 mM EDTA, pH 8.5 and sedimentation data recorded at 4°C at a rotor speed of 45000 rpm, using both interference and absorbance optics. A series of 150 scans, 5 minutes apart, was recorded for each sample, using a step size of 0.003 cm in continuous mode and three averages. Sample concentrations ranged from 7  $\mu$ M to 44  $\mu$ M. The samples (380  $\mu$ l) were loaded into 12 mm double sector centrepieces.

Purified XSBD in 50 mM potassium phosphate, pH 7.1 was used for SV experiments conducted at 45000 rpm and 4°C and sedimentation data recorded using both absorbance and interference optics. A series of 200 scans, 15 minutes apart with a step size of 0.003 cm in continuous mode and five averages were recorded for each sample. Sample concentrations ranged from 8 µM to 50 µM. The samples (380 µl) were loaded into 12 mm double sector centrepieces.

For the analysis of stoichiometric XDD:E3 mixtures, samples were prepared by keeping the concentration of E3 fixed at 4.9 µM and varying the XDD concentrations accordingly to achieve XDD:E3 ratios of 4:1 to 1:3. Samples were dialysed extensively against TEB prior to data acquisition. The samples (380 µl) were loaded into 12 mm double sector centrepieces. A rotor speed of 45000 rpm was selected and interference optics scans were collected at 4°C every minute until sedimentation was complete. SV analysis of the purified XDD/E3 complex was conducted as described above for the XDD:E3 stoichiometric mixtures and covered a concentration range of 6-44 µM. Sedimentation profiles were analysed with the computer program SEDFIT (Schuck, 2000) (see Sections 2.2.1.1 and 3.4.2 for details). Finite element analysis in SEDFIT was also used to determine the true sedimentation coefficients of all samples. These were extrapolated to infinite dilution to give a sedimentation coefficient independent of concentration,  $s_{20,w}^0$ .

### 5.2.5 Sedimentation equilibrium analytical ultra-centrifugation

Sedimentation equilibrium (SE) data were collected for E3, XDD, XSBD, XDD:E3 stoichiometric mixtures as well as the purified XDD/E3 complex using interference optics. All samples used for the collection of SE data had been subjected to SV analysis first and the same buffer conditions were used. Details of the experimental set-up can be found in Table 5.1 and Section 3.4.3. Attainment of all equilibrium experiments was ascertained with WinMATCH ([www.biotech.uconn.edu/au/](http://www.biotech.uconn.edu/au/)) when no net movement of protein was observed in scans recorded three hours apart. SE data were analysed using single experiment and global analysis in the Beckman XL-A/XL-I software implemented in MicroCal ORIGIN.

Alternatively, multi-speed analysis fitting each sample concentration singly as well as globally in SEDPHAT (Vistica et al., 2004) as described in Sections 2.2.2.1 and 3.4.3 was also used. In order to determine the weight-average molecular weight of samples independent of concentration,  $M_w^0$ , the apparent weight-average molecular weights,  $M_{w,app}$  determined for each sample concentration were extrapolated to infinite dilution.

SE analysis of purified XDD/E3 complex was carried out and the data analysed as described above, but included fitting of the second virial coefficient,  $B$ . A starting estimate for  $B$  of XDD/E3 was calculated using the program COVOL (Harding et al., 1999) based on molecule dimensions and charge. The values of  $M_w^0$  and  $B$  at infinite dilution,  $B^0$  were determined by plotting  $1/M_{w,app}$  against concentration (in g/ml), where  $M_w^0$  is the inverse of the y intercept and  $B^0$  can be calculated from the slope.

Protein	Speed (rpm)	Centrepiece	Path length (mm)	Volume ( $\mu$ l)	Replicates	Step size (cm)
E3	12000	Double sector or	12	120	20	0.001
	17000					
	21000	Six channel	12	80		
XDD	25000	Double sector or	3	30	15	0.001
	29000					
	35000	Six channel	12	80		
XSBD	25000	Double sector	12	120	15	0.001
	35000					
	45000					
XDD:E3 stoichiometric mixtures	8500	Double sector	3	30	20	0.001
	12000					
	16000					
XDD/E3	10500	Double sector	3	30	20	0.001
	15000					
	18000					

**Table 5.1** Summary of parameters used for sedimentation equilibrium experiments

### 5.2.6 Isothermal titration calorimetry

XDD and E3 were dialysed overnight in 25 mM Tris-HCl, pH 7.0. E3 at a concentration of 40.7  $\mu$ M was injected in 10  $\mu$ l aliquots into the reaction cell containing 6.2  $\mu$ M XDD at 25°C. Purified GST-XLD was exposed to 50 mM DTT for several hours before dialysing both GST-

XLD and E3 overnight in 50 mM Tris-HCl, 2 mM EDTA, pH 7.5. GST-XLD at a concentration of 43.6  $\mu$ M was injected in 10  $\mu$ l aliquots into the reaction cell containing 4.1  $\mu$ M E3. This experiment was done at 10°C and 25°C. Data were analysed using non-linear regression in the MicroCal ORIGIN software package, assuming a simple binding model (see Section 3.4.4). All ITC experiments were performed by Mrs. Margaret Nutley in the laboratory of Prof. Alan Cooper, University of Glasgow. The XDD/E3 ITC experiment was prepared by Dr. Alison Prior, University of Glasgow.

### 5.2.7 Small angle x-ray scattering and *ab initio* modelling

SAXS data for E3, XDD and XDD/E3 were collected on beamline X33 of the EMBL Outstation Hamburg at the storage ring DORIS III of the Deutsches Elektronen Synchrotron (DESY) using a camera length of 2.6 m. Protein concentrations of 1.8, 5.6, 10.8 and 17.5 mg/ml were used for E3 data collection. XDD scattering curves were obtained for concentrations of 0.4, 4.8 and 11.1 mg/ml, while XDD/E3 data were recorded for concentrations of 1.5, 6.3, 9.6 and 22.6 mg/ml. Scattering data for XSBD were obtained on beamline 2.1 at the SRS Daresbury, UK using a concentration of 7 mg/ml at a single camera length of 1 m. More details can be found in section 3.4.5.

The programs GASBOR (Svergun et al., 2001; Petoukhov & Svergun, 2003) and DAMMIN (Svergun, 1999) were used for *ab initio* reconstruction of E3, XSBD as well as the XDD/E3 subcomplex. Since E3 is known to be a homodimer with a two-fold symmetry axis, P2 symmetry enabled in GASBOR and DAMMIN was used for reconstructions, while no symmetry was imposed during the modelling process of XSBD and the XDD/E3 complex. More details on *ab initio* modelling can be found in Sections 2.4.2.3 and 3.5.4.

### 5.2.8 Homology, hydrodynamic and rigid body modelling

Homology models of individual proteins and domains were obtained as described in Section 3.5.2 and superimposed onto *ab initio* models obtained from small angle x-ray scattering where appropriate using the program SITUS (Wriggers & Birmanns, 2001; Wriggers & Chacón, 2001). In order to obtain a homology model of the human XDD/E3 complex the crystal structure obtained for the E2-SBD/E3 complex (Mande et al., 1996) (PDB ID 1EBD) was used as a template. Models of XDD/E3 with lipoyl domains in different positions were generated (see Section 5.3.3.6) and their sedimentation coefficients,  $s$  calculated using the program HYDROPRO (García de la Torre et al., 2000; García de la Torre, 2001). For the purpose of rigid body modelling with the program Rayuela (Nöllmann et al., 2005), the complex was defined by five "domains": E3, XSBD1, XSBD2, XLD1 and XLD2. Rayuela was used to determine the lowest energy conformation for all five domains as judged by comparison to the corresponding experimental data. The best model obtained with Rayuela was used for superimposition onto the *ab initio* model using the program SITUS (Wriggers & Birmanns, 2001; Wriggers & Chacón, 2001).

### 5.2.9 Determination of the XDD redox state

XDD (30  $\mu\text{g}$ ) was pre-incubated with and without 3 mM DTT (reactions 4, 5)\* for 30 minutes at room temperature. Control reactions were set up for XDD with 25  $\mu\text{g}$  E3 (reaction 3), 25  $\mu\text{g}$  E3 and 10 mM  $\text{NAD}^+$  (reaction 1) or 10 mM NADH (reaction 2). E3BP-LD (XLD) was used as a further control: XLD (20  $\mu\text{g}$ ) was incubated with 25  $\mu\text{g}$  E3 and 10 mM  $\text{NAD}^+$  or 10 mM NADH (reactions 6,7). Monomethoxypolyethylene glycol (mPEG) 5000 maleimide was added to a final concentration of 1 mM and reactions were incubated at 25°C for 30 minutes. Reactions were stopped by the addition of excess DTT and proteins were resolved by SDS PAGE. Further information can be found in Section 3.3.7.

\* Reactions were numbered as they appear on SDS PAGE (Section 5.3.3.8).

## 5.3 Results and analysis

### 5.3.1 Characterisation of E3

#### 5.3.1.1 Homology modelling

Residues 18–496 of human E3 were successfully modelled using SWISS-MODEL (Guex & Peitsch, 1997; Schwede et al., 2003; Kopp & Schwede, 2004) based on the three-dimensional structure available for the *S. cerevisiae* enzyme (Toyoda et al., 1998b). The two sequences are very closely related, displaying 58% sequence identity and 75% sequence similarity overall (Fig. 5.2A). The interface domain is the most highly conserved domain of E3 with 75% identity and 86% sequence similarity, while the FAD, the NAD and the central domains are slightly less well conserved with 53%, 50% and 48% sequence identity, respectively. A superimposition of the human model with the yeast template shows only relatively small differences in backbone positions (Fig. 5.2B).

Very recently, the crystal structures of human E3 complexed both with NAD and NADH (PDB ID 1ZMC, 1ZMD) have been published (Brautigam et al., 2005). However, superimposition of these coordinates with those for the homology model gave a very low rms deviation of 0.6 Å: the two structures are almost identical, differing primarily in the NAD domain.

#### 5.3.1.2 Analytical ultracentrifugation and hydrodynamic modelling

E3 is an obligate homodimer which requires its FAD cofactor for correct folding (Lindsay et al., 2000) and enzymatic function (Klyachko et al., 2005). Sedimentation velocity data (Fig. 5.3) confirmed the presence of a single main species present in E3 samples, corresponding to the E3 homodimer (Fig. 5.3A). A very small amount of a second, larger species with an apparent sedimentation coefficient of approximately 8 S can be seen at the highest concentration only. The second peak may correspond to a very low concentration of E3 tetramer or contaminant species. E3 tetramer formation only occurs at high concentrations and has been observed before (Klyachko et al., 2005).

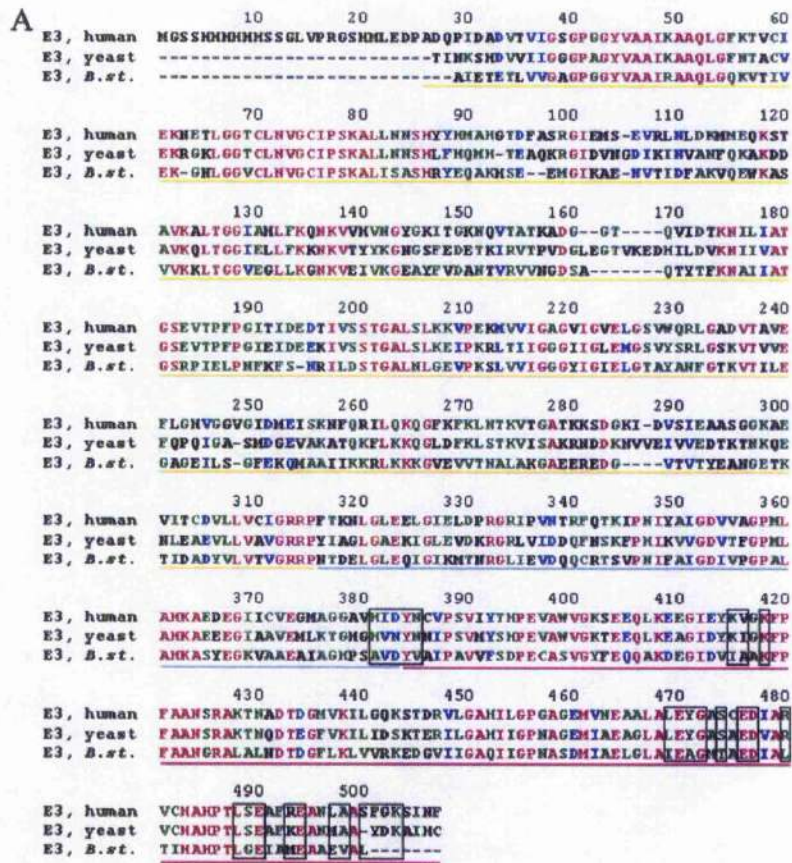


**Figure 5.2** Sequence alignment and homology modelling of human E3

(A) The amino acid sequences of human, yeast and *B. stearothermophilus* E3 were aligned. The FAD (—), NADH (—), central (—), and interface (—) domains are indicated. Residues known or thought to be involved in binding of the subunit binding domain of E3BP are boxed. Residues identical in all three sequences are shown in purple, amino acids identical in two of three sequences are shown in green, and residues whose charge has been conserved are depicted in blue. (B) Front view of superimposed yeast and human E3. Yeast E3 is coloured according to secondary structure in purple (helix), yellow (sheet), and cyan (turns), while the human homology model is shown in grey.

Finite element analysis with a single-species model yields the true sedimentation coefficients for E3 at all experimental concentrations. These were then extrapolated to infinite dilution to give a sedimentation coefficient for E3 independent of concentration of  $s_{20,w}^0 = 5.83 \pm 0.02$  S and  $5.81 \pm 0.03$  S determined from absorbance and interference data, respectively (Fig. 5.3B). The sedimentation coefficient is lower than that of a hydrated sphere of the same mass and partial specific volume as E3 ( $s = 6.7$  S), indicating an increase in its hydrodynamic radius and thus elongation in shape.

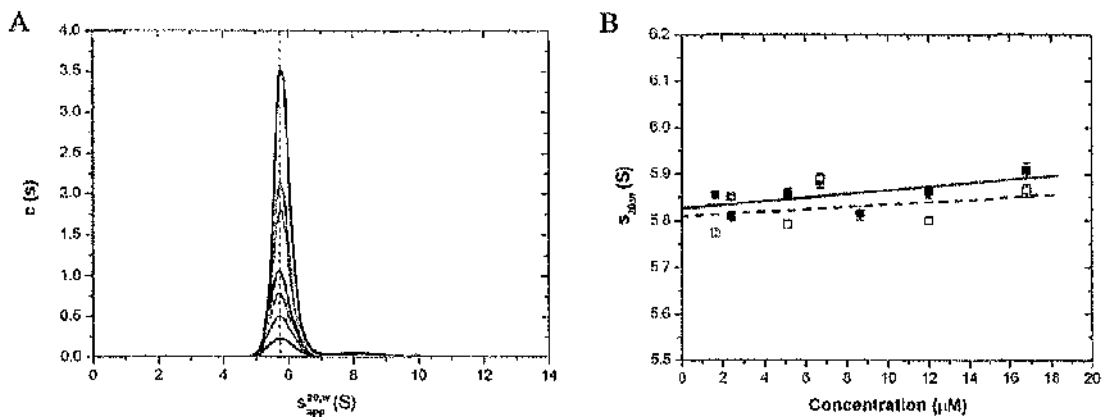


**Figure 5.3 Sedimentation velocity analysis of E3**

(A)  $c(s)$  distribution from SV absorbance data collected for a range of E3 concentrations ( $\sim 1.7 \mu$ M,  $\sim 2.4 \mu$ M,  $\sim 5.1 \mu$ M,  $\sim 6.7 \mu$ M,  $\sim 8.7 \mu$ M,  $\sim 12 \mu$ M,  $\sim 17 \mu$ M). (B) Determination of concentration independent  $s_{20,w}^0$  for E3 data recorded using absorbance ( $\blacksquare$ ) and interference optics ( $\square$ , dashed line).

The high resolution structures determined for E3 from other organisms, such as yeast and *B. stearothersophilus* all show butterfly-shaped molecules. Hence, this increase in the hydrodynamic radius of E3 was expected. HYDROPRO was used to obtain a calculated sedimentation coefficient of 5.7 S for the homology model of the human E3 dimer. The result agrees very well with the experimentally determined value of  $s$  of 5.8 S. The slight difference in the calculated and experimental values of  $s$  are presumably due to slight differences in the structure of human E3 when compared to the model.

The dimeric nature of E3 was also confirmed by sedimentation equilibrium experiments where the molecular weight of E3 was determined to be  $101 \pm 3$  kDa, in good agreement with

the value predicted from the E3 amino acid sequence of 106 kDa (Fig. 5.4). Analysis of the individual SE data sets using a single species model in SEDPHAT shows an increase in the apparent molecular weight,  $M_{w,app}$  with increasing E3 concentration, indicative of the presence of a second, higher molecular weight species, in agreement with observations from SV.

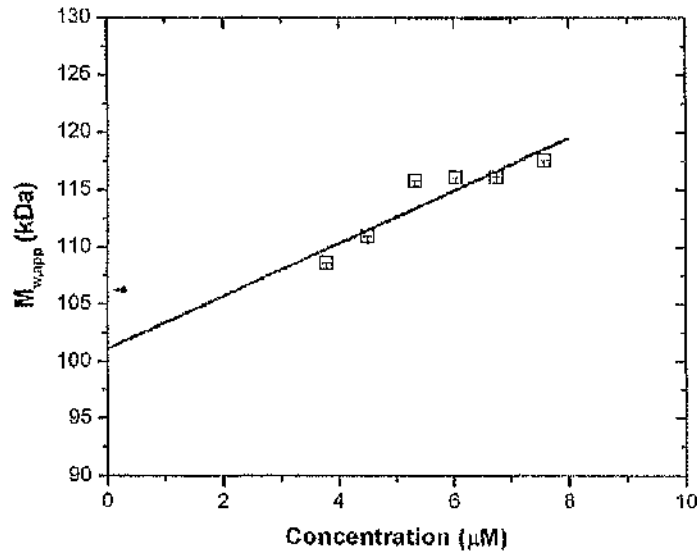


**Figure 5.4** Sedimentation equilibrium analysis of E3

$M_{w,app}$  was determined for each sample and extrapolated to zero concentration. Data from the same cell but recorded at different speeds were analysed simultaneously using the multi-speed equilibrium routine in SEDPHAT with a single species model. The calculated molecular weight of dimeric E3 is indicated by an arrow.

Using global analysis and fitting of a second component, the  $M_{w,app}$  of the main species was  $102 \pm 4$  kDa while the  $M_{w,app}$  of the second species was determined to be  $182 \pm 4$  kDa which is somewhat lower than the calculated molecular weight of the E3 tetramer of 212 kDa. The data could not be fitted satisfactorily with a self-association model, possibly due to the small amount of tetramer present. Alternatively, the second species may represent a contaminant protein not visible in SDS PAGE gels. Presence of a contaminant protein seems more likely as E3 was purified using gel filtration chromatography prior to AUC experiments which should separate the E3 dimer and tetramer species. Furthermore, the use of gel filtration is supposed to prevent more tetramer formation (Klyachko et al., 2005). A higher molecular weight contaminant would be expected to co-elute with E3 assuming it is more globular in shape than E3 itself.

### 5.3.1.3 Small angle x-ray scattering and *ab initio* modelling

The scattering curve obtained for E3 (Fig. 5.5A) also confirms its status as a homodimer using a molecular weight estimate obtained by extrapolation of the scattering intensity to zero angle,  $I(0)$  of 112 kDa. The slightly elevated value is due to experimental error. Guinier analysis and the program GNOM (Semenyuk & Svergun, 1991; Svergun, 1992) were used to determine the radius of gyration,  $R_g$  to be  $38 \pm 1 \text{ \AA}$  and  $37 \pm 1 \text{ \AA}$ , respectively. The distance distribution function,  $p(r)$  (Fig. 5.5B) shows the slightly elongated shape of E3 and was used to estimate the maximum particle dimension,  $D_{\max}$ , of  $130 \text{ \AA}$ . The  $R_g$  and  $D_{\max}$  determined for the E3 homology model with the program CRY SOL (Svergun et al., 1995) were  $32 \text{ \AA}$  and  $129 \text{ \AA}$ , respectively and therefore agree very well with the experimental values. This clearly indicates that the homology model – and by implication the yeast structure – adequately describes the molecular shape of human E3.

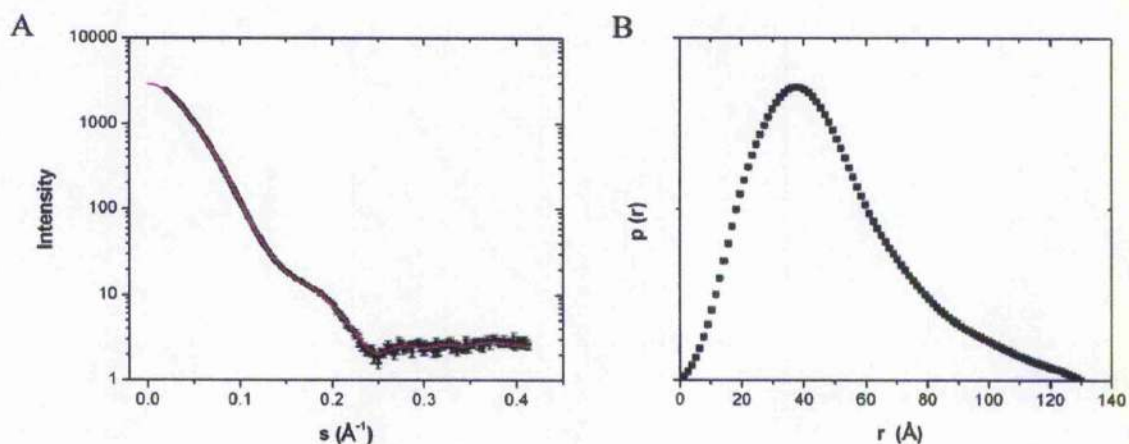


**Figure 5.5** Small angle x-ray scattering of E3

The scattering curve for E3 (—) and the shape scattering curve from GNOM (—) are shown in (A). The distance distribution  $p(r)$  (B) was calculated using GNOM. Error bars are shown but not visible due to their small size.

Crystallisation of E3 was attempted in order to determine its structure at high resolution, but all protein crystals obtained were unsuitable for structure determination; similar observations have been made previously for the crystallisation and structure determination of porcine E3 (Toyoda et al., 1998a). Instead, the SAXS data were used to obtain a three-dimensional structure of E3. Recently, the high resolution structure of human E3 has been solved (Brautigam et al., 2005).

*Ab initio* modelling of E3 scattering data with GASBOR and DAMMIN produced an elongated particle, which superimposes well onto the E3 homology model (Fig. 5.6) despite being somewhat more anisotropic than the homology model. Only the NAD domain of E3 is not satisfactorily positioned within the electron density of the model, presumably because of differences between the solution and crystal structures. Superimposition of the atomic structures determined for human and yeast E3 revealed only relatively minor differences in backbone positions. However, possible rearrangements in the E3 solution structure with respect to the crystal structure can be accommodated within the model density. A theoretical sedimentation coefficient of 5.82 S assuming a hydration of 0.36 g/g was calculated for the *ab initio* model using HYDROPRO, in excellent agreement with the sedimentation velocity data obtained for E3 ( $s_{20,w}^{\circ} = 5.8$  S).

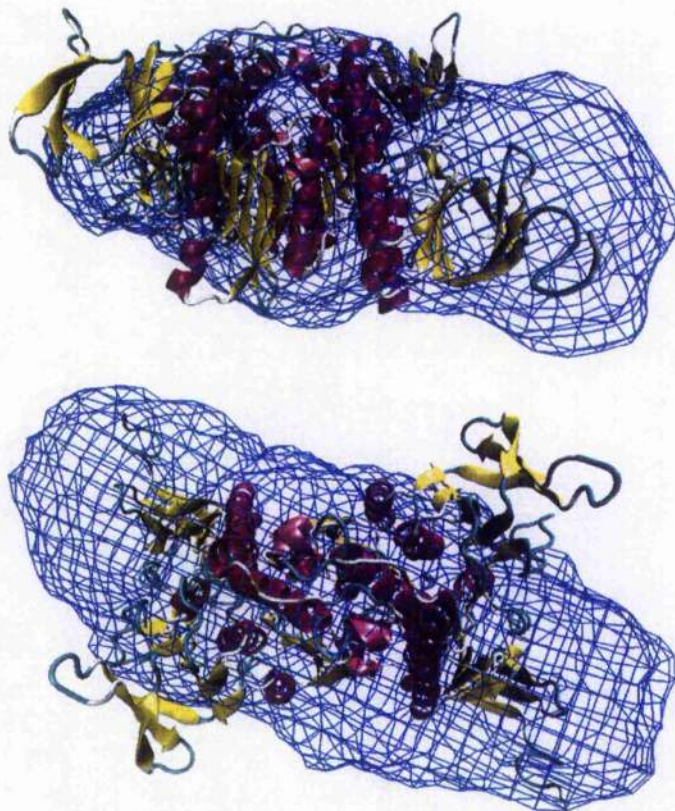


**Figure 5.6** Superimposition of the homology and *ab initio* models of E3  
Front and side views of a superimposition of the *ab initio* model (blue wiremesh) and the homology model of human E3 (cartoon).

### 5.3.2 Characterisation of XDD and XSBD

Full-length E3BP is difficult to work with owing to its tendency to aggregate and precipitate. In order to circumvent these problems two shorter constructs consisting of the E3BP lipoyl and/or subunit binding domains, termed XDD and XSBD, respectively, were used instead.

#### 5.3.2.1 Homology modelling of XDD and XSBD

The LD and SBD are reasonably well conserved, exhibiting 36% and 34% sequence identity with the corresponding E2 domains from *B. stearothermophilus*, respectively (Fig. 5.7). Due to a lack of structural information on the linker region connecting the lipoyl and subunit binding domains, a complete homology model of the E3BP didomain (XDD) could not be constructed.

The LD and SBD were therefore modelled independently using human and *Bacillus* E2 domains as templates, respectively (see Section 3.5.2). The structure of the E2-SBD used for modelling comprises only the minimum number of amino acid residues required for binding of E2 to E1 and E3 in *Bacillus*. Therefore, not all residues of the E3BP subunit binding domain (XSBD) construct used are accounted for in the homology model. In order to produce a model structure for the didomain construct, both domains were placed approximately 65 Å apart, based on previous EM data (Zhou et al., 2001a; 2001b) and overall PDC dimensions.

#### 5.3.2.2 Analytical ultracentrifugation of XDD

SV data show that XDD is monodisperse at low concentrations, although formation of dimers can be observed at concentrations higher than approximately 0.4 mg/ml (22 μM) (Fig. 5.8A), while formation of high-order oligomers and aggregate occurs at concentrations above 3 mg/ml (data not shown).

Finite element analysis of the SV data, assuming the presence of two species, yields the true sedimentation coefficients for XDD at all experimental concentrations. These were then

	10	20	30	40	50	60
E2, human	SLPPHQKVPLPSLSPTMQAGT	IARWEKKEGDKINEGDL	IAEVEDKATVGFESLEE	CYMA		
E3BP, human	-----	-----	-----	-----	-----	-----
E2, <i>B.st.</i>	-----	-----	-----	-----	-----	-----
	70	80	90	100	110	120
E2, human	KILVAEGTRDVP	IGAIICITV	GKPEDIEAF	KNYTLDS	SAAPTQ	QAAPAPTPAATASPTTP
E3BP, human	-----	-----	-----	-----	-----	-----
E2, <i>B.st.</i>	-----	-----	-----	-----	-----	-----
	130	140	150	160	170	180
E2, human	SAQAPGSSYP	PHMQVLLPAL	SPMTMGTV	QWEEKVGEK	SEGDL	LAETDKATIGFEV
E3BP, human	-----	-----	-----	-----	-----	-----
E2, <i>B.st.</i>	-----	-----	-----	-----	-----	-----
	190	200	210	220	230	240
E2, human	QEEGYLAKIL	VPEGTRD	VPLGTPLC	IIVEKEAD	---ISAFAD	YRPTTEVTDLKPQVPPPTP
E3BP, human	SDDGILAKIV	VEEGSKN	IRLGS	LIGLIVEEGED	WKWVEIP	KDVGPPPPVSKPSEPRPSP
E2, <i>B.st.</i>	PVKGKVL	EILVPEG	IVATV	GQTLITL	DAPGYEN	-----MTFKGQEQQEAKKE
	250	260	270	280	290	300
E2, human	PPVAAV	PPPTPQ	LAPTPSTP	CPATPAG	PKGRV	FVDPLAKKLAVEKGI
E3BP, human	EPQISIP	VKKEHIP	GTLRF	RLSPAARN	ILEKHS	LDASQGTATGPRGIFTKEDALKVQLK
E2, <i>B.st.</i>	EKTETV	SKEEKV	DAVAP	NAPAAEA	EAGPNRRV	IAMPVSRKYAREKGV-----DIRLVQ
	310	320	330	340	350	360
E2, human	GTGPDGRIT	KKDID	SFVPSK	VAPA-----	PAAVV	PTGPGMAPVPTGVFTDIPISNI
E3BP, human	QTGKITE	SRPTP	APTATP	TAPSPL	QATAGP	SYPRVIPPVSTPGQPNVAVGTFTEIPASNI
E2, <i>B.st.</i>	GTGKNGR	VLKED	IDAF	LAGGAK	PAPAAA	-----EKAAPAAAKPATTEGEFPE
	370	380	390	400	410	420
E2, human	RRVIAQ	RLMQSK	QTI	PHYLLS	-CKYGEV	LLVRKELNKILEGR-SKISVND
E3BP, human	RRVIAK	RLTESK	STVPH	AYATAD	CDLGAV	LKVRQDLVK---DD-IKVSVND
E2, <i>B.st.</i>	RRVIAK	AMVH	SKHTA	PHVTL	MDEADV	TKLVAHRRKKFKIAAEKGIKLTFLPVVVKALVSA
	430	440	450	460	470	480
E2, human	CLKVPEAN	SSWMD	TVIR--	QNHVV	DVSVAV	STPAGLITP
E3BP, human	LKQMPD	VNVSWD	GEGPK--	QLPF	IDISV	AVATDKGLLTP
E2, <i>B.st.</i>	LREY	PVLNTS	IDDE	TEEII	QKHYYN	IGIAAD
	490	500	510	520	530	540
E2, human	TKAREG	KLQPH	EFQGG	TFTIS	NLGMF	GIKNFS
E3BP, human	KKARDG	KLLPE	EYQGG	SFSIS	NLGMF	GIDET
E2, <i>B.st.</i>	EKARDG	KLTPG	EMKAS	CTIT	NI	GSAGG
	550	560	570	580		
E2, human	---FDV	ASMMS	VTLS	CDHR	VVDG	AVGAQW
E3BP, human	NAKLQ	QRQL	ITV	TMSS	SRVVD	DELATR
E2, <i>B.st.</i>	---I	VAAP	MLAL	SL	SFD	HRMID

Figure 5.7 Sequence alignment of E2 and E3BP

The amino acid sequences of human E2 and E3BP and *B. stearothermophilus* E2 were aligned. The lipoyl domains (—), subunit binding domain (—) and C-terminal acetyltransferase domain (—) are indicated. Residues identical in all three sequences are shown in red, amino acids identical in two of three sequences are shown in green, and residues whose charge has been conserved are depicted in blue.

extrapolated to infinite dilution to give  $s$  for XDD independent of concentration of  $s_{20,w}^o = 1.87 \pm 0.03$  S and  $1.91 \pm 0.02$  S determined from absorbance and interference data, respectively (Fig. 5.8B). Again, the value obtained for the XDD sedimentation coefficient is lower than that calculated for a hydrated sphere ( $s = 2.3$  S) in accordance with previous observations in which the linker region has been described as a flexible, yet extended structure (Green et al., 1992). The elongated structure of XDD was therefore expected and confirms observations from size exclusion chromatography (see Section 5.3.3.2).

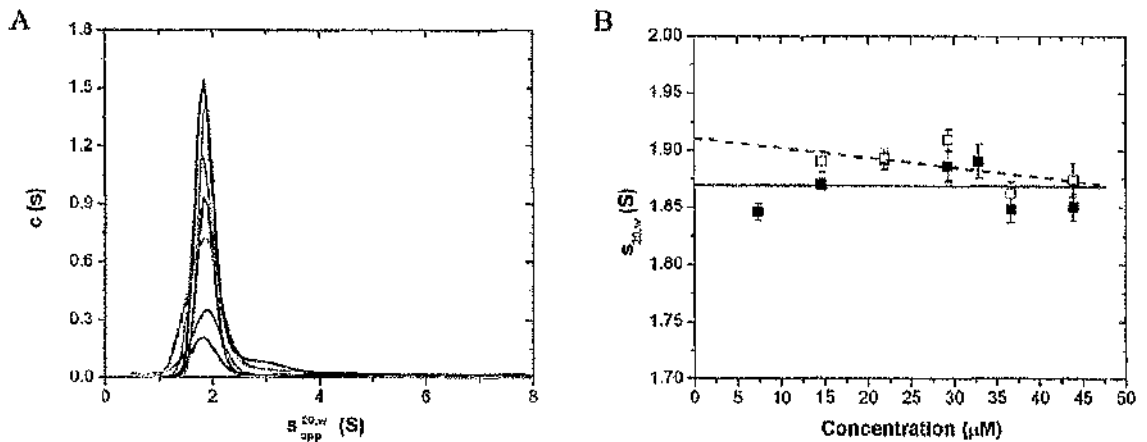


**Figure 5.8 Sedimentation velocity analysis of XDD**

(A)  $c(s)$  distribution of SV absorbance data collected for a range of XDD concentrations ( $-7.3 \mu$ M,  $-14.7 \mu$ M,  $-22.0 \mu$ M,  $-29.3 \mu$ M,  $-32.9 \mu$ M,  $-36.6 \mu$ M,  $-43.9 \mu$ M). (B) Determination of concentration independent  $s_{20,w}^o$  for XDD data recorded using absorbance ( $\blacksquare$ ) and interference optics ( $\square$ , dashed line).

SE data obtained for XDD show a rise in the apparent whole cell, weight-average molecular weight,  $M_{w,app}$  with increasing sample concentration, indicative of self-association and/or aggregate formation (Fig. 5.9). The molecular weight of XDD independent of concentration,  $M_w^o$  was determined to be  $27.1 \pm 1.8$  kDa, which is considerably higher than the molecular weight predicted from its amino acid composition of 19.7 kDa. Similarly,  $M_{w,app}$  of XDD obtained from global analysis with a single species was  $25.2 \pm 4.0$  kDa. However, data fits improved considerably when two species were used for global analysis of the SE data with molecular weights of  $20.5 \pm 3.8$  kDa and  $35.5 \pm 3.8$  kDa, respectively. The molecular weight of the second species is a little lower than expected for an XDD dimer (39.4 kDa), but within

the limits of experimental error. However, the data could not be fitted satisfactorily with a self-association model.

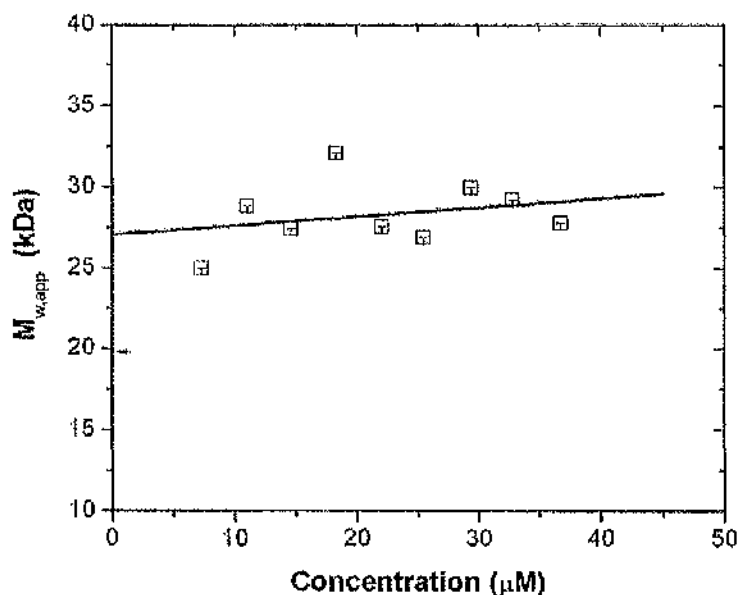


**Figure 5.9 Sedimentation equilibrium analysis of XDD**

$M_{v,\text{app}}$  was determined for each sample and extrapolated to zero concentration. Data from the same cell but recorded at different speeds were analysed simultaneously using the multi-speed equilibrium routine in SEDPHAT with a single species model. The calculated molecular weight of XDD is indicated by an arrow.

The existence of E3BP dimers has been suggested before (Sanderson et al., 1996b; Hiromasa et al., 2004), but was unexpected in this experiment because the authors described the C-terminal domain of E3BP as responsible for self- as well as E2 association. The C-terminal domain is absent from the XDD construct, while both the lipoyl and subunit binding domains seem unlikely candidates for dimer formation – certainly such an interaction has never been reported. Lastly, the N-terminal His-tag could be responsible for dimerisation, however, due to the presence of a metal chelator, EDTA, in the buffer this seems unlikely. His-tag induced dimer formation is commonly caused by leaching of metal ions from the column during metal chelate purification. Most probably, the results represent the initial stages of aggregate formation which has been observed before, especially for XDD concentrations above 0.4 mg/ml.

Data were also analysed taking into account non-ideality arising from the elongated shape and charge of XDD by fitting of the second virial coefficient,  $B$ . Agreement of  $M_{w,app}$  from global analysis ( $20.2 \pm 2.5$  kDa) with the expected molecular weight of XDD was substantially improved, although a small concentration-dependent increase in  $M_{w,app}$  from analysis of individual cells was still apparent. The values obtained experimentally for the second virial coefficient,  $B$  of  $10.3 \times 10^{-5}$  ml mol  $g^{-2}$ ,  $8.6 \times 10^{-5}$  ml mol  $g^{-2}$  and  $9.1 \times 10^{-5}$  ml mol  $g^{-2}$  (for rotor speeds 25000, 29000 and 35000 rpm, respectively) correspond well to  $B$  calculated with COVOL (Harding et al., 1999) of  $8.4 \times 10^{-5}$  ml mol  $g^{-2}$ .

### 5.3.2.3 Small angle x-ray scattering of XDD

SAXS analysis of XDD was problematic, as the protein has a tendency to aggregate at the concentrations required for SAXS experiments. In order to circumvent this problem XDD was kept at low concentrations ( $< 0.4$  mg/ml) and only concentrated immediately prior to SAXS experiments. However, even this approach could not prevent protein aggregation as evidenced by the molecular weight values estimated from the scattering intensity to zero angle,  $I(0)$ :  $M_w$  increased from 25 kDa to 33 kDa and 80 kDa for sample concentrations of 0.4 mg/ml, 4.8 mg/ml and 11.1 mg/ml with a concomitant increase in  $R_g$ . The scattering data obtained for the lowest concentration sample seem to be alone in not containing a significant amount of aggregate as the difference in molecular weight compared to the calculated value of 19.7 kDa is within the experimental error -- molecular weight estimation using SAXS is not particularly accurate. However, due to the low sample concentration the data are noisy and could not be used for *ab initio* modelling. The elongated structure of XDD is still apparent from the scattering curve (Fig. 5.10A), as expected from previous cryo-EM data of PDC (Zhou et al., 2001b). In contrast, the  $D_{max}$  of 25 Å determined from the XDD distance distribution function,  $p(r)$  (Fig. 5.10B) is much shorter than the anticipated length of 80-100 Å. The reason for this large discrepancy is probably the poor statistics of the data. Since the LD and SBD are interconnected by an extended polypeptide chain, scattering from the two domains – due to their larger size – is thought to dominate the scattering pattern, while scattering from the linker is very weak. The two domains are similar in size and their longest dimension is approximately 25 Å, corresponding to the  $D_{max}$  observed in the distance distribution function shown in Fig. 5.10B. Usually this problem would be overcome by increasing the sample

concentration and thus acquiring data with improved statistics, but this was not possible for XDD.

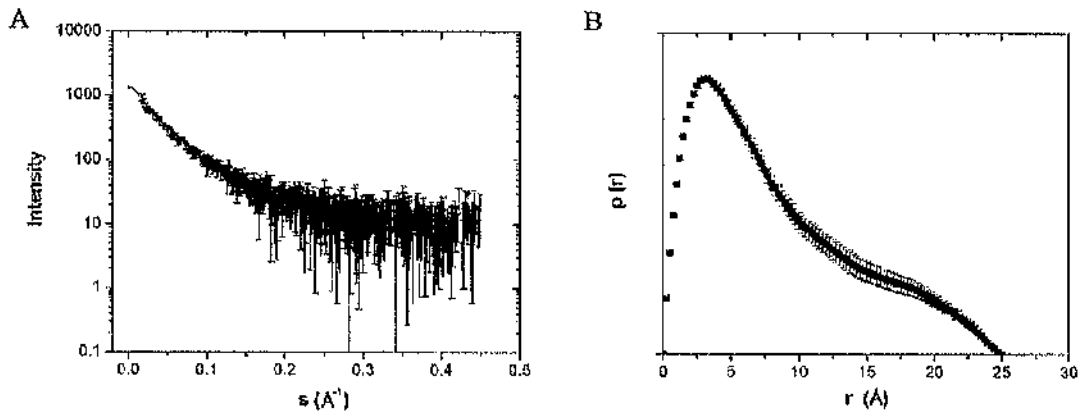


**Figure 5.10 Small angle x-ray scattering of XDD**

The scattering curve for XDD at 0.4 mg/ml (○) and the shape scattering curve from GNOM (—) are shown in (A). The distance distribution  $p(r)$  (B) was calculated using GNOM.

#### 5.3.2.4 Circular dichroism of XSBD

Western blotting with antibodies raised against bovine full-length E3BP was employed initially to confirm XSBD identity (data not shown). In addition, circular dichroism (CD) was used to determine correct protein folding (see Section 3.3.7). From the CD spectrum and comparison against typical proteins, XSBD was found to consist of 35%  $\alpha$ -helix, 7%  $\beta$ -sheet, 23% turns with 35% of residues left disordered, consistent with a folded subunit binding domain surrounded by linker residues present in an extended conformation.

#### 5.3.2.5 Analytical ultracentrifugation of XSBD

SV experiments confirm that XSBD is monodisperse over a wide concentration range (Fig. 5.11A). Using finite element analysis of the data in SEDFIT the true sedimentation coefficients of XSBD were determined for each sample and extrapolated to infinite dilution to determine  $s_{20,w}^0 = 1.06 \pm 0.02$  S and  $1.08 \pm 0.02$  S for absorbance and interference data,

respectively (Fig. 5.11B). The sedimentation coefficient calculated for an equivalent hydrated sphere was 1.26 S, indicating that XSBD is somewhat elongated in shape as part of the linker regions are present on either side of the domain proper.

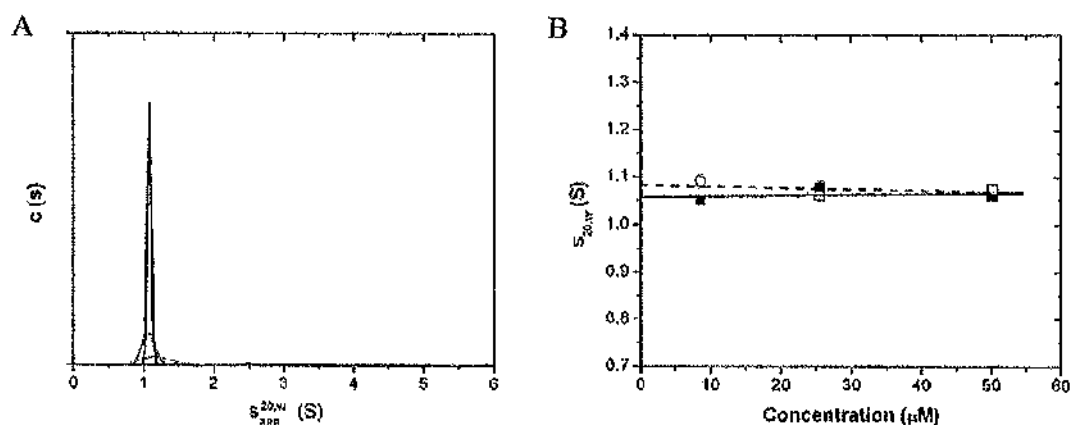


**Figure 5.11 Sedimentation velocity analysis of XSBD**

(A)  $c(s)$  distribution of SV interference data collected for XSBD ( $-$  8.5  $\mu$ M,  $-$  25.5  $\mu$ M,  $-$  50.2  $\mu$ M). (B) Determination of concentration independent  $s_{20,w}^0$  for XSBD data recorded using absorbance ( $-$ ■ $-$ ) and interference optics ( $\square$ , dashed line).

SE data confirm the monodisperse nature of XSBD. Only a very slight rise in the apparent whole cell molecular weight,  $M_{w,app}$  with increasing sample concentration is apparent in Fig. 5.12. The molecular weight independent of concentration,  $M_w^0$  was determined to be  $9.6 \pm 2.0$  kDa, in good agreement with the calculated molecular weight of 8.5 kDa.

Similarly, using global analysis with a single species the molecular weight of XSBD was determined to be  $9.9 \pm 4.4$  kDa. The fit to the data was improved further by using global analysis with two species, resulting in molecular weights of  $8.8 \pm 3.7$  kDa and  $13.2 \pm 3.7$  kDa, respectively. The second species presumably represents a small amount of XSBD dimers and/or contaminating protein. However, as shown in Fig. 5.12, the effect of the second species on the XSBD equilibrium data is negligible over a large concentration range.

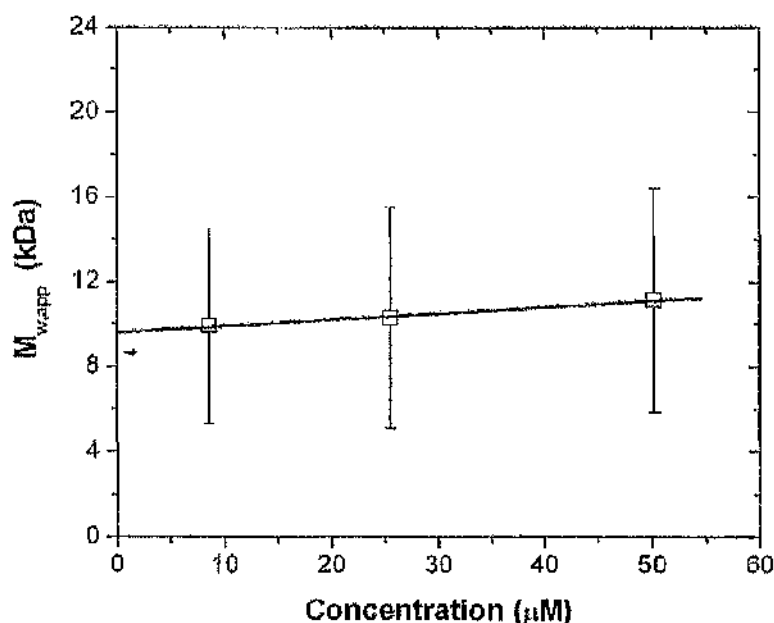


**Figure 5.12 Sedimentation equilibrium analysis of XSBD**

$M_{w,app}$  was determined for each sample and extrapolated to zero concentration. Data from the same cell but recorded at different speeds were analysed simultaneously using the multi-speed equilibrium routine in SEDPHAT with a single species model. The calculated molecular weight of XSBD is indicated by an arrow.

### 5.3.2.6 Small angle x-ray scattering and *ab initio* modelling of XSBD

Due to a lack of protein, scattering data for XSBD were recorded only for a single concentration. However, inspection of the low angle region of the scattering curve (Fig. 5.13A) did not reveal any indication of inter-particle interference. The radius of gyration,  $R_g$ , as determined using the Guinier approximation is  $20 \pm 1 \text{ \AA}$ . The distance distribution function,  $p(r)$  is shown in Fig. 5.13B. The  $D_{max}$  is  $69 \pm 2 \text{ \AA}$  and the  $R_g$  calculated from the  $p(r)$  function is  $21 \pm 1 \text{ \AA}$ , in good agreement with the value obtained from the Guinier approximation. The  $R_g$  and  $D_{max}$  determined for the XSBD homology model with the program CRY SOL were  $10 \text{ \AA}$  and  $24 \text{ \AA}$ , respectively, and thus considerably lower than the values determined for  $R_g$  and  $D_{max}$  experimentally. This discrepancy can be explained by the absence of a total of 37 residues from the N- and C-terminal linker regions of XSBD due to a lack of structural information.

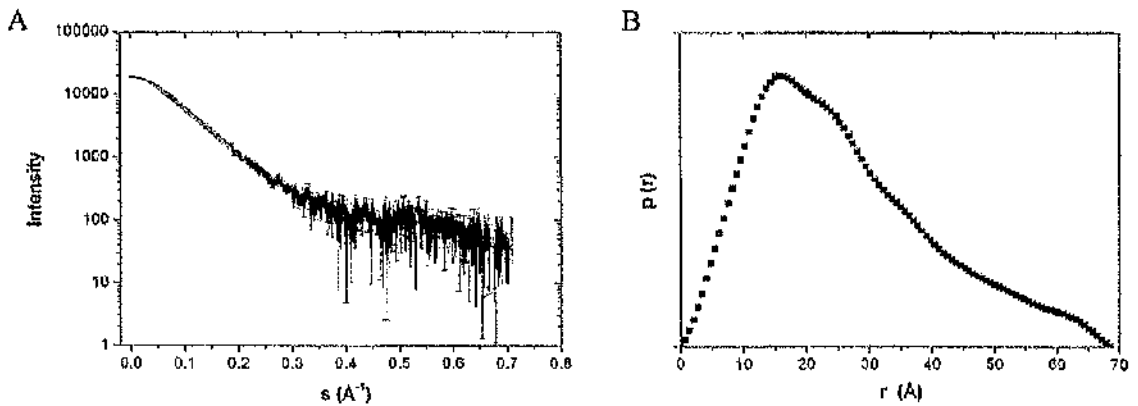


**Figure 5.13 Small angle x-ray scattering of XSBD**

The scattering curve of XSBD (---) and the shape scattering curve from GNOM (—) are shown in (A). The distance distribution  $p(r)$  (B) was calculated using GNOM. Error bars are shown, but not visible due to their small size.

The *ab initio* model of XSBD (Fig. 5.14) clearly shows this increase in size with respect to the homology model. The central domain of the *ab initio* model was superimposed separately with the XSBD homology model in SITUS and the fit works very well. However, the regions thought to accommodate the XSBD N- and C-terminal linker regions are considerably larger than expected. A SAXS curve contains time-averaged as well as radially averaged structural information. As both linkers are thought to be reasonably flexible they will adopt a large variety of slightly different conformations over the time-scale of the experiment. This is reflected in the *ab initio* model where both termini resemble separate domains rather than extended polypeptide chains.

### 5.3.3 Cross-bridge formation between E3BP and E3

#### 5.3.3.1 Preparation of the XDD/E3 subcomplex

The XDD/E3 subcomplex was reconstituted from purified proteins at a ratio of 3:1 (XDD:E3). Due to the large difference in molecular weight between the XDD/E3 complex and XDD, the two species were easily separated by size exclusion chromatography (Fig. 5.15A) where the complex elutes from the column first, followed by uncomplexed XDD (Fig. 5.15B). The XDD/E3 complex is very stable; E3 is extremely protease resistant (Lindsay et

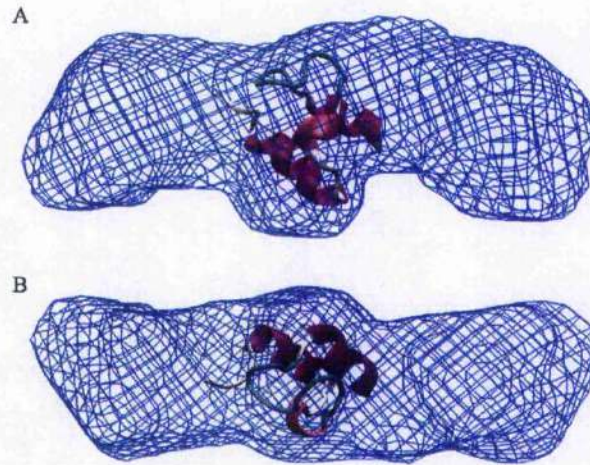


**Figure 5.14 Superimposition of the homology and *ab initio* models of XSBD**

Top (A) and side (B) views of the XSBD homology model (cartoon) superimposed onto the *ab initio* model (blue wiremesh).

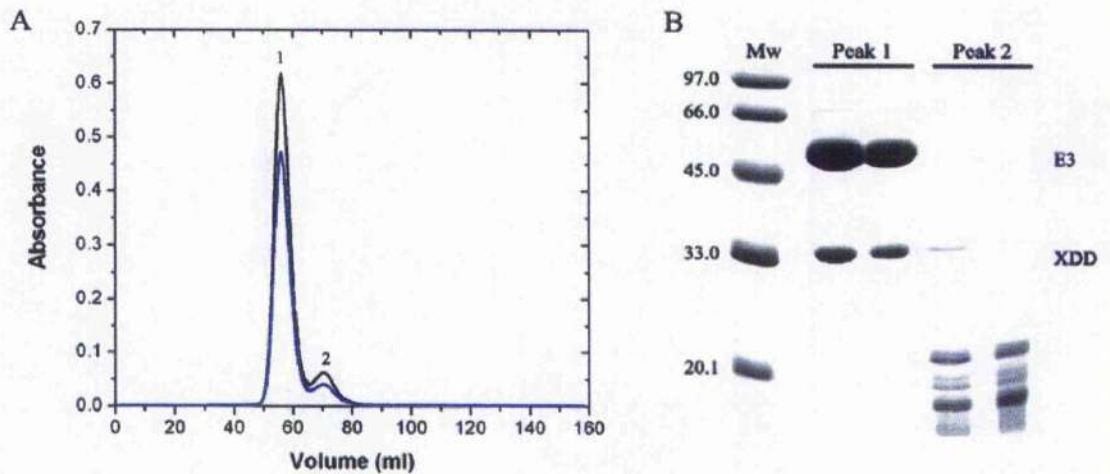


**Figure 5.15 Purification of the XDD/E3 subcomplex**

Gel filtration chromatography (GFC) of XDD/E3 (A). The peaks corresponding to XDD/E3 (1) and XDD (2) are indicated. Protein absorbance was recorded at 280 nm (—) and 260 nm (---). The protein peaks obtained from GFC were analysed by SDS PAGE (B). The positions of E3 and XDD are indicated. Molecular weights (Mw) are shown in kDa.

al., 2000) and also protects XDD from proteolytic cleavage, while uncomplexed XDD is very sensitive to the presence of proteases (Fig. 5.15B).

### 5.3.3.2 Gel filtration analysis of XDD/E3 and its constituent proteins

When compared to the standard curve (Fig. 5.16) only the molecular weight of E3 is consistent with the molecular weight calculated from its amino acid composition of 106 kDa. Estimates for the apparent molecular weights,  $M_{w,app}$ , of XDD and the XDD/E3 complex of approximately 60 kDa and 300 kDa far exceed their predicted molecular weights of 19.7 kDa and 144 kDa, respectively. This is indicative of the anisotropic shapes of the molecules and in consequence of their enlarged hydrodynamic radii when compared to other globular proteins of similar molecular weights. This result confirms the data obtained for XDD (see Section 5.3.2), E3 (see Section 5.3.1) and XDD/E3 (see below) by AUC and SAXS.

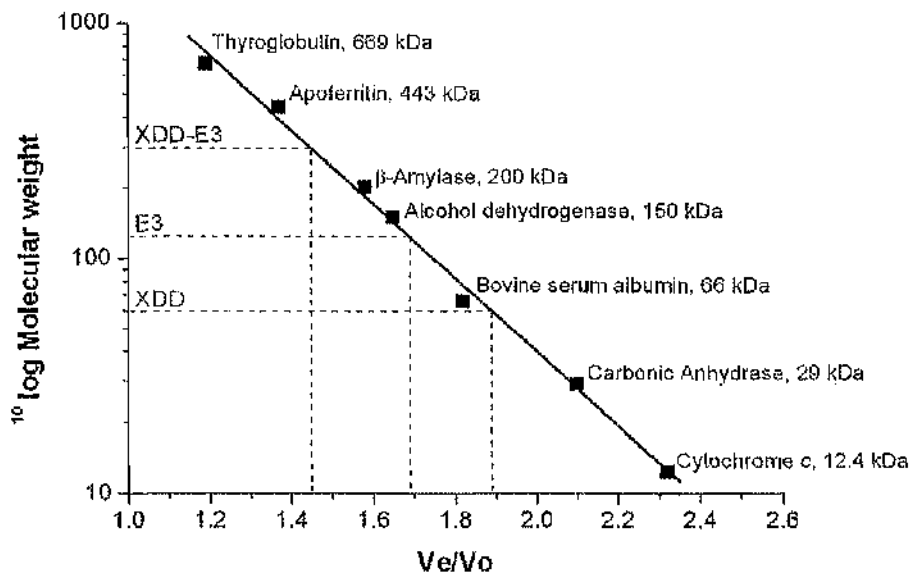


**Figure 5.16** Molecular weight determination using gel filtration chromatography

A Sephacryl S-300 gel filtration column was standardised using globular proteins of known molecular weights. The logarithm of the molecular weights was plotted versus the ratio of elution to void volume ( $V_e/V_o$ ) in order to obtain a standard curve. The elution positions of XDD, E3 and the XDD/E3 complex are indicated.

### 5.3.3.3 Non-denaturing PAGE

Initial binding studies were carried out by mixing either XSBD or XDD with E3 at different molar ratios and subjecting them to non-denaturing PAGE. The addition of XSBD or XDD to E3 results in a noticeable bandshift which increases as more XSBD or XDD is added. At a stoichiometry of 2:1 all of the E3 present is shifted into the lower mobility band corresponding to the XSBD/E3 (Fig. 5.17A) or XDD/E3 (Fig. 5.17B) complex. At stoichiometries lower than 2:1, excess E3 is seen (Fig. 5.17), while at stoichiometries higher than 2:1, excess XDD remains (Fig. 5.17B). At the pH used to conduct non-denaturing PAGE (pH 8.8), XSBD moves towards the cathode and thereby out of the gel due to its high pI of 9.9. No intermediates in complex formation have been observed.

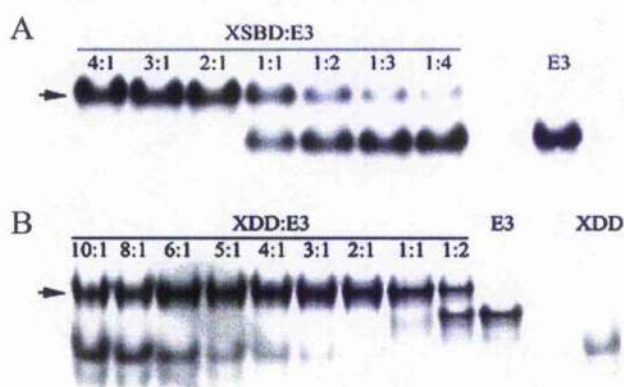


**Figure 5.17** Non-denaturing PAGE of different XSBD:E3 and XDD:E3 stoichiometries. Stoichiometric mixtures of E3 and XSBD (A) or XDD (B) were pre-incubated at 25°C for 15 minutes. As the amount of XSBD/XDD increases a shift from the position corresponding to E3 into that for the complex is observed, indicating the formation of a tight complex. The positions of the complex band are shown by arrows. At stoichiometries above 2:1 free XDD is seen in addition to the complex band. Free XSBD migrates towards the cathode and thereby out of the gel due to its high pI of 9.9.

### 5.3.3.4 Analytical ultracentrifugation of XDD/E3

SV experiments were conducted for uncomplexed E3 and XDD as well as for different XDD:E3 stoichiometries and the sedimentation profiles fitted using  $c(s)$  analysis in SEDFIT (Schuck, 2000). The  $c(s)$  profiles of free XDD and E3 show single peaks with apparent sedimentation coefficients of 2.0 S and 5.9 S, respectively (Fig. 5.18A). Fig. 5.18B clearly shows the complete disappearance of the XDD peak at a stoichiometry of 2:1. The E3 and

XDD/E3 peaks overlap completely, although the peak position is slightly shifted to an apparent sedimentation coefficient of 5.7 S for XDD/E3. A globular protein of higher molecular weight is expected to sediment faster (and therefore have a higher sedimentation coefficient) than a protein of lower molecular weight. Therefore, it can be inferred that the complex has an extended shape which offsets the gain in molecular weight with respect to free E3, and causes it to sediment at the same speed as E3, confirming previous observations from gel filtration chromatography (see Section 5.3.3.2).

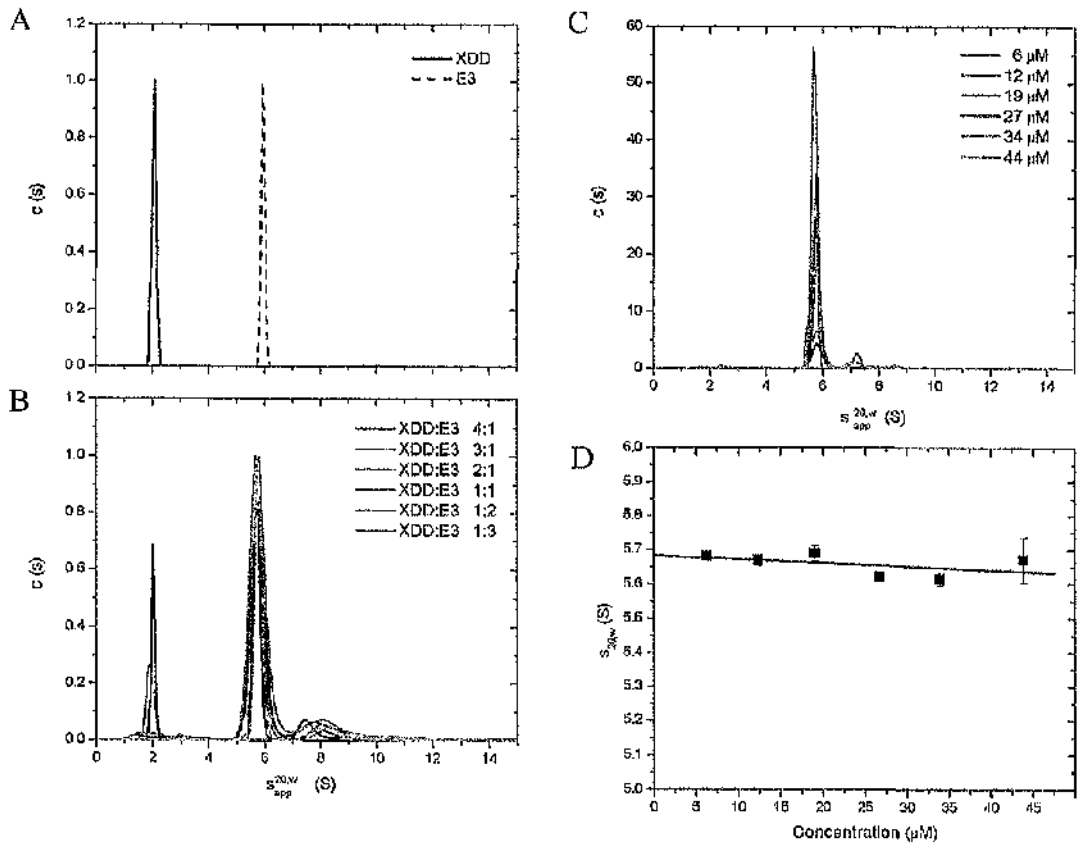


**Figure 5.18 Sedimentation velocity analysis of XDD:E3 stoichiometric mixtures and purified XDD/E3 complex**

$c(s)$  analysis of SV data for uncomplexed E3 and XDD (**A**) as well as different XDD:E3 stoichiometric mixtures (**B**),  $c(s)$  analysis for a range of concentrations of purified XDD/E3 complex (**C**) and determination of  $s_{app}^{20,w}$  for XDD/E3 (**D**).

The small broad peak around 7.5-8 S observed at all stoichiometries corresponds to aggregate species and is greatly reduced if the complex is purified to uniformity by gel filtration prior to AUC analysis (Fig. 5.18C).  $c(s)$  analysis of SV profiles from the purified complex also show that a single species is present in solution bar a small amount of aggregate that is present at high concentrations only, a result substantiated by non-denaturing PAGE (data not shown). No free protein or intermediates are observed at any concentration, in accordance with the expected tight interaction between XDD and E3. Finite element analysis with a single-species model yields the true sedimentation coefficients for XDD/E3 at all experimental concentrations. These were then extrapolated to infinite dilution to give a sedimentation coefficient for XDD/E3 independent of concentration of  $s_{20,w}^0 = 5.68 \pm 0.05$  S (Fig. 5.18D).

The apparent whole cell, weight-average molecular weight,  $M_{w,app}$ , was determined for each XDD:E3 stoichiometric mixture using SE. The  $M_{w,app}$  peaks, as expected, at a stoichiometry of 2:1 (Fig. 5.19) when all protein present is associated into complex, owing to the tight interaction between XDD and E3. At all other molar ratios, free XDD or E3 is observed, thus depressing  $M_{w,app}$ . The value of  $M_{w,app}$  at a molar ratio of 2:1 (XDD:E3) of 137 kDa is lower than expected when compared to the calculated molecular weight of 144 kDa. This is attributable to the non-ideal behaviour of the complex. SE data for XDD/E3 complex purified by gel filtration were also analysed: agreement with the expected molecular weight was substantially improved when non-ideality arising from molecular shape and charge was taken into account. The values obtained experimentally for the second virial coefficient  $B$  of  $7.2 \times 10^{-4}$  ml mol  $g^{-2}$ ,  $1.7 \times 10^{-4}$  ml mol  $g^{-2}$  and  $2.9 \times 10^{-4}$  ml mol  $g^{-2}$  (for rotor speeds 10500, 15000 and 18000 rpm, respectively) correspond very well to  $B$  calculated with COVOL (Harding et al., 1999) of  $1.7 \times 10^{-4}$  ml mol  $g^{-2}$ .

When non-ideality is accounted for the molecular weight estimates for XDD/E3 are 151 kDa, 142 kDa and 141 kDa for rotor speeds 10500, 15000 and 18000 rpm, respectively. These values compare very well to the calculated  $M_w$  of 144 kDa for a 2:1 complex of XDD:E3. When non-ideality is included in the data analysis for the 2:1 stoichiometric mixture of XDD:E3,  $M_{w,app}$  is increased to 147 kDa, 142 kDa and 141 kDa for rotor speeds 8500, 12000 and 16000 rpm, respectively, in excellent agreement with the results for the purified complex and the calculated molecular weight. For all other stoichiometric mixtures of XDD:E3,  $M_{w,app}$

decreases with increasing rotor speed which is indicative of the presence/formation of high molecular weight aggregate, as shown also by the SV results in Fig. 5.18B. Only for the 1:1 stoichiometric mixture are all  $M_{w,app}$  estimates consistently lower than the calculated molecular weight. This is due to the choice of fitting limits. Aggregate would be steeply distributed and is thus effectively excluded from the subsequent analysis, resulting in an underestimate of  $M_{w,app}$ . Because stoichiometric mixtures other than 2:1 contain more than one species (plus aggregate), when the data are trimmed to exclude aggregate, the exponential describing the heavier component is disproportionately affected, resulting in a corresponding reduction in  $M_{w,app}$ .

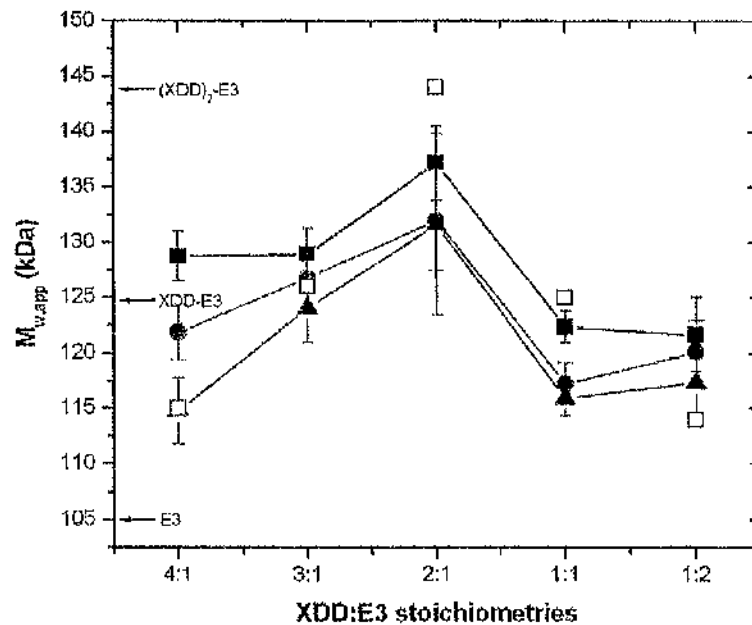


**Figure 5.19 Sedimentation equilibrium analysis of XDD:E3 stoichiometries**

SE experiments of stoichiometric mixtures of XDD:E3 were done at 8500 (■), 12000 (\*) and 16000 rpm (▲) in order to determine  $M_{w,app}$  for each stoichiometry.  $M_{w,app}$  values calculated on the basis of a very strong interaction between XDD and E3 are also shown (□). The molecular weights of E3, XDD-E3 and  $(XDD)_2$ -E3 calculated from the amino acid sequence are indicated.

### 5.3.3.5 Isothermal titration calorimetry

The heats of interaction of XDD with E3 were determined using ITC. Complex formation is exothermic (i.e. negative peaks in the ITC output) (Fig. 5.20A). Differential thermal binding curves were obtained by integration of the data and analysed using standard non-linear regression in order to obtain estimates of the binding stoichiometry, equilibrium association constant and enthalpy of binding (Fig. 5.20B). The data confirm the tight binding of XDD to E3 ( $K_a = 2.8 \times 10^7 \text{ M}^{-1}$ ) with a stoichiometry of 2:1. Binding is characterised by a large, favourable enthalpy change ( $\Delta H = -12.1 \text{ kcal/mol}$ ) and a small negative entropy change ( $T\Delta S = -1.7 \text{ kcal/mol}$ ). This experiment confirms similar ITC results of the interaction of full-length E3BP with E3 (Brown, 2002) which show that full-length E3BP binds E3 with similar affinity and identical stoichiometry.

### 5.3.3.6 Homology and hydrodynamic modelling of XDD/E3

Homology modelling was used in combination with AUC and SAXS (see below) to gain more insight into the XDD/E3 structure. A model of the human XDD/E3 complex was built from homology models (generated with SWISS-MODEL) for E3, E3BP-LD and SBD (see Section 5.3.2.1). The structure of the *B. stearothermophilus* E2-SBD/E3 complex (Mande et al., 1996) was used to position the human E3 and XSBD homology models with respect to each other. The second XSBD molecule was positioned exploiting the two-fold symmetry axis of E3. Several models with different positioning of the two lipoyl domains LD1 and LD2 were generated (Fig. 5.21), while taking into account available biochemical and structural data. In an extended conformation, both LD1 and LD2 were located approximately 65 Å from the SBDs, in accordance with previous EM data (Zhou et al., 2001a; Zhou et al., 2001b; Milne et al., 2002) and overall PDC dimensions. The resulting model XDD/E3<sub>ext</sub> (Fig. 5.21C) has a maximum dimension,  $D_{\text{max}}$ , of 227 Å. The lack of structural information for the linker region and the paucity of related sequences meant that it was not possible to model part of the linker using either homology or secondary structure modelling. A second complex model with both LDs docked in the E3 active sites and a  $D_{\text{max}}$  of 134 Å, XDD/E3<sub>dock</sub> (Fig. 5.21A) was also generated. In the process Lys97 was positioned 14 Å from E3 residues Cys45 and Cys50, allowing accommodation of the lipoic acid cofactor linked to Lys97 (Howard et

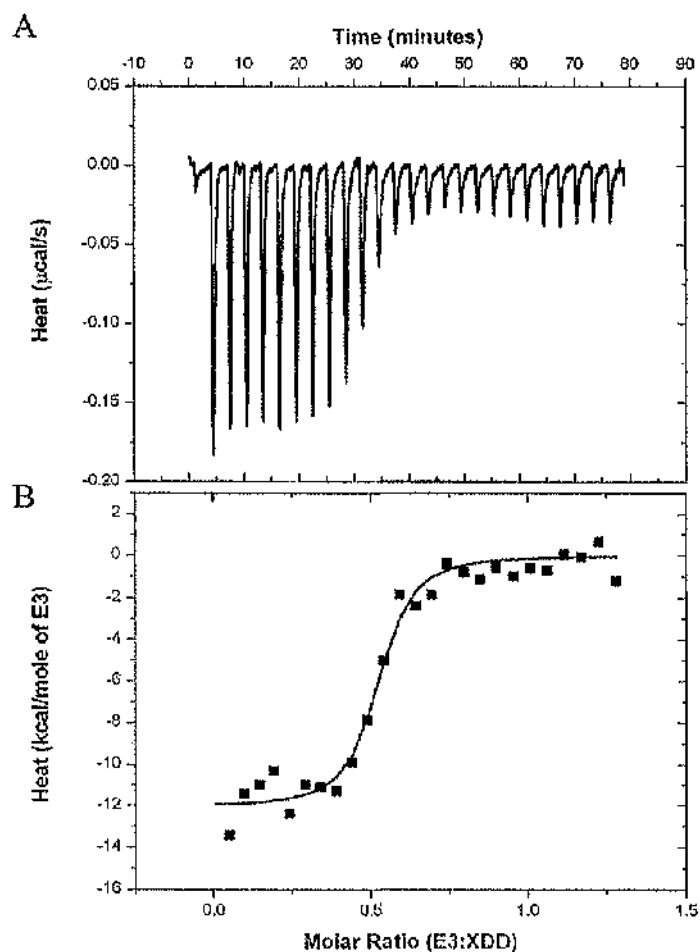


**Figure 5.20** Isothermal titration calorimetry of XDD and E3

(A) Raw data obtained from a series of 10  $\mu\text{l}$  injections of E3 into XDD at 25°C and plotted as heat versus time. (B) Binding isotherms created by plotting the areas under the peaks in (A) against the molar ratio of E3 injected. The best fit shown was obtained by least-squares fitting using a simple binding model and gives a stoichiometry of 0.5 (E3:XDD) which is equivalent to 2:1 (XDD:E3).

al., 1998), in agreement with data from mutation studies on the E3 enzyme mechanism (Leung et al., 1990; Kim et al., 1992). Although other E3 residues involved in the binding of the LD are not known, access to the E3 active site is only possible from one side of the molecule. The presence of the FAD and NAD<sup>+</sup> cofactors otherwise obstructs the interaction between the lipoate and the cysteine pair (Toyoda et al., 1998b). An intermediate model with one LD present in the extended conformation and the second docked in the active site, and a  $D_{\max}$  of 156 Å, XDD/E3<sub>int</sub>, (Fig. 5.21B) was also produced. Sedimentation coefficients of 5.3 S, 5.9 S and 6.5 S were calculated for XDD/E3<sub>extn</sub>, XDD/E3<sub>int</sub> and XDD/E3<sub>dock</sub>, respectively, using the program HYDROPRO (García de la Torre et al., 2000; García de la Torre, 2001). Accordingly, the XDD/E3<sub>int</sub> model with one docked and one extended LD gave the best agreement with the experimentally determined  $s$  of 5.68 S and also agrees best with the experimentally determined  $D_{\max}$  of 158 Å (see below).

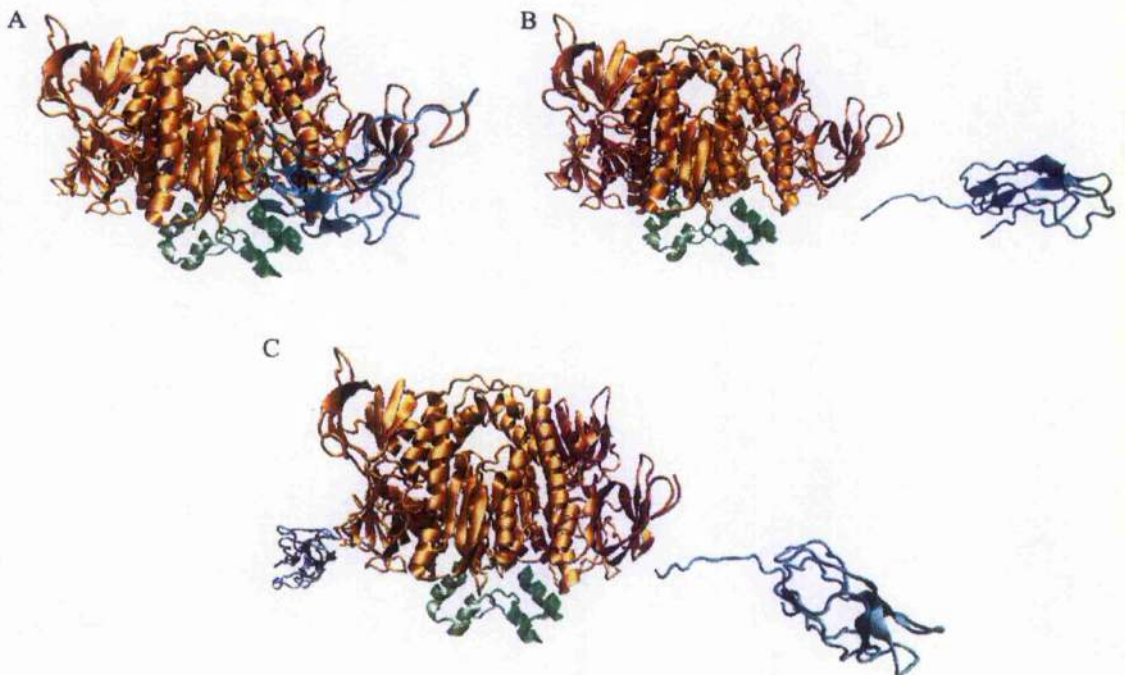


**Figure 5.21 Homology models generated for the XDD/E3 complex**

Front views are shown of XDD/E3<sub>dock</sub> (A) with both lipoyl domains docked in the E3 active sites, XDD/E3<sub>int</sub> (B) with one docked and one extended LD, and XDD/E3<sub>extn</sub> (C) with both LDs extended away from E3. E3 is shown in orange, the SBDs in lime and green, and the two LDs in blue and cyan.

### 5.3.3.7 Small angle x-ray scattering and rigid body modelling

Small angle x-ray scattering (SAXS) curves for purified XDD/E3 complex were acquired at three different protein concentrations to account for the effects of interparticle interference (Fig. 5.22A). The radius of gyration  $R_g$  determined using the Guinier approximation, is  $38 \pm 1$  Å. The particle distribution function,  $p(r)$  is shown in Fig. 5.22B. The  $D_{\max}$  is  $158 \pm 5$  Å and the  $R_g$  calculated from the  $p(r)$  function is  $41 \pm 1$  Å (Fig. 5.22B) which agrees well with the value obtained using the Guinier approximation.

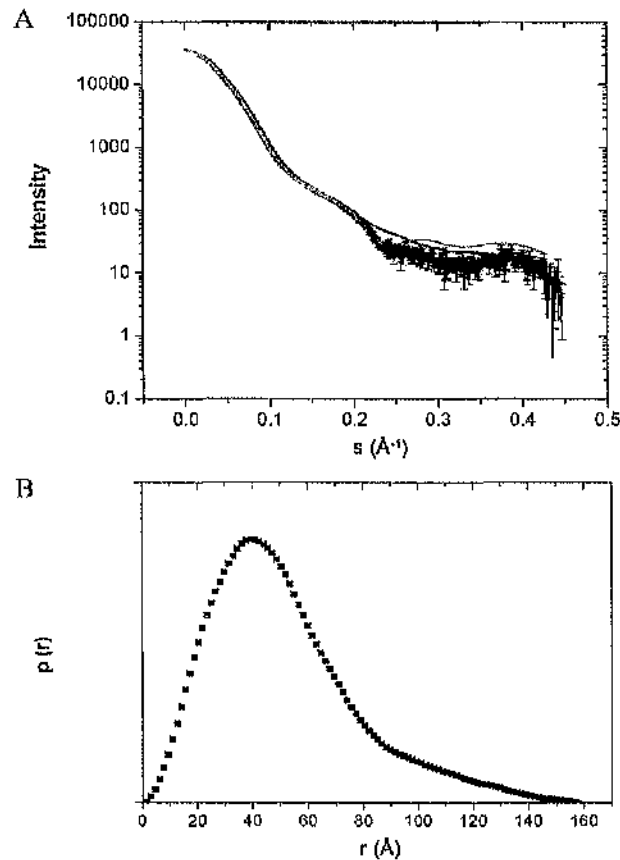


**Figure 5.22** Small angle x-ray scattering of XDD/E3

The scattering curve for XDD/E3 (—) is shown in (A). The shape scattering curve from GNOM (---) and the calculated scattering curves determined for the models obtained from *ab initio* (· · ·) and rigid body modelling (— · —) are also shown. The distance distribution  $p(r)$  (B) was calculated using GNOM. Error bars are shown but not visible due their small size.

*Ab initio* shape restoration produced an elongated, asymmetric structure (Fig. 5.23). Direct rigid body modelling was used in combination with *ab initio* modelling to analyse the structure of the XDD/E3 complex: using translations and rotations, the lowest energy conformation of each “domain” (E3, XSBD1, XSBD2, XLD1, XLD2) within the complex was determined using the program Rayuela (Nöllmann et al., 2005) as judged by fits to the SAXS data. This model was superimposed upon the *ab initio* model (Fig. 5.23). While most of the complex model fits very well into the SAXS envelope, it was not possible to fit residues 265-297 which form part of the E3 NAD domain. The same range of residues also could not be accommodated by the E3 *ab initio* model when superimposed onto the homology model (see Section 5.3.1.3), indicating structural differences between the solution and atomic structures of E3, presumably due to the effects of crystal packing. Binding of XDD to E3 is unlikely to cause conformational changes within E3, as the high resolution structures determined for human E3BP/E3 (Ciszak et al., 2006) as well as E2/E3 and E2/E1 complexes from *B. stearrowthermophilus* (Mande et al., 1996; Frank et al., 2005) suggest a lock-and-key rather than an induced fit mechanism.

### 5.3.3.8 Redox states of lipoyl domains within the XDD/E3 complex

In order for E3BP lipoyl domains (XLD) to interact with the E3 active site the lipoate needs to be present in its reduced form. As NADH was not present in the buffer of protein preparations or at any stage during the purification process, the lipoate cofactor of XDD was reduced by the addition of DTT during protein purification and immediately prior to SAXS experiments. DTT is often added to SAXS samples to prevent x-ray induced protein aggregation due to radical formation.

Monomethoxypolyethylene glycol (mPEG) 5000 maleimide was used to covalently modify reduced cysteine and lipoate thiol groups, thus increasing the apparent molecular weight of XDD and retarding its progress during SDS PAGE (Fig. 5.24, lane 4). Control reactions for XDD were set up as well, containing E3 and either NAD<sup>+</sup> (lane 1) or NADH (lane 2). NADH and E3 cause complete reduction of the lipoate cofactor and bandshift of XDD, while NAD<sup>+</sup> and E3 provide a negative control by reoxidation of the lipoate. Some

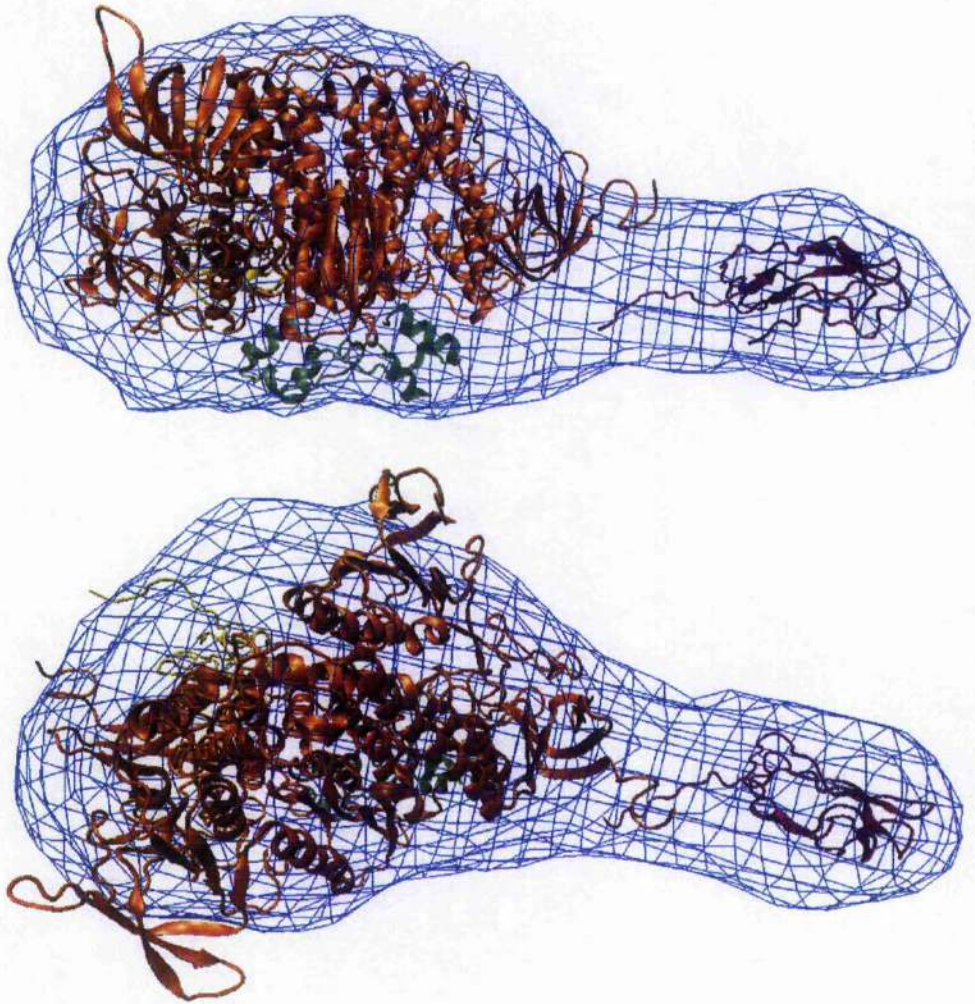


**Figure 5.23 Superimposition of XDD/E3 models from *ab initio* and rigid body modelling**

The *ab initio* model is shown as a blue wire mesh. Homology models of the five "domains" used for rigid body modelling are shown as follows: E3, orange; XSBD 1 & 2, green; XLD1, purple; XLD2, yellow. Two orthogonal views are shown.

mPEG maleimide modification can still be seen in the presence of  $\text{NAD}^+$ ; as XDD will form a tight complex with E3 in solution, steric hindrance may be responsible for this behaviour. A further control experiment looking at the modification of purified E3BP lipoyl domain (XLD) in the presence of E3 and  $\text{NAD}^+$  and/or  $\text{NADH}$  was conducted under the same reaction conditions. The LD on its own is not able to associate tightly with E3 and is completely re-oxidised in the presence of E3 and  $\text{NAD}^+$ . High molecular weight bands are caused by mPEG maleimide modification of E3.

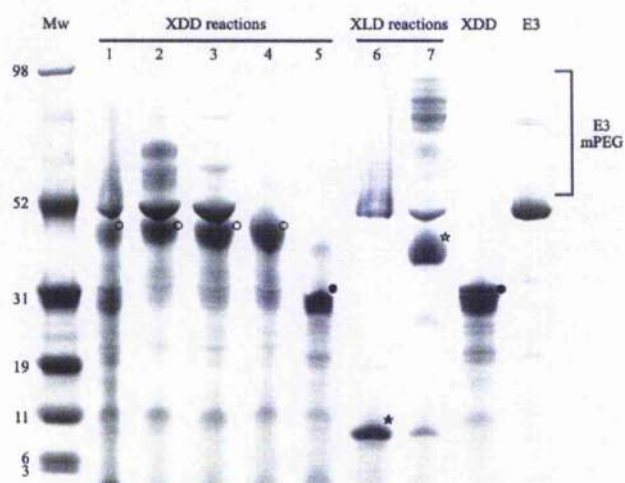


**Figure 5.24 SDS PAGE analysis of mPEG maleimide treated XDD**

XDD (reactions 1-5) and XLD (reactions 6-7) were treated with mPEG maleimide. XDD was incubated with E3 and  $\text{NAD}^+$  (1), E3 and  $\text{NADH}$  (2), E3 and DTT (3), DTT only (4) or on its own (5) before exposure to mPEG maleimide. Control XLD reactions were incubated with E3 and  $\text{NAD}^+$  (6), and E3 and  $\text{NADH}$  (7). Untreated XDD and E3 were used as additional controls. Bands of unmodified XDD (●) and mPEG maleimide modified XDD (○) as well as unmodified XLD (★) and mPEG maleimide modified XLD (☆) are indicated. Bands resulting from mPEG maleimide binding to E3 are also shown. Molecular weights (Mw) are shown in kDa.

### 5.3.3.9 Interaction of E3 with the E3BP lipoyl domain

ITC was employed to determine whether the E3BP-LD in its reduced form is able to interact with E3 on its own. Experiments were done at two temperatures,  $10^\circ\text{C}$  and  $25^\circ\text{C}$  (data not shown) in order to ensure that equivalence in the enthalpy and entropy terms at one particular temperature could not mask a possible interaction. However, no binding was observed at

either temperature, leading to the conclusion that the lipoyl domain probably requires pre-orientation from the subunit binding domain in order to form a stable complex.

## 5.4 Discussion

The evidence presented here demonstrates that two E3BP-derived molecules interact with a single E3 homodimer, thus enabling the formation of 2:1 stoichiometric "cross-bridges" in human PDC. These findings are in direct contrast to the crystal structures obtained for the *B. stearrowthermophilus* E3/E2SBD (Mande et al., 1996) and human E3/E3BP-SBD complexes (Ciszak et al., 2006) where only one SBD is associated with E3 due to steric hindrance by a loop in E3BP which prevents binding of a second SBD. Comparison of the crystal structures determined for unbound (Brautigam et al., 2005) and bound human E3 (Ciszak et al., 2006) as well as yeast E3 (Toyoda et al., 1998b) yields only very small differences in coordinates. The highly homologous (54% identical) human and yeast E3 may crystallise similarly. As the results presented in this chapter were determined in solution it is thought that either crystal packing and/or crystallisation buffer compositions affect the structures determined for eukaryotic E3 and the E3/E3BP-SBD complex. Unfortunately, E3 is too large for structure determination via NMR spectroscopy. However, SAXS data suggest that the solution conformation of free human E3 is slightly more elongated and flattened than that in the crystal structure. The solution conformations of other proteins, including yeast pyruvate decarboxylase (Svergun et al., 2000) can differ significantly from their crystal structures (Trehwella et al., 1988; Vigh et al., 1989; Svergun et al., 1997a; Nakasako et al., 2001; Kozak & Jurga, 2002). While the 1:1 stoichiometry of bacterial PDC E2-SBD/E1 and E2-SBD/E3 has been confirmed via surface plasmon resonance (Lessard et al., 1996) and ITC (Jung et al., 2002a; 2003), the stoichiometry of eukaryotic PDC has remained undetermined, until now.

The binding surfaces involved in the association of human E3 with E3BP-SBD are thought to be different to those in the *B. stearrowthermophilus* PDC: in the prokaryotic complex E3 and E2-SBD interact via an electrostatic zipper (Mande et al., 1996). However, the amino acid sequence of E3BP-SBD has undergone significant changes and is more hydrophobic in character, including a number of surface residues. It is therefore thought to interact with a

complementary hydrophobic patch on E3, adjacent to the known binding site of prokaryotic E2 and further away from the two-fold axis of E3. Thermodynamics seem to support this hypothesis: a detailed analysis of the interactions of *B. stearothermophilus* E2 didomain (DD; consisting of the E2 lipoyl and subunit binding domains) with E1 and E3 (Jung & Perham, 2003; Jung et al., 2003) carefully characterised the thermodynamic differences in the formation of the E2-DD/E1 and E2-DD/E3 complexes, respectively. The authors used a number of point mutants of both E1 and E3 as well as the wild-type enzymes to dissect the thermodynamic contribution of different residues to complex formation. While the Gibbs free energy,  $\Delta G^\circ$  of both interactions is very similar, the E2-DD/E1 association is characterised by a large, favourable enthalpy change and a small, negative entropy change. In contrast, the interaction of E2-DD with E3 is described by an unfavourable enthalpy change and large, positive entropy change (Jung et al., 2002a). Electrostatic interactions are present in both complexes, however E2-DD/E1 formation in *Bacillus* seems to involve additional hydrophobic contacts when compared to the E2-DD/E3 complex. As evidenced by microcalorimetry in Section 5.3.3.5 the interaction of the human XDD with E3 is also defined by a large, favourable enthalpy change and a small, negative entropy change, very similar to the E2-DD/E1 association in *Bacillus*, thus signalling the possible importance of hydrophobic interactions in human XDD/E3 complex formation. However, further experiments using point mutants analogous to those used by Jung et al. (2002b; 2003) are required to obtain more conclusive data.

Comparison of eukaryotic E3 crystal structures with those of prokaryotes also shows that even though the overall structure is highly conserved, the amino acid sequence identity of E3 is rather low. The region of E3 associated with E2 interaction in prokaryotes has undergone significant changes in human and *S. cerevisiae* E3 that result in a more neutral surface potential (Toyoda et al., 1998b). Thus, a slight shift in the location of the E3BP binding site away from the two-fold axis on E3 may be sufficient to allow binding of two E3BP molecules simultaneously.

The low resolution x-ray scattering structure determined for the human XDD/E3 subcomplex conclusively verifies its 2:1 stoichiometric relationship and high stability. Unexpectedly, the subcomplex proved to be highly asymmetric. These data are compatible with a model in

which one LD is peripherally extended away from the E3 dimer whereas the second LD is docked into one of the E3 active sites that are located at the monomer-monomer interface. During XDD purification, the lipoyl group was maintained in its dithiol form by the presence of DTT. Reduced lipoate is the true substrate for E3 and its reoxidation by E3 is prevented by the absence of  $\text{NAD}^+$ . The redox state of the lipoamide cofactor was confirmed by modification with PEG 5000 maleimide, a thiol group reagent that leads to a dramatic increase in the apparent  $M_w$  of XDD, provided it is present in its reduced form. That only one of the two LDs is found near the E3 active site, suggests E3 may operate by a flip-flop mechanism: only one E3 active site in turn can accept a LD, house its reduced lipoamide cofactor and catalyse its re-oxidation. This would be similar to the mechanism proposed previously for E1, where different steps of the reaction are performed in each of the active sites at any given moment (Khailova & Korochkina, 1985; Ciszak et al., 2003). However, more experiments are required to substantiate this hypothesis and, in addition, it will be of interest to determine the SAXS solution structure of the XDD/E3 complex with its lipoamide cofactors in their oxidised states as this would be predicted to form a more extended and symmetrical structure when compared to its reduced counterpart.

# Chapter 6

## Characterisation of the E2/E1 subcomplex and its constituents

### 6.1 Introduction

E2 is central to eukaryotic PDC core formation due to its self-association into a 60-meric pentagonal dodecahedron via its C-terminal domain, while the N-terminal “swinging arms” project outwards. As described in Chapter 1, in *Bacillus* and other Gram-positive bacteria E2 provides the framework for its interaction with both E1 and E3 at a stoichiometry of 1:1, as determined using surface plasmon resonance (SPR), microcalorimetry and protein crystallography (Lessard et al., 1996; Jung et al., 2002a; 2003; Frank et al., 2005). In contrast, subunit interactions in eukaryotic PDC are more differentiated due to the presence of an additional protein, E3BP. Consequently, E2 interacts specifically with E1 and has largely lost the ability to bind E3 – residual PDC activity is observed only if E3 is present in large excess (McCartney et al., 1997). Similarly, patients with E3BP deficiency display only 10-20% of normal levels of PDC activity (Robinson et al., 1990; Marsac et al., 1993; Ling et al. 1998; Brown et al., 2002).

While the *Bacillus* PDC core is capable of binding up to 60 E1 or 60 E3 molecules during reconstitution experiments (Lessard et al., 1995; 1998; Domingo et al., 1999), the maximum number of E1 molecules able to associate with the eukaryotic PDC core is 30 (Roche et al., 1993). However, the PDC core is not necessarily always fully occupied: when PDC was isolated from bovine heart muscle and kidney, differential E1 occupation was observed (Roche et al., 1993), reflecting the different metabolic requirements of the two tissues. Analogous to subcomplex formation between E3BP and E3, the reported stoichiometries for E2 and E1 within eukaryotic PDC suggest the possibility of formation of 2:1 stoichiometric subcomplexes. Thus, at maximal occupancy, 30 E1 molecules could associate with the 60-meric E2 core.

The crystal structure determined for the E1/E2-SBD subcomplex from *B. stearotheophilus* shows unequivocally that association of a second molecule of E2-SBD to E1 is not possible as the binding site for E2-SBD is located across the two-fold axis. Occupation of both binding sites on E1 would result in steric clashes in one of the loop regions (Frank et al., 2005). The association of two molecules of E2 with one heterotetramer of E1 therefore requires either a change in the location of E2-SBD binding and/or a structural change in the conformation of E2-SBD and/or E1.

E2 also provides binding sites for PDC kinase (PDK) and PDC phosphatase (PDP). While E1 associates with the E2 via its subunit binding domain (E2-SBD), both PDK and PDP interact with the inner lipoyl domain (ILD). This results in the juxtaposition of E1 and PDK/PDP in a manner ideal for the regulation of PDC activity which is controlled by the phosphorylation state of E1.

This chapter presents preliminary data for the characterisation of the subcomplex formed between native bovine E1 and a didomain construct of E2 (E2DD) analogous to XDD (Fig. 5.1) consisting of the inner LD and the SBD. Both proteins were also analysed individually *in vitro*. In addition, the stoichiometry and affinity of the interaction of E1 with E2DD was investigated using AUC and ITC. A low resolution structure of the E2DD/E1 complex was obtained from SAXS.

## 6.2 Materials and methods

### 6.2.1 Sample preparation

Individual proteins were purified as outlined in Section 4.2.3. E2DD/E1 complex was reconstituted from the purified proteins at a stoichiometric ratio of 3:1 (E2DD:E1) using a final size exclusion step on a Sephacryl S-300 column (Amersham, USA) in MEB buffer to remove unbound E2DD. For details of all buffers used refer to Section 4.2.3.

### 6.2.2 Gel filtration analysis

Gel filtration chromatography (GFC) was employed to obtain estimates of the relative molecular weights of E1, E2DD and purified E2DD/E1 complex. A Sephacryl S-300 column (Amersham, USA) was standardised with a range of GFC protein markers (Sigma, USA). Blue dextran was used to determine the void volume,  $V_0$ . The logarithms of protein molecular weights were plotted versus the ratio of elution volume to void volume ( $V_e/V_0$ ) to produce a standard curve.

### 6.2.3 Sedimentation velocity analytical ultracentrifugation

SV experiments were performed as described in Section 3.4.2. Purified E2DD was dialysed against TEB and sedimentation data recorded at 4°C at a rotor speed of 49000 rpm, using both interference and absorbance optics in separate experiments. A series of 150 scans, 15 minutes apart with a step size of 0.001 cm in continuous mode was recorded at 278 nm for each sample using absorbance optics. A total of 400 scans, 1 minute apart, was recorded using interference optics. Sample concentrations ranged from 8.5  $\mu\text{M}$  to 84.9  $\mu\text{M}$ . The samples (380  $\mu\text{l}$ ) were loaded into 12 mm double sector centrepieces.

Purified bovine E1 was dialysed against PEB and sedimentation data recorded at 4°C at a rotor speed of 45000 rpm, using both interference and absorbance optics in separate experiments. A series of 100 scans, 11 minutes apart, was recorded for each sample at 278 nm with a step size of 0.002 cm in continuous mode using absorbance optics. A total of 500

scans, 1 minute apart, was recorded using interference optics. Sample concentrations ranged from 1.2  $\mu\text{M}$  to 5.9  $\mu\text{M}$ . The samples (380  $\mu\text{l}$ ) were loaded into 12 mm double sector centrepieces.

For the analysis of stoichiometric E2DD:E1 mixtures, samples were prepared by keeping the concentration of E1 fixed at 2.3  $\mu\text{M}$  and varying the E2DD concentrations accordingly to achieve E2DD:E1 ratios of 4:1 to 1:3. Samples were dialysed extensively against PEB prior to data acquisition. A rotor speed of 45000 rpm was selected and absorbance and interference optics scans were collected at 4°C in separate experiments. A series of 100 scans, 11 minutes apart, was recorded for each sample at 278 nm with a step size of 0.002 cm in continuous mode using absorbance optics. A total of 500 scans, 1 minute apart, was recorded using interference optics. The samples (380  $\mu\text{l}$ ) were loaded into 12 mm double sector centrepieces. SV analysis of the purified E2DD/E1 complex was conducted as described above for the E2DD:E1 stoichiometric mixtures and covered a concentration range of 1-5  $\mu\text{M}$ .

Sedimentation profiles were analysed with the computer program SEDFIT (Schuck, 2000) (see Sections 2.2.1.1 and 3.4.2 for details). Finite element analysis in SEDFIT was also used to determine the true sedimentation coefficients of all samples. These were extrapolated to infinite dilution to give a sedimentation coefficient independent of concentration,  $s_{20,w}^0$ .

### 6.2.4 Sedimentation equilibrium analytical ultracentrifugation

SE data were collected for E2DD and purified E2DD/E1 complex using interference optics. All samples used for the collection of SE data had been subjected to SV analysis first and the same buffer conditions were used. Details of the experimental set-up can be found in Table 6.1 and Section 3.4.3. Attainment of equilibrium was ascertained with WinMATCH ([www.biotech.uconn.edu/auff/](http://www.biotech.uconn.edu/auff/)). SE data were analysed using single experiment and global analysis in the Beckman XL-A/XL-I software implemented in MicroCal ORIGIN. Alternatively, multi-speed analysis (fitting each sample concentration singly as well as globally) in SEDPHAT (Vistica et al., 2004) as described in Sections 2.2.2.1 and 3.4.3 was used. In order to determine the molecular weight of samples independent of concentration,

$M_w^0$ , the whole cell, weight-average molecular weights,  $M_{w,app}$ , determined for each sample concentration were extrapolated to infinite dilution.

Protein	Speed (rpm)	Centrepiece	Thickness (mm)	Volume ( $\mu$ l)	Replicates	Step size (cm)
E2DD	26500 32000	Double sector	12	120	15	0.001
E2DD/E1	9000 12500 15000	Double sector	12	120	20	0.001

**Table 6.1** Summary of parameters used for sedimentation equilibrium experiments

### 6.2.5 Isothermal titration calorimetry

E2DD and E1 were dialysed overnight in MEB. E2DD at a concentration of 386  $\mu$ M was injected in 10  $\mu$ l aliquots into the reaction cell containing 22  $\mu$ M E1 at 25°C. Data were analysed using non-linear regression in the MicroCal ORIGIN software package, assuming a simple binding model (see Section 3.4.4). ITC experiments were performed by Mrs. Margaret Nutley in the laboratory of Prof. Alan Cooper, University of Glasgow.

### 6.2.6 Small angle x-ray scattering and *ab initio* modelling

SAXS data for E1, E2DD and E2DD/E1 were collected at beamline 2.1 of the SRS Daresbury, UK. A protein concentration of 1.0 mg/ml was used for E1 data collection. E2DD scattering curves were obtained for concentrations of 2.7, 12.0 and 16.8 mg/ml, while E2DD/E1 data were recorded for concentrations of 3.4, 7.0 and 13.8 mg/ml. Two camera lengths (4.25 m and 1 m) were used; only the highest concentration sample of each protein was recorded at the shorter sample-to-detector distance of 1 m. More details can be found in section 3.4.5.

The program DAMMIN (Svergun et al., 1999) was used for *ab initio* reconstruction of the E2DD/E1 subcomplex. No symmetry was imposed during the modelling process. More details on *ab initio* modelling can be found in Section 2.4.2.3.

### 6.2.7 Homology and hydrodynamic modelling

A homology model of human E2-SBD was obtained as described in Section 3.5.2. In order to obtain a model of the human E2DD/E1 complex the crystal structure obtained for the E2-SBD/E1 complex from *B. stearothermophilus* (Frank et al., 2005) (PDB ID 1W85) was used as a template. Models of E2DD/E1 with lipoyl domains in different positions were generated (see Section 6.3.3.5) and superimposed onto the *ab initio* model using the program SITUS (Wriggers & Chacón, 2001; Wriggers & Birmanns, 2001).

## 6.3 Results and analysis

### 6.3.1 Characterisation of E1

#### 6.3.1.1 Analytical ultracentrifugation and hydrodynamic modelling of E1

Sedimentation velocity experiments (Fig. 6.1) show that the preparation of E1 used in this project was not monodisperse. E1 was purified using gel filtration (Section 4.3.3.6) in order to remove any aggregate present. SDS PAGE analysis of the purification (Section 4.3.3.6) did not reveal any contamination of the sample visible by staining with Coomassie. The minor peaks shown in the E1  $c(s)$  distribution (Fig. 6.1A) therefore must correspond to dissociation and possibly degradation products as well as protein aggregate of E1 formed over time. The main species is E1 with an apparent sedimentation coefficient,  $s_{app}$  of 7.8 S. The two smaller peaks may correspond to separate E1 $\alpha$  and  $\beta$  subunits and  $\alpha\beta$  heterodimers, respectively. The difference in molecular weight of the two subunits is only 4.3 kDa and they are therefore expected to form overlapping peaks.

Finite element analysis was used to determine the true sedimentation coefficient for E1. Each data set was fitted with a model of 3–4 non-interacting species depending on E1 concentration and the  $c(s)$  distribution. These were then extrapolated to infinite dilution to give  $s_{20,w}^0 = 7.88 \pm 0.11$  S (Fig. 6.1B). As the crystal structure for human E1 has been solved (Ciszak et al., 2003), its sedimentation coefficient was calculated using the program HYDROPRO (García de la Torre et al., 2000; 2001) to be 8.3 S. This value is somewhat higher than that determined experimentally for bovine E1. As the bovine and human enzymes are thought to be very closely related – no amino acid sequence is available for bovine E1 – it seems likely that the overall structure is conserved. Thus E1 must be more elongated in solution than it is in the crystal structure, which could be a consequence of crystal packing effects. Both the experimental and calculated sedimentation coefficient for human E1 are lower than that of a hydrated sphere of equivalent mass ( $s = 8.6$  S), also indicating an increase in the hydrodynamic radius.

Due to the heterogeneity of the E1 preparation sedimentation equilibrium experiments were not conducted. Despite recent advances in SE data analysis that allow fitting of more than one component, most programs cannot satisfactorily model an experimental system consisting of more than three or four species. Similarly, SAXS data obtained for E1 could not be analysed due to sample heterogeneity.

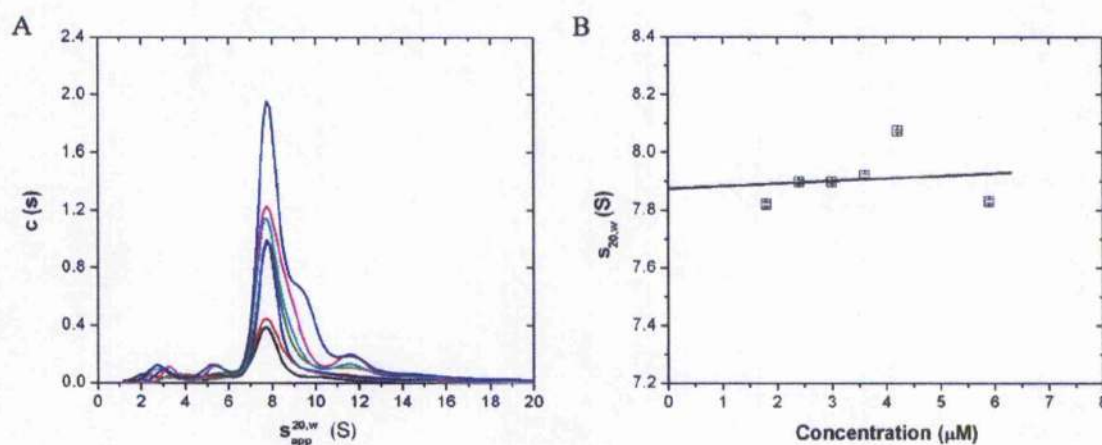


**Figure 6.1 Sedimentation velocity analysis of bovine E1**

(A)  $c(s)$  distribution derived from SV interference data collected for a range of E1 concentrations (— 1.2  $\mu\text{M}$ , — 1.8  $\mu\text{M}$ , — 2.4  $\mu\text{M}$ , — 3.0  $\mu\text{M}$ , — 3.6  $\mu\text{M}$ , — 4.2  $\mu\text{M}$ , — 5.9  $\mu\text{M}$ ). (B) Determination of  $s_{20,w}^0$  from E1 data recorded using interference optics.

## 6.3.2 Characterisation of E2DD

### 6.3.2.1 Analytical ultracentrifugation of E2DD

SV data show that E2DD is monodisperse over a large range of concentrations (Fig. 6.2A). Finite element analysis of the SV data with a single species yields the true sedimentation coefficients for E2DD at all experimental concentrations. These were then extrapolated to infinite dilution to give  $s_{20,w}^0 = 1.77 \pm 0.01$  S (Fig. 6.2B). Again, the value obtained for the E2DD sedimentation coefficient is lower than that calculated for a hydrated sphere of equivalent mass ( $s = 2.4$  S). This result agrees well with previous observations for XDD (see Section 5.3.2) and reports in which the linker region has been described as a flexible, yet extended structure (Green et al., 1992). The elongated structure of E2DD was therefore expected and confirms observations from size exclusion chromatography (see Section 6.3.3.2).

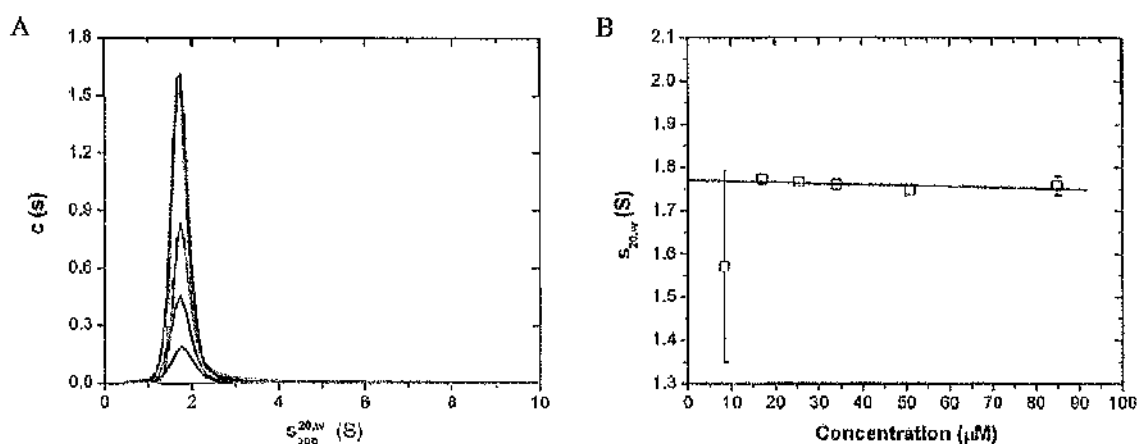


**Figure 6.2** Sedimentation velocity analysis of E2DD

(A)  $c(s)$  distribution derived from SV interference data collected for a range of E2DD concentrations ( $\sim 8.5 \mu\text{M}$ ,  $\sim 17.0 \mu\text{M}$ ,  $\sim 25.5 \mu\text{M}$ ,  $\sim 34.0 \mu\text{M}$ ,  $\sim 50.9 \mu\text{M}$ ). (B) Determination of  $s_{20,w}^0$  from E2DD data recorded using interference optics.

SE data obtained for E2DD show a small decrease in its apparent whole cell, weight-average molecular weight,  $M_{w,app}$  with increasing sample concentration, possibly indicative of non-ideality due to the elongated shape of the molecule (Fig. 6.3). The molecular weight of E2DD independent of concentration,  $M_w^0$  was determined to be  $27.5 \pm 1.4$  kDa, which is somewhat higher than the molecular weight predicted from its amino acid composition of 23.9 kDa.

Similarly, the apparent molecular weight of E2DD obtained from global analysis with a single species was  $27.3 \pm 4.0$  kDa. Fitting including a second species was unsuccessful and does not seem warranted given the monodispersity of E2DD determined by sedimentation velocity.

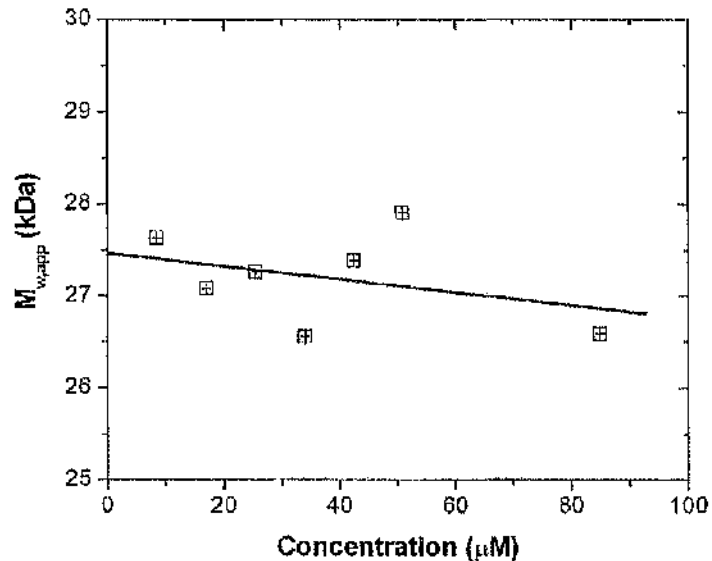


**Figure 6.3** Sedimentation equilibrium analysis of E2DD

$M_{w,app}$  was determined for each sample and extrapolated to zero concentration. Data from the same cell but recorded at different rotor speeds were analysed simultaneously using the multi-speed equilibrium routine in SEDPHAT with a single species model.

### 6.3.2.2 Small angle x-ray scattering of E2DD

SAXS analysis of E2DD was problematic, due to the formation of aggregate species as can be seen from the steep slope of the scattering curve at very low angles (Fig. 6.4). Individual frames were always checked for x-ray induced aggregate formation (see Section 3.4.5), but no such process could be detected. Therefore, it seems reasonable to suppose that aggregates formed prior to x-ray exposure as a consequence of protein concentration, even though no aggregation was observed in AUC experiments.

The data could not be fitted satisfactorily with GNOM (Semenyuk & Svergun, 1991; Svergun, 1992), especially at low angles, which is another indication that the sample was not

monodisperse. Using Guinier analysis, the radius of gyration,  $R_g$  was determined to be  $84 \pm 11 \text{ \AA}$  and  $97 \pm 6 \text{ \AA}$  for sample concentrations of 2.7 mg/ml and 12 mg/ml, respectively. This value is much larger than expected for E2DD and another indicator of aggregate formation; in comparison, monodisperse XDD, a molecule of similar molecular weight and shape has an  $R_g$  of only 27  $\text{\AA}$ . Due to these problems *ab initio* modelling of E2DD was not possible.

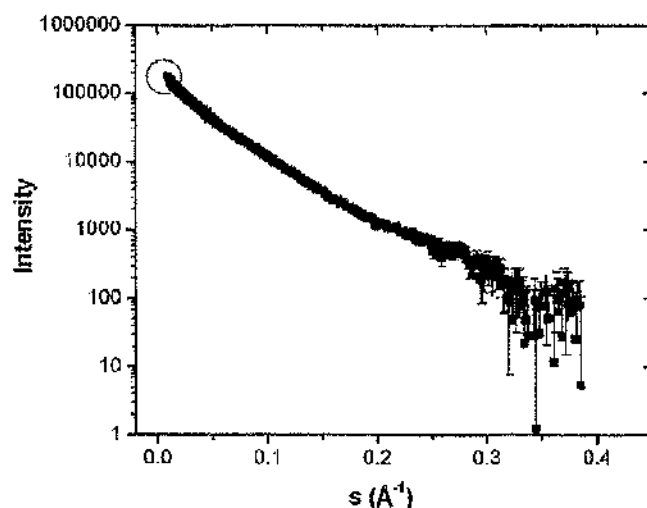


**Figure 6.4** Small angle x-ray scattering curve of E2DD

The region of the scattering curve indicative of the presence of aggregate species is circled (—).

### 6.3.3 Cross-bridge formation between E2DD and E1

#### 6.3.3.1 Generation of the E2DD/E1 complex

The E2DD/E1 complex was reconstituted from purified proteins at a ratio of 3:1 (E2DD:E1). Due to the large difference in molecular weight between the E2DD/E1 complex and E2DD, the two species were easily separated by size exclusion chromatography (Fig. 6.5A) where aggregated material eluted from the column first, followed by the E2DD/E1 complex and uncomplexed E2DD. The E2DD/E1 complex is more stable than either protein on its own. However, both proteins are prone to degradation.

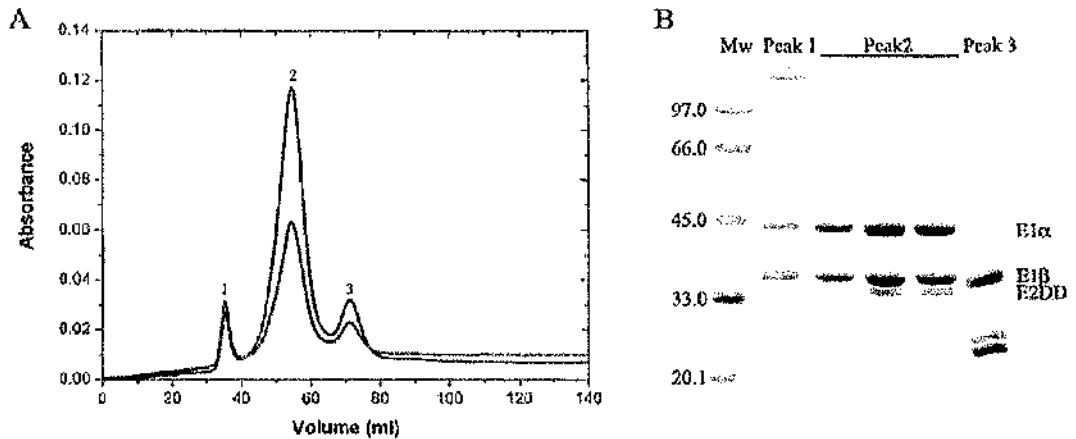


### Figure 6.5 Generation of the E2DD/E1 complex

(A) Gel filtration chromatography (GFC) of E2DD/E1. The peaks corresponding to aggregate (1), E2DD/E1 (2) and E2DD (3) are indicated. Protein absorbance was recorded at 280 nm (—) and 260 nm (---). (B) The protein peaks obtained from GFC were analysed by SDS PAGE. The positions of the E1 subunits and E2DD are indicated. Molecular weights (Mw) are shown in kDa.

#### 6.3.3.2 Gel filtration analysis of E2DD/E1 and its constituents

When compared to the standard curve (Fig. 6.6) the molecular weights of all proteins exceed their molecular weights predicted from their amino acid sequences. The apparent molecular weights,  $M_{v,app}$ , of E2DD, E1 and the E2DD/E1 complex ( $\approx 62$  kDa, 250 kDa and 320 kDa, respectively) far exceed their predicted molecular weights (24 kDa, 152 kDa and 200 kDa, respectively). This is indicative of their anisotropic shapes and consequently enlarged hydrodynamic radii when compared to globular proteins of similar molecular weights. This result is in agreement with data obtained for E2DD (see Section 6.3.2), E1 (see Section 6.3.1) and E2DD/E1 (see below) by AUC and SAXS.

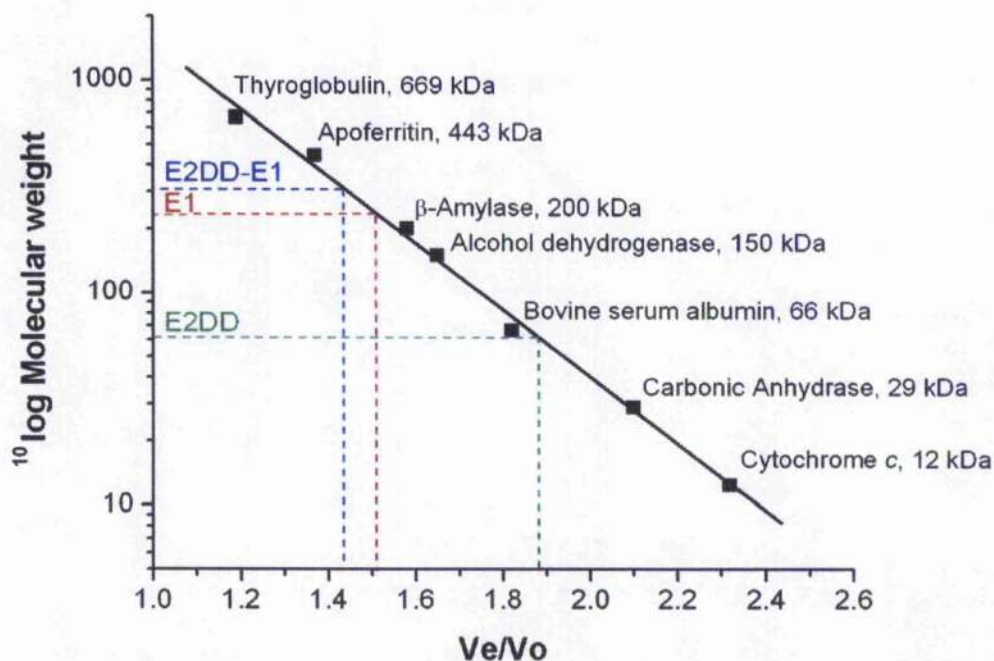


**Figure 6.6 Molecular weight estimation using gel filtration chromatography**

A Sephacryl S-300 gel filtration column was standardised using globular proteins of known molecular weights. The logarithm of the molecular weights was plotted versus the ratio of elution to void volume ( $V_e/V_o$ ) in order to obtain a standard curve. The elution positions of E2DD, E1 and the E2DD/E1 complex are indicated.

### 6.3.3.3 Analytical ultracentrifugation of E2DD/E1

Sedimentation velocity (SV) experiments were conducted for uncomplexed E1 and E2DD and different E2DD:E1 stoichiometries and the sedimentation profiles fitted using  $c(s)$  analysis in SEDFIT (Schuck, 2000). The  $c(s)$  profiles of free E2DD and E1 show one main peak with an apparent sedimentation coefficient of 2.0 S and 7.8 S, respectively (Fig. 6.7A,C). However, several minor peaks are apparent for both proteins in the  $c(s)$  profile derived from interference data (Fig. 6.7D), while a second peak for E1 is observed in the analysis of the absorbance data (Fig. 6.7B). The absorbance data in Fig. 6.7B clearly show the complete disappearance of the E2DD peak at a stoichiometry of 2:1, analogous to the results obtained for XDD/E3. The E1 and E2DD/E1 peaks overlap completely, although the peak position is slightly shifted to an apparent sedimentation coefficient of 7.3 S for E2DD/E1. The interference data present a

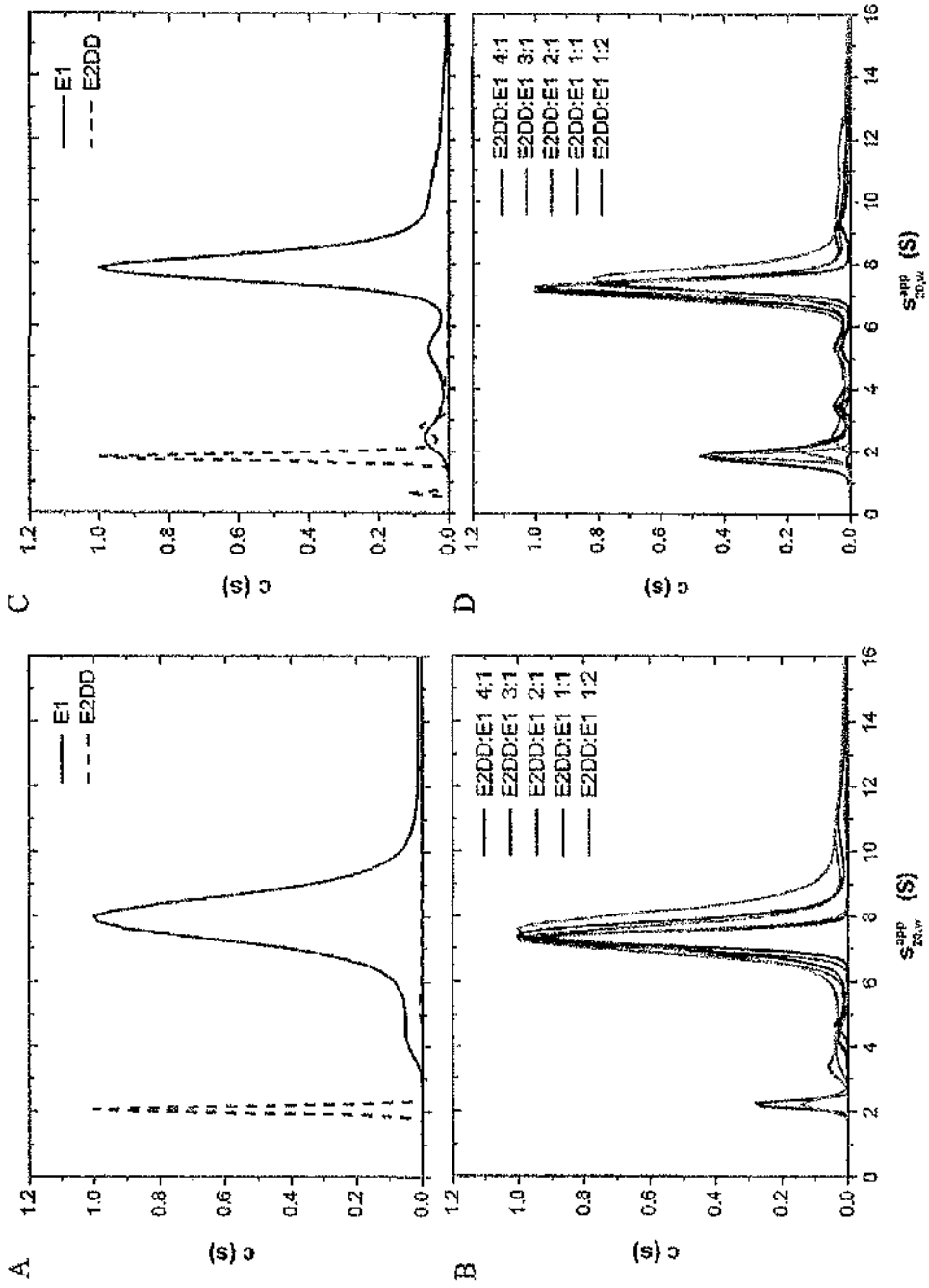


**Figure 6.7 Sedimentation velocity analysis of E2DD:E1 stoichiometric mixtures**  
 $c(s)$  distribution derived from SV absorbance data collected for uncomplexed E2DD and E1 (A) and different E2DD:E1 stoichiometric mixtures (B).  $c(s)$  distribution derived from SV interference data collected for uncomplexed E2DD and E1 (C) and E2DD:E1 stoichiometric mixtures (D).

more complex picture: a small E2DD peak remains at a stoichiometry of 2:1 (E2DD:E1) (Fig. 6.7D) and only disappears at a ratio of 1:1 (E2DD:E1). However, this discrepancy is due to not all of the E1 being binding competent as evidenced by the existence of two minor peaks and one large peak. Therefore, not all of the E2DD can participate in complex formation. E2DD has a comparatively low molar extinction coefficient at 278 nm ( $\epsilon = 9800 \text{ M}^{-1}$ ) and its residual signal is too low for detection with absorbance optics at the concentrations used in these AUC studies. In addition, the main peak in the 1:1 (E2DD:E1) sample is shifted slightly to the right with respect to samples containing excess E2DD, indicative of the presence of both E2DD/E1 complex and uncomplexed E1. A globular protein of higher molecular weight is expected to sediment faster (and therefore have a higher sedimentation coefficient) than a protein of lower molecular weight. Therefore, it can be inferred that the complex has an extended shape which offsets the gain in molecular weight with respect to free E1, and causes it to sediment at roughly the same speed as E1, confirming previous observations from gel filtration chromatography (see Section 6.3.3.2). The same conclusion can be drawn from comparison of the apparent sedimentation coefficient of E2DD/E1 (7.3 S) with  $s$  calculated for a hydrated sphere of the same molecular weight and partial specific volume as the complex ( $s = 10.3 \text{ S}$ ).

Several minor species that do not correspond to either uncomplexed E2DD or E1 were observed at all stoichiometries. They correspond to a complex mixture of dissociated and aggregate species, but can be significantly reduced if the complex is purified to uniformity by gel filtration prior to AUC analysis (Fig. 6.8A).  $c(s)$  analysis of SV profiles from the purified complex also show that a single species is present in solution bar small amounts of dissociation products and aggregate which are, however, negligible when compared to the total amount of protein. No free protein or intermediates are observed at any concentration, in accordance with the expected tight interaction between E2DD and E1. Finite element analysis with three discrete species yields the true sedimentation coefficients for E2DD/E1 at all experimental concentrations. These were then extrapolated to infinite dilution to give a sedimentation coefficient for E2DD/E1 independent of concentration,  $s_{20,w}^0$  of  $7.36 \pm 0.06 \text{ S}$  (Fig. 6.8B).

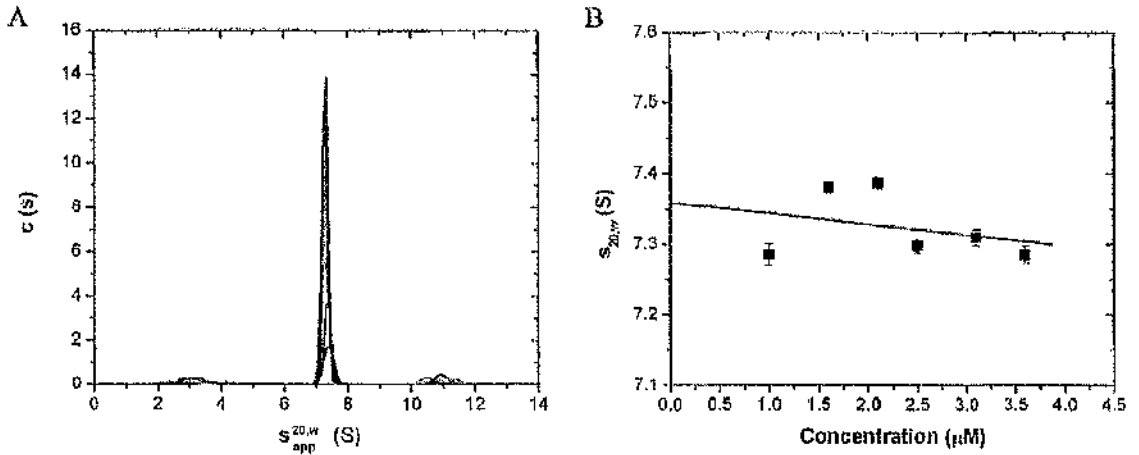


**Figure 6.8 Sedimentation velocity analysis of purified E2DD/E1 complex**

(A)  $c(s)$  distribution derived from SV interference data collected for a range of E2DD/E1 complex concentrations ( $\sim 1.0 \mu\text{M}$ ,  $\sim 1.6 \mu\text{M}$ ,  $\sim 2.1 \mu\text{M}$ ,  $\sim 2.4 \mu\text{M}$ ,  $\sim 3.1 \mu\text{M}$ ,  $\sim 3.6 \mu\text{M}$ ). (B) Determination of concentration independent  $s_{20,w}^0$  from the E2DD/E1 complex data recorded using interference optics.

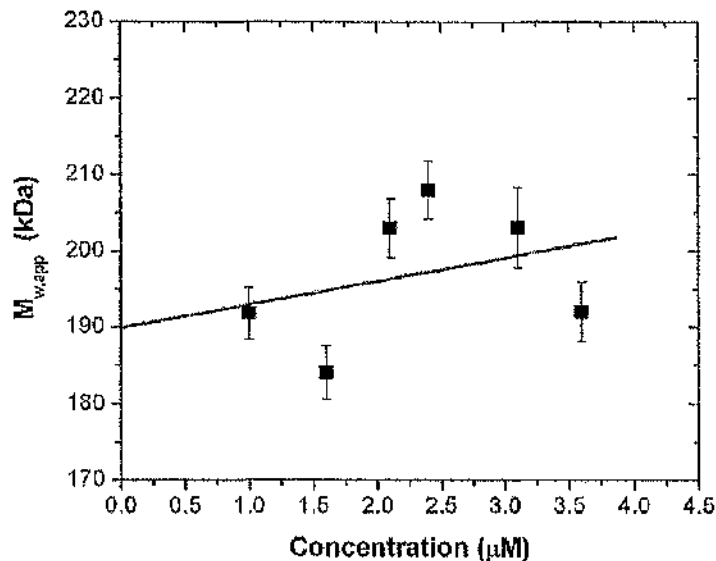


**Figure 6.9 Sedimentation equilibrium analysis of purified E2DD/E1 complex**

$M_{w,app}$  was determined for each sample and extrapolated to zero concentration. Data from the same cell but recorded at different rotor speeds were analysed simultaneously using the multi-speed equilibrium routine in SEDPHAT with a single species model.

Due to the presence of several other species apart from E2DD/E1 and uncomplexed E2DD or E1, sedimentation equilibrium (SE) experiments of the stoichiometric E2DD:E1 mixtures were not performed as the data analysis was deemed too unreliable. Instead, the purified E2DD/E1 complex was subjected to SE analysis which confirmed the 2:1 stoichiometric complex formation as its molecular weight was determined to be  $190 \pm 11$  kDa (Fig. 6.9), in good agreement with the value predicted from the E1 and E2DD amino acid sequences (200 kDa). Analysis of the individual SE data sets using a single species model in SEDPHAT (Schuck, 2003; Vistica et al., 2004) shows an increase in the apparent whole cell, weight-average molecular weight,  $M_{w,app}$  with increasing E2DD/E1 concentration, indicative of aggregate formation. Indeed, using global analysis and fitting of a second component, the molecular weight of the main species was  $199 \pm 4$  kDa while the second species was determined to be  $676 \pm 9$  kDa. Aggregate probably formed during SE data acquisition due to the long experimental times required, as no appreciable amount of aggregate was formed during sedimentation velocity studies (Fig. 6.8A).

#### 6.3.3.4 Isothermal titration calorimetry

An initial attempt to determine the strength of the E2DD/E1 interaction was made using ITC. Measuring the heats of interaction of E2DD with E1, complex formation was found to be exothermic, i.e. the peaks in the ITC output are negative (Fig. 6.10A). A differential thermal binding curve was obtained by integration of the data and analysed using standard non-linear regression (Fig. 6.10B) in order to obtain estimates of the binding stoichiometry, equilibrium association constant ( $K_a$ ) and enthalpy of binding ( $\Delta H$ ). The data confirm the tight binding of E2DD to E1 ( $K_a = 9.88 \times 10^7 \text{ M}^{-1}$ ), although the analysis relies on too few data points and is near the limit ( $K_a \geq 10^8 \text{ M}^{-1}$ ) of accurate determination. Binding is characterised by a large, favourable enthalpy change ( $\Delta H = -10.2 \text{ kcal/mol}$ ) and a small positive entropy change ( $T\Delta S = 0.72 \text{ kcal/mol}$ ). The stoichiometry of binding of 0.3 (E2DD:E1), i.e. 3 molecules of E2DD are bound per 10 molecules of E1, is much lower than expected. This result was completely unexpected and probably caused by the non-specific aggregation of E1 prior to and during ITC. Aggregation was obvious from visual inspection of the sample at the end of the experiment. Since the affinity of E2DD for E1 is extremely high it should be possible to use

much lower concentrations of E1 in a repeat experiment which will hopefully substantially reduce, if not eliminate, E1 aggregation.

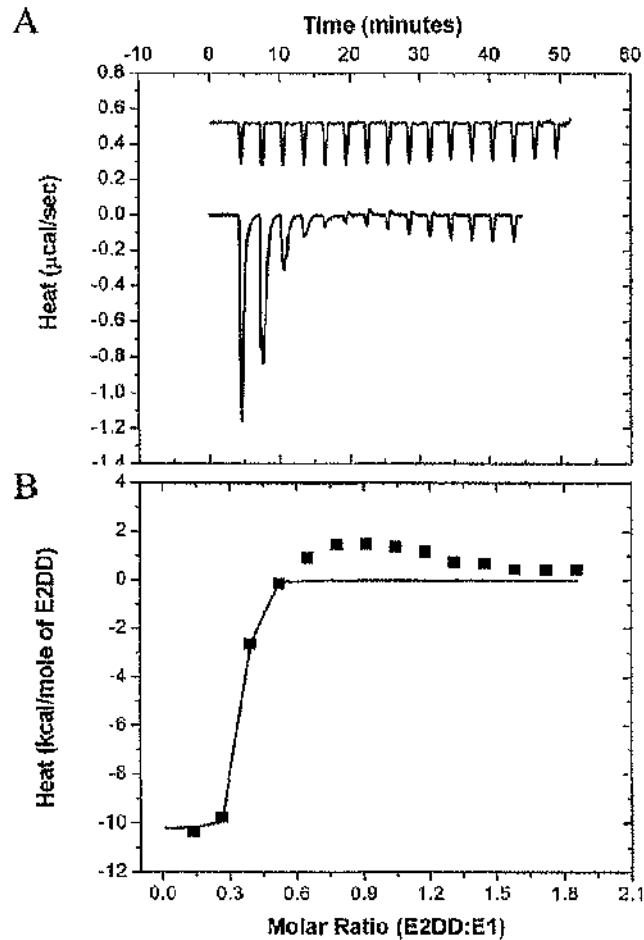


**Figure 6.10 Isothermal titration calorimetry of E2DD and E1**

(A) Raw data obtained from a series of 10 µl injections of E1 into E2DD at 25°C. (B) Binding isotherms created by plotting the areas under the peaks in (A) against the molar ratio of E2DD injected. The best fit shown was obtained by least-squares fitting using a simple binding model and gives a stoichiometry of 0.3 (E2DD:E1).

### 6.3.3.5 Homology modelling of E2DD/E1

Homology modelling was used in combination with AUC and SAXS (see below) to gain more insight into the E2DD/E1 structure. A model of the E2DD/E1 complex was built from

atomic structures solved for human E1 (Ciszak et al., 2003), the human E2-ILD (Howard et al., 1998) and a homology model of the E2-SBD. The structure of the *B. stearotherophilus* E2-SBD/E1 complex (Frank et al., 2005) was used to position E1 and E2-SBD with respect to each other. The second E2-SBD molecule was positioned exploiting the two-fold symmetry axis of E1. Several models with different positioning of LD1 and LD2 were generated (Fig. 6.11), while taking into account known overall dimensions of the PDC: all lipoyl domains were located approximately 60 Å from the SBDs, sampling three different orientations with respect to E2-SBD/E1. Two models have similar  $D_{max}$  values of ca. 200 Å, but E2DD/E1 $_{\gamma}$  is somewhat smaller with a  $D_{max}$  of ca. 185 Å.

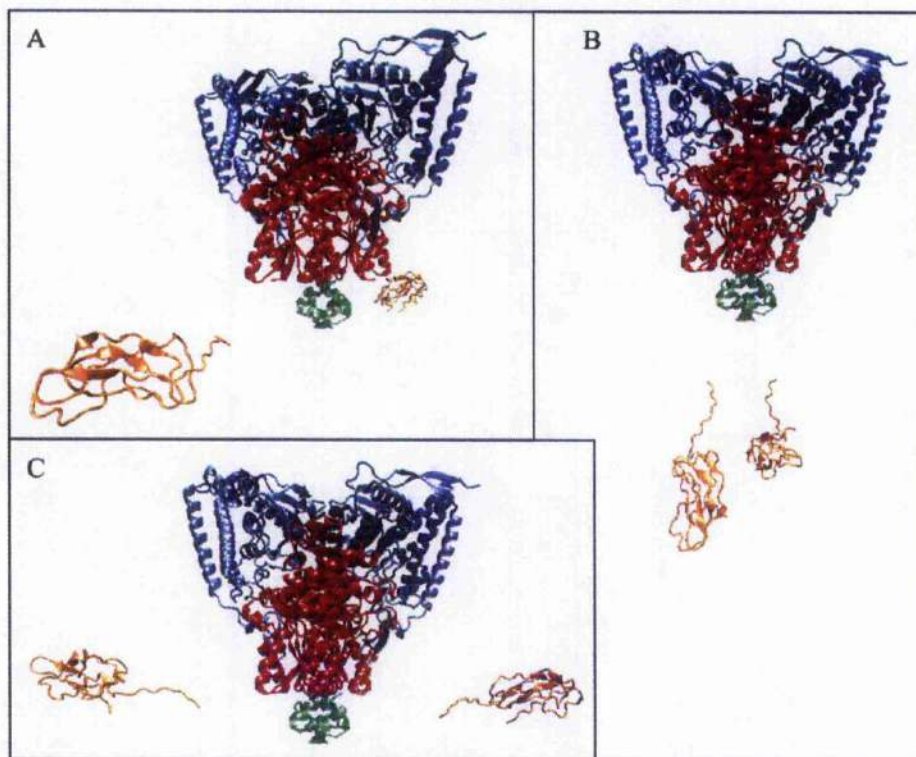


**Figure 6.11** Models of the human E2DD/E1 complex

E2DD/E1 $_z$  (A), E2DD/E1 $_{\gamma}$  (B) and E2DD/E1 $_x$  (C). Only the LDs (orange) are present in different positions. The other subunits shown are E1 $_{\alpha}$  (blue), E1 $_{\beta}$  (red) and the E2-SBD (green). Due to a lack of structural information, the linker regions could not be fully modelled.

### 6.3.3.6 Small angle x-ray scattering of E2DD/E1

SAXS curves for purified E2DD/E1 complex were acquired at three protein concentrations to account for the effects of interparticle interference (Fig. 6.12A). The radius of gyration,  $R_g$  determined using the Guinier approximation, is  $56 \pm 2 \text{ \AA}$ . The particle distribution function,  $p(r)$  is shown in Fig. 6.12B. The  $D_{\max}$  is  $175 \pm 5 \text{ \AA}$  and  $R_g$  calculated from the  $p(r)$  function is  $53 \pm 1 \text{ \AA}$  which agrees well with the value obtained using the Guinier approximation.

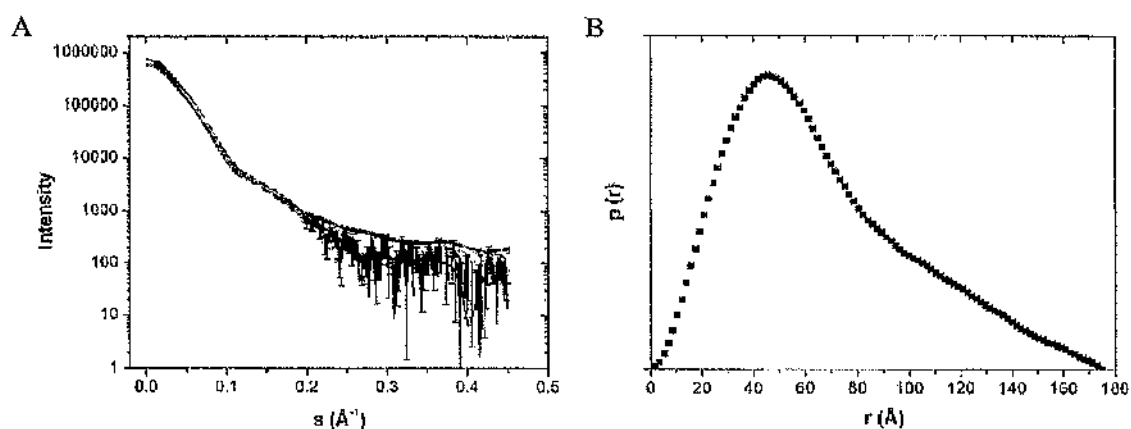


**Figure 6.12** Small angle x-ray scattering of E2DD/E1

(A) The scattering curve recorded for E2DD/E1 (—). The shape scattering curve from GNOM (---) and CRY SOL scattering curves calculated for E2DD/E1<sub>x</sub> (· · ·), E2DD/E1<sub>y</sub> (---) and E2DD/E1<sub>z</sub> (—) are also shown. (B) The distance distribution function  $p(r)$  was calculated using GNOM. Error bars are shown but are too small to be visible.

*Ab initio* shape restoration produced an elongated, asymmetric structure (Fig. 6.13). Of three rough initial models (Fig. 6.11) with LDs in different positions with respect to E1, only one (E2DD/E1<sub>y</sub>) can be superimposed satisfactorily onto the *ab initio* model (Fig. 6.13). However, even this superimposition leaves considerable parts of the model outwith the recorded electron density (Fig. 6.13A-C). The model can only be fully covered if the density corresponding to all 12 *ab initio* reconstructions is shown (Fig. 6.13D,E). The reason why the models are essentially too small is unclear. It is interesting to note, however, that the scattering intensity at zero angle,  $I(0)$  of the three E2DD/E1 models calculated with CRY SOL is somewhat lower than that obtained from a GNOM fit of the experimental data (Fig. 6.12A). Even though the E2DD/E1 models lack a number of residues from the E2DD linker region

and His-tag, these residues are not thought to contribute significantly to the scattering curve. Further experiments are required to fully elucidate the solution structure of E2DD/E1.

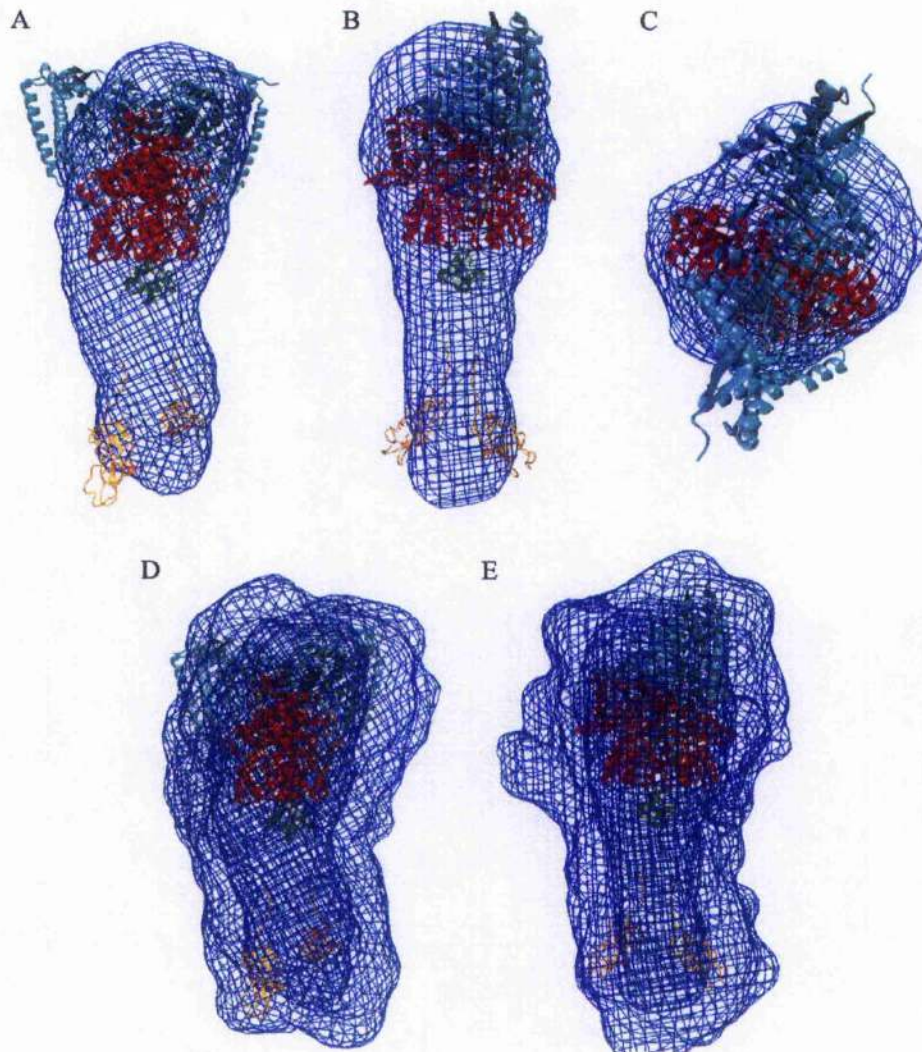


**Figure 6.13** Superimposition of E2DD/E1 and *ab initio* models

Front (A,D), side (B,E) and top views (C) of the E2DD/E1 model superimposed onto the DAMMIN *ab initio* model (blue wiremesh). Density corresponding to all superimposed DAMMIN models (outer wiremesh) is shown in (D) and (E). E1 $\alpha$  (cyan), E1 $\beta$  (red), E2SBD (green) and E2-LD (orange) are depicted.

## 6.4 Discussion

The results presented in this chapter indicate that 30 E1 heterotetramers are capable of interacting with up to 60 E2-derived constructs, forming 2:1 (E2DD:E1) stoichiometric complexes, although more experiments are required for a definitive answer. The main problem with the experimental set-up and data interpretation is the tendency of both uncomplexed E1 and E2DD to form non-specific aggregates, although the complex – especially at lower concentrations – seems to be more stable as observed by a combination of sedimentation velocity and equilibrium AUC studies.

The formation of 2:1 stoichiometric cross-bridges is in direct contrast to results obtained for the interaction of *B. stearrowthermophilus* E1 and E2-SBD as determined by surface plasmon resonance (Lessard et al., 1996) and microcalorimetry (Jung et al., 2002a; 2003). Furthermore, the crystal structure determined for the *B. stearrowthermophilus* E1/E2-SBD complex (Frank et al., 2005) shows that the SBD is bound across the two-fold axis of E1 thus preventing association of a second SBD molecule due to steric hindrance. If E2/E1 cross-bridges do indeed exist in eukaryotic PDCs, this indicates that either the nature of the interaction is different and/or a change in the local structure of the E2-SBD and/or its binding site on E1. A crystal structure of human E1 is available (Ciszak et al., 2003) and it superimposes reasonably well onto *B. stearrowthermophilus* E1 complexed with E2-SBD with an rmsd of 1.4 Å. Most differences in the backbone structure can be observed in the E1 $\alpha$  subunits, not the E1 $\beta$  subunits involved in E2 binding. However, a SAXS study conducted on a number of metabolic enzymes from various sources, including yeast pyruvate decarboxylase has shown that considerable differences can be observed between the solution structures of proteins when compared to their cognate crystal structures (Svergun et al., 2000). In particular, presumably due to the absence of crystal packing forces, the solution structure of yeast pyruvate decarboxylase was less compact (Svergun et al., 2000) – an effect that has been observed for a number of other proteins as well (Trehwella et al., 1988; Katakoka et al., 1996; Svergun et al., 1997a; Nakasako et al., 2001; Kozak et al., 2002). If human E1 behaves in a similar fashion, inter-subunit contacts are likely to be affected and a looser association of the two E1 $\beta$  subunits could result in the availability of both E2 binding sites. Obviously, more experiments are required to elucidate this question: SAXS may provide part of the answer, while NMR studies of labelled E2-SBD interacting with unlabelled E1 should be more

definitive due to the presence of an additional set of dipolar couplings arising from the interaction of the two subunit binding domains.

Interestingly, preliminary analysis of the thermodynamics involved in the interaction of human E2DD with bovine E1 is characterised by a large, favourable enthalpy change and a small, positive entropy change, and is thus remarkably similar to bacterial E1/E2-SBD complex formation (Jung et al., 2002a). Association of human XDD and E3 is also comparable, albeit resulting in a small negative entropy change (see Section 5.3.3.5). However, the ITC experiments concerning E2DD/E1 interaction clearly need to be repeated in order to obtain reliable results. Furthermore, experiments using point mutants analogous to those used by Jung et al. (2002b; 2003) could be used to characterise the association of E2DD with E1 with respect to hydrophobic and electrostatic contributions.

Current concepts of PDC subunit architecture envisage the E2/E3BP core forming the structural and mechanistic framework for the assembly to which the E1 and E3 enzymes bind tightly but non-covalently. With respect to the results presented in chapters 5 and 6, the peripherally bound E1 and E3 enzymes are precisely positioned and oriented around its surface to facilitate optimal interaction of their active sites with the lipoyl 'swinging arms' of E2/E3BP during the catalytic cycle. In this model, E1 and E3 interactions with the 'core' assembly are passive in nature in the sense that they are not predicted to have a direct influence on the operation of the E2/E3BP core. However, the existence of a previously unrecognised level of ultrastructure resulting from the presence of a network of E3 and E1 cross-bridges around the surface of the E2/E3BP oligomer is predicted to introduce a considerable degree of restraint into the movement of the N-terminal 'swinging arms' of E3BP and E2, limiting in particular the degree of freedom enjoyed by E3BP and E2 lipoyl domains (Fig. 6.14). Since LDs are, in effect, substrates for all three active sites within the PDC, this more restrictive environment highlights some interesting questions concerning PDC mechanism and efficiency. In particular, it suggests that E1 may interact exclusively or preferentially with E2 lipoyl domains while E3 may interact similarly with E3BP-LDs as substrate, so it would appear unlikely that individual E2 or E3BP LDs are able to visit all three types of active site. This new structural feature is also compatible with the idea that specific subsets of LDs visit the various active sites of the constituent enzymes and defined

routes of migration may be involved in mediating the transfer of acetyl groups and reducing equivalents between E2 and E3BP lipoyl domains during the catalytic cycle.

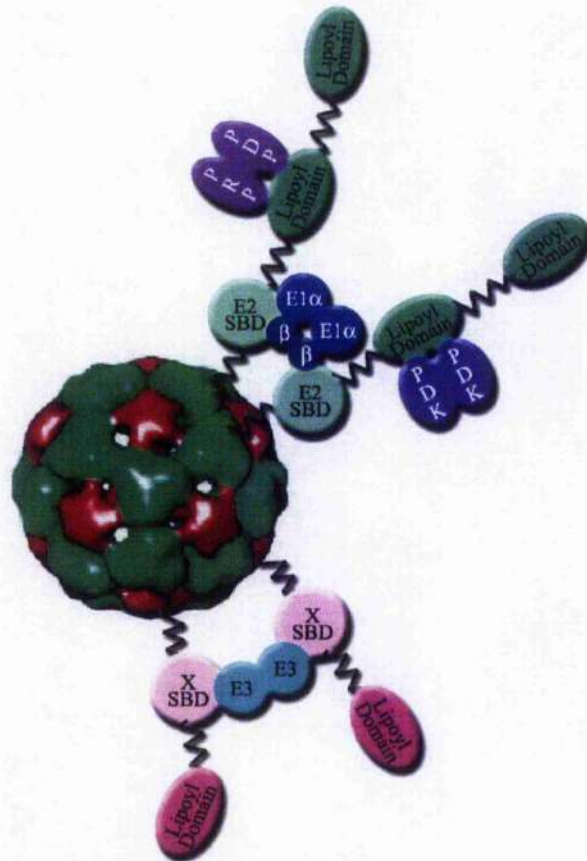


**Figure 6.14 Cross-bridge formation in human PDC**

Representative cross-bridges formed between E2 (green) and E1 (blue), and E3BP (X; magenta) and E3 (cyan) are shown. PDC kinase (PDK) and phosphatase (PDP, PRP) are also depicted. Molecules are not drawn to scale.

Another important aspect of PDC function that is influenced by its subunit organisation is regulation of its activity state by PDK and PDP. It has been reported that only 1-3 molecules of PDC kinase (PDK) are bound per complex (Yeaman et al., 1989). Both regulatory enzymes associate with the E2-ILD whereby the lipolate cofactor provides an important part of the recognition site. PDP and PDK act by de-/phosphorylation of E1 on any of three specific E1 $\alpha$  serine residues. Phosphorylation of E1 renders the complex inactive. Since only a few

molecules of PDK are present per complex, the enzyme has to migrate around the surface of the complex in order to act on the entire population of bound E1 molecules. A hand-over-hand mechanism has been proposed where the dimeric PDK molecule migrates from one inner lipoyl domain to its nearest neighbour. Its high-affinity for dimeric ILD glutathione S-transferase constructs suggests that PDK may transiently form cross-links with pairs of adjacent E2s as part of the molecular mechanism of migration (Liu et al., 1995a). Regular spacing of the E2 lipoyl domains linked by a system of E1 cross-bridges could greatly facilitate this type of movement and provide convenient access to the full repertoire of E1 substrate molecules.

# Chapter 7

## PDC core structure

### 7.1 Introduction

The PDC core of E2 (and E3BP) constitutes the central framework for interaction with the remaining PDC enzymes, E1 and E3. In Gram-negative bacteria, e.g. *E. coli*, the core adopts an octahedral conformation consisting of 24 E2 molecules. In contrast, in Gram-positive bacteria such as *B. stearothermophilus* and eukaryotes, the core is much larger, forming an icosahedron with 532 symmetry for the arrangement of its 60 E2 molecules (Reed & Oliver, 1968; Oliver & Reed, 1982; Wagenknecht et al., 1991). The crystal structure of the cores from *B. stearothermophilus* and *Enterococcus faecalis* at 4.4 Å and 4.2 Å resolution, respectively (PDB ID 1B5S) (Izard et al., 1999), provide clear insights into the structural organisation of E2 within the pentagonal dodecahedron (Fig. 1.3) where basic E2 trimers form the 20 vertices of the icosahedron and are interconnected by 30 bridges (Stoops et al., 1992; Izard et al., 1999).

Eukaryotes contain an additional core protein: E3 binding protein (E3BP), also termed protein X (De Marcucci & Lindsay, 1985; Jilka et al., 1986; Rahmatullah et al., 1989b), enabling the formation of specific subcomplexes between E3BP and E3, and E2 and E1. Using

densitometry Sanderson and colleagues (1996b) determined the stoichiometry of E2:E3BP within the bovine PDC core as 60:12. Similar results (12-15 E3BP molecules per core) were also obtained for the PDC core of *S. cerevisiae* (Maeng et al., 1994). Since an icosahedron has 12 pentagonal faces, it was proposed that one copy of E3BP was located in each face. Cryo-EM studies of yeast PDC core confirmed localisation of E3BP to each of its pentagonal faces, although it was suggested that E3BP actually bound on the inside of the PDC core near the tip of the E2 trimers, resulting in a close association of E3 with the pentagonal faces (Stoops et al., 1997).

An alternative model of mammalian PDC core formation has been proposed recently by Hiromasa and co-workers (2004) based on ultracentrifugation and SAXS studies on recombinant human E2 and E2/E3BP cores: instead of a 60:12 (E2:E3BP) "addition model" of PDC core formation the authors suggest that 12 E3BP molecules replace an equivalent number of E2 molecules, resulting in a stoichiometry of E2:E3BP of 48:12 ("substitution model").

The work described in this chapter sets out to identify experimental approaches that will enable us to define PDC core organisation. Several experimental techniques including analytical ultracentrifugation (AUC), small angle x-ray and neutron scattering (SAXS/SANS) were used for an initial characterisation of recombinant human PDC core. Where possible, the behaviour of recombinant human E2/E3BP core was compared to results obtained for native bovine core and intact bovine PDC.

## **7.2 Materials and methods**

### **7.2.1 Sample preparation**

Recombinant human E2/E3BP (E2/E3BP) core was purified as outlined in Section 4.2.3. Bovine PDC was obtained from heart muscle tissue as described in Section 3.3.2.7 and was also used to purify bovine E2/E3BP core (Sections 4.2.3). Purification procedures for E3 are also detailed in Sections 3.3.2 and 4.2.3.

## 7.2.2 Sedimentation velocity

Sedimentation velocity (SV) experiments were performed as described in Section 3.4.2. Purified recombinant human E2/E3BP core was dialysed against 50 mM Tris-HCl, 10 mM NaCl, pH 7.5 and sedimentation data recorded at 4°C at a rotor speed of 40000 rpm using interference optics only. A series of 450 scans, 30 seconds apart was recorded for each sample. Sample concentrations ranged from 52 nM to 194 nM. The samples (380 µl) were loaded into 12 mm double sector centrepieces. Sedimentation profiles were analysed with the  $c(s)$  routine in the computer program SEDFIT (Schuck, 2000). Weight-average sedimentation coefficients,  $s_w$ , were determined by peak integration of the  $c(s)$  profile. True sedimentation coefficients were obtained from finite element analysis (see Sections 2.2.2.1 and 3.4.2 for details).

## 7.2.3 Small angle scattering

### 7.2.3.1 Small angle x-ray scattering

Scattering data for human E2/E3BP core, bovine E2/E3BP core and bovine PDC were recorded at beamline 2.1 of the SRS Daresbury, UK. A protein concentration of 1.8 mg/ml was used for the collection of human E2/E3BP data. Scattering curves of bovine E2/E3BP core were obtained from concentrations of 0.8 and 1.6 mg/ml, while data for bovine PDC were recorded for concentrations of 0.8, 2.3 and 4.2 mg/ml. A single sample-to-detector distance of 4.25 m was used for the collection of human and bovine E2/E3BP core data, while an additional camera length of 1 m was employed to obtain scattering data from bovine PDC.

The program DAMMIN (Svergun, 1999) was used for *ab initio* reconstructions of human E2/E3BP, bovine E2/E3BP and bovine PDC. Since the icosahedral symmetry of eukaryotic PDC is well documented, DAMMIN reconstructions were done using icosahedral symmetry restraints. More details on *ab initio* modelling can be found in Section 2.4.2.3.

### 7.2.3.2 Small angle neutron scattering

Deuterated, recombinant human E2/E3BP core was provided by Dr. Phil Callow, Institut Laue-Langevin (ILL), Grenoble, France. Both protonated and deuterated human core were

purified as described in Section 4.2.3. E2/E3BP was reconstituted at a molar ratio of 12:1 with protonated E3 and extensively dialysed against buffer containing 50 mM potassium phosphate, pH 7.4. Deuterated core samples (0.75 mg/ml) were dialysed against buffer containing 40, 60 and 100% D<sub>2</sub>O. Samples containing protonated core (1.25 mg/ml) were dialysed against buffer containing 25, 40, 60 and 100% D<sub>2</sub>O. SANS datasets were collected on beamline D11 station at the ILL by Dr. Phil Callow. All experiments were performed at 4°C. Details of data collection and analysis can be found in Section 3.4.6.

## 7.3 Results and discussion

### 7.3.1 Sedimentation velocity of recombinant E2/E3BP core

Sedimentation velocity data from human E2/E3BP core clearly show the heterogeneous composition of the protein sample (Fig. 7.1A). Weight-average sedimentation coefficients,  $s_w$ , were determined to be 5, 11, 27 and 35 S by integration of each peak in the  $c(s)$  analysis. Finite element analysis was used to obtain the true sedimentation coefficients of the two major peaks which were corrected for concentration (Fig. 7.1B) to yield values for  $s_{20,w}^0$  of  $26.3 \pm 0.4$  S and  $33.6 \pm 0.1$  S. The sample seems to have undergone a certain amount of proteolysis, resulting in two major peaks: the peak around 35 S is thought to correspond to the intact human E2/E3BP core as its  $s_w$  compares favourably to the published values of 32 S for human (Hiromasa et al., 2004) and 35 S for bovine E2/E3BP core (Roche et al., 1993). The second major peak around 27 S probably corresponds to E2/E3BP core where some of the N-terminal arms of E2 and E3BP have been proteolytically cleaved. In particular, the extended linker sequences connecting the various lipoyl domains and subunit binding domains are prone to proteolysis, resulting in the two smaller peaks around 5 and 11 S. Proteolysis is not apparent from SDS PAGE (data not shown). However, the core has a much larger molecular weight and thus a higher capacity to bind Coomassie stain when compared to the significantly lower amounts of proteolysis products. The accuracy in the determination of  $s_w$  is also thought to be lower for the two smaller peaks. The sedimentation process of the two large species was fully recorded and used in the analysis. In contrast, sedimentation data of the two minor species is incomplete resulting in a more complicated and less accurate data analysis.

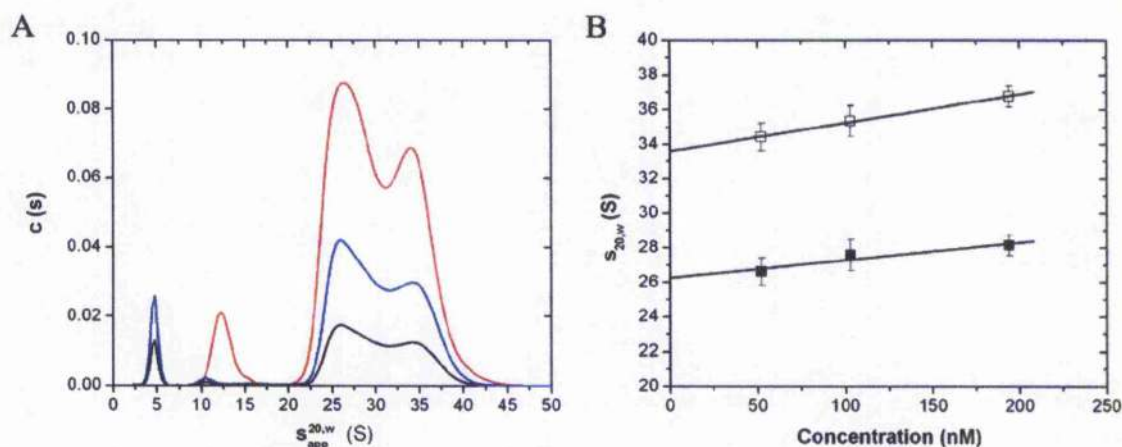


**Figure 7.1** Sedimentation velocity analysis of human E2/E3BP core

(A)  $c(s)$  distribution from SV interference data collected for 52 nM (—), 103 nM (—) and 194 nM (—) human E2/E3BP core. (B) Determination of concentration independent  $s_{20,w}^0$  for the two major peaks in the E2/E3BP  $c(s)$  analysis.

The average sedimentation coefficient of human E2/E3BP core is also considerably lower than that calculated for a solid sphere of the same molecular weight and partial specific volume: values of 76 S for the addition model and 67 S for the substitution model of PDC core, respectively were calculated. Without further information on the sedimentation behaviour of core composed solely from E2 it was not possible to distinguish between the two different models. The large discrepancy between calculated and experimental sedimentation coefficients for human E2/E3BP is due to the large internal cavity of the E2/E3BP core and highly solvated external “shell” of E2 and E3BP N-terminal arms resulting in a “drag effect” during sedimentation. The fact that human E2/E3BP core has a lower sedimentation coefficient than 60-meric E2 as reported by Hiromasa et al. (2004) does not necessarily indicate a lower molecular weight. The presence of 12 additional molecules of E3BP in each of the pentagonal faces would result in more solvent exposed surface, thus increasing hydration and non-ideality. Whether this effect is large enough to cause a decrease in the sedimentation coefficient as observed by the authors cannot be answered by SV alone.

A detailed study of human E2 and E2/E3BP core, including sedimentation equilibrium experiments, was not possible due to time and sample constraints, but should establish whether the E2 or the E2/E3BP core has the larger molecular weight, thus supporting either

the addition or the substitution model of human E2/E3BP core formation. The analysis of SE data for PDC core will be difficult: due to its enormous size (3.5/4.3 MDa for the substitution/addition model) SE runs have to be conducted at very low speeds (approximately 1900-3300 rpm) to cover an appropriate macromolecular distribution within the concentration gradients. Data acquisition at such low speeds is problematic although accuracy can be improved by using long solution columns. However, long columns take a very long time to reach equilibrium during which the core may undergo further degradation. The data published by Hiromasa and colleagues (2004) is based on very short columns (50  $\mu$ l). Furthermore, their analysis was done using the Beckman XL-A/XL-I software implemented in MicroCal ORIGIN which allows fitting of only a single species. Their SV data show, however, the presence of a small amount of aggregate in at least one of their samples which may have a profound effect on the final result if not fitted satisfactorily. Programs that allow the fitting of more than a single species are available (see Section 2.2.2.1). Also, the authors fail to mention how they arrived at initial estimates of the second virial coefficient,  $B$ , in order to account for non-ideality, exactly how  $B$  was implemented during data fitting and its consistency with its experimentally determined counterpart.

### 7.3.2 Small angle scattering of PDC and PDC core

#### 7.3.2.1 Small angle x-ray scattering

Due to sample constraints scattering data for human E2/E3BP core were obtained at only one concentration. However, inter-particle interference is not apparent in the recorded data and was unlikely to occur at the relatively low sample concentration used. Furthermore, the human and bovine scattering curves are almost identical (Fig. 7.2A), as expected for the PDC core particles from two mammalian species. An attempt to estimate the molecular weights of human and bovine core by extrapolation of the scattering intensity to zero angle,  $I(0)$ , did not provide satisfactory results. Scattering intensity is directly proportional to the total number of electrons within a particle and thus relates to its molecular weight. However, this extrapolation is more problematic to apply to very small and very large particles due to large differences in size when compared to the molecular weight standard – in this case E3 – as well as a 100 to 10000-fold increase in the experimental error when determining  $I(0)$ .

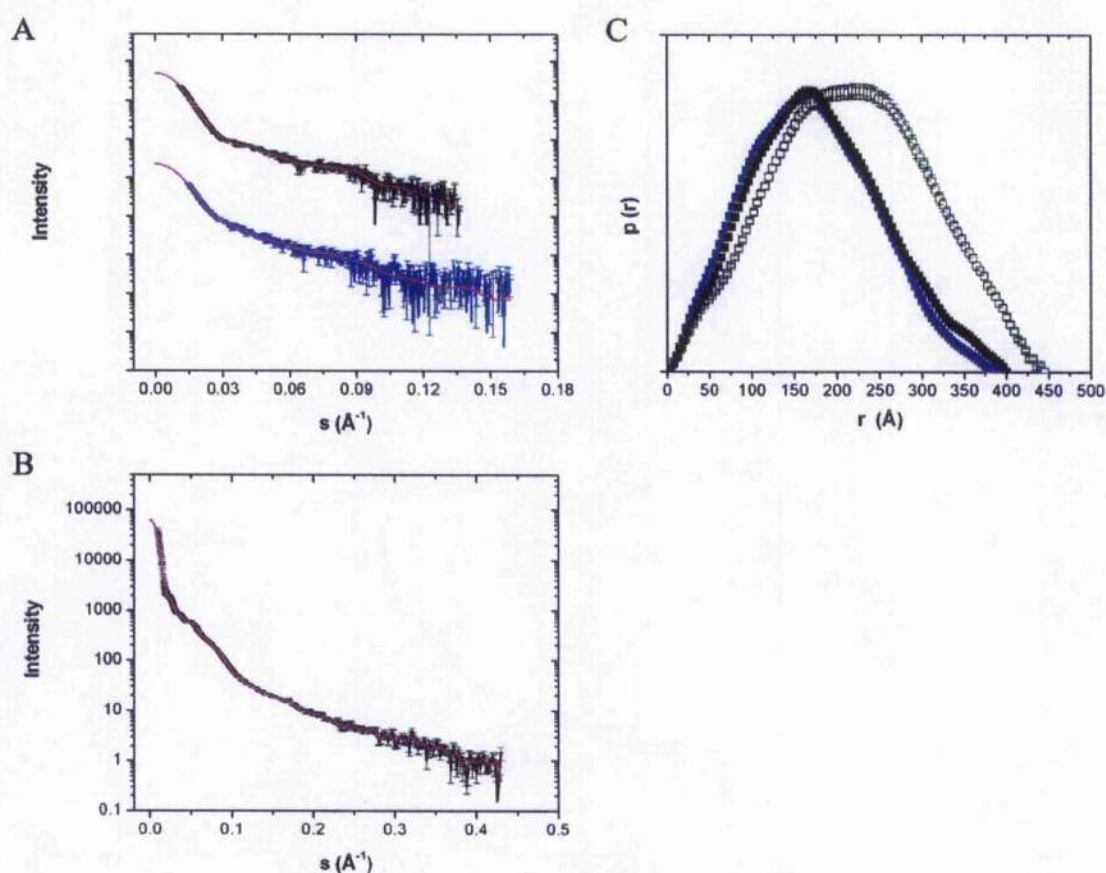


**Figure 7.2** Small angle x-ray scattering from PDC and PDC cores

(A) Scattering curves of human (—) and bovine (---) E2/E3BP core. (B) Scattering curve of bovine PDC (—). Shape scattering curves obtained using GNOM are shown (---). (C)  $p(r)$  distributions of human (■) and bovine (■) E2/E3BP core, and bovine PDC (□).

Guinier analysis and the program GNOM (Semenyuk & Svergun, 1991; Svergun, 1992) were used to determine the radius of gyration,  $R_g$ , of human E2/E3BP core ( $140 \pm 2$   $\text{\AA}$  and  $138 \pm 1$   $\text{\AA}$ , respectively). These values compare favourably with those obtained for bovine E2/E3BP of  $135 \pm 4$   $\text{\AA}$  and  $132 \pm 1$   $\text{\AA}$  from Guinier and GNOM analyses, respectively. In addition, the distance distribution functions,  $p(r)$ , of human and bovine E2/E3BP (Fig. 7.2C) clearly confirm the similarity of the scattering curves, and accordingly, the molecular shapes of the core particles. It also indicates that recombinantly expressed core seems to assemble into the same structure as native core. The maximum particle dimensions,  $D_{\max}$  were determined from the  $p(r)$  distribution as  $400 \pm 3$   $\text{\AA}$  and  $395 \pm 5$   $\text{\AA}$  for human and bovine E2/E3BP,

respectively, in excellent agreement with the particle diameter of 401 Å determined for bovine core using quasi-elastic light scattering (Roche et al., 1993). However, values of  $R_g$  of human E2/E3BP determined in this study are somewhat lower than those reported by Hiromasa et al. (2004) ( $150 \pm 2$  Å), while their  $D_{max}$  of 390 Å corresponds well to our own data.

Assuming that the core of human E2/E3BP has similar dimensions to that of *B. stearotherophilus* (Izard et al., 1999), the subtraction of the  $D_{max}$  determined using CRY SOL (Svergun et al., 1995) for *B. stearotherophilus* of 240 Å leaves approximately 80 Å for the N-terminal arms of E2. A length of approximately 80-90 Å for the swinging arms represents a sensible estimate and agrees with data obtained previously from quasi-elastic light scattering and cryo-EM (Roche et al., 1993; Milne et al., 2002; 2005).

Analysis of the scattering curve of bovine PDC (Fig. 7.2B,C) shows that PDC is larger and more spherical than the E2/E3BP cores, presumably due to the outer shell formed by the binding of E1 and E3. Guinier and GNOM analyses yielded  $R_g$  values of  $199 \pm 4$  Å and  $167 \pm 1$  Å, respectively. Using the Guinier approximation to estimate  $R_g$  is problematic in this case as it relies on only very few data points in the low angle region. Including data acquired at a longer sample-to-detector distance would remedy this, but there was not enough beamtime available to do this experiment. The  $D_{max}$  of  $450 \pm 4$  Å determined for bovine PDC from the distance distribution function (Fig. 7.2C) agrees well with data obtained previously using cryo-EM (Milne et al., 2002), although it is somewhat smaller than the diameters of 480 Å and 500 Å determined by quasi-elastic light scattering in solution and negative stain electron microscopy, respectively (Bleile et al., 1981; Roche et al., 1993). The differences in value probably reflect the different experimental approaches used, but may in part also be due to the effects of “breathing” of the PDC core, i.e. its thermally driven contraction and expansion (Zhou et al., 2001a). However, solution techniques such as SAXS and light scattering should yield time-average results, while cryo-EM is able to provide snap-shots of core molecules at different “breathing” stages.

*Ab initio* models of human and bovine E2/E3BP core as well as bovine PDC were produced with the computer program DAMMIN (Svergun, 1999) (Fig. 7.3) employing icosahedral

symmetry constraints during the modelling process in accordance with data available for eukaryotic PDC core formation (Stoops et al., 1992; 1997; Zhou et al., 2001b). Most models incorporate the same symmetry axes as the models obtained from cryo-EM, although some reconstructions used a different distribution of symmetry axes and were excluded from further analysis.

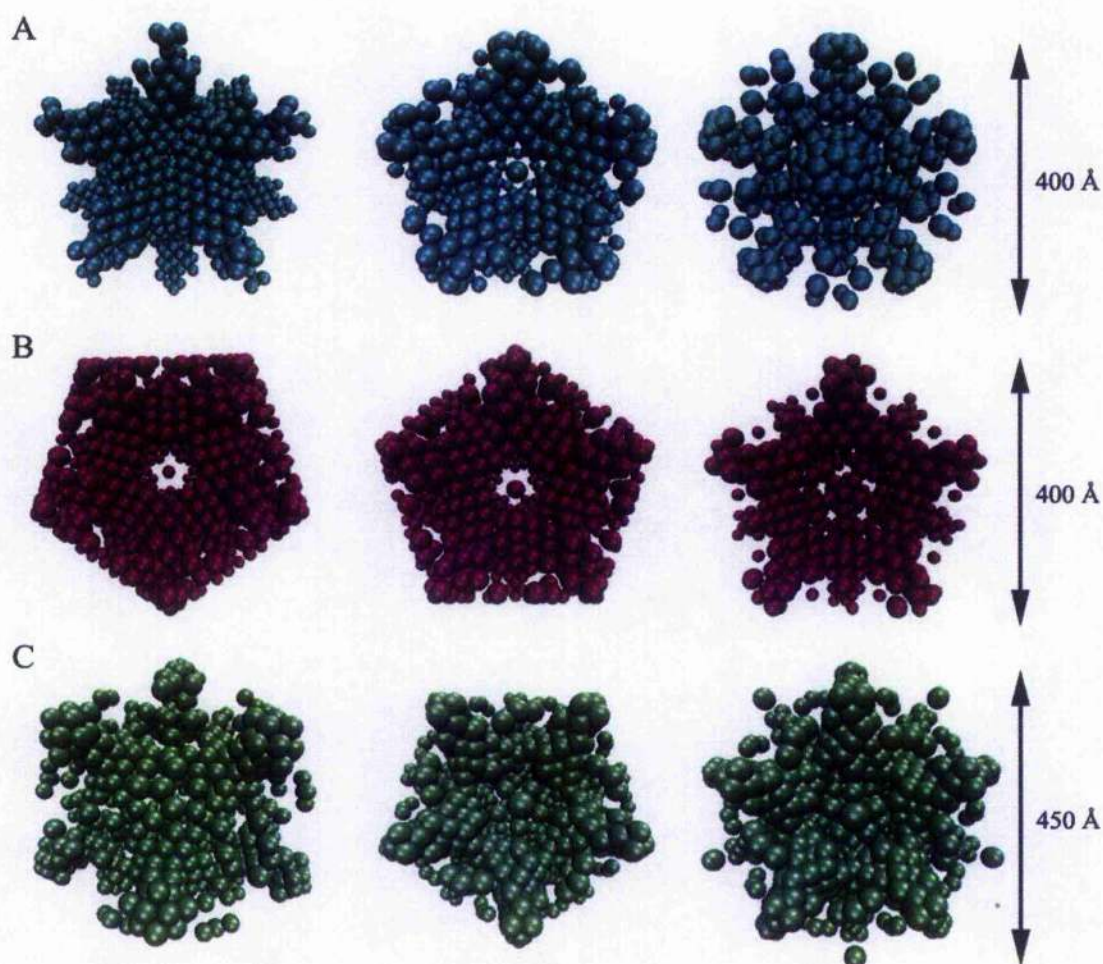


**Figure 7.3** *Ab initio* models of PDC and PDC cores  
*Ab initio* models were obtained using DAMMIN in reconstructions of human E2/E3BP (A), bovine E2/E3BP (B) and bovine PDC (C).

The position of E3BP within the PDC core cannot be determined from the SAXS *ab initio* models: reconstructions result in some models with “empty” pentagonal faces, in line with the 48:12 substitution model, while others do show electron density in the pentagonal faces of the core, thus supporting the 60:12 addition model. However, DAMMIN reconstructions were nevertheless successful considering that hollow structures can sometimes pose considerable problems for the algorithm (Volkov & Svergun, 2003).

### 7.3.2.2 Small angle neutron scattering

Small angle neutron scattering (SANS) has two major advantages over SAXS: neutrons do not cause radiation damage to samples, thus preventing radiation-induced aggregation. Secondly, the different interactions of neutrons with hydrogen and deuterium enable “contrast matching” (Section 2.5.1). Ideally, E3BP would be selectively deuterated and reconstituted with protonated E2 to form the PDC core. Unfortunately, mammalian E2 and E3BP have to be co-expressed for correct core formation (see Section 1.4.3) (McCartney et al., 1997). Instead, deuterated E2/E3BP core (dE2/E3BP) was reconstituted with protonated E3 (pE3) in order to exploit E3 positioning to determine the localisation of E3BP within the PDC core.

Recording the scattering of pE3 and dE2/E3BP dialysed against buffers with different percentages of D<sub>2</sub>O allowed accurate determination of their respective matchpoints of 46% and 130%, respectively (Fig. 7.4). A matchpoint of 130% indicates efficient incorporation of the deuterium label into the overexpressed protein. With a matchpoint of 46%, the scattering contribution of pE3 in reconstituted dE2/E3BP•pE3 can be matched out completely. However, when recording the scattering of dE2/E3BP•pE3 in 100% D<sub>2</sub>O, the E2/E3BP core cannot be completely matched and still accounts for 30% of the overall sample scattering and thus influences subsequent data analysis. In order to obtain accurate data for future experiments the E2/E3BP core will have to be overexpressed in 65% rather than 100% deuterated media, so that its matchpoint is less than 100% D<sub>2</sub>O and the deuterated E2/E3BP core can be effectively matched by the solvent.

The scattering curves obtained for dE2/E3BP and dE2/E3BP•pE3 are shown in Fig. 7.5A,C. For dE2/E3BP in buffers containing 40% and 100% D<sub>2</sub>O respectively,  $R_g$  values of  $142 \pm 2 \text{ \AA}$  and  $142 \pm 6 \text{ \AA}$  were determined using GNOM. These values compare favourably to the  $R_g$  of  $145 \text{ \AA}$  determined by SAXS. The  $D_{\text{max}}$  was determined as  $425 \pm 5 \text{ \AA}$  for dE2/E3BP in both 40% and 100% D<sub>2</sub>O buffer (Fig. 7.5B) which is somewhat larger than the value obtained by SAXS (400 Å).

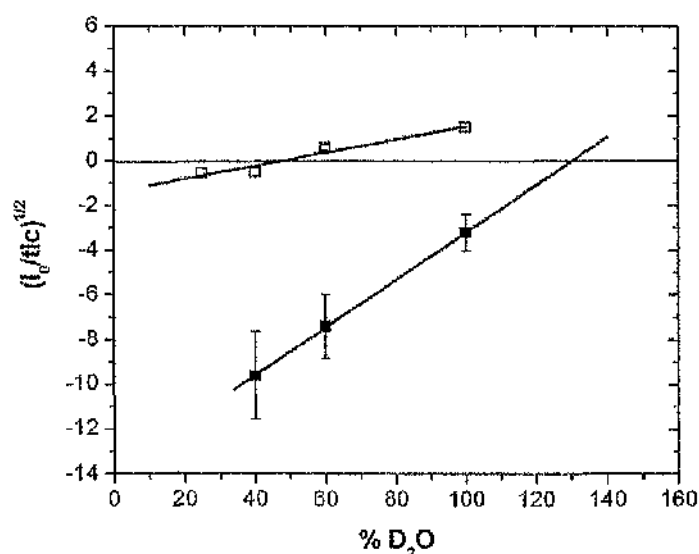


**Figure 7.4 Matchpoint determination for E3 and E2/E3BP core**

Scattering experiments for protonated E3 (□) and deuterated E2/E3BP core (■) were done in buffers containing 40, 60 and 100% D<sub>2</sub>O. Additional data were recorded for pE3 in buffers containing 20% D<sub>2</sub>O.

GNOM analysis of the scattering curves recorded for dE2/E3BP•pE3 in buffers containing 40% and 100% D<sub>2</sub>O, respectively (Fig. 7.5C), yielded  $R_g$  values of  $143 \pm 2 \text{ \AA}$  and  $136 \pm 8 \text{ \AA}$ . The decrease in  $R_g$  for dE2/E3BP•pE3 in 100% D<sub>2</sub>O (i.e. with the E2/E3BP core partially matched out) was unexpected, but lies within the experimental error. Furthermore, incomplete matching of one component has been known to affect data analysis in this way (P. Callow, personal communication). The  $D_{\text{max}}$  for dE2/E3BP•pE3 was determined as  $425 \text{ \AA}$  for samples in buffers containing 40% and 100% D<sub>2</sub>O (Fig. 7.5D).

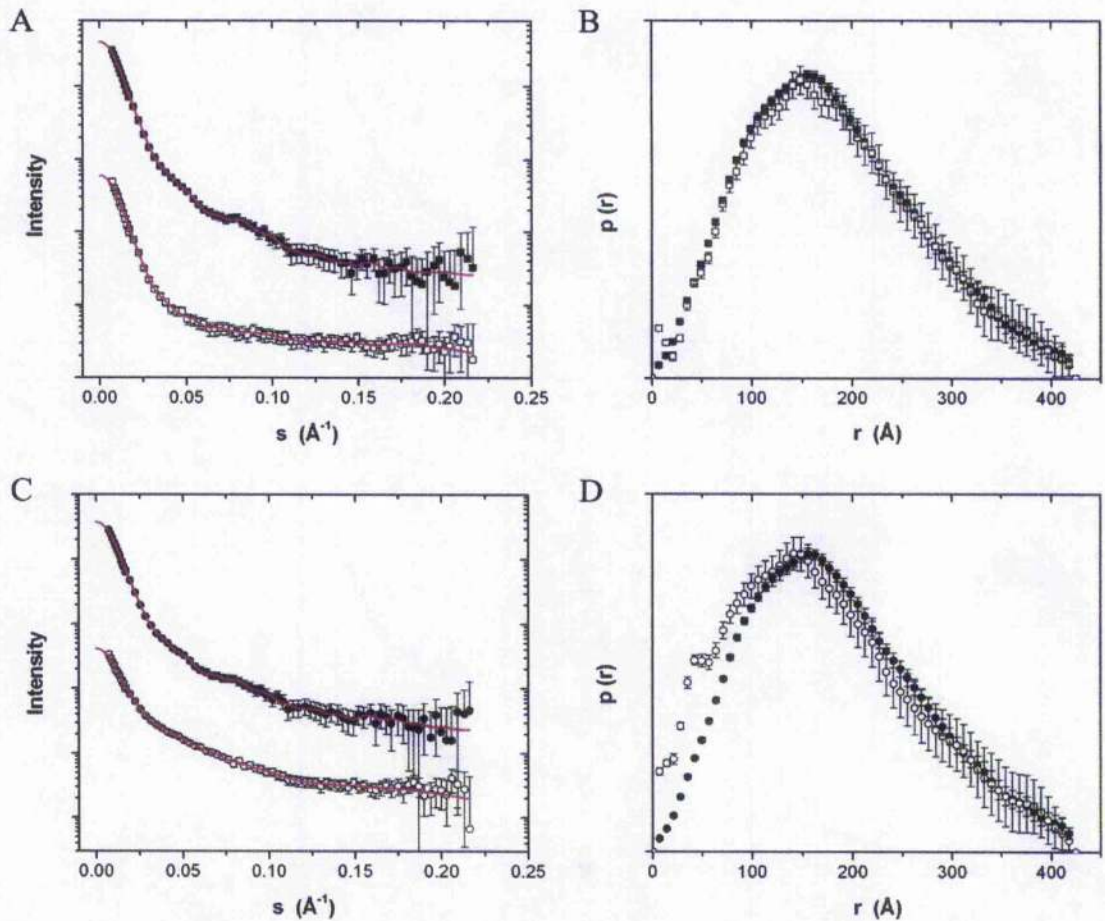


**Figure 7.5** Small angle neutron scattering of E2/E3BP core and E2/E3BP•E3

(A) Scattering curves of deuterated E2/E3BP core in 40% (■) and 100% D<sub>2</sub>O (□). The shape scattering curves obtained from GNOM (—) are shown. (B)  $p(r)$  distributions of deuterated E2/E3BP core in 40% (■) and 100% D<sub>2</sub>O (□). (C) Scattering curves of deuterated E2/E3BP•E3 in 40% (●) and 100% D<sub>2</sub>O (○). (D)  $p(r)$  distributions of deuterated E2/E3BP core in 40% (●) and 100% D<sub>2</sub>O (○).

Reconstructions of dE2/E3BP core in 40% D<sub>2</sub>O and partially matched out dE2/E3BP•E3 in 100% D<sub>2</sub>O were obtained separately with DAMMIN and superimposed onto each other (Fig. 7.6). The reconstruction of the dE2/E3BP core yielded an unexpected shape, as it seems shortened in one direction and with overall dimensions of 425 x 425 x 210 Å. The model consists of two parts: an inner core with a diameter of 270 Å and an outer shell with a thickness of 80 Å, presumably representing the C-terminal domains and N-terminal arms, respectively. In fact, with respect to its short axis the DAMMIN reconstruction is reminiscent of cryo-EM micrographs of the breathing PDC core (Zhou et al., 2001a). However, in contrast

to cryo-EM where pictures of individual molecules are taken (and later averaged), SANS is an inherently time-average technique and the resultant structure is expected to represent a time-average ensemble (i.e. a more spherical shape), not an extreme conformation.

Most probably the models obtained reflect the fact that more data (with better statistics) need to be collected: ideally, scattering data would be recorded using an additional camera length and more concentrated protein samples. Furthermore, at 3 hours, data collection times for each sample were very short when compared to published SANS experiments. However, due to time and sample constraints it was not possible to implement any of the above measures. The model shown in Fig. 7.6 was reconstructed using P52 instead of icosahedral (532) symmetry, as the introduction of an additional 3-fold axis introduced a minimum in the fit that was not observed in the experimental data (not shown). Possibly, this minimum is obscured due to the low scattering intensity and statistics of the data, resulting in a flattened particle, since using icosahedral symmetry for *ab initio* modelling of SAXS data did not present any problems at all. Possible sample heterogeneities due to limited proteolytic cleavage as observed by AUC (see Section 7.3.1) are not thought to influence SANS reconstructions significantly, since *ab initio* models obtained from SAXS seem unaffected.

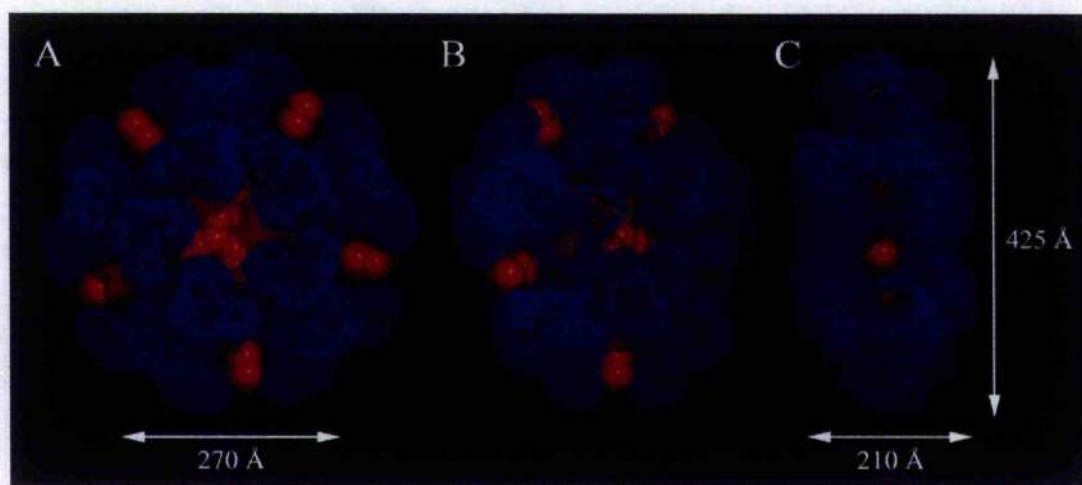


**Figure 7.6 Reconstructions of E2/E3BP and matched E2/E3BP•E3 from SANS data**  
Top (A) and side views rotated by 45° (B) and 90° (C). E2/E3BP core (blue) and partially matched dE2/E3BP•pE3 (red) were reconstructed from separate data sets.

Reconstructions of E3 from partially matched dE2/E3BP•pE3 show that this approach for locating E3 positioning with respect to the E2/E3BP core is indeed possible. Modelling of dE2/E3BP•pE3 using no symmetry constraints (not shown) as well as P2 (not shown) and P5 symmetry (Fig. 7.6) all produced comparable results as the density corresponding to E3 was distributed in a plane with respect to the dE2/E3BP core. However, as a consequence of the incomplete matching out of the dE2/E3BP core, the models obtained for E3 in this experiment may be misleading, since it is unclear how DAMMIN reconstructions will be affected by the residual scattering from the dE2/E3BP core. Therefore, no clear conclusion as to the core formation by E2 and E3BP can be drawn from the experiments described above, nor indeed from published material. However, a very strong point in favour of the substitution model is the ease of E3BP integration into the core when compared to the addition model: the C-terminal domains of E2 and E3BP are highly homologous. Therefore, E3BP should easily be able to interact with E2 molecules. In contrast, when integrating into a pentagonal face the interaction of E3BP with E2 is likely to be of a completely different nature, although the pentagonal opening within the core has a diameter of approximately 60-70 Å which is big enough for the accommodation of the E3BP C-terminal domain, assuming similar domain dimensions when compared to E2.

While neither AUC nor SAXS can provide a definitive description of PDC organisation, completion of SANS experiments employing contrast matching will provide unique insights into E2/E3BP core structure. In addition to the SANS experiment discussed above, contrast matching with deuterated E2 and protonated protein E3BP may also prove useful: even though E2 and protein E3BP have to be co-expressed for the formation of wild-type core, denaturation of bovine E2/E3BP and the subsequent slow removal of guanidine hydrochloride by dialysis resulted in the reformation of E2/E3BP particles, although integration of E3BP into the core was reduced to only 35% of wild-type levels (McCartney et al., 1997). Exploiting the availability of recombinant proteins, however, it may be possible to improve incorporation of E3BP into the core using excess E3BP during reconstitution experiments. Constructs containing the C-terminal, core forming domains of both E2 and E3BP only would be particularly suited to such a SANS experiment as removal of the mobile, N-terminal arm should considerably facilitate *ab initio* modelling. A completely different approach using labelled E3BP in fluorescence resonance energy transfer (FRET) studies may also yield

useful complementary results by estimating the intermolecular distance between neighbouring E3BP molecules. Clearly, more experiments are needed for the resolution of PDC core organisation. However, the work presented in this chapter helps to define feasible experimental strategies.

# Chapter 8

## Conclusions

Multi-enzyme assemblies and in particular the 2-oxoacid dehydrogenase complexes have been intensely studied in order to characterise the influence of protein-protein interactions on complex efficiency, cooperativity and regulation. While many aspects of function and structure of the 2-oxoacid dehydrogenase complexes (2-OADC) and their constituent enzymes are well understood, many questions remain. Hundreds of different mutations have been identified in PDC alone, and the links between clinical disease and complex dysfunction at a molecular level are often only poorly understood. Similarly, while the atomic structures of many 2-OADC constituent enzymes have been solved over the last 20 years, our understanding of how these individual components form into giant and highly complex assemblies is more tenuous. With particular reference to PDC, a large body of work has been dedicated to the detailed characterisation of PDC from *B. stearothermophilus* and certain other Gram-positive bacteria. Analysis of eukaryotic PDC, however, has been slower to progress, but is just as interesting and important given the significant differences between prokaryotic and eukaryotic PDC. With the discovery of E3BP as an additional component of eukaryotic PDC (De Marcucci & Lindsay, 1985; Jilka et al., 1986) and the concomitant specialisation of protein-protein interactions within the complex, determining the nature and effects of the specific E2/E1 and E3BP/E3 subcomplex formation on overall PDC organisation, function and regulation has been at the forefront of eukaryotic PDC research.

The work described in this thesis concerns the large-scale purification of individual PDC proteins from recombinant or native sources (Chapter 4) for use in a variety of subsequent biochemical and biophysical experiments. All proteins with the exception of bovine E1 and bovine E2/E3BP core were expressed as His-tag or GST fusion products in order to aid purification. Nevertheless, several chromatography steps were required for all proteins in order to obtain >95% pure preparations as judged by SDS PAGE and Coomassie blue staining.

Purified proteins were initially characterised individually and then used for the subsequent analysis of the stoichiometry of binding between human recombinant constructs of E3BP and E3 (Chapter 5), as well as human E2 and bovine E1 (Chapter 6). As expected, AUC and SAXS data confirmed E3 as a homodimer, while the E3BP-derived construct XDD was found by AUC to be monomeric in solution. The E3 solution structure determined by *ab initio* modelling of SAXS data is significantly different to the crystal structures solved for the human and yeast enzymes. In solution E3 seems less compact and more anisometric than in the crystal, possibly reflecting crystal packing forces.

In the case of the XDD/E3 subcomplex, data obtained from non-denaturing PAGE, AUC and ITC all confirmed a 2:1 stoichiometric interaction of XDD with E3. Similarly, analysis of data recorded for the purified XDD/E3 subcomplex by AUC and SAXS was in complete agreement and even allowed for the determination of a model for the subcomplex using SAXS *ab initio* modelling. Using hydrodynamic and rigid body modelling a molecular model was defined, based on homology models of both E3 and XDD. In the final model of the XDD/E3 subcomplex, E3 seems to adopt the same structural configuration as on its own. This may be why crystallisation studies of the XDD/E3 subcomplex failed to detect two XDD molecules bound per E3 homodimer (Ciszak et al., 2006). Intriguingly, the two XDD molecules were found to be non-equivalent: while one lipoyl domain was present in a conformation laterally extended away from the SBD, the other LD was found docked into the E3 active site, possibly indicating an E1-like flip-flop mechanism (Ciszak et al., 2003). However, further detailed enzymatic studies are required before drawing any further inferences from the solution structure.

Bovine E1, the E2-derived construct E2DD and their subcomplex were studied in a fashion analogous to E3 and E3BP. Lower yields from protein purification and decreased protein stability, in particular for E1, meant that characterisation of the E2DD/E1 subcomplex was fraught with difficulties. Analysis of stoichiometric mixtures of E2DD and E1 by sedimentation velocity AUC indicates the formation of 2:1 (E2DD/E1) subcomplexes. Further AUC and SAXS studies on the purified E2DD/E1 subcomplex confirmed this result, although subsequent *ab initio* and rigid body modelling of the SAXS data proved problematic.

The E2DD/E1 data do favour a 2:1 stoichiometric arrangement, resulting in the formation of "cross-bridges" on the PDC surface that precisely position and orient the peripherally bound E1 and E3. Presumably, such an arrangement would facilitate interaction of the lipoyl swinging arms of E2 and E3BP with the active sites during catalysis and directly affect the operation of the E2/E3BP core. A further consequence of cross-bridge formation would be the introduction of considerable constraints upon the mobility of the N-terminal E2 and E3BP arms, with particular emphasis on the lipoyl domains.

This new level of PDC ultrastructure is also thought to have profound effects on PDC regulation by PDK and PDP, as only a few molecules of the regulatory proteins are bound per complex (Yeaman, 1989). Both enzymes associate with PDC via the E2-ILD which in turn would be regularly spaced on the complex surface as a direct consequence of cross-bridge formation, ideal for the hand-over-hand mechanism of movement suggested for the dimeric PDK molecules (Liu et al., 1995a).

In comparison to the organisation of peripheral E1 and E3 with respect to the PDC core, a number of papers had been published on eukaryotic PDC core organisation. However, only over the last ten years have researchers begun to try to pinpoint the location of E3BP within the core. Two very different models were proposed based on various experimental techniques. Chapter 7 represents an effort to develop an experimental approach that will distinguish between the two core representations. Neither AUC nor SAXS are suitable on their own due to uncertainties in the data collection or interpretation inherent in both techniques and are further impeded by the enormous size of the PDC core itself. SANS, however, with its unique

ability to distinguish between different components of the same complex (in this case E3 and E2/E3BP) presents a viable alternative for future experiments.

# Bibliography

- Ackerman CJ, Harnett MM, Harnett W, Kelly SM, Svergun DI & Byron O (2003). 19 Å solution structure of the filarial nematode immunomodulatory protein, ES-62. *Biophys. J.* **84**, 489-500.
- Ævarsson A, Chuang JL, Wynn RM, Turley S, Chuang DT & Hol WGJ (2000). Crystal structure of human branched-chain alpha-ketoacid dehydrogenase and the molecular basis of multienzyme complex deficiency in maple syrup urine disease. *Struct. Fold. Des.* **8**, 277-291.
- Ævarsson A, Seger K, Turley S, Sokatch JR & Hol WGJ (1999). Crystal structure of 2-oxoisovalerate and dehydrogenase and the architecture of 2-oxo acid dehydrogenase multienzyme complexes. *Nature Struct. Biol.* **6**, 785-792.
- Allen AG & Perham RN (1991). 2 lipoyl domains in the dihydrolipoamide acetyltransferase chain of the pyruvate dehydrogenase multienzyme complex of *Streptococcus faecalis*. *FEBS Lett.* **287**, 206-210.
- Allen AG, Perham RN, Allison N, Miles JS & Guest JR (1989). Reductive acetylation of tandemly repeated lipoyl domains in the pyruvate dehydrogenase multienzyme complex of *Escherichia coli* is random order. *J. Mol. Biol.* **208**, 623-633.
- Allen MD, Broadhurst RW, Solomon RG & Perham RN (2005). Interaction of the E2 and E3 components of the pyruvate dehydrogenase multienzyme complex of *Bacillus*

- stearothermophilus*. Use of a truncated protein domain in NMR spectroscopy. *FEBS J.* **272**, 259-268.
- Amano K, Leung P, Rieger R, Quan C, Wang X, Marik J, Suen YF, Kurth MJ, Nantz MH, Ansari AA, Lam KS, Zeniya M, Matsuura E, Coppel RL & Gershwin ME (2005). Chemical xenobiotics and mitochondrial autoantigens in primary biliary cirrhosis: identification of antibodies against a common environmental, cosmetic, and food additive, 2-octynoic acid. *J. Immunol.* **174**, 5874-5883.
- Ambrose MC & Perham RN (1976). Spin-label study of mobility of enzyme-bound lipoyl acid in pyruvate dehydrogenase multienzyme complex of *Escherichia coli*. *Biochem. J.* **155**, 429-432.
- Angelides KJ & Hammes GG (1979). Structural and mechanistic studies of the alpha-ketoglutarate dehydrogenase multienzyme complex from *Escherichia coli*. *Biochemistry* **18**, 5531-5537.
- Aral B, Benelli C, Ait-Ghezala G, Amessou M, Fouque F, Maunoury C, Creau N, Kamoun P & Marsac C (1997). Mutations in *PDX1*, the human lipoyl-containing component X of the pyruvate dehydrogenase complex gene on chromosome 11p1, in congenital lactic acidosis. *Am. J. Hum. Genet.* **61**, 1318-1326.
- Arita K, Hashimoto H, Shimizu T, Nakashima K, Yamada M & Sato M (2004). Structural basis for calcium induced activation of human PAD4. *Nature Struct. Mol. Biol.* **11**, 777-783.
- Arjunan P, Nemeria N, Brunskill A, Chandrasekhar K, Sax M, Yan Y, Jordan F, Guest JR & Furey W (2002). Structure of the pyruvate dehydrogenase multienzyme complex E1 component from *Escherichia coli* at 1.85 Å resolution. *Biochemistry* **41**, 5213-5221.
- Aszódi A & Taylor WR (1996). Homology modelling by distance. *Fold. Des.* **1**, 325-334.

- Bao H, Kasten SA, Yan X & Roche TE (2004a). Pyruvate dehydrogenase kinase isoform 2 activity stimulated by speeding up the rate of dissociation of ADP. *Biochemistry* **43**, 13442-13451.
- Bao H, Kasten SA, Yan X & Roche TE (2004b). Pyruvate dehydrogenase kinase isoform 2 limited and further inhibited by slowing down the rate of dissociation of ADP. *Biochemistry* **43**, 13432-13441.
- Behal RH, Browning KS, Hall TB & Reed LJ (1989). Cloning and nucleotide sequence of the gene for protein X from *Saccharomyces cerevisiae*. *PNAS* **86**, 8732-8736.
- Behal RH, Debuysere MS, Demeler B, Hansen JC & Olson MS (1994). Pyruvate dehydrogenase multienzyme complex - characterization of assembly intermediates by sedimentation velocity analysis. *J. Biol. Chem.* **269**, 31372-31377.
- Berg A, De Kok A & Vervoort J (1994). Sequential  $^1\text{H}$  and  $^{15}\text{N}$  nuclear magnetic resonance assignments and secondary structure of the N-terminal lipoyl domain of the dihydrolipoyl transacetylase component of the pyruvate dehydrogenase complex from *Azotobacter vinelandii*. *Eur. J. Biochem.* **221**, 87-100.
- Berg A, Smits O, De Kok A & Vervoort J (1995). Sequential  $^1\text{H}$  and  $^{15}\text{N}$  nuclear magnetic resonance assignments and secondary structure of the lipoyl domain of the 2-oxoglutarate dehydrogenase complex from *Azotobacter vinelandii*. *Eur. J. Biochem.* **234**, 148-159.
- Berg A, Vervoort J & De Kok A (1996). Solution structure of the lipoyl domain of the 2-oxoglutarate dehydrogenase complex from *Azotobacter vinelandii*. *J. Mol. Biol.* **261**, 432-442.
- Berg A, Vervoort J & De Kok A (1997). Three-dimensional structure in solution of the N-terminal lipoyl domain of the pyruvate dehydrogenase complex from *Azotobacter vinelandii*. *Eur. J. Biochem.* **244**, 352-360.

- Berg A, Westphal AH, Bosma HJ & De Kok A (1998). Kinetics and specificity of reductive acylation of wild-type and mutated lipoyl domains of 2-oxo-acid dehydrogenase complexes from *Azotobacter vinelandii*. *Eur. J. Biochem.* **252**, 45-50.
- Berman JN, Chen GX, Hale G & Perham RN (1981). Lipoic acid residues in a take-over mechanism for the pyruvate dehydrogenase multienzyme complex of *Escherichia coli*. *Biochem. J.* **199**, 513-520.
- Berry A, Scrutton NS & Perham RN (1989). Switching kinetic mechanism and putative proton donor by directed mutagenesis of glutathione reductase. *Biochemistry* **28**, 1264-1269.
- Blass JP & Gibson GE (1991). The role of oxidative abnormalities in the pathophysiology of Alzheimer's disease. *Rev. Neurol.* **147**, 513-525.
- Blass JP & Gibson GE (1999). Cerebrometabolic aspects of delirium in relationship to dementia. *Dement. Geriatr. Cogn. Disord.* **10**, 335-338.
- Bleile DM, Hackert ML, Pettit FH & Reed LJ (1981). Subunit structure of dihydrolipoyl transacetylase component of pyruvate dehydrogenase complex from bovine heart. *J. Biol. Chem.* **256**, 514-519.
- Boden G, Chen X & Stein TP (2001). Gluconeogenesis in moderately and severely hyperglycemic patients with type 2 diabetes mellitus. *Am. J. Physiol. Endocrinol. Metab.* **280**, E23-E30.
- Bollag DM, Rozycki MD & Edelstein SJ (1996a). Concentrating protein solutions. In *Protein Methods*, Wiley-Liss, New York, pp. 83-106.
- Bollag DM, Rozycki MD & Edelstein SJ (1996b). Gel electrophoresis under nondenaturing conditions. In *Protein Methods*, Wiley-Liss, New York, pp. 155-172.

- Borges A, Hawkins CF, Packman LC & Perham RN (1990). Cloning and sequence-analysis of the genes encoding the dihydrolipoamide acetyltransferase and dihydrolipoamide dehydrogenase components of the pyruvate dehydrogenase multienzyme complex of *Bacillus stearothermophilus*. *Eur. J. Biochem.* **194**, 95-102.
- Boulatnikov I & Popov KM (2003). Formation of functional heterodimers by isozymes 1 and 2 of pyruvate dehydrogenase kinase. *Biochim. Biophys. Acta* **1645**, 183-192.
- Boulin CJ, Kempf R, Gabriel A & Koch MHJ (1988). Data acquisition systems for linear and area X-ray detectors using delay-line readout. *Nuclear Instruments & Methods in Physics Research Section A- Accelerators Spectrometers Detectors and Associated Equipment* **269**, 312-320.
- Bowker-Kinley MM, Davis WI, Wu P, Harris RA & Popov KM (1998). Evidence for existence of tissue-specific regulation of the mammalian pyruvate dehydrogenase complex. *Biochem. J.* **329**, 191-196.
- Brautigam CA, Chuang JL, Tomchick DR, Machius M & Chuang DT (2005). Crystal structure of human dihydrolipoamide dehydrogenase: NAD<sup>+</sup>/NADH binding and the structural basis of disease-causing mutations. *J. Mol. Biol.* **350**, 543-552.
- Brown AE (2002). Towards a recombinant model of human pyruvate dehydrogenase complex. University of Glasgow, PhD thesis.
- Brown GK, Brown RM, Scholem RD, Kirby JA & Dahl HH (1989a). The clinical and biochemical spectrum of human pyruvate dehydrogenase complex deficiency. *Ann. NY Acad. Sci.* **573**, 360-368.
- Brown GK, Otero LJ, Le Gris M & Brown RM (1994). Pyruvate dehydrogenase deficiency. *J. Med. Genet.* **31**, 875-879.

- Brown RM, Dahl HH & Brown GK (1989b). X-chromosome localization of the functional gene for the E1 $\alpha$  subunit of the human pyruvate dehydrogenase complex. *Genomics* **4**, 174-181.
- Brown RM, Head RA, Boubriak II, Leonard JV, Thomas NH & Brown GK (2004). Mutations in the gene for the E1 $\beta$  subunit: a novel cause of pyruvate dehydrogenase deficiency. *Hum. Genet.* **115**, 123-127.
- Brown RM, Head RA & Brown GK (2002). Pyruvate dehydrogenase E3 binding protein deficiency. *Hum. Genet.* **110**, 187-191.
- Bubber P, Haroutunian V, Fisch G, Blass JP & Gibson GE (2005). Mitochondrial abnormalities in Alzheimer brain: mechanistic implications. *Ann. Neurol.* **57**, 695-703.
- Burns G, Sykes PJ, Hatter K & Sokatch JR (1989). Isolation of a third lipoamide dehydrogenase from *Pseudomonas putida*. *J. Bacteriol.* **171**, 665-668.
- Byrd DJ, Krohn HP, Winkler L, Steinborn C, Hadam M, Brodehl J & Hunneman DIH (1989). Neonatal pyruvate dehydrogenase deficiency with lipoate responsive lactic acidemia and hyperammonaemia. *Eur. J. Pediatr.* **148**, 543-547.
- Carothers DJ, Pons G & Patel MS (1989). Dihydrolipoamide dehydrogenase: functional similarities and divergent evolution of the pyridine nucleotide-disulfide oxidoreductases. *Arch. Biochem. Biophys.* **268**, 409-425.
- Cate RL, Roche TE & Davis LC (1980). Rapid intersite transfer of acetyl groups and movement of pyruvate dehydrogenase component in the kidney pyruvate dehydrogenase complex. *J. Biol. Chem.* **225**, 7556-7562.
- Chacón P, Diaz JF, Moran F & Andreu JM (2000). Reconstruction of protein form with X-ray solution scattering and a genetic algorithm. *J. Mol. Biol.* **299**, 1289-1302.

- Chacón P, Moran F, Díaz JF, Pantos E & Andreu JM (1998). Low-resolution structures of proteins in solution retrieved from X-ray scattering with a genetic algorithm. *Biophys. J.* **74**, 2760-2775.
- Chen GL, Wang LJ, Liu SJ, Chuang C & Roche TE (1996). Activated function of the pyruvate dehydrogenase phosphatase through  $\text{Ca}^{2+}$ -facilitated binding to the inner lipoyl domain of the dihydrolipoyl acetyltransferase. *J. Biol. Chem.* **271**, 28064-28070.
- Ciszak E, Korotchkina LG, Hong YS, Joachimiak A & Patel MS (2001). Crystallization and initial X-ray diffraction analysis of human pyruvate dehydrogenase. *Acta Cryst.* **D57**, 465-468.
- Ciszak EM, Korotchkina LG, Dominiak PM, Sidhu S & Patel MS (2003). Structural basis for flip-flop action of thiamine pyrophosphate-dependent enzymes revealed by human pyruvate dehydrogenase. *J. Biol. Chem.* **278**, 21240-21246.
- Ciszak EM, Makal A, Hong YS, Vettaikorumakankauv AK, Korochkina LG & Patel MS (2006). How dihydrolipoamide dehydrogenase-binding protein binds dihydrolipoamide dehydrogenase in human pyruvate dehydrogenase complex. *J. Biol. Chem.* **281**, 648-655.
- Corpet F (1988). Multiple sequence alignment with hierarchical clustering. *Nucl. Acids Res.* **16**, 10881-10890.
- Craft S, Asthana S, Schellenberg G, Baker L, Boyt AA, Martins RN, Raskind M, Peskind E & Plymate S (2000). Insulin effects on glucose metabolism, memory, and plasma amyloid precursor protein in Alzheimer's disease differ according to apolipoprotein-E genotype. *Ann. NY Acad. Sci.* **903**, 222-228.
- Cuff JA, Clamp ME, Siddiqui AS, Finlay M & Barton GJ (1998). Jpred: a consensus secondary structure prediction server. *Bioinformatics* **14**, 892-893.

- Da Silva LA, De Marcucci OL & Kuhnle ZR (1993). Dietary polyunsaturated fats suppress the high-sucrose-induced increase of rat liver pyruvate dehydrogenase levels. *Biochim. Biophys. Acta* **1169**, 126-134.
- Dahl HH (1995). Pyruvate dehydrogenase E1 alpha deficiency: males and females differ yet again. *Am. J. Hum. Genet.* **56**, 553-557.
- Dahl HH, Brown RM, Hutchison WM, Maragos C & Brown GK (1990). A testis-specific form of the human pyruvate dehydrogenase E1 alpha subunit is coded for by an intronless gene on chromosome 4. *Genomics* **8**, 225-232.
- Dahl HH, Hansen LL, Brown RM, Danks DM, Rogers JG & Brown GK (1992). X-linked pyruvate dehydrogenase E1 $\alpha$  subunit deficiency in heterozygous females: variable manifestation of the same mutation. *J. Inherit. Metab. Dis.* **15**, 835-847.
- Dam J, Velikovsky CA, Mariuzza RA, Urbanke C & Schuck P (2005). Sedimentation velocity analysis of heterogeneous protein-protein interactions: Lamm equation modeling and sedimentation coefficient distributions  $c(s)$ . *Biophys. J.* **89**, 619-634.
- Damuni Z, Humphreys JS & Reed LJ (1984). Stimulation of pyruvate dehydrogenase phosphatase activity by polyamines. *Biochem. Biophys. Res. Commun.* **124**, 95-99.
- Damuni Z & Reed LJ (1987). Purification and characterization of a divalent cation-independent, spermine-stimulated protein phosphatase from bovine kidney mitochondria. *J. Biol. Chem.* **262**, 533-538.
- Danson MJ, Fersht AR & Perham RN (1978). Rapid intra-molecular coupling of active sites in pyruvate dehydrogenase complex of *Escherichia coli* - mechanism for rate enhancement in multimeric structures. *PNAS* **75**, 5386-5390.
- Dardel F, Davis AL, Laue ED & Perham RN (1993). Three-dimensional structure of the lipoyl domain from *Bacillus stearothermophilus* pyruvate dehydrogenase multienzyme complex. *J. Mol. Biol.* **229**, 1037-1048.

- Dardel F, Laue ED & Perham RN (1991). Sequence-specific <sup>1</sup>H-NMR assignments and secondary structure of the lipoyl domain of the *Bacillus stearothermophilus* pyruvate dehydrogenase multienzyme complex. *Eur. J. Biochem.* **201**, 203-209.
- De Kok A, Hengeveld AF, Martin A & Westphal AH (1998). The pyruvate dehydrogenase multi-enzyme complex from Gram-negative bacteria. *Biochim. Biophys. Acta* **1385**, 353-366.
- De Marcucci OG, Hodgson JA & Lindsay JG (1986). The Mr-50 000 polypeptide of mammalian pyruvate dehydrogenase complex participates in the acetylation reactions. *Eur. J. Biochem.* **158**, 587-594.
- De Marcucci OG, Hunter A & Lindsay JG (1985). Low immunogenicity of the common lipoamide dehydrogenase subunit (E3) of mammalian pyruvate dehydrogenase and 2-oxoglutarate dehydrogenase multienzyme complexes. *Biochem. J.* **226**, 509-517
- De Marcucci OG & Lindsay JG (1985). Component X - an immunologically distinct polypeptide associated with mammalian pyruvate dehydrogenase multi-enzyme complex. *Eur. J. Biochem.* **149**, 641-648.
- De Meirleir L, Lissens W, Benelli C, Marsac C, De Klerk J, Scholte J, van Diggelen O, Kleijer W, Seneca S & Liebaers I (1998). Pyruvate dehydrogenase complex deficiency and absence of subunit X. *J. Inherit. Metab. Dis.* **21**, 9-16.
- De Vivo DC (1998). Complexities of the pyruvate dehydrogenase complex. *Neurology* **51**, 1247-1249.
- Denton RM, Randle PJ & Martin BR (1972). Stimulation by calcium ions of pyruvate dehydrogenase phosphatase. *Biochem. J.* **128**, 161-163.
- Deonarain MP, Berry A, Scrutton NS & Perham RN (1989). Alternative proton donors/acceptors in the catalytic mechanism of the glutathione reductase of *Escherichia coli*: the role of histidine-439 and tyrosine-99. *Biochemistry* **28**, 9602-9607.

- Dey R, Aral B, Abitbol M & Marsac C (2002). Pyruvate dehydrogenase deficiency as a result of splice-site mutations in the *PDX1* gene. *Mol. Genet. Met.* **76**, 344-347.
- Dey R, Mine M, Desguerre I, Slama A, Van Den Berghe L, Brivet M, Aral B & Marsac C (2003). A new case of pyruvate dehydrogenase deficiency due to a novel mutation in the *PDX1* gene. *Ann. Neurol.* **53**, 273-277.
- Di Mauro S & De Vivo DC (1996). Genetic heterogeneity in Leigh syndrome. *Ann. Neurol.* **40**, 5-7.
- Domingo GJ, Chauhan HJ, Lessard IAD, Fuller C & Perham RN (1999). Self-assembly and catalytic activity of the pyruvate dehydrogenase multienzyme complex from *Bacillus stearothermophilus*. *Eur. J. Biochem.* **266**, 1136-1146.
- Dumas M (2000). Sleeping sickness, a reemerging sickness. *Bull. Acad. Natl. Med.* **184**, 1867-1882.
- Engelman DM & Moore PB (1972). A new method for the determination of biological quaternary structure by neutron scattering. *PNAS* **69**, 1997-1999.
- Feigin LA & Svergun DI (1987). *Structure Analysis by Small Angle X-ray Scattering and Neutron Scattering*. Plenum Press, New York.
- Fiedler E, Thorell S, Sandalova T, Golbik R, Konig S & Schneider G (2002). Snapshot of a key intermediate in enzymatic thiamin catalysis: crystal structure of the alpha-carbanion of (alpha,beta-dihydroxyethyl)-thiamin diphosphate in the active site of transketolase from *Saccharomyces cerevisiae*. *PNAS* **99**, 591-595.
- Fouque F, Marsac C & Benelli C (1998). The pyruvate dehydrogenase complex: from molecular organization to clinical issues. *Med. Sci.* **14**, 1366-1374.
- Frank RAW, Pratap J, Pei XY, Perham RN & Luisi BF (2005). The molecular origins of specificity in the assembly of a multienzyme complex. *Structure* **13**, 1119-1130.

- Frank RAW, Titman CM, Pratap J, Luisi BF & Perham RN (2004). A molecular switch and proton wire synchronize the active sites in thiamine enzymes. *Science* **306**, 872-876.
- Frey P, Flournoy DS, Gruys K & Yang YS (1989). Intermediates in reductive transacetylation catalyzed by pyruvate dehydrogenase complex. *Ann. NY Acad. Sci.* **573**, 21-35.
- Fujiwara K, Okomura-Ikeda K & Motokawa Y (1994). Purification and characterisation of lipoyl-AMP:N epsilon-lysine lipoyltransferase from bovine liver mitochondria. *J. Biol. Chem.* **269**, 16605-16609.
- Fujiwara K, Okomura-Ikeda K & Motokawa Y (1996). Lipoylation of acyltransferase components of alpha-ketoacid dehydrogenase complexes. *J. Biol. Chem.* **271**, 12932-12936.
- Fussey SP, Ali ST, Guest JR, James OF, Bassendine MF & Yeaman SJ (1990). Reactivity of primary biliary cirrhosis sera with *Escherichia coli* dihydrolipoamide acetyltransferase (E2p): characterization of the main immunogenic region. *PNAS* **87**, 3987-3991.
- Fussey SP, Bassendine MF, Fittes D, Turner IB, James OF & Yeaman SJ (1989). The E1 alpha and beta subunits of the pyruvate dehydrogenase complex are M2'd' and M2'e' autoantigens in primary biliary cirrhosis. *Clin. Sci.* **77**, 365-368.
- Fussey SP, Guest JR, James OF, Bassendine MF & Yeaman SJ (1988). Identification and analysis of the major M2 autoantigens in primary biliary cirrhosis. *PNAS* **85**, 8654-8658.
- Fussey SP, Lindsay JG, Fuller C, Perham RN, Dale S, James OFW, Bassendine MF & Yeaman SJ (1991). Autoantibodies in primary biliary cirrhosis - analysis of reactivity against eukaryotic and prokaryotic 2-oxo acid dehydrogenase complexes. *Hepatology* **13**, 467-474.
- García de la Torre J (2001). Hydration from hydrodynamics. General considerations and applications of bead modelling to globular proteins. *Biophys. Chem.* **93**, 159-170.

- García de la Torre J, Huertas ML & Carrasco B (2000). Calculation of hydrodynamic properties of globular proteins from their atomic-level structure. *Biophys. J.* **78**, 719-730.
- Geoffroy V, Fouque F, Benelli C, Poggi F, Saudubray JM, Lissens W, Meirleir LD, Marsac C, Lindsay JG & Sanderson SJ (1996). Defect in the X-lipoyl-containing component of the pyruvate dehydrogenase complex in a patient with a neonatal lactic acidemia. *Pediatrics* **97**, 267-272.
- Ghosh RE, Egelhaaf SU & Rennie AR (1989). A computing guide for small-angle scattering experiments, report no. ILL98GHI4T. In *Technical Report Institut Laue-Langevin*, Grenoble, France.
- Gibson GE, Haroutunian V, Zhang H, Park LC, Shi Q, Lesser M, Mohs RC, Sheu RK & Blass JP (2000). Mitochondrial damage in Alzheimer's disease varies with apolipoprotein E genotype. *Ann. Neurol.* **48**, 297-303.
- Giebeler R (1992). The Optima XLA: a new analytical ultracentrifuge with a novel precision absorption optical system. In *Analytical Ultracentrifugation in Biochemistry and Polymer Science*, SE Harding, AJ Rowe & JC Horton, eds. The Royal Society of Chemistry, Cambridge, pp. 16-25.
- Gilbert GA & Jenkins RC (1956). Boundary problems in the sedimentation and electrophoresis of complex systems in rapid reversible equilibrium. *Nature* **177**, 853-854.
- Glatter O (1977). New method for evaluation of small-angle scattering data. *J. Appl. Cryst.* **10**, 415-421.
- Glatter O (1980). Computation of distance distribution functions and scattering functions of models for small-angle scattering experiments. *Acta Phys. Austriaca* **52**, 243-256.
- Glatter O & Kratky O (1982). *Small Angle X-Ray Scattering*, Academic Press, London.

- Goeddel D, Heyneker H, Hozumi T, Arentzen R, Itakura K, Yansura D, Ross M, Miozzari G, Crea R & Seeburg P (1979a). Direct expression in *Escherichia coli* of a DNA sequence coding for human growth hormone. *Nature* **281**, 544-548.
- Goeddel D, Kleid D, Bolivar F, Heyneker H, Yansura D, Crea R, Hirose T, Kraszewski A, Itakura K & Riggs A (1979b). Expression in *Escherichia coli* of chemically synthesized genes for human insulin. *PNAS* **76**, 106-110.
- Gopalakrishnan S, Rahmatullah M, Radke GA, Powers-Greenwood S & Roche TE (1989). Role of protein X in the function of the mammalian pyruvate dehydrogenase complex. *Biochem. Biophys. Res. Commun.* **160**, 715-721.
- Graham LD, Packman LC & Perham RN (1989). Kinetics and specificity of reductive acylation of lipoyl domains from 2-oxo acid dehydrogenase multienzyme complexes. *Biochemistry* **8**, 1574-1581.
- Grande HJ, Van Telgen HJ & Veeger C (1976). Symmetry and asymmetry of the pyruvate dehydrogenase complexes from *Azotobacter vinelandii* and *Escherichia coli* as reflected by fluorescence and spin-label studies. *Eur. J. Biochem.* **71**, 509-518.
- Green JD, Laue ED, Perham RN, Ali S & Guest JR (1995). Three-dimensional structure of a lipoyl domain from the dihydrolipoyl acetyltransferase component of the pyruvate dehydrogenase multienzyme complex of *Escherichia coli*. *J. Mol. Biol.* **248**, 328-343.
- Green JD, Perham RN, Ullrich SJ & Appella E (1992). Conformational studies of the interdomain linker peptides in the dihydrolipoyl acetyltransferase component of the pyruvate dehydrogenase multienzyme complex of *Escherichia coli*. *J. Biol. Chem.* **267**, 23484-23488.
- Gudi R, Bowker-Kinley MM, Kedishvili NY, Zhao Y & Popov KM (1995). Diversity of the pyruvate dehydrogenase kinase gene family in humans. *J. Biol. Chem.* **270**, 28989-28994.

- Guest JR, Attwood MM, Machado RS, Matqi KY, Shaw JE & Turner SL (1997). Enzymological and physiological consequences of restructuring the lipoyl domain content of the pyruvate dehydrogenase complex of *Escherichia coli*. *Microbiology* **143**, 457-466.
- Guest JR, Lewis HM, Graham LD, Packman LC & Perham RN (1985). Genetic reconstruction and functional analysis of the repeating lipoyl domains in the pyruvate dehydrogenase multienzyme complex of *Escherichia coli*. *J. Mol. Biol.* **185**, 743-754.
- Guex N & Peitsch M (1997). SWISS-MODEL and the Swiss-PdbViewer: an environment for comparative protein modeling. *Electrophoresis* **18**, 2714-2723.
- Guinier A & Fournet G (1955). Small Angle Scattering of X-Rays, Wiley, New York.
- Hackert ML, Oliver RM & Reed LJ (1983). Evidence for a multiple random coupling mechanism in the alpha-ketoglutarate dehydrogenase multienzyme complex of *Escherichia coli*: a computer model analysis. *PNAS* **80**, 2226-2230.
- Hanlon S, Lamers K, Lauterbach G, Johnson R & Schachman HK (1962). Ultracentrifuge studies with absorption optics. I. An automatic photoelectric scanning absorption system. *Arch. Biochem. Biophys.* **99**, 157-174.
- Harding SE, Horton JC, Jones S, Thornton JM & Winzor DJ (1999). COVOL: an interactive program for evaluating second virial coefficients from the triaxial shape or dimensions of rigid macromolecules. *Biophys. J.* **76**, 2432-2438.
- Harmych S, Arnette R & Komuniecki R (2002). Role of dihydrolipoyl dehydrogenase (E3) and a novel E3-binding protein in the NADH sensitivity of the pyruvate dehydrogenase complex from anaerobic mitochondria of the parasitic nematode, *Ascaris suum*. *Mol. Biochem. Parasitol.* **125**, 135-146.
- Harris RA, Bowker-Kinley MM, Huang B & Wu P (2002). Regulation of the activity of the pyruvate dehydrogenase complex. *Adv. Enzyme Regul.* **42**, 249-259.

- Harris RA, Bowker-Kinley MM, Wu P, Jeng J & Popov KM (1997). Dihydrolipoamide dehydrogenase-binding protein of the human pyruvate dehydrogenase complex. DNA-derived amino acid sequence, expression, and reconstitution of the pyruvate dehydrogenase complex. *J. Biol. Chem.* **272**, 19746-19751.
- Harris RA, Huang B & Wu P (2001). Control of pyruvate dehydrogenase kinase gene expression. *Adv. Enzyme Regul.* **41**, 269-288.
- Hasson MS, Muscate A, McLeish MJ, Polovnikova LS, Gerlt JA, Kenyon GL, Petsko GA & Ringe D (1998). The crystal structure of benzoylformate decarboxylase at 1.6 Å resolution: diversity of catalytic residues in thiamin diphosphate-dependent enzymes. *Biochemistry* **37**, 9918-9930.
- Hawkins CF, Borges A & Perham RN (1989). A common structural motif in thiamine pyrophosphate-binding enzymes. *FEBS Lett.* **255**, 77-82.
- Head RA, Brown RM, Zolkipli Z, Shahdadpuri R, King MD, Clayton PT & Brown GK (2005). Clinical and genetic spectrum of pyruvate dehydrogenase deficiency: dihydrolipoamide acetyltransferase (E2) deficiency. *Ann. Neurol.* **58**, 234-241.
- Heller WT, Abusamhadneh E, Finley N, Rosevear PR & Trewella J (2002). The solution structure of a cardiac troponin C-troponin I-troponin T complex shows a somewhat compact troponin C interacting with an extended troponin I-troponin T component. *Biochemistry* **41**, 15654-15663.
- Heller WT, Krueger JK & Trewella J (2003). Further insights into calmodulin-myosin light chain kinase interaction from solution scattering and shape restoration. *Biochemistry* **42**, 10579-10588.
- Heller WT, Vigil D, Brown S, Blumenthal DK, Taylor SS & Trewella J (2004). C subunits binding to the protein kinase A RI alpha dimer induce a large conformational change. *J. Biol. Chem.* **279**, 19084-19090.

- Hengeveld AF, Schoustra SE, Westphal AH & De Kok A (1999). Pyruvate dehydrogenase from *Azotobacter vinelandii*. Properties of the N-terminally truncated enzyme. *Eur. J. Biochem.* **265**, 1098-1107.
- Hipps DS, Packman LC, Allen MD, Fuller C, Sakaguchi K, Appella E & Perham RN (1994). The peripheral subunit binding domain of the dihydrolipoyl acetyltransferase component of the pyruvate dehydrogenase complex of *Bacillus stearothermophilus* - preparation and characterization of its binding to the dihydrolipoyl dehydrogenase component. *Biochem. J.* **297**, 137-143.
- Hiromasa Y, Fujisawa T, Aso Y & Roche TE (2004). Organization of the cores of the mammalian pyruvate dehydrogenase complex formed by E2 and E2 plus the E3-binding protein and their capacities to bind the E1 and E3 components. *J. Biol. Chem.* **279**, 6921-6933.
- Hodgson JA, De Marcucci OG & Lindsay JG (1986). Lipoic acid is the site of substrate-dependent acetylation of component X in ox heart pyruvate dehydrogenase multienzyme complex. *Eur. J. Biochem.* **158**, 595-600.
- Hong YS, Kerr DS, Liu TC, Lusk M, Powell BR & Patel MS (1997). Deficiency of dihydrolipoamide dehydrogenase due to two mutant alleles (E340K and G101del). Analysis of a family and prenatal testing. *Biochim. Biophys. Acta* **1362**, 160-168.
- Hong YS, Korman SH, Lee J, Ghoshal P, Wu Q, Barash V, Kang S, Oh S, Kwon M, Gutman A, Rachmel A & Patel MS (2003). Identification of a common mutation (Gly194Cys) in both Arab Moslem and Ashkenazi Jewish patients with dihydrolipoamide dehydrogenase (E3) deficiency: possible beneficial effect of vitamin therapy. *J. Inherit. Metab. Dis.* **26**, 816-818.
- Hough MA, Grossmann JG, Antonyuk SV, Strange RW, Doucette PA, Rodriguez JA, Whitson LJ, Hart PJ, Hayward LJ, Valentine JS & Hasnain SS (2004). Dimer destabilisation in superoxide dismutase may result in disease-causing properties: structures of motor neuron disease. *PNAS* **101**, 5976-5981.

- Howard MJ, Fuller C, Broadhurst RW, Perham RN, Tang JG, Quinn J, Diamond AG & Yeaman SJ (1998). Three-dimensional structure of the major autoantigen in primary biliary cirrhosis. *Gastroenterology* **115**, 139-146.
- Hoyer S (2004). Causes and consequences of disturbances of cerebral glucose metabolism in sporadic Alzheimer disease: therapeutic implications. *Adv. Exp. Med. Biol.* **541**, 135-152.
- Huang B, Gudi R, Wu P, Harris RA, Hamilton J & Popov KM (1998). Isoenzymes of pyruvate dehydrogenase phosphatase. DNA-derived amino acid sequences, expression, and regulation. *J. Biol. Chem.* **273**, 17680-17688.
- Humphrey W, Dalke A & Schulten K (1996). VMD: visual molecular dynamics. *J. Mol. Graph.* **14**, 33-40.
- Ibel K & Stuhmann HB (1975). Comparison of neutron and X-ray scattering of dilute myoglobin solutions. *J. Mol. Biol.* **93**, 255-265.
- Itakura K, Hirose T, Crea R, Riggs A, Heyneker H, Bolivar F & Boyer H (1977). Expression in *Escherichia coli* of a chemically synthesized gene for hormone somatostatin. *Science* **198**, 1056-1063.
- Iwayama T, Leung PSC, Rowley M, Munoz S, Nishioka M, Nakagawa T, Dickson ER, Coppel RL, Mackay IR & Gershwin ME (1992). Comparative immunoreactive profiles of Japanese and American patients with primary biliary cirrhosis against mitochondrial autoantigens. *Int. Arch. All. Immunol.* **99**, 28-33.
- Izard T, Ævarsson A, Allen MD, Westphal AH, Perham RN, De Kok A & Hol WG (1999). Principles of quasi-equivalence and Euclidean geometry govern the assembly of cubic and dodecahedral cores of pyruvate dehydrogenase complexes. *PNAS* **96**, 1240-1245.
- Jilka JM, Rahmatullah M, Kazemi M & Roche TE (1986). Properties of a newly characterized protein of the bovine kidney pyruvate dehydrogenase complex. *J. Biol. Chem.* **261**, 1858-1867.

- Jones DD, Horne HR, Reche PA & Perham RN (2000). Structural determinants of post-translational modification and catalytic specificity for the lipoyl domains of the pyruvate dehydrogenase multienzyme complex of *Escherichia coli*. *J. Mol. Biol.* **295**, 289-306.
- Joplin R & Gershwin ME (1997). Ductular expression of autoantigens in primary biliary cirrhosis. *Semin. Liver Dis.* **17**, 97-103.
- Joplin RE, Wallace LL, Lindsay JG, Palmer JM, Yeaman SJ & Neuberger JM (1997). The human biliary epithelial cell plasma membrane antigen in primary biliary cirrhosis: pyruvate dehydrogenase X? *Gastroenterology* **113**, 1727-1733.
- Jordan SW & Cronan JE (1997). A new metabolic link. The acyl carrier protein of lipid synthesis donates lipoic acid to the pyruvate dehydrogenase complex in *Escherichia coli* and mitochondria. *J. Biol. Chem.* **272**, 17903-17906
- Jordan SW & Cronan JE (2003). The *Escherichia coli lipB* gene encodes lipoyl (octanoyl)-acyl carrier protein protein transferase. *J. Bacteriol.* **185**, 1582-1589
- Jung III, Bowden SJ, Cooper A & Perham RN (2002a). Thermodynamic analysis of the binding of component enzymes in the assembly of the pyruvate dehydrogenase multienzyme complex of *Bacillus stearothermophilus*. *Prot. Sci.* **11**, 1091-1100.
- Jung HI, Cooper A & Perham RN (2002b). Identification of key amino acid residues in the assembly of enzymes into the pyruvate dehydrogenase complex of *Bacillus stearothermophilus*: a kinetic and thermodynamic analysis. *Biochemistry* **41**, 10446-10453.
- Jung HI, Cooper A & Perham RN (2003). Interactions of the peripheral subunit-binding domain of the dihydrolipoyl acetyltransferase component in the assembly of the pyruvate dehydrogenase multienzyme complex of *Bacillus stearothermophilus*. *Eur. J. Biochem.* **270**, 4488-4496.

- Jung HI & Perham RN (2003). Prediction of the binding site on E1 in the assembly of the pyruvate dehydrogenase multienzyme complex of *Bacillus stearothermophilus*. *FEBS Lett.* **555**, 405-410.
- Kalia YN, Brocklehurst SM, Hipps DS, Appella E, Sakaguchi K & Perham RN (1993). The high-resolution structure of the peripheral subunit-binding domain of dihydrolipoamide acetyltransferase from the pyruvate dehydrogenase multienzyme complex of *Bacillus stearothermophilus*. *J. Mol. Biol.* **230**, 323-341.
- Karplus PA & Schulz GE (1987). Refined structure of glutathione-reductase at 1.54 Å resolution. *J. Mol. Biol.* **195**, 701-729.
- Kato M, Chuang JL, Tso SC, Wynn RM & Chuang DT (2005). Crystal structure of pyruvate dehydrogenase kinase 3 bound to lipoyl domain 2 of human pyruvate dehydrogenase complex. *EMBO J.* **24**, 1763-1774.
- Kern D, Kern G, Neef H, Tittmann K, Killenberg-Jabs M & Wikner C (1997). How thiamine diphosphate is activated in enzymes. *Science* **275**, 67-70.
- Khailova LS & Korochkina LG (1985). Half-of-the-site reactivity of the decarboxylating component of the pyruvate dehydrogenase complex from pigeon breast muscle with respect to 2-hydroxyethyl thiamine pyrophosphate. *Biochem. Int.* **11**, 509-516.
- Khailova LS, Korochkina LG & Severin SE (1990). In *Biochemistry and Physiology of TDP Enzymes*, H Bisswanger & J Ullrich, eds. VCH Weinheim, Blaubeuren, Germany, pp. 251-265.
- Kim H & Patel M (1992). Characterization of two site-specifically mutated human dihydrolipoamide dehydrogenases (His452Gln and Glu457Gln). *J. Biol. Chem.* **267**, 5128-5132.

- Kleiger G, Perry J & Eisenberg D (2001). 3D structure and significance of the GPhiXXG helix packing motif in tetramers of the E1beta subunit of pyruvate dehydrogenase from the archeon *Pyrobaculum aerophilum*. *Biochemistry* **46**, 14484-14492.
- Klingbeil MM, Walker DJ, Arnette R, Sidawy E, Hayton K, Komuniecki PR & Komuniecki R (1996). Identification of a novel dihydrolipoyl dehydrogenase-binding protein in the pyruvate dehydrogenase complex of the anaerobic parasitic nematode *Ascaris suum*. *J. Biol. Chem.* **271**, 5451-5457.
- Klivenyi P, Starkov AA, Calingasan NY, Gardian G, Browne SE, Yang L, Bubber P, Gibson GE, Patel MS & Beal MF (2004). Mice deficient in dihydrolipoamide dehydrogenase show increased vulnerability to MPTP, malonate and 3-nitropropionic acid neurotoxicity. *J. Neurochem.* **88**, 1352-1360.
- Klyachko NL, Shchedrina V, Efimov AV, Kazakov SV, Gazaryan IG, Kristal BS & Brown AM (2005). pH-dependent substrate preference of pig heart lipoamide dehydrogenase varies with oligomeric state: response to mitochondrial matrix acidification. *J. Biol. Chem.* **280**, 16106-16114.
- Kolobova E, Tuganova A, Boulatnikov I & Popov KM (2001). Regulation of pyruvate dehydrogenase activity through phosphorylation at multiple sites. *Biochem. J.* **358**, 69-77.
- Konarev PV, Petoukhov MV & Svergun DI (2001). MASSHA - a graphics system for rigid-body modelling of macromolecular complexes against solution scattering data. *J. Appl. Cryst.* **34**, 527-532.
- Konarev PV, Volkov VV, Sokolova AV, Koch MHJ & Svergun DI (2003). PRIMUS: a Windows PC-based system for small-angle scattering data analysis. *J. Appl. Cryst.* **36**, 1277-1282.
- Kong Y, Ming D, Wu Y, Stoops JK, Zhou ZH & Ma J (2003). Conformational flexibility of pyruvate dehydrogenase complexes: a computational analysis by quantized elastic deformational model. *J. Mol. Biol.* **330**, 129-135.

- Korotchkina LG & Patel MS (1995). Mutagenesis studies of the phosphorylation sites of recombinant human pyruvate dehydrogenase. Site-specific regulation. *J. Biol. Chem.* **270**, 14297-14304.
- Korotchkina LG & Patel MS (2001). Site specificity of four pyruvate dehydrogenase kinase isoenzymes toward the three phosphorylation sites of human pyruvate dehydrogenase. *J. Biol. Chem.* **276**, 37223-37229.
- Kovina MV & Kochetov GA (1998). Cooperativity and flexibility of active sites in homodimeric transketolase. *FEBS Lett.* **440**, 81-87.
- Kozak M & Jurga S (2002). A comparison between the crystal and solution structures of *Escherichia coli* asparaginase II. *Acta Biochim. Pol.* **49**, 509-513.
- Kozin MB & Svergun DI (2001). Automated matching of high- and low-resolution structural models. *J. Appl. Cryst.* **34**, 33-41.
- Kratky O & Pils I (1972). Recent advances and applications of diffuse x-ray small-angle scattering on biopolymers in dilute solutions. *Quart. Rev. Biophys.* **5**, 481-537.
- Kuriyan J (1991). Convergent evolution of similar function in two structurally divergent enzymes. *Nature* **352**, 172-174.
- Kuriyan J, Kong XP, Krishna TSR, Sweet RM, Murgolo NJ, Field H, Cerami A & Henderson GB (1991). X-ray structure of trypanothione reductase from *Crithidia fasciculata* at 2.4 Å resolution. *PNAS* **88**, 8764-8768.
- Laemmli U (1970). Cleavage of structural proteins during the assembly of the head of bacteriophage T4. *Nature* **227**, 680-685.
- Lamm O (1929). Die Differentialgleichung der Ultrazentrifugierung. *Ark. Mat. Astr. Fys.* **21B**, 1-4.

- Lattman EE (1989). Rapid calculation of the solution scattering profile from a macromolecule of known structure. *Proteins* **5**, 149-155.
- Laue TM (1994). An on-line interferometer for the XLA ultracentrifuge. *Prog. Coll. Polym. Sci.* **94**, 74-81.
- Laue TM, Anderson AL & Weber BW (1997). Prototype fluorimeter for the XLA/XLI analytical ultracentrifuge. In *Ultrasensitive Biochemical Diagnostics*, G Cohn & S Soper, eds. SPIE Proceedings, Bellingham, pp. 196-204.
- Laue TM, Shah BD, Ridgeway TM & Pelletier SL (1992). Computer-aided interpretation of analytical sedimentation data for proteins. In *Analytical Ultracentrifugation in Biochemistry and Polymer Science*, SE Harding, AJ Rowe & JC Horton, eds. Royal Society for Chemistry, London, pp. 90-125.
- Lawson JE, Behal RH & Reed LJ (1991a). Disruption and mutagenesis of the *Saccharomyces cerevisiae Pdx1* gene encoding the protein X component of the pyruvate dehydrogenase complex. *Biochemistry* **30**, 2834-2839.
- Lawson JE, Niu XD & Reed LJ (1991b). Functional analysis of the domains of dihydrolipoamide acetyltransferase from *Saccharomyces cerevisiae*. *Biochemistry* **30**, 11249-11254.
- Lebowitz J, Lewis MS & Schuck P (2002). Modern analytical ultracentrifugation in protein science: a tutorial review. *Prot. Sci.* **11**, 2067-2079.
- Lee KK, Gan L, Tsuruta H, Hendrix RW, Duda RL & Johnson JE (2004). Evidence that a local refolding event triggers maturation of HK97 bacteriophage capsid. *J. Mol. Biol.* **340**, 419-433.
- Lessard IA, Domingo GJ, Borges A & Perham RN (1998). Expression of genes encoding the E2 and E3 components of the *Bacillus stearothermophilus* pyruvate dehydrogenase

- complex and the stoichiometry of subunit interaction in assembly *in vitro*. *Eur. J. Biochem.* **258**, 491-501.
- Lessard IA & Perham RN (1995). Interaction of component enzymes with the peripheral subunit-binding domain of the pyruvate dehydrogenase multienzyme complex of *Bacillus stearothermophilus*: stoichiometry and specificity in self-assembly. *Biochem. J.* **306**, 727-733.
- Lessard IAD, Fuller C & Perham RN (1996). Competitive interaction of component enzymes with the peripheral subunit-binding domain of the pyruvate dehydrogenase multienzyme complex of *Bacillus stearothermophilus*: kinetic analysis using surface plasmon resonance detection. *Biochemistry* **35**, 16863-16870.
- Leung PSC, Iwayama T, Coppel RL & Gershwin ME (1990). Site-directed mutagenesis of lysine within the immunodominant autoepitope of PDC-E2. *Hepatology* **12**, 1321-1328.
- Leung PSC, Van de Water J, Coppel RL, Nakanuma Y, Munoz S & Gershwin ME (1996). Molecular aspects and the pathological basis of primary biliary cirrhosis. *J. Autoimmun.* **9**, 119-128.
- Li L, Radke GA, Ono K & Roche TE (1992). Additional binding sites for the pyruvate dehydrogenase kinase but not for protein X in the assembled core of the mammalian pyruvate dehydrogenase complex: binding region for the kinase. *Arch. Biochem. Biophys.* **296**, 497-504.
- Lindsay H, Beaumont E, Richards SD, Kelly SM, Sanderson SJ, Price NC & Lindsay JG (2000). FAD insertion is essential for attaining the assembly competence of the dihydrolipoamide dehydrogenase (E3) monomer from *Escherichia coli*. *J. Biol. Chem.* **275**, 36665-36670.
- Ling MF, McEachern G, Seyda A, MacKay N, Scherer SW, Bratinova S, Beatty B, Giovannucci-Uzielli ML & Robinson BH (1998). Detection of a homozygous four base

- pair deletion in the protein X gene in a case of pyruvate dehydrogenase complex deficiency. *Hum. Mol. Genet.* **7**, 501-505.
- Linn TC, Pettit FH & Reed LJ (1969). Alpha-keto acid dehydrogenase complexes: comparative studies of regulatory properties of the pyruvate dehydrogenase complexes from kidney, heart, and liver mitochondria. *PNAS* **62**, 227-234.
- Lissens W, De Meirlier L, Seneca S, Liebaers I, Brown GK, Brown RM, Ito M, Naito E, Kuroda Y, Kerr DS, Wexler ID, Patel MS, Robinson BH & Seyda A (2000). Mutations in the X-linked pyruvate dehydrogenase (E1) alpha subunit gene (*PDHA1*) in patients with a pyruvate dehydrogenase complex deficiency. *Hum. Mutat.* **15**, 209-219.
- Liu S, Baker JC & Roche TE (1995a). Binding of the pyruvate dehydrogenase kinase to recombinant constructs containing the inner lipoyl domain of the dihydrolipoyl acetyltransferase component. *J. Biol. Chem.* **270**, 793-800.
- Liu S, Gong X, Yan X, Peng T, Baker JC, Li L, Robben PM, Ravindran S, Andersson LA, Cole AB & Roche TE (2001). Reaction mechanism for mammalian pyruvate dehydrogenase using natural lipoyl domain substrate. *Arch. Biochem. Biophys.* **286**, 123-135.
- Liu TC, Korotchkina LG, Hyatt SL, Vettaikorumakankauv NN & Patel MS (1995b). Spectroscopic studies of the characterization of recombinant human dihydrolipoamide dehydrogenase and its site-directed mutants. *J. Biol. Chem.* **270**, 15545-15550.
- Long SA, Quan C, Van de Water J., Nantz MH, Kurth MJ, Barsky ME, Colvin ME & Coppel RL (2005). Immunoreactivity of organic mimetopes of the E2 component of pyruvate dehydrogenase: connecting xenobiotics with primary biliary cirrhosis. *J. Immunol.* **167**, 2956.
- Mackay IR, Whittingham S, Fida S, Myers M, Ikuno N, Gershwin ME & Rowley MJ (2000). The peculiar autoimmunity of primary biliary cirrhosis. *Immunol. Rev.* **174**, 226-237.

- Maeng CY, Yazdi MA, Niu XD, Lee HY & Reed LJ (1994). Expression, purification and characterization of the dihydrolipoamide dehydrogenase-binding protein of the pyruvate dehydrogenase complex from *Saccharomyces cerevisiae*. *Biochemistry* **33**, 13801-13807.
- Mande SS, Sarfaty S, Allen MD, Perham RN & Hol WG (1996). Protein-protein interactions in the pyruvate dehydrogenase multienzyme complex: dihydrolipoamide dehydrogenase complexed with the binding domain of dihydrolipoamide acetyltransferase. *Structure* **4**, 277-286.
- Maniatis T, Fritsch EF & Sambrook J (1987a). Gel electrophoresis. In *Molecular cloning - a laboratory manual*, Cold Spring Harbor Laboratory Press, Cold Spring Harbor, pp. 149-186.
- Maniatis T, Fritsch EF & Sambrook J (1987b). Introduction of plasmid and bacteriophage DNA into *Escherichia coli*. In *Molecular cloning - a laboratory manual*, Cold Spring Harbor Laboratory Press, Cold Spring Harbor, pp. 247-268.
- Marquez JA, Smith CIE, Petoukhov MV, Lo Surdo P, Mattsson PT, Knekt M, Westlund A, Scheffzek K, Saraste M & Svergun DI (2003). Conformation of full-length Bruton tyrosine kinase (Btk) from synchrotron X-ray solution scattering. *EMBO J.* **22**, 4616-4624.
- Marsac C, Stansbie D, Bonne G, Cousin J, Jehenson P, Benelli C, Leroux JP & Lindsay G (1993). Defect in the lipoyl-bearing protein X subunit of the pyruvate dehydrogenase complex in 2 patients with encephalomyelopathy. *J. Pediatr.* **123**, 915-920.
- Mattevi A, Obmolova G, Kalk KH, van Berkel WJH & Hol WG (1993a). Three-dimensional structure of lipoamide dehydrogenase from *Pseudomonas fluorescens* at 2.8 Å resolution. *J. Mol. Biol.* **230**, 1200-1215.
- Mattevi A, Obmolova G, Kalk KH, Westphal AH, De Kok A & Hol WG (1993b). Refined crystal structure of the catalytic domain of dihydrolipoyl transacetylase (E2p) from *Azotobacter vinelandii* at 2.6 Å resolution. *J. Mol. Biol.* **230**, 1183-1199.

- Mattevi A, Obmolova G, Schulze E, Kalk KH, Westphal AH, De Kok A & Hol WG (1992a). Atomic structure of the cubic core of the pyruvate dehydrogenase multienzyme complex. *Science* **255**, 1544-1550.
- Mattevi A, Obmolova G, Sokatch JR, Betzel C & Hol WG (1992b). The refined crystal structure of *Pseudomonas putida* lipoamide dehydrogenase complexed with NAD<sup>+</sup> at 2.45 Å resolution. *Proteins* **13**, 336-351.
- Mattevi A, Obmolova G, Kalk KH, Teplyakov A & Hol WGJ (1993c). Crystallographic analysis of substrate binding and catalysis in dihydrolipoyl transacetylase. *Biochemistry* **32**, 3887-3901.
- Mattevi A, Schierbeek AJ & Hol WG (1991). Refined crystal structure of lipoamide dehydrogenase from *Azotobacter vinelandii* at 2.2 Å resolution. *J. Mol. Biol.* **220**, 975-994.
- Mayers RM, Butlin RJ, Kilgour E, Leighton B, Martin D, Myatt J, Orme JP & Holloway BR (2003). AZD7545, a novel inhibitor of pyruvate dehydrogenase kinase 2 (PDHK2), activates pyruvate dehydrogenase *in vivo* and improves blood glucose control in obese (fa/fa) Zucker rats. *Biochem. Soc. Trans.* **31**, 1165-1167.
- Mayers RM, Leighton B & Kilgour E (2005). PDH kinase inhibitors: a novel therapy for Type II diabetes? *Biochem. Soc. Trans.* **33**, 367-370.
- McCartney R (1998). Folding and assembly studies on the composition of mammalian PDC and OGDC. University of Glasgow, PhD thesis.
- McCartney R, Sanderson SJ & Lindsay JG (1997). Refolding and reconstitution studies on the transacetylase protein X (E2/X) subcomplex of the mammalian pyruvate dehydrogenase complex: evidence for specific binding of the dihydrolipoamide dehydrogenase component to sites on reassembled E2. *Biochemistry* **36**, 6819-6826.

- Miles JS, Guest JR, Radford SE & Perham RN (1988). Investigation of the mechanism of active-site coupling in the pyruvate dehydrogenase multienzyme complex of *Escherichia coli* by protein engineering. *J. Mol. Biol.* **202**, 97-106.
- Miller JR, Busby RW, Jordan SW, Cheek J, Henshaw TF, Ashley GW, Broderick JB, Cronin JE & Marletta MA (2000). *Escherichia coli* LipA is a lipoyl synthase: *in vitro* biosynthesis of lipoylated pyruvate dehydrogenase complex from octanoyl-acyl carrier protein. *Biochemistry* **39**, 15166-15678
- Milne JLS, Shi D, Rosenthal PB, Sunshine JS, Domingo GJ, Wu XW, Brooks BR, Perham RN, Henderson R & Subramaniam S (2002). Molecular architecture and mechanism of an icosahedral pyruvate dehydrogenase complex: a multifunctional catalytic machine. *EMBO J.* **21**, 5587-5598.
- Milne JLS, Wu X, Borgnia MJ, Lengyel JS, Brooks BR, Shi D, Perham RN & Subramaniam S (2005). Molecular structure of a 9 MDa icosahedral pyruvate dehydrogenase sub-complex containing the E2 and E3 enzymes using cryo-electron microscopy. *J. Biol. Chem.*, in press.
- Morrell JA, Orme J, Butlin RJ, Roche TE, Mayers RM & Kilgour E (2003). AZD7545 is a selective inhibitor of pyruvate dehydrogenase kinase 2. *Biochem. Soc. Trans.* **31**, 1168-1170.
- Morris TW, Reed KE & Cronan JE (1994). Identification of the gene encoding lipoate protein ligase A of *Escherichia coli*. Molecular cloning and characterisation of the *lplA* gene and gene product. *J. Biol. Chem.* **239**, 16091-16100.
- Morris TW, Reed KE & Cronin JE (1995). Lipoic acid metabolism in *Escherichia coli*: the *lplA* and *lipB* genes define redundant pathways for ligation of lipoyl groups to apoprotein. *J. Bacteriol.* **177**, 1-10
- Morten KJ, Beattie P, Brown GK & Matthews PM (1999). Dichloroacetate stabilizes the mutant E1alpha subunit in pyruvate dehydrogenase deficiency. *Neurology* **53**, 612-616.

- Muller YA, Lindqvist Y, Furey W, Schulz GE, Jordan F & Schneider G (1993). A thiamine diphosphate binding fold revealed by comparison of the crystal structures of transketolase, pyruvate oxidase and pyruvate decarboxylase. *Structure* **1**, 95-103.
- Naito E, Ito M, Yakota I, Saijo T, Ogawa Y & Kuroda Y (2002). Diagnosis and molecular analysis of three male patients with thiamine-responsive pyruvate dehydrogenase complex deficiency. *J. Neurol. Sci.* **201**, 33-37.
- Nakasako M, Fujisawa T, Adachi S, Kudo T & Higuchi S (2001). Large-scale domain movements and hydration structure changes in the active-site cleft of unligated glutamate dehydrogenase from *Thermococcus profundus* studied by cryogenic x-ray crystal structure analysis and small-angle x-ray scattering. *Biochemistry* **40**, 3069-3079.
- Neagle J, De Marcucci O, Dunbar B & Lindsay JG (1989). Component X of mammalian pyruvate dehydrogenase complex: structural and functional relationship to the lipoate acetyltransferase (E2) component. *FEBS Lett.* **253**, 11-15.
- Neagle JC & Lindsay JG (1991). Selective proteolysis of the protein X subunit of the bovine heart pyruvate dehydrogenase complex - effects on dihydrolipoamide dehydrogenase (E3) affinity and enzymatic properties of the complex. *Biochem. J.* **278**, 423-427.
- Neveling U, Bringer-Meyer S & Sahm H (1998a). Gene and subunit organization of bacterial pyruvate dehydrogenase complexes. *Biochim. Biophys. Acta* **1385**, 367-372.
- Neveling U, Klasen R, Bringer-Meyer S & Sahm H (1998b). Purification of the Pyruvate Dehydrogenase Multienzyme Complex of *Zymomonas mobilis* and Identification and Sequence Analysis of the Corresponding Genes. *J. Bacteriol.* **180**, 1540-1548.
- Nöllmann M, Stark WM & Byron O (2004). Low-resolution reconstruction of a synthetic DNA Holliday junction. *Biophys. J.* **86**, 3060-3069.
- Nöllmann M, Stark WM & Byron O (2005). A global multi-technique approach to study low-resolution solution structures. *J. Appl. Cryst.* **38**, 874-887.

- Odievre MH, Chretien D, Munnich A, Robinson BH, Dumoulin R, Masmoudi S, Kadhom N, Rotig A, Rustin P & Bonnefort JP (2005). A novel mutation in the dihydrolipoamide dehydrogenase E3 subunit gene (DLD) resulting in an atypical form of  $\alpha$ -ketoglutarate dehydrogenase deficiency. *Hum. Mutat.* **25**, 323-324.
- Oliver RM & Reed LJ (1982). In *Electron Microscopy of Proteins Vol.2*, R Harris, ed. Academic Press, London, pp. 1-48.
- Packman LC & Perham RN (1986). Chain folding in the dihydrolipoyl acyltransferase components of the 2-oxo acid dehydrogenase complexes from *Escherichia coli* - identification of a segment involved in binding the E3 subunit. *FEBS Lett.* **206**, 193-198.
- Pan K & Jordan F (1998). D,L-S-methylipoic acid methyl ester, a kinetically viable model for S-protonated lipoic acid as the oxidizing agent in reductive acyl transfers catalyzed by the 2-oxoacid dehydrogenase multienzyme complexes. *Biochemistry* **37**, 1357-1364.
- Patel MS & Harris RA (1995). Mammalian alpha-keto acid dehydrogenase complexes: gene regulation and genetic defects. *FASEB J.* **9**, 1164-1172.
- Patel MS & Korotchkina LG (2001). Regulation of mammalian pyruvate dehydrogenase complex by phosphorylation: complexity of multiple phosphorylation sites and kinases. *Exp. Mol. Med.* **33**, 191-197.
- Patel MS & Korotchkina LG (2003). The biochemistry of the pyruvate dehydrogenase complex. *Biochem. Mol. Biol. Education* **31**, 5-15.
- Patel MS, Naik MT, Johnson M & Dey R (1996). In  *$\alpha$ -Keto Acid Dehydrogenase Complexes*, MS Patel, TE Roche & RA Harris, eds. Birkhäuser Verlag, Basel, Switzerland, pp. 197-211.
- Patel MS, Naik S, Wexler ID & Kerr DS (1995). Gene regulation and genetic defects in the pyruvate dehydrogenase complex. *J. Nutr.* **125**, 1753S-1757S.

- Patel MS & Roche TE (1990). Molecular biology and biochemistry of pyruvate dehydrogenase complexes. *FASEB J.* **4**, 3224-3233.
- Peitsch M, Schwede T & Guex N (2000). Automated protein modelling - the proteome in 3D. *Pharmacogenomics* **1**, 257-266.
- Perham RN (1991). Domains, motifs, and linkers in 2-oxo acid dehydrogenase multienzyme complexes: a paradigm in the design of a multifunctional protein. *Biochemistry* **30**, 8501-8512.
- Perham RN (2000). Swinging arms and swinging domains in multifunctional enzymes: catalytic machines for multistep reactions. *Ann. Rev. Biochem.* **69**, 961-1004.
- Perham RN, Duckworth HW & Roberts GC (1981). Mobility of polypeptide chain in the pyruvate dehydrogenase complex revealed by proton NMR. *Nature* **292**, 474-477.
- Perkins S (1988). X-ray and neutron solution scattering. In *New Comprehensive Biochemistry*, A Neuberger & L van Deenen, eds. Elsevier, Amsterdam, pp. 143-263.
- Petoukhov MV, Eady NAJ, Brown KA & Svergun DI (2002). Addition of missing loops and domains to protein models by X-ray solution scattering. *Biophys. J.* **83**, 3113-3125.
- Petoukhov MV & Svergun DI (2003). New methods for domain structure determination of proteins from solution scattering data. *J. Appl. Cryst.* **36**, 540-544.
- Petoukhov MV & Svergun DI (2005). Global rigid body modeling of macromolecular complexes against small-angle scattering data. *Biophys. J.* **89**, 1237-1250.
- Petoukhov MV, Svergun DI, Konarev PV, Ravasio S, van den Heuvel RHH, Curti B & Vanoni MA (2003). Quaternary structure of *Azospirillum brasilense* NADPH-dependent glutamate synthase in solution as revealed by synchrotron radiation x-ray scattering. *J. Biol. Chem.* **278**, 29933-29939.

- Pettit FH, Roche TE & Reed LJ (1972). Function of calcium ions in pyruvate dehydrogenase phosphatase activity. *Biochem. Biophys. Res. Commun.* **49**, 563-571.
- Pierce MM, Raman CS & Nall BT (1999). Isothermal titration calorimetry of protein-protein interactions. *Methods* **19**, 213-221.
- Plum F & Posner JB (1980). *The Diagnosis of Stupor and Coma*, FA Davis, Philadelphia.
- Popov KM, Kedishvili NY, Zhao Y, Gudi R & Harris RA (1994). Molecular cloning of the p45 subunit of pyruvate dehydrogenase kinase. *J. Biol. Chem.* **269**, 29720-29724.
- Powers-Greenwood SL, Rahmatullah M, Radke GA & Roche TE (1989). Separation of protein X from the dihydrolipoyl transacetylase component of the mammalian pyruvate dehydrogenase complex and function of protein X. *J. Biol. Chem.* **264**, 3655-3657.
- Provencher SW & Glockner J (1981). Estimation of globular protein secondary structure from circular dichroism. *Biochemistry* **20**, 33-37.
- Quinn J, Diamond AG, Masters AK, Brookfield DE, Wallis NG & Yeaman SJ (1993). Expression and lipoylation in *Escherichia coli* of the inner lipoyl domain of the E2 component of the human pyruvate dehydrogenase complex. *Biochem. J.* **289**, 81-85.
- Radford SE, Laue ED, Perham RN, Martin S & Appella E (1989a). Conformational flexibility and folding of synthetic peptides representing an interdomain segment of polypeptide chain the pyruvate dehydrogenase complex of *Escherichia coli*. *J. Biol. Chem.* **264**, 767-775.
- Radford SE, Laue ED, Perham RN, Miles JS & Guest JR (1987). Segmental structure and protein domains in the pyruvate dehydrogenase multienzyme complex of *Escherichia coli*. Genetic reconstruction *in vitro* and  $^1\text{H}$ -NMR spectroscopy. *Biochem. J.* **247**, 641-649.

- Radford SE, Perham RN, Ulrich SJ & Appella E (1989b). Antibodies against an inter-domain segment of polypeptide chain inhibit active-site coupling in the pyruvate dehydrogenase multienzyme complex. *FEBS Lett.* **250**, 336-340.
- Rahmatullah M, Gopalakrishnan S, Andrews PC, Chang CL, Radke GA & Roche TE (1989a). Subunit associations in the mammalian pyruvate dehydrogenase complex. Structure and role of protein X and the pyruvate dehydrogenase component binding domain of the dihydrolipoyl transacetylase component. *J. Biol. Chem.* **264**, 2221-2227.
- Rahmatullah M, Gopalakrishnan S, Radke GA & Roche TE (1989b). Domain structures of the dihydrolipoyl transacetylase and the protein X components of mammalian pyruvate dehydrogenase complex. Selective cleavage by protease Arg C. *J. Biol. Chem.* **264**, 1245-1251.
- Rahmatullah M, Radke GA, Andrews PC & Roche TE (1990). Changes in the core of the mammalian-pyruvate dehydrogenase complex upon selective removal of the lipoyl domain from the transacetylase component but not from the protein X component. *J. Biol. Chem.* **265**, 14512-14517.
- Rahmatullah M & Roche TE (1987). The catalytic requirements for reduction and acetylation of protein X and the related regulation of various forms of resolved pyruvate dehydrogenase kinase. *J. Biol. Chem.* **262**, 10265-10271.
- Ralston G (1993). Introduction to Analytical Ultracentrifugation, Beckman, Fullerton, USA.
- Ramadan DG, Head RA, Al-Tawari A, Habeeb Y, Zaki M, Al-Ruqum F, Besley GTN, Wraith JE, Brown RM & Brown GK (2004). Lactic acidosis and developmental delay due to deficiency of E3 binding protein (protein X) of the pyruvate dehydrogenase complex. *J. Inherit. Metab. Dis.* **27**, 477-485.
- Randle PJ (1986). Fuel selection in animals. *Biochem. Soc. Trans.* **14**, 799-806.

- Randle PJ, Priestman DA, Mistry S & Halsall A (1994). Mechanisms modifying glucose oxidation in diabetes mellitus. *Diabetologia* **37**, S155-S161.
- Reed LJ (1974). Multienzyme complexes. *Acc. Chem. Res.* **7**, 40-46.
- Reed LJ (2001). A trail of research from lipoic acid to alpha-keto acid dehydrogenase complexes. *J. Biol. Chem.* **276**, 38329-38336.
- Reed LJ & Hackert ML (1990). Structure-function relationships in dihydrolipoamide acyltransferases. *J. Biol. Chem.* **265**, 8971-8974.
- Reed LJ, Lawson JE, Niu XD & Yan J (1996). In  *$\alpha$ -Keto Acid Dehydrogenase Complexes*, MS Patel, TE Roche & RA Harris, eds. Birkhäuser Verlag, Basel, Switzerland, pp. 131-138.
- Reed LJ & Oliver RM (1968). The multienzyme alpha-keto acid dehydrogenase complexes. *Brookhaven Symp. Biol.* **21**, 397-412.
- Reiman EM, Caselli RJ, Yun LS, Chen K, Bandy D, Minoshima S, Thibodeau SN & Osborne D (1996). Preclinical evidence of Alzheimer's disease in persons homozygous for the epsilon 4 allele for apolipoprotein E. *New Engl. J. Med.* **334**, 752-758.
- Ricaud PM, Howard MJ, Roberts EL, Broadhurst RW & Perham RN (1996). Three-dimensional structure of the lipoyl domain from the dihydrolipoyl succinyltransferase component of the 2-oxoglutarate dehydrogenase multienzyme complex of *Escherichia coli*. *J. Mol. Biol.* **264**, 179-190.
- Richards SD (1999). Protein-protein interactions within the 2-oxoacid dehydrogenase complexes. University of Glasgow, PhD thesis.
- Roberts GC, Duckworth HW, Packman LC & Perham RN (1983). Mobility and active-site coupling in 2-oxo acid dehydrogenase complexes. *Ciba Found. Symp.* **93**, 47-71.

- Robinson BH (1995). Lactic acidemia - disorders of pyruvate carboxylase, pyruvate dehydrogenase. In *The Metabolic and Molecular Basis of Inherited Disease*, CR Scriver, AL Beaudet, WS Sly & D Valle, eds. McGraw Hill, New York, pp. 1479-1499.
- Robinson BH, MacKay N, Petrova-Benedict R, Ozalp I, Coskun T & Stacpoole PW (1990). Defects in the E2 lipoyl transacetylase and the X-lipoyl containing component of the pyruvate dehydrogenase complex in patients with lactic acidemia. *J. Clin. Invest.* **85**, 1821-1824.
- Robinson BH, MacMillan H, Petrova-Benedict R & Sherwood WG (1987). Variable clinical presentation in patients with defective E1 component of pyruvate dehydrogenase complex. *J. Pediatr.* **111**, 525-533.
- Roche TE, Hiromasa Y, Turkan A, Gong X, Peng T, Yan X, Kasten SA, Bao H & Dong J (2003). Essential roles of lipoyl domains in the activated function and control of pyruvate dehydrogenase kinases and phosphatase isoform 1. *Eur. J. Biochem.* **270**, 1050-1056.
- Roche TE, Powers-Greenwood S, Shi W, Zhang WB, Ren SZ, Roche ED, Cox DJ & Sorensen CM (1993). Sizing of bovine heart and kidney pyruvate dehydrogenase complex and dihydrolipoyltransacetylase core by quasi-elastic light scattering. *Biochemistry* **32**, 5629-5637.
- Rosen BP (1995). Resistance mechanisms to arsenicals and antimonials. *J. Basic Clin. Physiol. Pharmacol.* **6**, 251-263.
- Rowles J, Scherer SW, Xi T, Majer M, Nickle DC, Rommers JM, Popov KM, Harris RA & Riebow NL (1996). Cloning and characterization of PDK4 on 7q21.3 encoding a fourth pyruvate dehydrogenase kinase isoenzyme in human. *J. Biol. Chem.* **271**, 22376-22382.
- Sanderson SJ, Khan SS, McCartney R, Miller C & Lindsay JG (1996a). Reconstitution of mammalian pyruvate dehydrogenase and 2-oxoglutarate dehydrogenase complexes: Analysis of protein X involvement and interaction of homologous and heterologous dihydrolipoamide dehydrogenases. *Biochem. J.* **319**, 109-116.

- Sanderson SJ, Miller C & Lindsay JG (1996b). Stoichiometry, organisation and catalytic function of protein X of the pyruvate dehydrogenase complex from bovine heart. *Eur. J. Biochem.* **236**, 68-77.
- Schachman HK (1959). *Ultracentrifugation in Biochemistry*, Academic Press, New York.
- Schachman HK, Gropper L, Hanlon S & Putney F (1962). Ultracentrifuge studies with absorption optics. II. Incorporation of a monochromator and its application to the study of proteins and interacting systems. *Arch. Biochem. Biophys.* **99**, 175-190.
- Schellenberger A (1998). Sixty years of thiamine diphosphate biochemistry. *Biochim. Biophys. Acta* **1385**, 177-186.
- Schierbeek AJ, Swarte M, Dijkstra BW, Vriend G, Read RJ, Hol WG, Drenth J & Betzel C (1989). X-ray structure of lipoamide dehydrogenase from *Azotobacter vinelandii* determined by a combination of molecular and isomorphous replacement techniques. *J. Mol. Biol.* **206**, 365-379.
- Schmidt B & Riesner D (1992). A fluorescence detection system for the analytical ultracentrifuge and its application to proteins, nucleic acids, viroids and viruses. In *Analytical Ultracentrifugation in Biochemistry and Polymer Science*, SE Harding, AJ Rowe & JC Horton, eds. The Royal Society of Chemistry, Cambridge, pp. 176-207.
- Schuck P (2000). Size distribution analysis of macromolecules by sedimentation velocity ultracentrifugation and Lamm equation modeling. *Biophys. J.* **78**, 1606-1619.
- Schuck P (2003). On the analysis of protein self-association by sedimentation velocity analytical ultracentrifugation. *Anal. Biochem.* **320**, 104-124.
- Schuck P, Perugini MS, Gonzales NR, Howlett GJ & Schubert D (2002). Size-distribution analysis of proteins by analytical ultracentrifugation: strategies and application to model systems. *Biophys. J.* **82**, 1096-1111.

- Schulz GE, Schirmer RH, Sachsenheimer W & Pai EF (1978). Structure of flavoenzyme glutathione reductase. *Nature* **273**, 120-124.
- Schulze E, Westphal AH, Hanemaaijer R & De Kok A (1993). Structure/function relationships in the pyruvate dehydrogenase complex from *Azotobacter vinelandii*. Role of the linker region between the binding and catalytic domain of the dihydrolipoyl transacetylase component. *Eur. J. Biochem.* **211**, 591-599.
- Scouten WH, Visser AJWG, Grande HJ & De Kok A (1980). Fluorescence polarization and energy-transfer studies on the pyruvate dehydrogenase complex of *Escherichia coli*. *Eur. J. Biochem.* **112**, 9-16.
- Semenyuk AV & Svergun DI (1991). GNOM - a program package for small angle scattering data processing. *J. Appl. Cryst.* **24**, 537-540.
- Sergienko SA & Jordan F (2002). Yeast pyruvate decarboxylase tetramers can dissociate into dimers along two interfaces. Hybrids of low-activity D28A (or D28N) and E477Q variants, with substitution of adjacent active center acidic groups from different subunits, display restored activity. *Biochemistry* **41**, 3952-3967.
- Sergienko SA, Wang J, Polovnikova L, Hasson MS, McLeish MJ, Kenyon GL & Jordan F (2000). Spectroscopic detection of transient thiamine diphosphate-bound intermediates on benzoylformate decarboxylase. *Biochemistry* **39**, 13862-13869.
- Seyda A, McEachern G, Haas R & Robinson BH (2000). Sequential deletion of C-terminal amino acids of the E1 $\alpha$  component of the pyruvate dehydrogenase (PDH) complex leads to reduced steady-state levels of functional E1 tetramers: implications for patients with PDH deficiency. *Hum. Mol. Genet.* **9**, 1041-1048.
- Seyda A & Robinson BH (2000). Expression and functional characterization of human protein X variants in SV40-immortalized protein X-deficient and E2-deficient human skin fibroblasts. *Arch. Biochem. Biophys.* **382**, 219-223.

- Shany E, Saada A, Landau D, Shaag A, HersHKovitz E & Elpeleg ON (1999). Lipoamide dehydrogenase deficiency due to a novel mutation in the interface domain. *Biochem. Biophys. Res. Commun.* **262**, 163-166.
- Shepherd GB & Hammes GG (1977). Fluorescence energy-transfer measurements in pyruvate dehydrogenase multienzyme complex from *Escherichia coli* with chemically modified lipoic acid. *Biochemistry* **16**, 5234-5241.
- Sheu KF & Blass JP (1999). The alpha-ketoglutarate dehydrogenase complex. *Ann. NY Acad. Sci.* **893**, 61-78.
- Sheu KF, Cooper AJ, Koike K, Koike M, Lindsay JG & Blass JP (1994). Abnormality of the alpha-ketoglutarate dehydrogenase complex in fibroblasts from familial Alzheimer's disease. *Ann. Neurol.* **35**, 312-318.
- Shi Q, Chen HL, Xu H & Gibson GE (2005). Reduction in the E2k subunit of the alpha-ketoglutarate dehydrogenase complex by antisense RNA exaggerates the response to oxidative stress. *J. Biol. Chem.* **280**, 10888-10896.
- Shoffner JM (1997). Oxidative phosphorylation defects and Alzheimer's disease. *Neurogen.* **1**, 13-19.
- Sims NR, Anderson MF, Hobbs LM, Kong JY, Phillips S, Powell JA & Zaidan E (2000). Impairment of brain mitochondrial function by hydrogen peroxide. *Brain Res. Mol. Brain Res.* **77**, 176-184.
- Small GW, Mazziotta JC, Collins MT, Baxter LR, Phelps ME, Mandelkern MA, Kaplan A, La Rue A, Adamson CF, Chang L & et al. (1995). Apolipoprotein E type 4 allele and cerebral glucose metabolism in relatives at risk for familial Alzheimer disease. *JAMA* **273**, 942-947.

- Sokolova A, Malfois M, Caldentey J, Svergun DI, Koch MHJ, Bamford D & Tuma R (2001). Solution structure of bacteriophage PRD1 vertex complex. *J. Biol. Chem.* **276**, 46187-46195.
- Spector S, Kuhlman B, Fairman R, Wong E, Boice JA & Raleigh DP (1998). Cooperative folding of a protein mini domain: the peripheral subunit-binding domain of the pyruvate dehydrogenase multienzyme complex. *J. Mol. Biol.* **276**, 479-489.
- Spector S, Rosconi M & Raleigh DP (1999b). Conformational analysis of peptide fragments derived from the peripheral subunit-binding domain from the pyruvate dehydrogenase multienzyme complex of *Bacillus stearothermophilus*: evidence for nonrandom structure in the unfolded state. *Biopolymers* **49**, 29-40.
- Spector S, Young P & Raleigh DP (1999a). Nativelike structure and stability in a truncation mutant of a protein minidomain: the peripheral subunit-binding domain. *Biochemistry* **38**, 4128-4136.
- Sreerama N & Woody RW (2000). Estimation of protein secondary structure from circular dichroism spectra: comparison of CONTIN, SELCON, and CDSSTR methods with an expanded reference set. *Anal. Biochem.* **287**, 252-260.
- Stacpoole PW, Henderson GN, Yan Z, Cornett R & James M (1998). Pharmacokinetics, metabolism and toxicology of dichloroacetate. *Drug Metab. Rev.* **30**, 499-539.
- Stacpoole PW, Moore GW & Kornhauser DM (1978). Metabolic effects of dichloroacetate in patients with diabetes mellitus and hyperlipoproteinemia. *N. Engl. J. Med.* **298**, 526-530.
- Stanley CJ & Perham RN (1980). Purification of 2-oxo acid dehydrogenase multienzyme complexes from ox heart by a new method. *Biochem. J.* **191**, 147-154.
- Stepp LR, Bleile DM, McRorie DK, Pettit FH & Reed LJ (1981). Use of trypsin and lipoamidase to study the role of lipoic acid moieties in the pyruvate and alpha-ketoglutarate dehydrogenase complexes of *Escherichia coli*. *Biochemistry* **20**, 4555-4560.

- Steussy CN, Popov KM, Bowker-Kinley MM, Sloan R, Harris RA & Hamilton JA (2001). Structure of pyruvate dehydrogenase kinase. Novel folding pattern for a serine protein kinase. *J. Biol. Chem.* **276**, 37443-37450.
- Stoops JK, Baker TS, Schroeter JP, Kolodziej SJ, Niu XD & Reed LJ (1992). 3-dimensional structure of the truncated core of the *Saccharomyces cerevisiae* pyruvate dehydrogenase complex determined from negative stain and cryoelectron microscopy images. *J. Biol. Chem.* **267**, 24769-24775.
- Stoops JK, Cheng RH, Yazdi MA, Maeng CY, Schroeter JP, Klueppelberg U, Kolodziej SJ, Baker TS & Reed LJ (1997). On the unique structural organization of the *Saccharomyces cerevisiae* pyruvate dehydrogenase complex. *J. Biol. Chem.* **272**, 5757-5764.
- Strumilo S (2005). Short-term regulation of the mammalian pyruvate dehydrogenase complex. *Acta Biochim. Pol.*, in press.
- Stuhrmann HB (1970). New method for determination of surface form and internal structure of dissolved globular proteins from small angle x-ray measurements. *Zeitschr. Phys. Chem.* **72**, 177-198.
- Sugden MS & Holness MJ (2003). Recent advances in regulating glucose oxidation at the level of the pyruvate dehydrogenase complex by PDKs. *Am. J. Physiol. Endocrinol. Metab.* **284**, E855-E862.
- Surh CD, Coppel RL & Gershwin ME (1990). Structural requirement for autoreactivity on human pyruvate dehydrogenase E2, the major autoantigen of primary biliary cirrhosis: implication for a conformational autoepitope. *J. Immunol.* **144**.
- Surh CD, Roche TE, Danner DJ, Ansari A, Coppel RL, Prindiville T, Dickson ER & Gershwin ME (1989). Antimitochondrial autoantibodies in primary biliary cirrhosis recognize cross-reactive epitope(S) on protein X and dihydrolipoamide acetyltransferase of pyruvate dehydrogenase complex. *Hepatology* **10**, 127-133.

- Svedberg T & Pedersen KO (1940). *The Ultracentrifuge*, Oxford University Press, London.
- Svergun DI (1992). Determination of the regularization parameter in indirect transform methods using perceptual criteria. *J. Appl. Cryst.* **25**, 495-503.
- Svergun DI (1999). Restoring low resolution structures of biological macromolecules from solution scattering using simulated annealing. *Biophys. J.* **76**, 2879-2886.
- Svergun DI, Barberato C & Koch MHJ (1995). CRY SOL - A program to evaluate x-ray solution scattering of biological macromolecules from atomic coordinates. *J. Appl. Cryst.* **28**, 768-773.
- Svergun DI, Barberato C, Koch MH, Feller L & Vachette P (1997a). Large differences are observed between the crystal and solution quaternary structures of allosteric aspartate transcarbamylase in the R state. *Proteins Struct. Funct. Genet.* **27**, 110-117.
- Svergun DI & Koch MHJ (2003). Small-angle scattering studies of biological macromolecules in solution. *Rep. Progr. Phys.* **66**, 1735-1782.
- Svergun DI, Petoukhov MV, Koch MH & Konig S (2000). Crystal versus solution structures of thiamine diphosphate-dependent enzymes. *J. Biol. Chem.* **275**, 297-302.
- Svergun DI, Petoukhov MV & Koch MHJ (2001). Determination of domain structure of proteins from X-ray solution scattering. *Biophys. J.* **80**, 2946-2953.
- Svergun DI & Stuhrmann HB (1991). New developments in direct shape determination from small-angle scattering. 1. Theory and model calculations. *Acta Cryst.* **A47**, 736-744.
- Svergun DI, Volkov VV, Kozin MB & Stuhrmann HB (1996). New developments in direct shape determination from small-angle scattering. 2. Uniqueness. *Acta Cryst.* **A52**, 419-426.

- Svergun DI, Volkov VV, Kozin MB, Stuhrmann HB, Barberato C & Koch MHJ (1997b). Shape determination from solution scattering of biopolymers. *J. Appl. Cryst.* **30**, 798-802.
- Szabo P, Sheu KF, Robinson RM, Grzeschik KH & Blass JP (1990). The gene for the alpha polypeptide of pyruvate dehydrogenase is X-linked in humans. *Am. J. Hum. Genet.* **46**, 874-878.
- Texter FL, Radford SE, Laue ED, Perham RN, Miles JS & Guest JR (1988). Site-directed mutagenesis and <sup>1</sup>H-NMR spectroscopy of an interdomain segment in the pyruvate dehydrogenase multienzyme complex of *Escherichia coli*. *Biochemistry* **27**, 289-296.
- Thieme R, Pai EF, Schirmer RH & Schulz GE (1981). Three-dimensional structure of glutathione reductase at 2 Å resolution. *J. Mol. Biol.* **152**, 763-782.
- Toyoda T, Kobayashi R, Sekiguchi T, Koike K, Koike M & Takenaka A (1998a). Crystallization and preliminary X-ray analysis of pig E3 lipoamide dehydrogenase. *Acta Cryst.* **54**, 982-985.
- Toyoda T, Suzuki K, Sekiguchi T, Reed LJ & Takenaka A (1998b). Crystal structure of eukaryotic E3 lipoamide dehydrogenase from yeast. *J. Biochem.* **123**, 668-674.
- Trewhella J, Carlson VA, Curtis EH & Heidorn DB (1988). Differences in the solution structures of oxidized and reduced cytochrome c measured by small-angle X-ray scattering. *Biochemistry* **27**, 1121-1125.
- Vachette P & Svergun D (2000). Small-angle x-ray scattering by solutions of biological macromolecules. In *Structure and Dynamics of Biomolecules*, E Fanchon, E Geissler, JL Hodeau, JR Regnard & PA Timmins, eds. Oxford University Press, Oxford, pp. 199-235.
- Van de Water J., Fregeau D, Davis P, Ansari A, Danner D, Leung P, Coppel R & Gershwin ME (1988a). Autoantibodies of primary biliary cirrhosis recognize dihydrolipoamide acetyltransferase and inhibit enzyme function. *J. Immunol.* **141**, 2321-2324.

- Van de Water J., Gershwin ME, Leung P, Ansari A & Coppel RL (1988b). The autoepitope of the 74 kDa mitochondrial autoantigen of primary biliary cirrhosis corresponds to the functional site of dihydrolipoamide acetyltransferase. *J. Exp. Med.* **167**, 1791.
- Vigh R, Cser L, Kilar F & Simon I (1989). Different segmental flexibility of human serum transferrin and lactoferrin. *Arch. Biochem. Biophys.* **275**, 181-184.
- Vistica J, Dam J, Balbo A, Yikilmaz E, Mariuzza RA, Rouault TA & Schuck P (2004). Sedimentation equilibrium analysis of protein interactions with global implicit mass conservation constraints and systematic noise decomposition. *Anal. Biochem.* **326**, 234-256.
- Voet J & Voet D (1995). *Biochemistry*, John Wiley, New York.
- Volkov VV & Svergun DI (2003). Uniqueness of *ab initio* shape determination in small-angle scattering. *J. Appl. Cryst.* **36**, 860-864.
- Wagenknecht T, Grassucci R, Radke GA & Roche TE (1991). Cryoelectron microscopy of mammalian pyruvate dehydrogenase complex. *J. Biol. Chem.* **266**, 24650-24656.
- Wagenknecht T, Grassucci R & Schaak D (1990). Cryoelectron microscopy of frozen-hydrated alpha-ketoacid dehydrogenase complexes from *Escherichia coli*. *J. Biol. Chem.* **265**, 22402-22408.
- Wallis NG, Allen MD, Broadhurst RW, Lessard IAD & Perham RN (1996). Recognition of a surface loop of the lipoyl domain underlies substrate channelling in the pyruvate dehydrogenase multienzyme complex. *J. Mol. Biol.* **263**, 463-474.
- Wallis NG & Perham RN (1994). Structural dependence of post-translational modification and reductive acetylation of the lipoyl domain of the pyruvate dehydrogenase multienzyme complex. *J. Mol. Biol.* **236**, 209-216.

- Westphal AH, Fabiz-Kijowska A, Kester H, Obels PP & De Kok A (1995). The interaction between lipoamide dehydrogenase and the peripheral-component-binding domain from the *Azotobacter vinelandii* pyruvate dehydrogenase complex. *Eur. J. Biochem.* **234**, 861-870.
- Wexler ID, Hemalatha SG, McConnell J, Buist NR, Dahl HH, Berry SA, Cederbaum SD, Patel MS & Kerr DS (1997). Outcome of pyruvate dehydrogenase deficiency treated with ketogenic diets: studies in patients with identical mutations. *Neurology* **49**, 1655-1661.
- Wieland OH (1983). The mammalian pyruvate dehydrogenase complex: structure and regulation. *Rev. Physiol. Biochem. Pharmacol.* **96**, 123-170.
- Wijburg FA, Barth PG, Bindoff LA, Birch-Machin MA, van der Blij JF, Ruitenbeck W, Turnbull DM & Schutgens RB (1992). Leigh syndrome associated with a deficiency of the pyruvate dehydrogenase complex: results of treatment with a ketogenic diet. *Neuropediatrics* **23**, 147-152.
- Wilkinson KD & Williams CH (1981). NADH inhibition and NAD<sup>+</sup> activation of *Escherichia coli* lipoamide dehydrogenase catalyzing the NADH-lipoamide reaction. *J. Biol. Chem.* **256**, 2307-2314.
- Williams CH (1965). Studies on lipoyl dehydrogenase from *Escherichia coli*. *J. Biol. Chem.* **240**, 4793-4800.
- Williams CH (1992). In *Chemistry and Biochemistry of Flavoenzymes*, F Müller, ed. CRC Boca Raton, FL, pp. 121-211.
- Williams CH, Allison N, Russell GC, Prongay AJ, Arscott LD, Datta S, Sahlman L & Guest JR (1989). Properties of lipoamide dehydrogenase and thioredoxin reductase from *Escherichia coli* altered by site-directed mutagenesis. *Ann. NY Acad. Sci.* **80**, 6105-6109.
- Wriggers W & Birmanns S (2001). Using SITUS for flexible and rigid-body fitting of multi-resolution single-molecule data. *J. Struct. Biol.* **133**, 193-202.

- Wriggers W & Chacón P (2001). Modeling tricks and fitting techniques for multi-resolution structures. *Structure* **9**, 779-788.
- Yang D, Gong X, Yakhnin A & Roche TE (1998). Requirements for the adaptor protein role of dihydrolipoyl acetyltransferase in the up-regulated function of the pyruvate dehydrogenase kinase and pyruvate dehydrogenase phosphatase. *J. Biol. Chem.* **273**, 14130-14137.
- Yang YS & Frey PA (1986). Dihydrolipoyl transacetylase of *Escherichia coli*. Formation of 8-S-acetyldihydrolipoamide. *Biochemistry* **25**, 8173-8178.
- Yeaman SJ (1989). The 2-oxo acid dehydrogenase complexes: recent advances. *Biochem. J.* **257**, 625-632.
- Yeaman SJ, Fussey SP, Danner DJ, James OF, Mutimer DJ & Bassendine MF (1988). Primary biliary cirrhosis: identification of two major M2 mitochondrial autoantigens. *Lancet* **8594**, 1067-1070.
- Yeaman SJ, Hutcheson ET, Roche TE, Pettit FH, Brown JR, Reed LJ, Watson DC & Dixon GH (1978). Sites of phosphorylation on pyruvate dehydrogenase from bovine kidney and heart. *Biochemistry* **17**, 2364-2370.
- Yi J, Nemeria N, McNally A & Jordan F (1996). Effect of substitutions in the thiamine diphosphate-magnesium fold on the activation of the pyruvate dehydrogenase complex from *Escherichia coli* by cofactors and substrate. *J. Biol. Chem.* **271**, 33192-33200.
- Yphantis DA, Lary JW, Stafford WF, Liu S, Olsen PH, Hayes DB, Moody TP, Ridgeway TM, Lyons DA & Lauc TM (1994). On-line data acquisition for the Rayleigh interference optical system of the analytical ultracentrifuge. In *Modern Analytical Ultracentrifugation*, TM Schuster & TM Laue, eds. Birkhäuser, Boston, pp. 209-226.
- Zaccai G (2000). How soft is a protein? A protein dynamics force constant measured by neutron scattering. *Science* **288**, 1604-1607.

- Zhou ZH, Liao WC, Cheng RH, Lawson JE, McCarthy DB, Reed LJ & Stoops JK (2001a). Direct evidence for the size and conformational variability of the pyruvate dehydrogenase complex revealed by three- dimensional electron microscopy - The "breathing" core and its functional relationship to protein dynamics. *J. Biol. Chem.* **276**, 21704-21713.
- Zhou ZH, McCarthy DB, O'Connor CM, Reed LJ & Stoops JK (2001b). The remarkable structural and functional organization of the eukaryotic pyruvate dehydrogenase complexes. *PNAS* **98**, 14802-14807.

